



Universiteit
Leiden
The Netherlands

Accelerating the photocatalytic water splitting in catalyst-dye complexes

Shao, Y.

Citation

Shao, Y. (2021, February 24). *Accelerating the photocatalytic water splitting in catalyst-dye complexes*. Retrieved from <https://hdl.handle.net/1887/3147173>

Version: Publisher's Version

License: [Licence agreement concerning inclusion of doctoral thesis in the Institutional Repository of the University of Leiden](#)

Downloaded from: <https://hdl.handle.net/1887/3147173>

Note: To cite this publication please use the final published version (if applicable).

Cover Page



Universiteit Leiden



The handle <http://hdl.handle.net/1887/3147173> holds various files of this Leiden University dissertation.

Author: Shao, Y.

Title: Accelerating the photocatalytic water splitting in catalyst-dye complexes

Issue date: 2021-02-24

Accelerating the Photocatalytic Water Splitting in Catalyst–Dye Complexes

Yang Shao

邵洋

Yang Shao

Accelerating the Photocatalytic Water Splitting in Catalyst–Dye Complexes

Ph.D. thesis, Leiden University

Cover and Bookmark designed by Yang Shao

Printed by PRINTSUPPORT4U || www.printsupport4u.nl

This research was financed by the Chinese Scholarship Council (Grant No. 201606450019) and Leiden University. The use of supercomputer facilities at SURFsara was sponsored by NWO Physical Sciences, with financial support from the Netherlands Organization for Scientific Research (NWO) in the context of the NWO Solar to Products program (project number 733.000.007).

Accelerating the Photocatalytic Water Splitting in Catalyst–Dye Complexes

PROEFSCHRIFT

ter verkrijging van
de graad van Doctor aan de Universiteit Leiden,
op gezag van Rector Magnificus prof.dr.ir. H. Bijl,
volgens besluit van het College voor Promoties
te verdedigen op woensdag 24 februari 2021
klokke 13:45 uur

door

Yang Shao

geboren te Shandong, China
in 1990

Promotiecommissie

Promotor: Prof. dr. Huub J. M. de Groot

Copromotor: Dr. Francesco Buda

Overige leden: Prof. dr. Hermen S. Overkleeft (Leiden University)
Prof. dr. Sylvestre Bonnet (Leiden University)
Prof. dr. Evert Jan Meijer (University of Amsterdam)
Prof. dr. Sandra Luber (University of Zurich)

For my parents, my wife, and my son

Table of Contents

List of Abbreviations ii

List of Symbolsiv

Chapter 1

Introduction & Computational Tools1

1.1. Introduction 3

1.1.1 Moving toward Sustainable Energy Sources 3

1.1.2 Natural Photosynthesis 4

1.1.3 Artificial Photosynthesis 5

1.1.4 Dye-sensitized Photoelectrochemical Cell 7

1.1.5 Catalytic Water Oxidation Mechanism 9

1.2. Computational Tools14

1.2.1 Density Functional Theory (DFT)14

1.2.2 Exchange-Correlation Functionals and Other Approximations 17

1.2.3 Car-Parrinello Molecular Dynamics (CPMD)18

1.2.4 Free Energy Calculations..... 20

1.3. Aim and Outline of This Thesis 21

1.4. References 23

Chapter 2

Photocatalytic Water Splitting Cycle in a Catalyst–dye Supramolecular Complex 27

2.1. Introduction..... 29

2.2 Computational Details..... 32

2.2.1 Geometry Optimization at DFT level 32

2.2.2 Constrained *ab initio* Molecular Dynamics 33

2.3. Results and Discussion 35

2.3.1 Second Catalytic Water Oxidation Step..... 36

2.3.2 Third Catalytic Water Oxidation Step: O–O Bond Formation41

2.3.2.1	Attacking Water Rearrangement and Electron Transfer.....	42
2.3.2.2	Proton Diffusion	45
2.3.3	Fourth Catalytic Water Oxidation Step.....	49
2.4.	Conclusions.....	51
2.5	References.....	53
A.	Appendix	57

Chapter 3

A Proton Acceptor near the Active Site Lowers Dramatically the O–O Bond Formation Energy Barrier.....69

3.1.	Introduction.....	71
3.2	Computational Details.....	74
3.3.	Results and Discussion.....	74
3.3.1	Inclusion and Equilibration of an OH ⁻ Ion in the Simulation Box.....	74
3.3.2	Photooxidation of the NDI and O–O Bond Formation.....	77
3.3.3	Spontaneous Proton Transfer Following OOH Ligand Formation	79
3.3.4	Activation Free Energy Barrier and Reaction Rate Evaluation.....	80
3.4.	Conclusions.....	83
3.5	References.....	84
3.A.	Appendix.....	87

Chapter 4

Tuning the Proton-Coupled Electron Transfer Rate by Ligand Modification in Catalyst–Dye Supramolecular Complexes 91

4.1.	Introduction.....	93
4.2.	Results and Discussion	96
4.2.1	Geometry Optimization of the WOC–dye Complexes	96
4.2.2	Equilibration of WOC–dye Complexes in the Explicit Solvent Model	98
4.2.3	Constrained MD Simulations of the O–O Bond Formation Step.....	99
4.2.4	Free Energy Profile and Reaction Rate Estimation	102
4.2.5	Coupling between Electronic and Nuclear Motions	104
4.3.	Conclusions.....	107
4.4	References	109
4.A.	Appendix	111

Chapter 5

Two-Channel Model for Electron Transfer in a Dye–Catalyst–Dye Supramolecular Complex	125
5.1. Introduction.....	127
5.2. Results and Discussion	130
5.2.1 Geometry Optimization of the Dye–WOC–Dye Complex with DFT.	130
5.2.2 Equilibration of the System and Photooxidation of two NDI Dyes.	131
5.2.3 Constrained AIMD Simulations and Catalytic Water Oxidation Steps.	132
5.2.4 Free Energy Profile and Reaction Rate Evaluation.	136
5.3. Conclusions	139
5.4. References	140
5.A. Appendix.....	142

Chapter 6

Conclusions and Outlook	153
6.1. Conclusions	155
6.2. Outlook	159
6.3. References	161

Appendices

Summary	163
Samenvatting	165
List of Publications	169
Curriculum Vitae	171
Acknowledgments	173

List of Abbreviations

ADF	Amsterdam Density Functional
AIMD	<i>Ab Initio</i> Molecular Dynamics
APT	Concerted Atom-Proton Transfer
BO	Born-Oppenheimer approximation
BOMD	Born-Oppenheimer Molecular Dynamics
bpy	2,2'-bipyridine
CB	Conduction Band
CFF	Consistent Force Field
CHARMM	Chemistry at HARvard Macromolecular Mechanics
COSMO	Conductor-like Screening Model
CPMD	Car-Parrinello Molecular Dynamics
cy	<i>p</i> -cymene
DCACP	Dispersion-Correcting Atom-Centered Potential
DFT	Density Functional Theory
DFT-MD	DFT-based Car-Parrinello Molecular Dynamics
DS-PEC	Dye-Sensitized Photoelectrochemical Cell
DSSC	Dye-sensitized Solar Cells
EPT	Concerted Electron-Proton Transfer
ET	Electron Transfer
FMD	Free Molecular Dynamics
FS	Final State
GEA	Gradient Expansion Approximation
GGA	Generalized Gradient Approximation
GTH	Goedecker-Teter-Hutter
HEC	Hydrogen-Evolving Catalyst
HOMO	Highest Occupied Molecular Orbital
IEM	Ion Exchange Membrane
IS	Initial State
I₂M	Oxo-oxo Coupling
KS	Kohn-Sham
LDA	Local Density Approximation
LUMO	Lowest Unoccupied Molecular Orbital
MD	Molecular dynamics
NCAP	Nonadiabatic Conversion by Adiabatic Passage
NDI	2,6-diethoxy-1,4,5,8-diimide-naphthalene
NPT	Isothermal-isobaric Ensemble

NVT	Canonical Ensemble
OEC	Oxygen Evolving Center
OPBE	OPTX-Perdew-Burke-Ernzerhof
OPTX	Handy's Optimized Exchange
PBC	Periodic Boundary Conditions
PBE	Perdew-Burke-Ernzerhof
PCET	Proton-Coupled Electron Transfer
PEC	Photoelectrochemical Cell
PEM	Proton Exchange Membrane
PSI	PhotoSystem I
PSII	PhotoSystem II
PV-E	PV-Electrolysis
PT	Proton Transfer
PV	Photovoltaics
SOMO	Singly Occupied Molecular Orbital
TD-DFT	Time-Dependent Density Functional Theory
TIP₃P	Transferable Intermolecular Potential with 3 Points
TS	Transition State
TZP	Triple-Zeta Polarized Basis Set
VDOS	Vibrational Density of States
VMD	Visual Molecular Dynamics
WNA	Water Nucleophilic Attack
WOC	Water Oxidation Catalyst

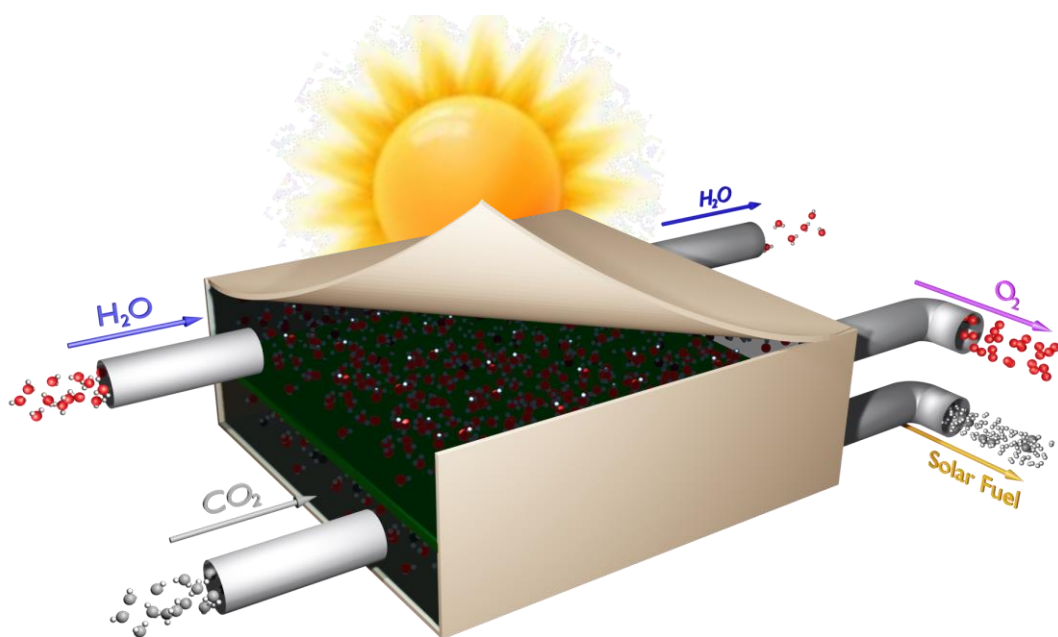
List of Symbols

A	pre-exponential frequency factor
d_{C-N}	C–N bond length
d_{C-N_ini}	C–N bond length of the initial intermediate
d_{C-N_fin}	C–N bond length of the final intermediate
$\langle d_{C-N} \rangle$	time-averaged C–N bond length
e	Euler's number
η	overpotential
$E[\rho]$	ground state energy
$E_{xc}[\rho]$	exchange-correlation functional
E_{tot}	total bonding energy
ΔE_{SOMO}	energy difference between molecular orbitals
ΔE_{int}	energy difference between intermediates
$\Delta \epsilon$	excitation energy around the transition state
f	oscillator strength
$g(r)$	radial distribution function
ΔG^*	activation free energy barrier
ΔG^o	thermodynamic driving force
ΔG	free energy change
ΔG_{calc}	calculated free energy change
ΔG_{exp}	experimentally measured free energy change
h	Planck constant
$J[\rho]$	classical Coulomb interaction
k	reaction rate
k_B	Boltzmann constant
ϕ_i	Kohn-Sham orbital
$n(r)$	coordination number
r	O...O distance
R	Universal gas constant
$\rho(\mathbf{r})$	electron density
S	total spin angular momentum
$2S+1$	spin multiplicity
T	thermodynamic temperature
$T[\rho]$	kinetic energy
σ	standard deviation
θ	dihedral angle
θ_{ini}	dihedral angle of the initial intermediate

θ_{fin}	dihedral angle of the final intermediate
$\langle \theta \rangle$	time-averaged dihedral angle
λ	constraint force
$\langle \lambda \rangle$	time-averaged constraint force
$\langle \lambda \rangle_{\text{r}}$	running average of constraint force
μ	fictitious mass of the electronic degrees of freedom
Λ_{ij}	Lagrange multipliers
$V_{\text{ee}}[\rho]$	electron-electron interaction
$V_{\text{ext}}[\rho]$	nucleus-electron interaction
$v_{\text{ext}}(\mathbf{r})$	external potential
ω	vibrational frequency

CHAPTER 1

Introduction & Computational Tools



Abstract

In this chapter the development of artificial photosynthesis, especially in dye-sensitized photoelectrochemical (DS-PEC) devices, and the context for this thesis is introduced. In addition, a brief outline of the various computational methods and supporting theories that are used throughout this thesis is presented.

1.1. Introduction

1.1.1 Moving toward Sustainable Energy Sources

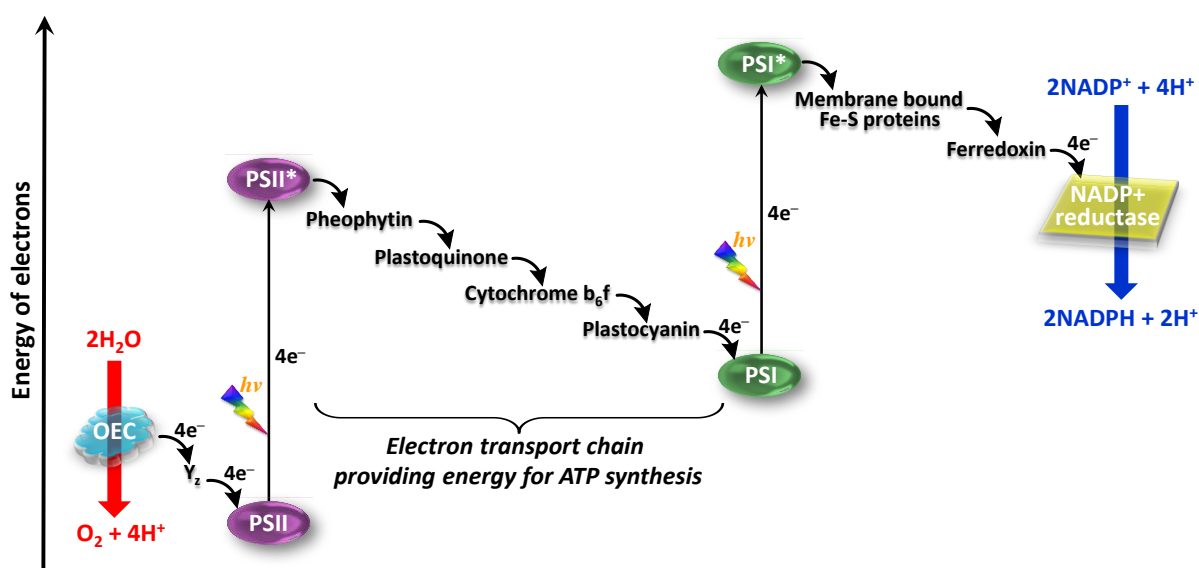
With the incremental rise of the global population and rapid development of industrialization and urbanization in the 21st century, the deterioration of environmental and energy crises has been aggravated due to the immoderate usage of non-renewable and carbon-based energy resources such as oil, coal, and natural gas. Currently, approximately 80% of the energy supply worldwide is provided by such fossil fuels, which are closely tied to severe environmental issues, *e.g.*, large quantities of emissions of carbon dioxide (CO₂), sulfur oxide, and other oxide particles, one of the major sources of greenhouse gases for global warming and air pollution.¹ In addition, the global energy consumption has grown at an alarming rate since 2000 without energy innovation to substantially reduce CO₂ emissions, and is predicted to steadily increase to 22 TW in 2030.² It is therefore imperative for humankind to search urgently for clean, sustainable, renewable, and environmentally friendly carbon-neutral/carbon-free alternatives of energy sources that have the potential to meet the present and future energy demand in the age of Anthropocene.³

Extensive research has been devoted to emerging alternatives such as photovoltaics (PV), dye-sensitized solar cells (DSSC), wind turbines, geothermal energy, tidal energy, and hydroelectric power plants. Renewables are expected to pass the level of 1 TW by 2025 at the latest, mainly due to PV and wind energy, and driven by the emerging economies from China and India. However, the regional dependence, as well as the difficulties and challenges in the storage and transportation of the converted energy in the form of electricity, is considered a hurdle on the way to full large-scale deployment and thus restrict the share of renewables in the future energy markets.⁴⁻⁵ Since more solar energy provided by the sun is delivered to the surface of the earth every hour than the global energy consumption for a whole year, and it is available almost anywhere, sunlight is considered the most abundant renewable energy source on the planet and to be the ultimate solution for the global energy problem facing humanity.⁶⁻⁷ Highly efficient conversion of solar energy to other forms of exploitable energy could therefore contribute to the realization of the green earth and a sustainable society. To displace energy carriers from fossil fuels, which are actually stored

sunlight, carbon-free solar fuels storing energy in the form of chemical bonds would be an attractive and practical option.⁸

1.1.2 Natural Photosynthesis

In nature, plants and organisms convert solar energy into chemically accessible energy in the form of chemical bonds via natural photosynthesis by utilizing sunlight, in which molecular oxygen (O_2) and energy-dense carbohydrates (e.g., sugar $C_6H_{12}O_6$) are produced from H_2O and CO_2 through a series of photochemical and chemical reactions, also known as ‘Z-scheme’ according to the shape of the flow diagram (see Scheme 1.1).^{5, 9}



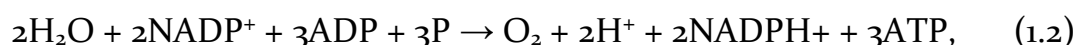
Scheme 1.1. Schematic representation of photosynthesis with the light-absorbing units PSI and PSII, the electron transport chain, the oxygen-evolving center (OEC), and $NADP^+$ reductase. Adapted from Ref. 5 with permission from The Royal Society of Chemistry.

Two coupled cofactor-protein complexes are involved in natural photosynthesis, denoted as photosystem II (PSII) and photosystem I (PSI), respectively (see Scheme 1.1).¹⁰ The absorption of sunlight by chlorophyll P680 ($P680 \rightarrow P680^*$) of PSII initiates the photosynthesis by pumping electrons to a nearby pheophytin and then to the acceptor side of PSI through rapid electron transfer (ET) steps, generating a charge-separated state (or electron-hole pairs) stable for hundreds of microseconds.¹¹ The oxidized $P680^+$ provides to the system a necessary driving force to perform redox-reactions and thus activates the photosynthetic water

oxidation and oxygen evolution occurring at the oxygen evolving complex (OEC) of PSII. The OEC consists of a cluster of four manganese ions and a calcium ion (Mn_4Ca). Driven by sunlight, two water molecules are oxidized to form molecular oxygen. Four electrons and protons (H^+) are released by PSII after four light absorption processes (see Scheme 1.1), as shown in eq. 1.1:



The electrons are transferred to PSI via plastoquinone and cytochrome b_6f molecules to regenerate P700 from the oxidized P700^+ , the chlorophyll molecules of PSI that are excited and oxidized after capturing a photon. Meanwhile, the reducing power generated by the electron transport chain is used by the ATP synthase complex to drive the conversion of ADP with inorganic phosphorus (P) into ATP. The protons are finally consumed in PSI together with the electrons from the excited P700^* for the reduction of NADP^+ to NADPH (nicotinamide adenine dinucleotide phosphate).¹²⁻¹³ The total net reaction for the natural photosynthesis is



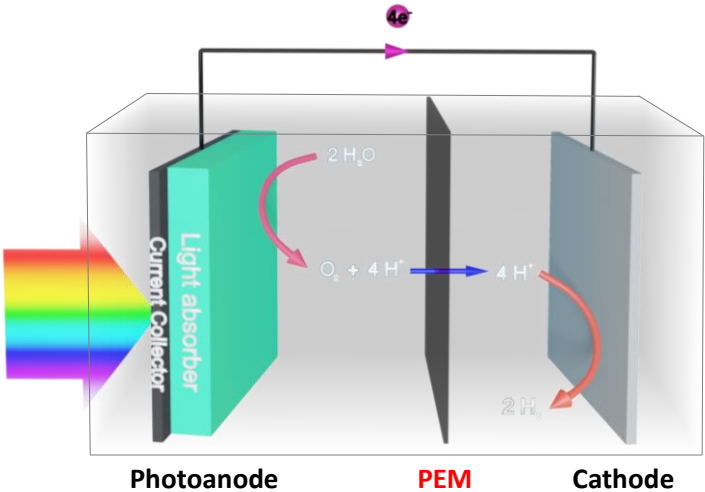
where the generated NADPH and ATP are subsequently used to fixate atmospheric CO_2 into carbohydrates in the light-independent Calvin-Benson-Bassham cycle.

1.1.3 Artificial Photosynthesis

As a product of mimicking the natural photosynthesis system, artificial photosynthesis has sprung up and attracted dramatically increasing interest in the field of renewable energy production in the past decades.¹³⁻¹⁶ The term artificial photosynthesis is commonly used to refer to any human-mediated process that captures and stores solar energy in the chemical bonds of useful and high-enthalpy chemicals, *i.e.* carbohydrates and so-called “solar fuels”. Solar energy can be converted either directly into chemical fuels via photoelectrochemical cells (PEC) or indirectly into fuels via PV-electrolysis (PV-E) systems driven by the electricity generated from solar energy (see Figure 1.1).^{14,}
¹⁷ Compared to centralized PV-E, decentralized PEC shows intrinsic advantages since the integration of the PV and electrocatalysis into one device enables it to

operate at low current density, reducing the overpotential and concentration losses.¹⁸ The production of solar fuels and chemicals in artificial photosynthesis has been increasingly investigated since the beginning of the the 21st century, in particular hydrogen production from water splitting, carbon-neutral fuel production from CO₂ reduction, ammonia production from nitrogen fixation, epoxide production from hydrocarbon oxygenation, and hydrogen peroxide production from oxygen reduction.¹⁹⁻²³

(a) Conventional PEC device



(b) PV-E device

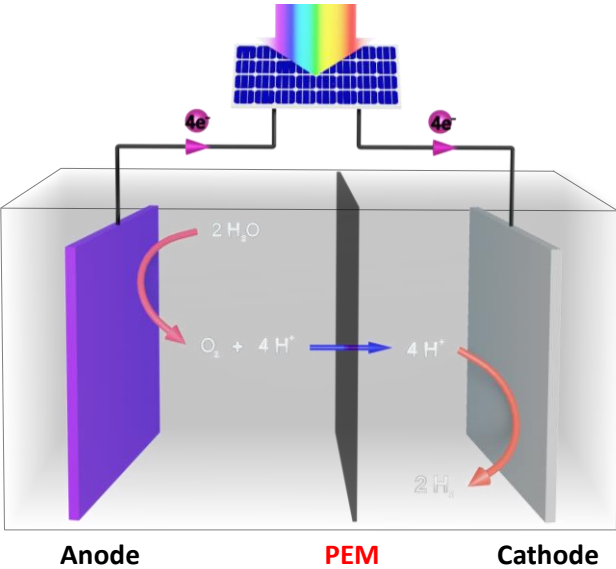


Figure 1.1. Schematic representation of light-driven water electrolysis via artificial photosynthetic systems. (a) Conventional PEC device model; (b) PVE device model. PEM (proton exchange membrane) indicates a proton exchange membrane for selective proton transport to the cathode.

As the smallest and simplest molecule among all the solar fuels, the energy-rich hydrogen (H_2) produces only water (H_2O) as its combustion product and from this perspective it is a most desirable and sustainable energy carrier to fulfill future increasing global energy requirements and to address the environmental pollution issues with zero emission of greenhouse gases.⁹ Molecular hydrogen can be derived from a wide variety of feedstocks, especially the cleavage of the abundant resource of water, which covers 70% of the earth. However, the majority of commercial H_2 being used is currently obtained primarily via steam reforming of hydrocarbons with fossil fuels as a feedstock, since H_2 is not readily available in nature. This is costly, complicated, and unsustainable.²⁴⁻²⁵ To employ H_2 as a real clean and long-term fuel on a large scale, extensive research effort is still required to develop techniques for the scalable, sustainable, economically viable production of H_2 from renewable sources, such as solar H_2 production by means of direct solar energy conversion from H_2O to storable and transportable carbon-free H_2 . In addition, solar-driven CO_2 reduction is also considered as a key process in artificial photosynthesis systems, in which the atmospheric CO_2 , one of the predominant greenhouse gases causing global warming and climate change, is fixed to synthesize valuable and sustainable carbon-neutral fuels.

1.1.4 Dye-sensitized Photoelectrochemical cell

Photoelectrochemical water splitting is a promising strategy for direct conversion of solar energy to storable H_2 or CO_2 -derived fuels with oxygen as a by-product, providing a sustainable source of renewable energy.²⁶ A PEC device should in principle combine three key functions governing natural photosynthesis: light harvesting by light absorbers, charge generation and separation in the light absorbers, as well as catalytic water oxidation and reduction.²⁷ Considerable efforts have been devoted to the development of high-efficiency PEC devices since the pioneering work by Fujishima and Honda in 1972, in which the photoelectrochemical water splitting into H_2 and O_2 was first demonstrated using a rutile TiO_2 semiconductor photoanode coupled with a platinum (Pt) cathode.²⁸ The use of rutile as photoanode, having a bandgap of 3.0 eV, limits the light absorption to ultraviolet (UV) region, and thus the quantum yield of water splitting under sunlight typically below 2%. Although other visible light-harvesting materials (*e.g.* $\alpha\text{-Fe}_2\text{O}_3$ ²⁹, WO_3 ³⁰, and BiVO_4 ³¹) have been investigated as possible photoanodes, the general drawbacks of them such as

narrow absorption in the solar spectrum, poor hole transport properties, and large bias voltages still need to be improved.¹² One alternative strategy for PEC devices would be to attach molecular photosensitizers onto the surface of the semiconductor anode. Besides, progress in the field is also being challenged by the fundamental understanding of the charge generation and separation processes, as well as the photocatalytic mechanisms, the search for efficient catalysts, *etc.*¹⁵

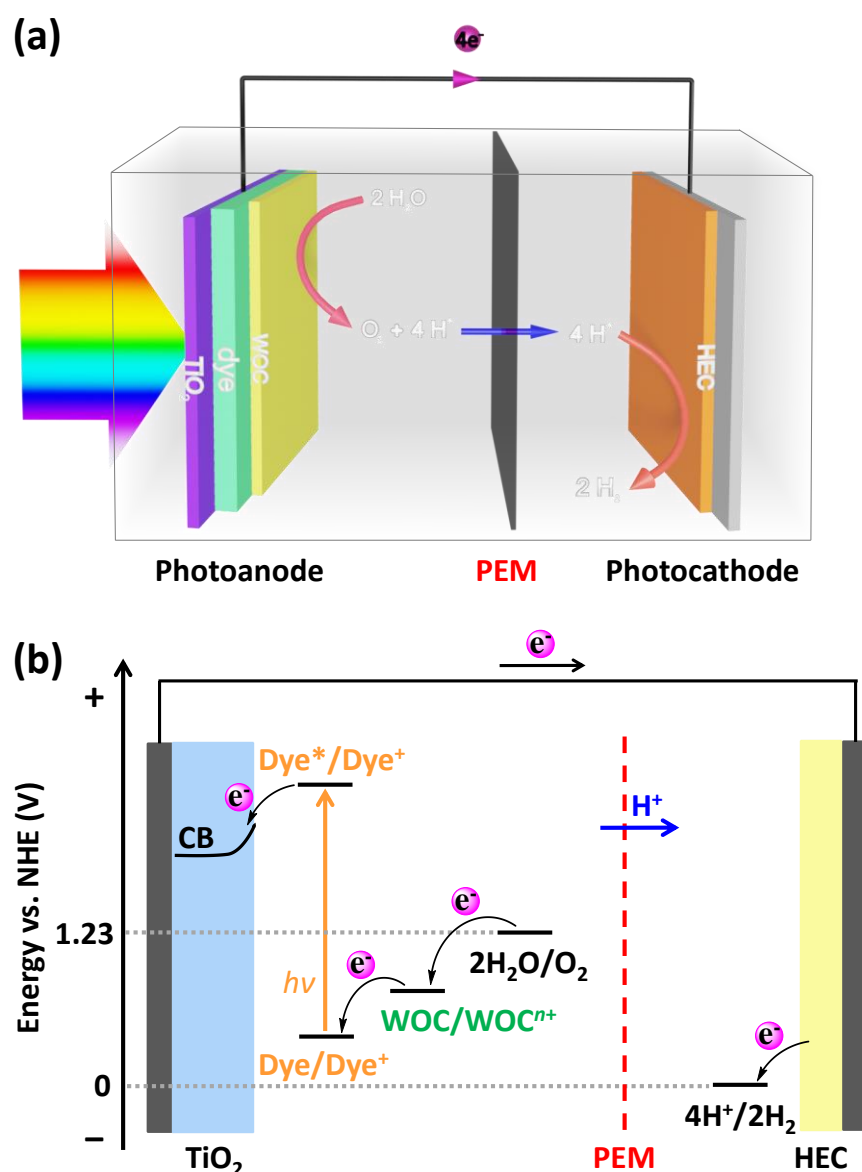


Figure 1.2. (a) Schematic representation of the DS-PEC device model for photocatalytic water splitting. (b) Schematic diagram of a proposed DS-PEC for solar-energy conversion. PEM indicates a proton exchange membrane for selective proton transport to the HEC. CB stands for the conduction band.

Inspired by DSSCs, visible light-harvesting sensitizers are integrated with water oxidation catalysts (WOCs) or hydrogen-evolving catalysts (HECs) on metal-oxide electrodes, thus overcoming the limitations imposed by the band gap of the metal oxide (*e.g.* TiO_2) material. In dye-sensitized PEC (DS-PEC) devices (see Figure 1.2), photons are absorbed in the photoanode, inducing the electron injection from the light-harvesting dye to the metal-oxide semiconductor and thus generating holes on the dye, the so-called charge separation process (see Figure 1.2b). The photo-oxidized dye should provide sufficient driving force for the catalytic multi-electron water oxidation half-reaction and serve as electron acceptor in the catalytic reaction. Under the catalysis of a WOC, water molecules are oxidized to molecular oxygen and protons by the photo-generated holes at the oxidized dye.

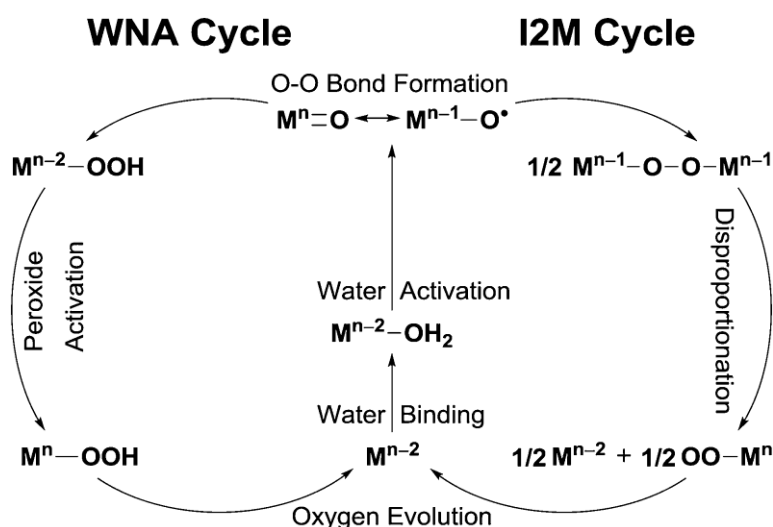
The photo-generated electrons migrate through an external circuit or electron-conducting membrane to the (photo)cathode, where protons are consumed for hydrogen production or CO_2 reduction.⁹ DS-PECs for solar-driven water splitting provide an opportunity to develop artificial photosynthetic devices in a scalable, affordable and sustainable way for direct solar-to-fuel conversion.

1.1.5 Catalytic water oxidation mechanism

The photocatalytic multi-electron water oxidation half-reaction occurs at the photoanode, requiring a high thermodynamic potential $E^0 \approx 1.23$ V, and has long been considered the most challenging and time-demanding step throughout the entire process limiting the overall yield and large-scale application of DS-PEC devices. In particular, the third catalytic water splitting step involving the O–O bond formation represents a thermodynamic and kinetic bottleneck because of the considerably high activation free energy barrier, especially when considering a single-site catalyst proceeding via a water nucleophilic attack (WNA) mechanism (see Scheme 1.2) partially due to the higher potentials required to produce a sufficiently electrophilic metal–oxo chemical species.³²

In both natural and artificial photosynthetic systems, the water oxidation proceeds via multiple photo-induced proton-coupled electron transfer (PCET) steps^{33–34}, which is broadly defined as any process involving the transfer of at least one electron and proton in a single kinetic step. Two general types of mechanisms for these PCET reactions have been widely accepted, either the sequential

mechanism in which the electron transfer and proton transfer (PT) occurs in a stepwise manner (ET first or PT first, see the extended eight-step Kok cycle in Figure 1.3a) or the concerted mechanism in which the movement of both electron and proton occurs simultaneously (also known as concerted electron-proton transfer (EPT)), (see Figure 1.3b).³⁵ In practice, the distinction between sequential and concerted PCET reactions is normally not rigorous and in part depends on the time scale that one considers. For example, a concerted PCET reaction identified at a long time scale is likely to be decoupled into two-step electron and proton transfer processes within short enough time scales. As a result, these two modes of PCET reactions are often experimentally hard to distinguish one from the other.³⁶ For the water oxidation in DS-PECs, the overall photocatalytic cycle consists of four PCET steps, which is a greatly uphill reaction requiring the input of energy (Gibbs energy of $+237.178 \text{ kJ mol}^{-1}$)¹², as depicted in Figure 1.3c showing the pH-independent free energy changes between intermediates along the photocatalytic water splitting cycle.³⁷ One should bear in mind that a concerted PCET (or EPT) process is normally desirable since it presents a lower energy barrier than that of a sequential PCET reaction. The sequence of these involved electron and proton transfer processes could therefore be fine-tuned to evoke concerted PCET and thus accelerate the catalytic water splitting, which can be achieved by ligand modification³⁸⁻⁴² of WOCs or solvent environmental tuning.⁴³⁻⁴⁶



Scheme 1.2. Overview of water nucleophilic attack (WNA) and oxo-oxo coupling (I2M) mechanisms for water oxidation catalysis. Copyright from Ref. 32 with permission from The Royal Society of Chemistry.

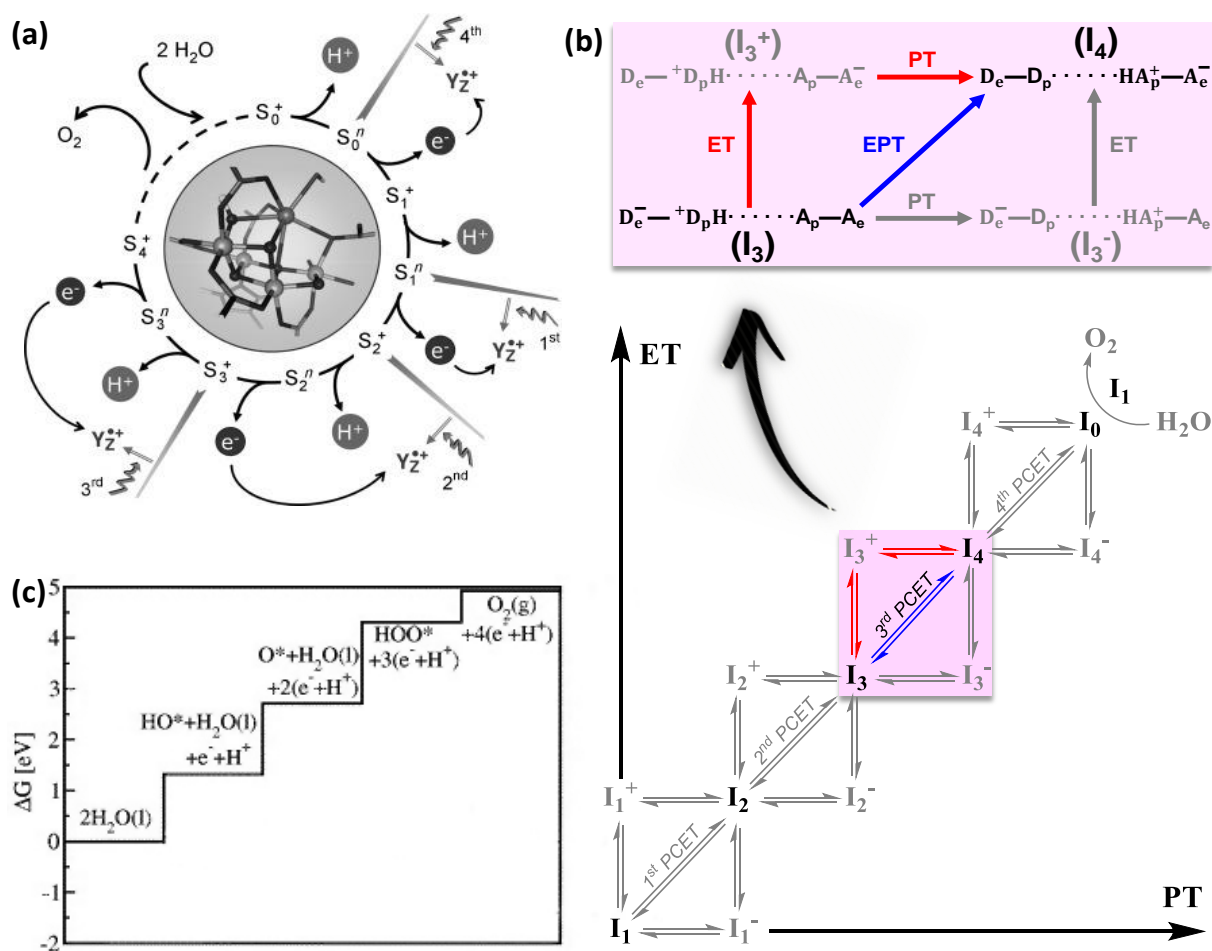


Figure 1.3. (a) Extended Kok's classical S-state cycle model including not only four oxidation but also four deprotonation steps by the Mn₄Ca complex in natural systems, as reproduced from Dau et al.³⁶ In the framework model the coupling between the ET step and the PT step is not covered. (b) The four PCET steps between intermediates (I_i) from I₁ to I₆ for water oxidation in a typical DS-PEC device. The vertical and horizontal double arrows correspond to the pathways of sequential mechanisms, either ET first or PT first. The diagonal double arrow denotes the broadly defined PCET and in the top panel the concerted mechanism labeled as EPT (concerted electron-proton transfer). The stable states are shown in black. The ligand exchange I₆ + H₂O → I₁ + O₂ is also indicated. The third step from I₃ to I₄ is specifically described in the top panel for clarity. The top panel is reproduced with permission from ref. 34. (c) The uphill free energy changes for the four PCET steps by a heterogeneous WOC at an overpotential of $\eta = -1.23$ V, where * indicates the adsorbents. Adapted with permission from ref. 37.

In a typical DS-PEC for water splitting, the photoanode combines necessarily two major fundamental components. First, ideal visible light-harvesting photosensitizers exhibit broad absorption in the solar spectrum, have robust anchoring groups to bind to the metal oxide semiconductor surface under aqueous conditions, show high charge carrier mobility, and establish an appropriate redox potential to drive the catalytic water oxidation at a WOC. Second, efficient WOCs modules have high intrinsic activity to overcome the reaction barriers, and show excellent optical and chemical stability, low overpotential, and high reaction rate for catalytic water oxidation. The way these two components are assembled plays a significant role in determining the photostability and efficiency of the DS-PEC device since fast electron transfer between the WOC and the oxidized sensitizer is critical to reducing the charge recombination from the semiconductor surface to the sensitizer and thus increasing the quantum yield.¹² A variety of strategies have been explored for the assembly of DS-PEC devices in the past years, for example, (i) the co-deposition method where the sensitizer and the WOC are deposited as separate moieties on the metal oxide semiconductor surface and (ii) the supramolecular approach where the sensitizer and the WOC are covalently bound forming a complex anchored onto the semiconductor surface.⁴⁷⁻⁴⁹ In particular, the supramolecular assembly approach by constructing WOC-dye dyads has experimentally and theoretically turned out to be able to facilitate rapid electron transfer from the WOCs to the oxidized sensitizers effectively in homogeneous systems.^{9, 50-52} On the other hand, a proper choice of the components in the WOC-dye supramolecular complex in light of the energetics and optical properties of sensitizers and WOCs provides an effective approach to the improvement of a dye-sensitized photoanode as well.⁵³⁻⁵⁵

Apart from developing novel dinuclear or multinuclear WOCs inspired by the Mn_4Ca complex in natural systems,³⁶ increasing attention has been focused on mononuclear WOCs since their first appearance in 2005, which breaks the dogma that at least two metal sites are required for catalytic water oxidation.⁵⁶⁻⁵⁸ The mononuclear complexes serving for water splitting provide guidance in the pursuit of cost-effective and efficient WOCs owing to their common advantages, including simple structures, ease of chemical modification, high catalytic activities, *etc.*^{32, 59} In addition, as an equally important component in the dye-sensitized photoanode, the oxidized sensitizer performs the task of stabilizing the

hole and acting as a primary electron acceptor during the catalytic water oxidation cycle, analogous to that of the redox-active tyrosine ($Y_Z^{\bullet+}$) near the OEC in PSII (see Figure 1.3a).³⁶ However, the search for ideal sensitizers is particularly challenging since rare molecules meet all the stringent requirements noted above so far.^{12, 60-61} Further optimization of the photoanode design can be achieved by the screening of light-absorbing dyes with excellent optical properties,⁶² inclusion of anchoring groups with established chemical and thermal stabilities,⁶³⁻⁶⁵ bridge units with rectifying properties,⁶⁶ and ancillary chromophores with complementary absorption properties and redox potentials.⁶⁷

In order to achieve further progress in the field of photoelectrochemical water splitting, computational techniques are and will be increasingly employed in the design and screening of optimal WOCs and sensitizers, in the estimation of the electronic, optical and overall properties of dye-sensitized photoanodes or DS-PEC devices, in the prediction of what happened and what will happen in the real systems that are being studied in response to variable conditions and parameters, in the fundamental understanding and unraveling of the electron transfer processes and catalytic water oxidation mechanisms, as well as in providing additional insights into various engineering problems.⁶⁸ The combination of experimental and theoretical approaches has turned out to be necessary to fully understand a given system or process since computational techniques constitute a very useful tool complementary to experiment serving as meaningful touchstones in an easier, reliable and efficient way, which are capable to avoid an expensive trial and error experimental strategy and provide a clear indication on the most cost-effective direction to undertake.³⁴ The collaboration between experimentalists and theoreticians will be critical for addressing the challenges of demonstrating photocatalytic water splitting at a near-unity yield.

Despite all the efforts in the development of novel DS-PEC devices with improved photoelectrodes⁶⁹⁻⁷⁰ or ion-exchange membranes⁷¹⁻⁷², the overall yield of the water oxidation half-reaction is still low, normally less than 20%.⁷³ Nevertheless, the motivation and determination for developing and optimizing high-performance artificial photosynthetic devices have remained and the work on artificial photosynthesis, especially concerning DS-PEC devices, is continuing to promote the realization of the green earth and sustainable society from the blueprint to reality.

1.2. Computational Tools

1.2.1 Density Functional Theory (DFT)

Considering that the nuclei are much heavier than the electrons in mass (about 2000 times), the nuclei move on much longer timescales than the electrons, allowing the electrons to respond almost instantaneously to the motion of the nuclei. In light of this fact, the Born-Oppenheimer (BO) approximation has been proposed in the early period of quantum mechanics, in which the electronic motion and the nuclear motion in molecules are treated separately, thus facilitating the description of the quantum states of molecules.⁷⁴ More precisely, in the BO approximation the motion of the atomic nuclei is neglected, *i.e.* the nuclei are assumed to be fixed at given positions when describing the electrons in a molecule. On this basis, the electronic structure (ground state and excited states) of given systems can be determined by solving the electronic Schrödinger equation as a function of the nuclear coordinates.

With the goal of simulating the behavior of atomic and molecular systems, density functional theory (DFT) has been widely used as one of the most popular and successful computational quantum mechanical approaches for *ab initio* calculations of the structural and dynamical properties of many-body systems. As Kohn noted in his Nobel lecture, DFT “has been most useful for systems of very many electrons where wave function methods encounter and are stopped by the “exponential wall”.⁷⁵ At variance from Hartree-Fock and multi-configuration theories that deal directly with the many-body wavefunction, in DFT the electronic energy of the system can be obtained as a functional of the electron density $\rho(\mathbf{r})$, which is defined as the average number of electrons per unit volume. The use of the electron density in obtaining an approximate solution to the Schrödinger equation and therefore describing the complicated physics behind the many-body electronic interactions, makes DFT computationally less expensive than wave function methods and yet sufficiently accurate.

At the heart of DFT, the Hohenberg-Kohn theorem states that the electron density determines all ground-state properties of the system, indicating the total energy of a many-body system as a functional of the ground-state density.⁷⁶

According to the form of the electronic Schrödinger equation, the energy functional of a many-electron interacting system can be written as

$$E[\rho] = T[\rho] + V_{\text{ext}}[\rho] + V_{\text{ee}}[\rho], \quad (1.3)$$

where the functional of the nucleus-electron interaction $V_{\text{ext}}[\rho]$ is explicitly known. It can be expressed in terms of a general external potential $v_{\text{ext}}(\mathbf{r})$ created either by the electrostatic field of the nuclei or external electric fields applied to the system

$$V_{\text{ext}}[\rho] = \int \rho(\mathbf{r}) v_{\text{ext}}(\mathbf{r}) d^3\mathbf{r}. \quad (1.4)$$

Unfortunately, the other two energy components, the kinetic energy functional $T[\rho]$, and the electron-electron interaction functional $V_{\text{ee}}[\rho]$, are unknown. In order to realize the direct minimization of the energy, proper approximations to these unknown terms are necessary.

In Kohn-Sham (KS) theory,⁷⁷ a fictitious system of N non-interacting electrons was proposed, in which a single determinant wavefunction in N “orbitals” $\{\phi_i\}$ was introduced to describe the N non-interacting electrons. These KS orbitals $\{\phi_i\}$ can be used to obtain the electron density of the KS non-interacting system

$$\rho(\mathbf{r}) = \sum_i^N |\phi_i(\mathbf{r})|^2 \quad (1.5)$$

in atomic units, in which the Coulomb’s constant, electron mass, elementary charge and the reduced Planck’s constant are defined to be 1. The kinetic energy for the many-body system is expressed in terms of $\{\phi_i\}$ according to

$$\begin{aligned} T[\rho] &= T_s[\rho] + T_c[\rho] \\ &= -\frac{1}{2} \sum_i^N \langle \phi_i | \nabla^2 | \phi_i \rangle + T_c[\rho], \end{aligned} \quad (1.6)$$

where $T_s[\rho]$ is the kinetic energy of the KS non-interacting reference system and the kinetic correlation energy $T_c[\rho]$ indicates the remaining unknown part of the kinetic energy for the actual interacting many-body system.

Considering that the classical Coulomb interaction $J[\rho]$ accounts for a significant component of the electron-electron interaction $V_{\text{ee}}[\rho]$ in many-body systems, the total

$V_{ee}[\rho]$ can be expressed as the sum of two parts, the known classical Coulomb interaction $J[\rho]$ and the unknown non-classical part $V_{nc}[\rho]$ integrated over all space

$$\begin{aligned} V_{ee}[\rho] &= J[\rho] + V_{nc}[\rho] \\ &= \frac{1}{2} \iint \frac{\rho(\mathbf{r})\rho(\mathbf{r}')}{|\mathbf{r} - \mathbf{r}'|} d\mathbf{r}d\mathbf{r}' + V_{nc}[\rho] \end{aligned} \quad (1.7)$$

The ground state energy of the many-body system is then formulated as

$$\begin{aligned} E[\rho] &= T[\rho] + V_{\text{ext}}[\rho] + V_{ee}[\rho] \\ &= (T_s[\rho] + T_c[\rho]) + V_{\text{ext}}[\rho] + (J[\rho] + V_{nc}[\rho]) \\ &= T_s[\rho] + V_{\text{ext}}[\rho] + J[\rho] + (T_c[\rho] + V_{nc}[\rho]) \\ &= T_s[\rho] + V_{\text{ext}}[\rho] + J[\rho] + E_{xc}[\rho], \end{aligned} \quad (1.8)$$

where the exchange-correlation functional $E_{xc}[\rho]$ is introduced to represent the total error made in using non-interacting kinetic energy and in treating the electron-electron interaction classically.

With a given approximation for the $E_{xc}[\rho]$, the minimization of the energy functional leads to the KS equations

$$\left[-\frac{1}{2} \nabla^2 + v_{\text{ext}}(\mathbf{r}) + \int \frac{\rho(\mathbf{r}')}{|\mathbf{r} - \mathbf{r}'|} d\mathbf{r}' + v_{xc}(\mathbf{r}) \right] \phi_i(\mathbf{r}) = \varepsilon_i \phi_i(\mathbf{r}), \quad (1.9)$$

where the local exchange-correlation potential $v_{xc}(\mathbf{r})$ is the functional derivative of the exchange-correlation functional with respect to the density

$$v_{xc}(\mathbf{r}) = \frac{\delta E_{xc}[\rho]}{\delta \rho}. \quad (1.10)$$

The self-consistent-field solution of the KS equations provides the ground state energy, which depends on the given/approximated $E_{xc}[\rho]$ functional.

Although there is still no explicit form available for the key exchange-correlation functional $E_{xc}[\rho]$, luckily $E_{xc}[\rho]$ is in general energetically substantially smaller than any other known terms, theoretically allowing for reasonable simple approximations of $E_{xc}[\rho]$ to obtain accurate estimates of the ground-state many-body energy.

1.2.2 Exchange-Correlation Functionals and Other Approximations

In the search for an exact formulation for density functionals, $E_{xc}[\rho]$ can be expressed as

$$\begin{aligned} E_{xc}(\rho) &= \min_{\Psi \rightarrow \rho} \langle \Psi | T + V_{ee} | \Psi \rangle - T_s[\rho] - J[\rho] \\ &= (T[\rho] - T_s[\rho]) + (V_{ee}[\rho] - J[\rho]). \end{aligned} \quad (1.11)$$

To develop accurate exchange-correlation functionals for DFT, the form of $E_{xc}[\rho]$ has to be approximated in a sufficiently precise way for different applications, which will determine the level of accuracy of the DFT results. With this goal, a variety of density functional approximations have been proposed, leading to great improvements in practical expressions for $E_{xc}[\rho]$, such as the local density approximation (LDA), the gradient expansion approximation (GEA), the generalized gradient approximation (GGA), and the Hybrid Exchange Functionals.⁷⁸

In particular, the introduction of the first derivative of the density in GGA leads to an energy functional that depends not only on the density but also on the gradient of the density, taking into account as well the non-homogeneity of the true electron density, and then initially enables the satisfactory application of DFT in the chemistry community. The general form for a GGA functional is

$$E_{xc}^{GGA}[\rho, \nabla \rho] = \int \rho(\mathbf{r}) v_{xc}(\rho(\mathbf{r}), \nabla \rho(\mathbf{r})) d\mathbf{r}. \quad (1.12)$$

As one of the best-performing GGA functionals, OPBE,⁷⁹ which combines Handy's optimized exchange (OPTX) with the PBE correlation, is primarily used in this thesis since the OPBE functional has shown to be able to accurately describe the transition-metal complexes, especially regarding the prediction of spin states.

In DFT, molecular orbitals are usually expanded as a linear combination of basis functions, most often atomic-like orbitals. However, when dealing with periodic systems, an alternative basis set consists of plane waves within a chosen cut-off energy. The choice of the basis set determines the level of accuracy and efficiency in DFT calculations. In the ADF (Amsterdam Density Functional software package⁸⁰⁻⁸¹) calculations, the Slater-type basis set, all-electron TZP (triple- ζ

polarized), is used for the considered systems, which provides an excellent balance between the accuracy of the results and the computational cost.

To further improve the computational efficiency of DFT-based calculations, pseudopotentials have been proposed to dramatically simplify the electronic structure calculations and thus save valuable computing time by replacing the core (i.e. non-valence) electrons and the strong nuclear potential with a softer potential (or pseudopotential) in a reliable way. Furthermore, the use of pseudopotentials in conjunction with a plane-wave basis set is a commonly used approach in electronic structure calculations. Specifically, the Car-Parrinello Molecular Dynamics program⁸² (CPMD) extensively used in this thesis, makes use of the plane wave/pseudopotential implementation of DFT, with pseudopotentials in the separable (Kleinman-Bylander) form.⁸³⁻⁸⁴

Additionally, considering that the van der Waals interactions play a significant role in most chemical systems, dispersion corrections developed by Grimme are also added to account for the effect of van der Waals forces in the systems.⁸⁵

1.2.3 Car-Parrinello Molecular Dynamics (CPMD)

Molecular dynamics (MD) is a powerful technique to investigate the real-time evolution of a system of interacting particles and thus to analyze equilibrium thermodynamic and dynamic properties of rather complex many-body systems at an atomistic level of description. In MD simulations the trajectories of atoms and molecules are governed by classical mechanics and Newton's laws of motion are used to predict the spatial position of each atom in the system as a function of time. Electrons are not present explicitly in MD simulations and the forces exerted on each atom are computed from molecular mechanics force fields comprised of empirical parameters, which are fitted to available experimental data or to results of quantum mechanical calculations. The simplified description of interatomic interaction and atomic motion, the poor transferability of force-fields, together with the insufficient predictive power in simulating chemical bonding processes are severe limitations of classical MD methods to provide a realistic quantitative analysis of the behavior and properties of real systems, especially when dealing with chemical reactions. Therefore, attractive approaches based on first principles are desirable to remove these limitations, such as in *ab initio* molecular dynamics (AIMD). However, AIMD simulations to increase the

accuracy and predictive power normally come at a significant computational cost because of the need to solve the electronic problem to compute atomic forces.

The CPMD approach, introduced by Car and Parrinello in 1985,⁸⁶⁻⁸⁷ is an extremely efficient implementation of AIMD. While in the straightforward Born-Oppenheimer Molecular Dynamics (BOMD) method explicit minimization of the electronic density functional is required at each time step, in CPMD this is done only for the initial nuclear configuration. In CPMD, a fictitious Newtonian dynamics is introduced for the electronic variables that keeps the electrons on the electronic ground state corresponding to each instantaneous ionic configuration, leading to a system of coupled electron-ion dynamics. More specifically, the electronic structure is only minimized for the initial configuration in CPMD simulations and then evolved in time using an extended Lagrangian formulation, which in turn provides accurate forces to drive the nuclear dynamics. The Euler-Lagrange equations of motion resulting from the Lagrangian are

$$M_I \frac{d^2}{dt^2} \mathbf{R}_I = -\nabla_I E[\{\phi_i\}, \mathbf{R}_I] \quad (1.13)$$

and

$$\mu \frac{d^2}{dt^2} \phi_i(\mathbf{r}, t) = -\frac{\delta E}{\delta \phi_i^*(\mathbf{r}, t)} + \sum_j \Lambda_{ij} \phi_j(\mathbf{r}, t) \quad (1.14)$$

for the dynamics of the nuclei with mass M and the evolution of the electrons respectively, where μ is the fictitious mass of the electronic degrees of freedom, Λ_{ij} the Lagrange multipliers associated to the orthonormalization condition of the KS orbitals ϕ_i , and E the energy functional as expressed in equation 1.8.

With such an algorithm, the computational cost of CPMD simulations is significantly lowered owing to the simultaneous calculation of the nuclear trajectory and corresponding instantaneous electronic ground state, thus allowing the dynamical investigation of relatively large systems (several hundred atoms) for a time scale of the order of ~ 10 ps in practical applications. Although in principle AIMD can be used in conjunction with any electronic structure method, DFT is most commonly employed to solve the electronic problems with the advantage of highly balanced accuracy and computing time.

1.2.4 Free Energy Calculations

Activated processes, such as the PCET steps in artificial photosynthetic water splitting, are customarily regarded as rare events occurring with low frequency. In these processes a transition occurs between two stable states, the initial state (IS) and final state (FS), separated by an activation free energy barrier (ΔG^*), which is the free energy change from the initial state of stable reactants to the transition state (TS). If the activation free energy barrier is very high compared to the thermal energy $k_B T$, the reaction is very unlikely to proceed spontaneously within the typical MD simulation time scale, which therefore leads to a low probability to locate the system close to the transition state.

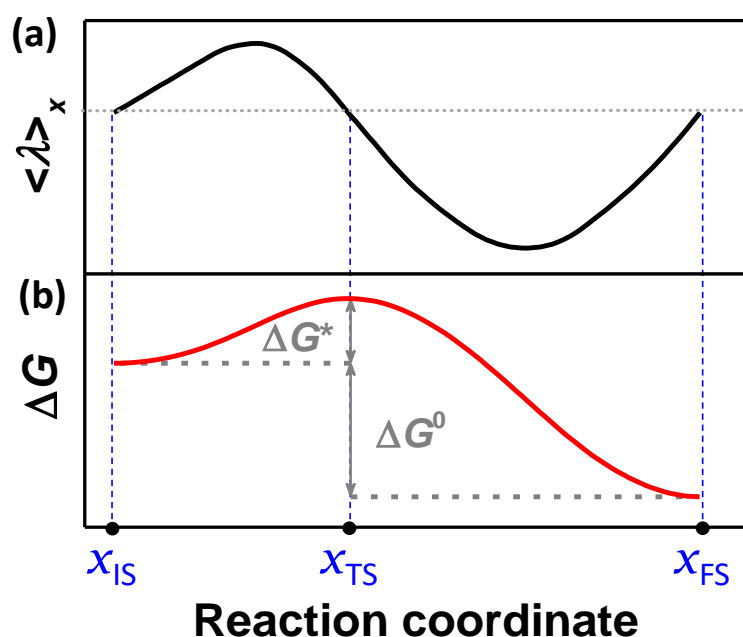


Figure 1.4 (a) Time-averaged constraint force represented by the Lagrangian multiplier $\langle \lambda \rangle_x$ as a function of the reaction coordinate x . (b) Free energy profile along the reaction coordinate computed from thermodynamic integration. ΔG^0 represents the thermodynamic driving force.

The “bottleneck” regions of the phase space would be rarely reached during a DFT-based Car-Parrinello MD (DFT-MD) simulation. The so-called Blue Moon approach,⁸⁸ is a constrained MD method,⁸⁹⁻⁹⁰ and is employed in this thesis to compute the free energy profile along the photocatalytic water oxidation reaction consisting of four PCET steps. Particular attention is devoted to the third PCET

step involving the O–O bond formation process. To do so, the reaction coordinate, a function of the positions of the nuclei (in this thesis the distance between two atoms), is constrained to a series of fixed values in the range of $x_{IS} < x < x_{FS}$ along a certain reaction path, where x_{IS} corresponds to the reaction coordinate at the initial state and x_{FS} the reaction coordinate at the final state. For each value of the reaction coordinate x a time-averaged constraint force (or mean force) $\langle \lambda \rangle_x$ is obtained, where λ is the Lagrangian multiplier associated to the constraint at x . This time-averaged constraint force should be equal to zero at an equilibrium or transition state, *i.e.*, $\langle \lambda \rangle_{x_{IS}} = 0$, $\langle \lambda \rangle_{x_{TS}} = 0$, and $\langle \lambda \rangle_{x_{FS}} = 0$ (see Figure 1.4). The free energy change for each catalytic step is then obtained by thermodynamic integration of the time-averaged constraint force along the reaction path

$$\Delta G(x) = \int_{x_{IS}}^{x_{FS}} \langle \lambda \rangle_x dx. \quad (1.15)$$

According to standard transition state theory,⁹¹⁻⁹² the reaction rate (k) determined by the activation free energy barrier ΔG^* can be expressed as

$$k = \frac{k_B T}{h} \cdot e^{-\frac{\Delta G^*}{RT}}, \quad (1.16)$$

where R and T are the universal gas constant and thermodynamic temperature, respectively. One should keep in mind that in the DFT-MD simulations protons are treated classically and thus proton tunneling effects are neglected. In the current study, only the activation energy barrier is considered as the main factor governing the reaction rate.

1.3. Aim and Outline of This Thesis

PCET plays a crucial role in a wide range of biological and chemical reactions concerning energy conversion processes, such as natural and artificial photosynthesis. Given that the overall catalytic water oxidation consists of four consecutive PCET steps, sequential or concerted, it is therefore of fundamental significance to unveil the intrinsic catalytic mechanism as well as the factors determining the PCET rate and thus to find strategies to facilitate the catalytic water oxidation. Computational tools provide a powerful and essential technique

for the understanding and engineering of efficient DS-PEC devices for water splitting.

In Chapter 2, constrained AIMD simulations are performed to explore the photocatalytic water splitting cycle driven by a supramolecular WOC–dye complex integrating a mononuclear Ru-based WOC with a fully organic naphthalene-diimide (NDI) dye in explicit water solvent and to estimate the free energy profile for each catalytic step. The proton and electron dynamics are followed to demonstrate the effect of spin alignment and solvent rearrangement in facilitating the PCET processes.

Since the O–O bond formation process via water nucleophilic attack has been confirmed to be the thermodynamic and kinetic bottleneck in photocatalytic water oxidation due to the considerably high activation free energy barrier, in Chapter 3 a proton acceptor group (OH^-) is introduced in the hydration shell near the catalytic active site to investigate how and to what extent the solvent tuning, in this case the introduction of an extra proton acceptor, can accelerate the O–O bond formation process in a WOC–dye supramolecular complex by means of CPMD simulations.

Recent analysis of PCET reactions acknowledges the importance of nonadiabatic terms connecting electronic states, which are usually treated as probabilistic events for the conversion of reactants into products in the context of nonadiabatic transition state theory.^{34, 93} Constrained AIMD simulations are carried out to investigate the rate-limiting step in catalytic water oxidation in a series of WOC–dye supramolecular complexes functionalized with different alkyl groups on the catalyst component to understand if and how the resonant coupling between electronic and nuclear motions can accelerate the PCET rate in the O–O bond formation process in Chapter 4.

In Chapter 5, a two-channel model for ET in a dye–WOC–dye supramolecular complex is proposed for photocatalytic water splitting, in which a Ru-based WOC is covalently bonded to two NDI dyes. The two-channel model with two separate electron-transfer channels is investigated by constrained AIMD simulations to estimate the probability of the concurrent ET event from the WOC to the two separate dyes and to explore the possible intermediates involved and the sequence of ET/PT/PCET events along the photocatalytic water splitting cycle.

1.4. References

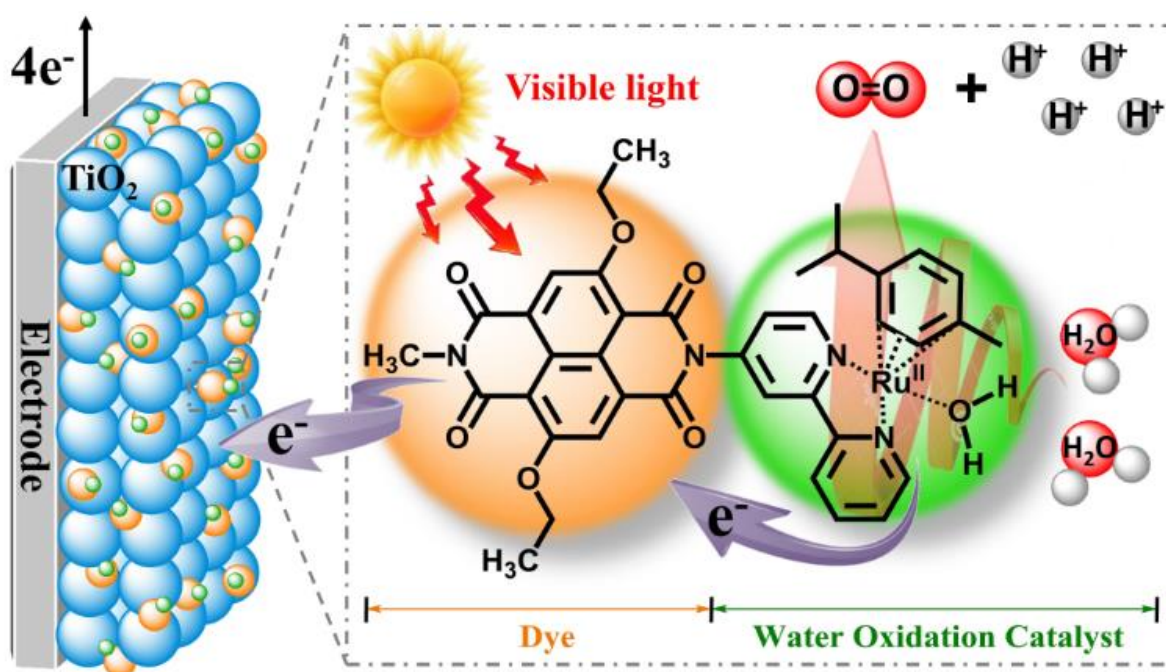
- [1] Purchase, R. L.; de Groot, H. J. M. *Interface Focus* **2015**, *5*, 20150014.
- [2] Hisatomi, T.; Domen, K. *Faraday Discuss.* **2017**, *198*, 11-35.
- [3] Pinaud, B. A.; Benck, J. D.; Seitz, L. C.; Forman, A. J.; Chen, Z.; Deutsch, T. G.; James, B. D.; Baum, K. N.; Baum, G. N.; Ardo, S.; Wang, H.; Miller, E.; Jaramillo, T. F. *Energy Environ. Sci.* **2013**, *6*, 1983-2002.
- [4] Lewis, N. S.; Nocera, D. G. *Proc. Natl. Acad. Sci.* **2006**, *103*, 15729-15735.
- [5] Berardi, S.; Drouet, S.; Francas, L.; Gimbert-Surinach, C.; Guttentag, M.; Richmond, C.; Stoll, T.; Llobet, A. *Chem. Soc. Rev.* **2014**, *43*, 7501-7519.
- [6] Kärkäs, M. D.; Verho, O.; Johnston, E. V.; Åkerman, B. *Chem. Rev.* **2014**, *114*, 11863-12001.
- [7] Chu, S.; Li, W.; Yan, Y.; Hamann, T.; Shih, I.; Wang, D.; Mi, Z. *Nano Futures* **2017**, *1*, 022001.
- [8] Ronge, J.; Bosserez, T.; Martel, D.; Nervi, C.; Boarino, L.; Taulelle, F.; Decher, G.; Bordiga, S.; Martens, J. A. *Chem. Soc. Rev.* **2014**, *43*, 7963-7981.
- [9] Yu, Z.; Li, F.; Sun, L. *Energy Environ. Sci.* **2015**, *8*, 760-775.
- [10] Dau, H.; Zaharieva, I. *Acc. Chem. Res.* **2009**, *42*, 1861-1870.
- [11] de Wijn, R.; van Gorkom, H. J. *Biochim. Biophys. Acta, Bioenerg.* **2002**, *1553*, 302-308.
- [12] Swierk, J. R.; Mallouk, T. E. *Chem. Soc. Rev.* **2013**, *42*, 2357-2387.
- [13] Cox, N.; Pantazis, D. A.; Neese, F.; Lubitz, W. *Interface Focus* **2015**, *5*, 20150009.
- [14] Zhang, B.; Sun, L. *Chem. Soc. Rev.* **2019**, *48*, 2216-2264.
- [15] Bozal-Ginesta, C.; Durrant, J. R. *Faraday Discuss.* **2019**, *215*, 439-451.
- [16] Ye, S.; Ding, C.; Liu, M.; Wang, A.; Huang, Q.; Li, C. *Adv. Mater.* **2019**, *31*, 1902069.
- [17] Jacobsson, T. J.; Fjallstrom, V.; Edoff, M.; Edvinsson, T. *Energy Environ. Sci.* **2014**, *7*, 2056-2070.
- [18] Purchase, R.; Cogdell, R.; Breitling, F.; Stadler, V.; Hulst, N. v.; Kramer, G.-J.; Ramirez, A.; Zwiijnenberg, R.; Kallergi, A.; Baan, J. B. d.; Rudra, I.; de Groot, H. J. M. *Semi-Synthetic Responsive Matrices for Artificial Photosynthesis, In Series on Chemistry, Energy and the Environment*, (Eds.: K. M., Kadish, R. Gullard), World Scientific, **2019**; pp. 47-69.
- [19] Ardo, S.; Fernandez Rivas, D.; Modestino, M. A.; Schulze Greiving, V.; Abdi, F. F.; Alarcon Llado, E.; Artero, V.; Ayers, K.; Battaglia, C.; Becker, J.-P.; Bederak, D.; Berger, A.; Buda, F.; Chinello, E.; Dam, B.; Di Palma, V.; Edvinsson, T.; Fujii, K.; Gardeniers, H.; Geerlings, H.; Hashemi, S. M.; Haussener, S.; Houle, F.; Huskens, J.; James, B. D.; Konrad, K.; Kudo, A.; Kunturu, P. P.; Lohse, D.; Mei, B.; Miller, E. L.; Moore, G. F.; Muller, J.; Orchard, K. L.; Rosser, T. E.; Saadi, F. H.; Schüttauf, J.-W.; Seger, B.; Sheehan, S. W.; Smith, W. A.; Spurgeon, J.; Tang, M. H.; van de Krol, R.; Vesborg, P. C. K.; Westerik, P., *Energy Environ. Sci.* **2018**, *11*, 2768-2783.
- [20] Shaner, M. R.; Atwater, H. A.; Lewis, N. S.; McFarland, E. W. *Energy Environ. Sci.* **2016**, *9*, 2354-2371.
- [21] Jia, J.; Seitz, L. C.; Benck, J. D.; Huo, Y.; Chen, Y.; Ng, J. W. D.; Bilir, T.; Harris, J. S.; Jaramillo, T. F. *Nat. Commun.* **2016**, *7*, 13237.
- [22] Gutierrez, R. R.; Haussener, S. *J. Electrochem. Soc.* **2016**, *163*, H1008-H1018.
- [23] Haas, T.; Krause, R.; Weber, R.; Demler, M.; Schmid, G. *Nat. Catal.* **2018**, *1*, 32-39.
- [24] Abdalla, A. M.; Hossain, S.; Nisfindy, O. B.; Azad, A. T.; Dawood, M.; Azad, A. K. *Energy Convers. Manage.* **2018**, *165*, 602-627.
- [25] Gibson, E. A. *Chem. Soc. Rev.* **2017**, *46*, 6194-6209.
- [26] Grätzel, M. *Nature* **2001**, *414*, 338-344.
- [27] Monti, A.; de Ruiter, J. M.; de Groot, H. J. M.; Buda, F. *J. Phys. Chem. C* **2016**, *120*, 23074-23082.
- [28] Fujishima, A.; Honda, K. *Nature* **1972**, *238*, 37-38.
- [29] Sivula, K.; Le Formal, F.; Grätzel, M. *ChemSusChem* **2011**, *4*, 432-449.
- [30] Kalanur, S. S.; Duy, L. T.; Seo, H. *Top. Catal.* **2018**, *61*, 1043-1076.

- [31] Park, Y.; McDonald, K. J.; Choi, K.-S. *Chem. Soc. Rev.* **2013**, *42*, 2321-2337.
- [32] Shaffer, D. W.; Xie, Y.; Concepcion, J. J. *Chem. Soc. Rev.* **2017**, *46*, 6170-6193.
- [33] Hammes-Schiffer, S. *Chem. Rev.* **2010**, *110*, 6937-6938.
- [34] Hammes-Schiffer, S. *J. Am. Chem. Soc.* **2015**, *137*, 8860-8871.
- [35] Hammes-Schiffer, S. *Energy Environ. Sci.* **2012**, *5*, 7696-7703.
- [36] Dau, H.; Limberg, C.; Reier, T.; Risch, M.; Roggan, S.; Strasser, P. *ChemCatChem* **2010**, *2*, 724-761.
- [37] Rossmeisl, J.; Qu, Z. W.; Zhu, H.; Kroes, G. J.; Nørskov, J. K. *J. Electroanal. Chem.* **2007**, *607*, 83-89.
- [38] Maji, S.; Vigara, L.; Cottone, F.; Bozoglian, F.; Benet-Buchholz, J.; Llobet, A. *Angew. Chem. Int. Ed.* **2012**, *51*, 5967-5970.
- [39] Garrido-Barros, P.; Funes-Ardoiz, I.; Drouet, S.; Benet-Buchholz, J.; Maseras, F.; Llobet, A. *J. Am. Chem. Soc.* **2015**, *137*, 6758-6761.
- [40] Wilson, A. D.; Newell, R. H.; McNevin, M. J.; Muckerman, J. T.; Rakowski DuBois, M.; DuBois, D. L. *J. Am. Chem. Soc.* **2006**, *128*, 358-366.
- [41] Bediako, D. K.; Solis, B. H.; Dogutan, D. K.; Roubelakis, M. M.; Maher, A. G.; Lee, C. H.; Chambers, M. B.; Hammes-Schiffer, S.; Nocera, D. G. *Proc. Natl. Acad. Sci.* **2014**, *111*, 15001-15006.
- [42] Solis, B. H.; Maher, A. G.; Honda, T.; Powers, D. C.; Nocera, D. G.; Hammes-Schiffer, S. *ACS Catal.* **2014**, *4*, 4516-4526.
- [43] Song, N.; Concepcion, J. J.; Binstead, R. A.; Rudd, J. A.; Vannucci, A. K.; Dares, C. J.; Coggins, M. K.; Meyer, T. J. *Proc. Natl. Acad. Sci.* **2015**, *112*, 4935-4940.
- [44] Coggins, M. K.; Zhang, M.-T.; Chen, Z.; Song, N.; Meyer, T. J. *Angew. Chem. Int. Ed.* **2014**, *53*, 12226-12230.
- [45] Chen, Z.; Concepcion, J. J.; Song, N.; Meyer, T. J. *Chem. Commun.* **2014**, *50*, 8053-8056.
- [46] Stewart, D. J.; Concepcion, J. J.; Brennaman, M. K.; Binstead, R. A.; Meyer, T. J. *Proc. Natl. Acad. Sci.* **2013**, *110*, 876-880.
- [47] Ding, X.; Gao, Y.; Ye, L.; Zhang, L.; Sun, L. *ChemSusChem* **2015**, *8*, 3992-3995.
- [48] Moore, G. F.; Blakemore, J. D.; Milot, R. L.; Hull, J. F.; Song, H.-e.; Cai, L.; Schmuttenmaer, C. A.; Crabtree, R. H.; Brudvig, G. W. *Energy Environ. Sci.* **2011**, *4*, 2389-2392.
- [49] Ji, Z.; He, M.; Huang, Z.; Ozkan, U.; Wu, Y. *J. Am. Chem. Soc.* **2013**, *135*, 11696-11699.
- [50] Li, F.; Jiang, Y.; Zhang, B.; Huang, F.; Gao, Y.; Sun, L. *Angew. Chem. Int. Ed.* **2012**, *51*, 2417-2420.
- [51] Vagnini, M. T.; Smeigh, A. L.; Blakemore, J. D.; Eaton, S. W.; Schley, N. D.; D'Souza, F.; Crabtree, R. H.; Brudvig, G. W.; Co, D. T.; Wasielewski, M. R. *Proc. Natl. Acad. Sci.* **2012**, *109*, 15651-15656.
- [52] Frischmann, P. D.; Mahata, K.; Würthner, F. *Chem. Soc. Rev.* **2013**, *42*, 1847-1870.
- [53] Luo, J.; Im, J.-H.; Mayer, M. T.; Schreier, M.; Nazeeruddin, M. K.; Park, N.-G.; Tilley, S. D.; Fan, H. J.; Grätzel, M. *Science* **2014**, *345*, 1593-1596.
- [54] Sun, K.; Liu, R.; Chen, Y.; Verlage, E.; Lewis, N. S.; Xiang, C. *Adv. Energy Mater.* **2016**, *6*, 1600379.
- [55] Ding, X.; Zhang, L.; Wang, Y.; Liu, A.; Gao, Y. *Coord. Chem. Rev.* **2018**, *357*, 130-143.
- [56] Zong, R.; Thummel, R. P. *J. Am. Chem. Soc.* **2005**, *127*, 12802-12803.
- [57] Hetterscheid, D. G. H.; Reek, J. N. H. *Angew. Chem. Int. Ed.* **2012**, *51*, 9740-9747.
- [58] Cao, R.; Lai, W.; Du, P. *Energy Environ. Sci.* **2012**, *5*, 8134-8157.
- [59] Watabe, S.; Tanahashi, Y.; Hirahara, M.; Yamazaki, H.; Takahashi, K.; Mohamed, E. A.; Tsubonouchi, Y.; Zahran, Z. N.; Saito, K.; Yui, T.; Yagi, M. *Inorg. Chem.* **2019**, *58*, 12716-12723.
- [60] Kishore, R. S. K.; Kel, O.; Banerji, N.; Emery, D.; Bollot, G.; Mareda, J.; Gomez-Casado, A.; Jonkheijm, P.; Huskens, J.; Maroni, P.; Borkovec, M.; Vauthey, E.; Sakai, N.; Matile, S. *J. Am. Chem. Soc.* **2009**, *131*, 11106-11116.

- [61] Swierk, J. R.; Méndez-Hernández, D. D.; McCool, N. S.; Liddell, P.; Terazono, Y.; Pahk, I.; Tomlin, J. J.; Oster, N. V.; Moore, T. A.; Moore, A. L.; Gust, D.; Mallouk, T. E. *Proc. Natl. Acad. Sci.* **2015**, *112*, 1681-1686.
- [62] Belić, J.; van Beek, B.; Menzel, J. P.; Buda, F.; Visscher, L. *J. Phys. Chem. A* **2020**, *124*, 6380-6388.
- [63] Ambrosio, F.; Martsinovich, N.; Troisi, A. *J. Phys. Chem. Lett.* **2012**, *3*, 1531-1535.
- [64] Zhang, L.; Cole, J. M. *ACS Appl. Mater. Interfaces* **2015**, *7*, 3427-3455.
- [65] Materna, K. L.; Crabtree, R. H.; Brudvig, G. W. *Chem. Soc. Rev.* **2017**, *46*, 6099-6110.
- [66] Monti, A.; Negre, C. F. A.; Batista, V. S.; Rego, L. G. C.; de Groot, H. J. M.; Buda, F. *J. Phys. Chem. Lett.* **2015**, *6*, 2393-2398.
- [67] Monti, A.; de Groot, H. J. M.; Buda, F. *J. Phys. Chem. C* **2014**, *118*, 15600-15609.
- [68] Emeter, M. E. Introduction to Computational Techniques. In *Environmental Modeling Using Satellite Imaging and Dataset Re-processing*, Springer International Publishing: Cham, 2019; pp. 19-37.
- [69] Xu, P.; McCool, N. S.; Mallouk, T. E. *Nano Today* **2017**, *14*, 42-58.
- [70] Wang, D.; Eberhart, M. S.; Sheridan, M. V.; Hu, K.; Sherman, B. D.; Nayak, A.; Wang, Y.; Marquard, S. L.; Dares, C. J.; Meyer, T. J. *Proc. Natl. Acad. Sci.* **2018**, *115*, 8523-8528.
- [71] Chabi, S.; Papadantonakis, K. M.; Lewis, N. S.; Freund, M. S. *Energy Environ. Sci.* **2017**, *10*, 1320-1338.
- [72] Ran, J.; Wu, L.; He, Y.; Yang, Z.; Wang, Y.; Jiang, C.; Ge, L.; Bakangura, E.; Xu, T. *J. Membr. Sci.* **2017**, *522*, 267-291.
- [73] Janna Olmos, J. D.; Becquet, P.; Gront, D.; Sar, J.; Dąbrowski, A.; Gawlik, G.; Teodorczyk, M.; Pawlak, D.; Kargul, J. *RSC Adv.* **2017**, *7*, 47854-47866.
- [74] Born, M.; Oppenheimer, R. *Ann. Phys.* **1927**, *389*, 457-484.
- [75] Kohn, W. *Rev. Mod. Phys.* **1999**, *71*, 1253-1266.
- [76] Hohenberg, P.; Kohn, W. *Phys. Rev.* **1964**, *136*, B864-B871.
- [77] Kohn, W.; Sham, L. J. *Phys. Rev.* **1965**, *140*, A1133-A1138.
- [78] Cohen, A. J.; Mori-Sánchez, P.; Yang, W. *Chem. Rev.* **2012**, *112*, 289-320.
- [79] Swart, M.; Ehlers, A. W.; Lammertsma, K. *Mol. Phys.* **2004**, *102*, 2467-2474.
- [80] te Velde, G.; Bickelhaupt, F. M.; Baerends, E. J.; Fonseca Guerra, C.; van Gisbergen, S. J. A.; Snijders, J. G.; Ziegler, T. *J. Comput. Chem.* **2001**, *22*, 931-967.
- [81] ADF2017, SCM. Theoretical Chemistry, Vrije Universiteit, Amsterdam, The Netherlands, <http://www.scm.com>.
- [82] CPMD, <http://www.cpmd.org>, Copyright IBM Corp., 1990-2019; Copyright MPI für Festkörperforschung Stuttgart, 1997-2001.
- [83] Kleinman, L.; Bylander, D. M. *Phys. Rev. Lett.* **1982**, *48*, 1425-1428.
- [84] Lin, I. C.; Coutinho-Neto, M. D.; Felsenheimer, C.; von Lilienfeld, O. A.; Tavernelli, I.; Rothlisberger, U. *Phys. Rev. B* **2007**, *75*, 205131.
- [85] Grimme, S.; Ehrlich, S.; Goerigk, L. *J. Comput. Chem.* **2011**, *32*, 1456-1465.
- [86] Car, R.; Parrinello, M. *Phys. Rev. Lett.* **1985**, *55*, 2471-2474.
- [87] Marx, D.; Hutter, J., *Ab initio molecular dynamics: basic theory and advanced methods*. Cambridge University Press, **2009**.
- [88] Ciccotti, G.; Ferrario, M. *Mol. Simul.* **2004**, *30*, 787-793.
- [89] Ensing, B.; Meijer, E. J.; Blöchl, P. E.; Baerends, E. J. *J. Phys. Chem. A* **2001**, *105*, 3300-3310.
- [90] Sprik, M.; Ciccotti, G. *J. Chem. Phys.* **1998**, *109*, 7737-7744.
- [91] Eyring, H. *J. Chem. Phys.* **1935**, *3*, 107-115.
- [92] Laidler, K. J.; King, M. C. *J. Phys. Chem.* **1983**, *87*, 2657-2664.
- [93] Hammes-Schiffer, S.; Tully, J. C. *J. Chem. Phys.* **1995**, *103*, 8528-8537.

CHAPTER 2

Photocatalytic Water Splitting Cycle in a Catalyst–dye Supramolecular Complex



This chapter is based on:

Shao Yang, Jessica M. de Ruiter, Huub J.M. de Groot, and Francesco Buda, *The Journal of Physical Chemistry C*, **2019**, 123, 21403–21414, DOI: 10.1021/acs.jpcc.9bo6401.

2

Abstract

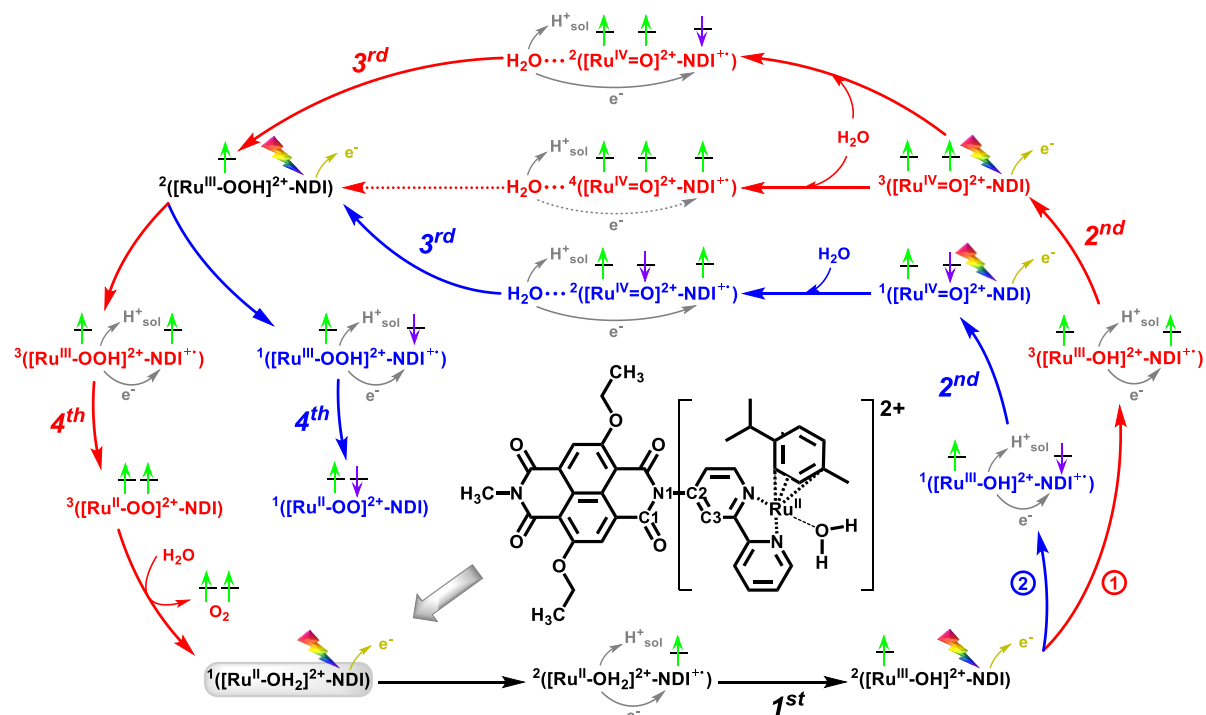
The basic idea of a DS-PEC cell, inspired by natural photosynthesis, is to couple the photo-induced charge separation process to the catalytic water splitting. The photo-oxidized dye coupled to a WOC should exert a thermodynamic driving force for the catalytic cycle, while water provides the electrons for regenerating the oxidized dye. These conditions impose specific energetic constraints on the molecular components of the photoanode in the DS-PEC. Here we consider a supramolecular complex integrating a mononuclear Ru-based WOC with a fully organic NDI dye that is able to perform fast photo-induced electron injection into the conduction band of the titanium-dioxide semiconductor anode. By means of constrained AIMD simulations in explicit water solvent, it is shown that the oxidized NDI provides enough driving force for the whole photocatalytic water splitting cycle. The results provide strong evidence for the significant role of spin alignment and solvent rearrangement in facilitating the proton-coupled electron transfer processes. The predicted activation free energy barriers confirm that the O–O bond formation is the rate-limiting step. Our results expand the current understanding of the photocatalytic water oxidation mechanism and provide *ex-ante* computational guidelines for the optimization of high-performance DS-PEC devices.

2.1. Introduction

As the largest exploitable renewable energy source by far, solar energy has the potential to be an alternative to fossil fuel derived energy and to reduce environmental pollution.^{1–2} The direct conversion of solar energy to storable chemical fuel is a promising strategy for providing a sustainable source of clean energy.^{3–4} Inspired by natural photosynthesis and the successful photocatalytic water oxidation achieved in PSII, remarkable effort has been devoted to the development of efficient artificial photosynthesis devices for solar-to-fuel conversion.^{5–12} A PEC cell performs this task by splitting water molecules into O₂, protons, and electrons at the anode, and evolving energy-rich H₂ or CO₂ derivatives at the cathode.^{13–15} The water oxidation half-reaction is currently considered the most challenging and limiting step for the development of efficient PEC devices for the production of solar fuels.^{16–18}

In the past decades, several systems have been proposed to facilitate the photocatalytic four-electron oxidation of water.^{19–20} In a DS-PEC the photoanode combines visible light-absorbing photosensitizers for light harvesting and charge separation, and a WOC for water splitting.^{21–25} The way these components are assembled will determine the efficiency and photostability of the device.²⁵ Much effort has been devoted to the exploration of assembling strategies: among others, the co-deposition method where the photosensitizer and the WOC are deposited as separate moieties on the semiconductor surface, and the supramolecular approach where the dye and WOC are covalently bound forming a complex anchored onto the semiconductor surface.^{17,19} The performance of a dye-sensitized photoanode can be improved by a proper choice of the components in the WOC–dye supramolecular complex taking into account the energetics and light-absorbing properties of photosensitizers and WOCs.^{26–32} It is also challenging to find an ideal dye that can absorb a significant region of the visible spectrum and have at the same time an appropriate redox potential to drive the whole catalytic water oxidation cycle coupled with an efficient WOC.²⁵ Computational studies constitute a very useful tool complementary to experiment by predicting reaction mechanisms and electronic properties of dye-sensitized photoanodes, thus avoiding an expensive trial and error strategy and providing a clear indication on the most cost effective direction to undertake.^{33–38}

Scheme 2.1. Proposed photocatalytic water splitting cycle by Ru-based WOC–dye system, consisting of four catalytic steps.^a



^aThe cycle starts from the $[(\text{cy})\text{Ru}^{\text{II}}\text{bpy}(\text{H}_2\text{O})]^{2+}\text{-NDI}$ intermediate (indicated shortly as $1([\text{Ru}^{\text{II}}\text{-OH}_2]^{2+}\text{-NDI})$) on the bottom-left of the scheme. The $[\text{Ru}^{\text{II}}\text{-OH}_2]^{2+}$ motif can have singlet, triplet, or quintet spin multiplicity and it was calculated that the singlet multiplicity has the lower energy by 1 – 2 eV, which is due to the strong ligand field in the complex.³⁹ The schematic structure of this starting intermediate is shown explicitly in the inset. It is assumed that each light flash induces an electron injection (golden arrows) from the NDI to the semiconductor electrode or to the next stage in a tandem cell, leading to the photooxidation of NDI: $\text{NDI} \rightarrow \text{NDI}^{+*}$. Green (α electrons) and purple (β electrons) vertical arrows depict the spin of unpaired electrons located on the WOC and NDI. For each catalytic step we consider all possible spin alignments between unpaired electrons on the WOC and on the NDI^{+*} , resulting in two alternative routes: ① in red and ② in blue. For the first step (in black), only the doublet state is possible. The dashed arrow indicates a process that is found to be thermodynamically unfavorable. H^+_{sol} represents the proton transferred to the solvent. The outer most pathway is most favorable according to the simulations. The superscript on the left indicates the spin multiplicity $2S+1$ for each intermediate.

We recently investigated *in silico* a supramolecular complex $[(\text{cy})\text{Ru}^{\text{II}}\text{bpy}(\text{H}_2\text{O})]^{2+}\text{-NDI}$ ($\text{cy} = p\text{-cymene}$, $\text{bpy} = 2,2'\text{-bipyridine}$, $\text{NDI} = 2,6\text{-diethoxy-1,4,5,8-diimide-naphthalene}$; $1([\text{Ru}^{\text{II}}\text{-OH}_2]^{2+}\text{-NDI})$ in Scheme 2.1) anchored on a TiO_2 semiconductor surface.⁴⁰ The catalytic cycle of the mononuclear WOC $[(\text{cy})\text{Ru}^{\text{II}}\text{bpy}(\text{H}_2\text{O})]^{2+}$ has been systematically examined by means of a combination of theoretical and experimental techniques,³⁹ and

ascertain whether the NDI dye considered in this work has the basic energetic requirements, *i.e.*, enough oxidation power, to drive the whole catalytic cycle for water oxidation.²⁵ (see schematic energy diagram in Figures 2.1a). Moreover, by means of constrained AIMD simulations in explicit water solvent, we establish the free energy profile for all the catalytic reaction steps starting from the oxidized WOC–dye intermediates (see Scheme 2.1). This allows also to determine the activation energy ΔG^* that can be used to estimate the reaction rate. The effect of spin alignment between unpaired electrons on the WOC and on the NDI⁺ is also explored (see route ① and ② in Scheme 2.1). In particular, for the second step starting from the oxidized WOC–dye intermediates ¹([Ru^{III}–OH]²⁺–NDI⁺) (route ②) and ³([Ru^{III}–OH]²⁺–NDI⁺) (route ①) are considered, for the third step the intermediates ²([Ru^{IV}=O]²⁺–NDI⁺) and ⁴([Ru^{IV}=O]²⁺–NDI⁺), and for the fourth step the intermediates ¹([Ru^{III}–OOH]²⁺–NDI⁺) and ³([Ru^{III}–OOH]²⁺–NDI⁺), respectively. A negative free energy change ΔG° is found for all the consecutive PCET steps, thus indicating that the oxidized NDI⁺ is fit for purpose. The calculated activation free energy barriers ΔG^* show that the O–O bond formation is the rate-limiting step. The AIMD simulations clarify the coupling between the electron transfer process and the bond-breaking/-forming events.⁵⁶ Moreover, the explicit inclusion of the solvent highlights the active role of the water rearrangement in the PCET processes. The gained insight in the photocatalytic water oxidation mechanism provides guidelines for the design and optimization of efficient photoanodes for DS-PEC devices.

2.2 Computational Details

2.2.1 Geometry Optimization at DFT level

The initial geometry of all the catalytic intermediates of the WOC–dye supramolecular complex were optimized using DFT calculations employing the OPBE exchange-correlation functional⁵⁷ and the TZP basis set.⁴⁰ The OPBE functional has shown to be accurate in describing transition-metal complexes, including Ru-based WOCs.^{58–63} In Table A2.2 we show a comparison between OPBE results and those obtained with the more commonly used PBE functional, which provides very similar results. In the geometry optimization, the continuum solvation model COSMO^{64–65} for water was used. These static calculations are performed with the ADF software package.^{66–67}

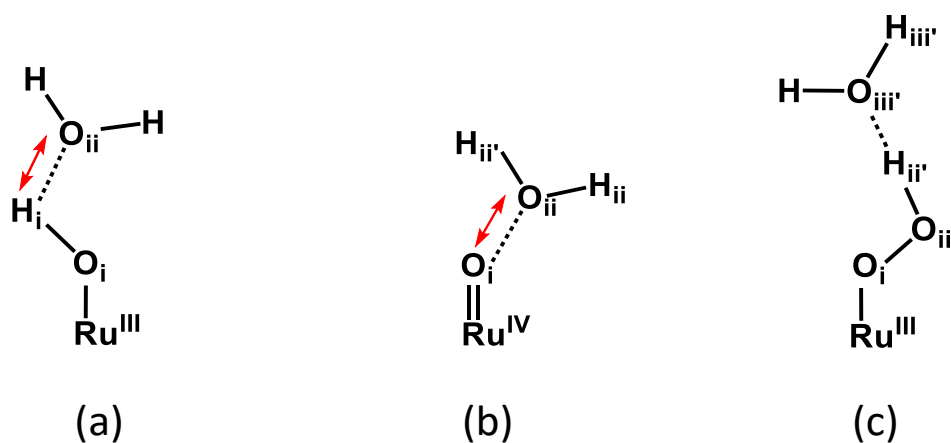
2.2.2 Constrained *ab initio* Molecular Dynamics

To obtain a realistic description of the catalytic reaction steps, the solvent was explicitly introduced in the simulations.^{61, 68} An orthorhombic box of dimensions $25.1 \times 17.7 \times 14.4 \text{ \AA}^3$ was used, containing the $[\text{WOC}]^{2+}$ –dye solute and 162 water molecules. The explicitly solvated systems were investigated through AIMD for the singly oxidized form of the complex ($[\text{WOC}]^{2+}$ –dye⁺) using the CPMD program.⁶⁹ The solvent environment for the CPMD simulations (pure neutral water, no ion included) was generated using Discovery Studio 2.5.⁷⁰ Prior to the AIMD simulations, the solvent was equilibrated using the TIP3P model implemented in the CHARMM force field and CFF partial charge parameters at 300 K,⁷¹ while the $[\text{WOC}]^{2+}$ –dye complex was kept fixed. The volume was then adjusted using constant pressure (NPT simulations at atmospheric pressure for 0.2 ns), after which the system was further allowed to evolve with constant volume (NVT simulations for 2 ns).

A so-called regeneration step is carried out at the beginning of each PCET step by first removing the excess solvated proton from the simulation box and performing an unconstrained AIMD simulation of ~360 fs at room temperature to equilibrate the system. Subsequently, one electron is removed from the simulation box, and the oxidized state is further re-equilibrated for another ~360 fs at room temperature.

All the CPMD simulations were performed in an aqueous environment at 300 K, using GTH pseudopotentials for the ruthenium transition metal,⁷² and DCACP pseudopotentials for the remaining atoms,⁷³ together with a plane wave cutoff of 70 Ry and the OPBE exchange-correlation functional. The water molecules are treated at the same DFT quantum-mechanical level as the solute, which is essential for the accurate description of the PCET steps following photoinduced electron injection from the NDI dye into the semiconductor. Periodic boundary conditions are applied with a time step of $\delta t = 5 \text{ a.u.}$ (1 a.u. = 0.0242 fs). Trajectory analysis and visualization for the CPMD output were carried out using VMD program.^{74–75}

Scheme 2.2. The schematic structure of the hydroxide (a), oxo (b), and hydroperoxide ligand (c) with a nearby solvent water molecule.^a



^aThe red double-sided arrow indicates the reaction coordinate considered for the (a) $[\text{Ru}^{\text{III}}-\text{OH}]^{2+} \cdots \text{H}_2\text{O}$ and (b) $[\text{Ru}^{\text{IV}}=\text{O}]^{2+} \cdots \text{H}_2\text{O}$ during the constrained MD simulations. The labeling of the atoms that are involved in the reaction steps is used throughout this paper.

Given that the catalytic reaction steps are unlikely to occur spontaneously during the typical AIMD simulation time scale, constrained MD and the so-called Blue Moon approach were employed as a rare event simulation technique.⁷⁶⁻⁷⁸ The reaction coordinate (in this case the distance between two atoms shown in Scheme 2.2) is constrained to a series of fixed values along a reaction path for both route ① and ②:

- (i) for the second PCET step (see Scheme 2.1), the distance between the proton (H_i) of the hydroxide ligand coordinated to the Ru atom and the oxygen (O_{ii}) of one solvent water molecule in the vicinity of $^2([\text{Ru}^{\text{III}}-\text{OH}]^{2+})$ is constrained in the range 1.6 – 1.0 Å (see Scheme 2.2a);
- (ii) for the third PCET step, the distance between the oxygen (O_i) coordinated to the Ru atom and the oxygen (O_{ii}) of one solvent water molecule is constrained in the range 3.0 – 1.5 Å (see Scheme 2.2b);
- (iii) for the fourth PCET step, no constraint is applied in the simulations (see Scheme 2.2c).

For each value of the reaction coordinate a time-averaged constraint force $\langle \lambda \rangle$ is obtained. This time-averaged constraint force is equal to zero at an equilibrium or transition state. The free energy change for each catalytic step is then obtained by thermodynamic integration along the reaction path.^{56, 79-81}

2.3. Results and Discussion

The whole photocatalytic water splitting cycle via both route ① and ②, as depicted in Scheme 2.1, is explored with AIMD simulations in explicit water solvent. In previous work we have shown that, when excited with visible light, the NDI is able to inject an electron into a TiO₂ semiconductor surface on a time scale of ~1 ps.⁴⁰ Therefore we assume that at the beginning of the simulation for each catalytic step, the system is already in its oxidized form: [WOC]²⁺–dye⁺.

Table 2.1. Computed activation free energy barrier ΔG^* (in kcal mol⁻¹), thermodynamic driving force ΔG^o (in kcal mol⁻¹), and estimated reaction rate k (in s⁻¹) for the four redox couples along the whole catalytic cycle and different spin alignments along the routes ① and ② shown in Scheme 2.1.^a

Step	Route	2S+1	Initial state			Final state		ΔG^*	ΔG^o	k
1 st	①+②	2	[Ru ^{II} –OH ₂] ²⁺ –NDI ⁺			[Ru ^{III} –OH] ²⁺ –NDI + H ⁺ _{sol}		1.7	–4.0	3.6×10 ¹¹
			↑			↑				
2 nd	① ②	3 1	[Ru ^{III} –OH] ²⁺ –NDI ⁺			[Ru ^{IV} =O] ²⁺ –NDI + H ⁺ _{sol}		2.3 4.6	–10.7 –1.1	1.3×10 ¹¹ 2.8×10 ⁹
			↑	↑	↑	↑				
			↑	↓	↑	↓				
3 rd	① ②	2 4 2	[Ru ^{IV} =O] ²⁺ –NDI ⁺ + H ₂ O _{sol}			[Ru ^{III} –OOH] ²⁺ –NDI + H ⁺ _{sol}		15.9 9.0	–8.5 –17.1	15.7 1.7×10 ⁶
			↑	↑	↓	↑				
			↑	↑	↑					
			↑	↓	↑	↑				
4 th	①+②	1 3	[Ru ^{III} –OOH] ²⁺ –NDI ⁺			[Ru ^{II} –OO] ²⁺ –NDI + H ⁺ _{sol}				
			↑		↓					
			↑	↑	↑	↑				

^aFor each intermediate it is indicated explicitly where the unpaired electrons are localized, on the Ru-based catalyst or on the NDI (↑ for the α electron and ↓ for the β electron). 2S+1 is the spin multiplicity of the system. H⁺_{sol} and H₂O_{sol} represent the solvated proton and a solvent water molecule, respectively. For the 3rd step the $S = 3/2$ state turns out to be thermodynamically unfavorable compared to the $S = 1/2$ configuration in route ①. The 4th step is found to proceed spontaneously at room temperature for both spin states, which implies no significant activation barrier. The results for the first step are from reference 40.

Before starting the AIMD simulations, we have checked with static DFT calculations whether the SOMO on the oxidized dye is lower in energy than the HOMO localized on the catalyst, since this is a basic energetic requirement to allow for electron transfer from the WOC to the dye, thus regenerating the

ground state of the dye for the next photoinduced catalytic step (see Figure 2.1). It is found that this energy level alignment is indeed satisfied for all the intermediates in the catalytic cycle following route ①, which turned out to be the most favorable route: The orbital energy difference is in the range $\sim 0.1 - 0.3$ eV (see Figure A2.2 and Table A2.2 in appendix).

Table 2.1 summarizes the computed activation free energy barrier ΔG^* , the free energy change from the initial to the final state (thermodynamic driving force ΔG^0), and estimated reaction rate k for the whole catalytic cycle and different spin alignments shown in Scheme 2.1. In the following we discuss in detail the most favorable catalytic cycle, while results concerning thermodynamically unfavorable catalytic steps are reported in the appendix for comparison.

We have previously shown that the first PCET catalytic step ($[\text{Ru}^{\text{II}}-\text{OH}_2]^{2+}-\text{NDI}^{+*} \rightarrow [\text{Ru}^{\text{III}}-\text{OH}]^{2+}-\text{NDI} + \text{H}^+_{\text{sol}}$) is exothermic with a thermodynamic driving force $\Delta G^0 \approx -4$ kcal mol $^{-1}$ (~ 0.17 eV) and presents a very low activation free energy barrier $\Delta G^* \approx 1.7$ kcal mol $^{-1}$ (~ 0.074 eV), which is only $\sim 3 k_{\text{B}}T$ at room temperature, corresponding with a very fast rate (see Table 2.1).⁴⁰ In the following sections the successive PCET catalytic water oxidation steps are discussed.

2.3.1 Second Catalytic Water Oxidation Step

The system with the oxidized intermediate $^3([\text{Ru}^{\text{III}}-\text{OH}]^{2+}-\text{NDI}^{+*})$ in the $S = 1$ state (see route ① in Scheme 2.1) is equilibrated at room temperature without constraint for ~ 2 ps (see Figure 2.2). By tracing the spin density along the free MD simulation trajectory we observe the photoinduced hole localized on the oxidized NDI^{+*} and one unpaired electron localized on the catalyst as expected (see Figure 2.2, inset). The analysis of the MD trajectory shows the hydroxide ligand forming a strong hydrogen bond with a nearby water molecule with an average distance $d(\text{H}_i-\text{O}_{\text{ii}})$ of ~ 1.7 Å (see Figure 2.2). Although we can observe some spontaneous attempts of proton transfer from the hydroxide to the neighboring water molecule, this process may occur on a time scale that is still prohibitive for AIMD.⁴⁰ Thus we use constrained AIMD to analyze the second PCET step shown in eq. 2.1, where H^+_{sol} represents the solvated proton:



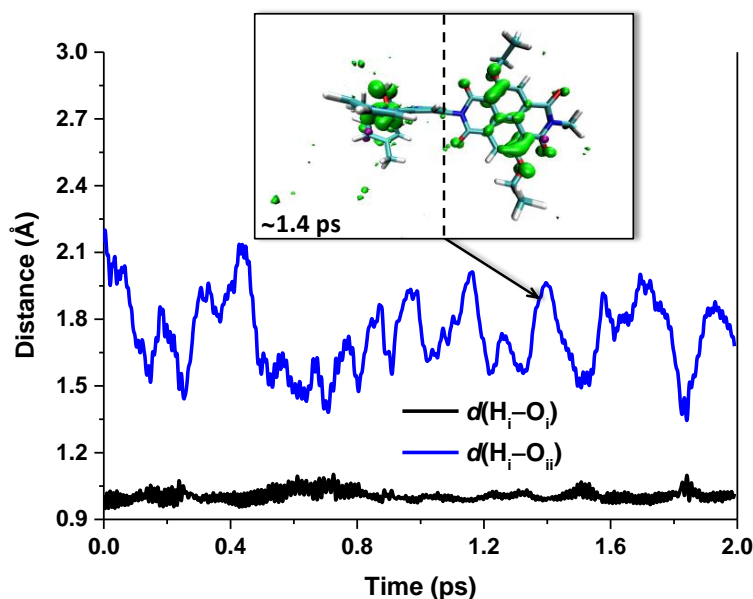


Figure 2.2. Time evolution of the geometrical parameter $d(\text{H}_i\text{--O}_i)$ (black line) and $d(\text{H}_i\text{--O}_{ii})$ (blue line) along the free MD simulation trajectory for the oxidized intermediate $^3([\text{Ru}^{\text{III}}\text{--OH}]^{2+}\text{--NDI}^{+\bullet})$ in route ①. See scheme 2.2 for the atomic labelling. We can observe a shortened $d(\text{H}_i\text{--O}_{ii}) \approx 1.3 \text{ \AA}$ and a corresponding stretched $d(\text{H}_i\text{--O}_i) \approx 1.1 \text{ \AA}$ at several time intervals ($\sim 0.25 \text{ ps}$, $\sim 0.71 \text{ ps}$, and $\sim 1.84 \text{ ps}$), which can be interpreted as spontaneous attempts of proton transfer from the hydroxide to the neighboring water molecule. The inset shows the spin density isosurface (green) computed at a snapshot taken at $\sim 1.4 \text{ ps}$, clearly indicating that one unpaired α electron is localized on the catalyst and the other unpaired α electron on the oxidized $\text{NDI}^{+\bullet}$.

Given the average $d(\text{H}_i\text{--O}_{ii})$ of $\sim 1.7 \text{ \AA}$ extracted from the unconstrained MD simulation, a series of constrained MD simulations are performed with $d(\text{H}_i\text{--O}_{ii})$ as the reaction coordinate (see Scheme 2.2), which is shortened gradually from 1.6 \AA to 1.05 \AA (noted in grey in Figure 2.3), to estimate the free energy profile along the reaction path. To test the stability of the obtained intermediate $^3([\text{Ru}^{\text{IV}}\text{=O}]^{2+}\text{--NDI})$ in the catalytic cycle, we also perform a free MD run at the end, following the 1.05 \AA constrained simulation. The variation of the total spin density localized on the catalyst (black line), the time evolution of the geometrical parameter $d(\text{H}_i\text{--O}_i)$ (magenta line), and the distance between Ru and H_3O^+ along different constrained MD trajectories are collected in Figure 2.3, top, middle and bottom, respectively.

For the first two MD trajectories with constrained distances 1.6 and 1.4 \AA , one unpaired electron is localized on the oxidized $\text{NDI}^{+\bullet}$ dye and the other unpaired electron on the catalyst (see Figure 2.3, inset a). The spin density initially localized on the oxidized $\text{NDI}^{+\bullet}$ gradually moves to the catalyst as a result of the shortening

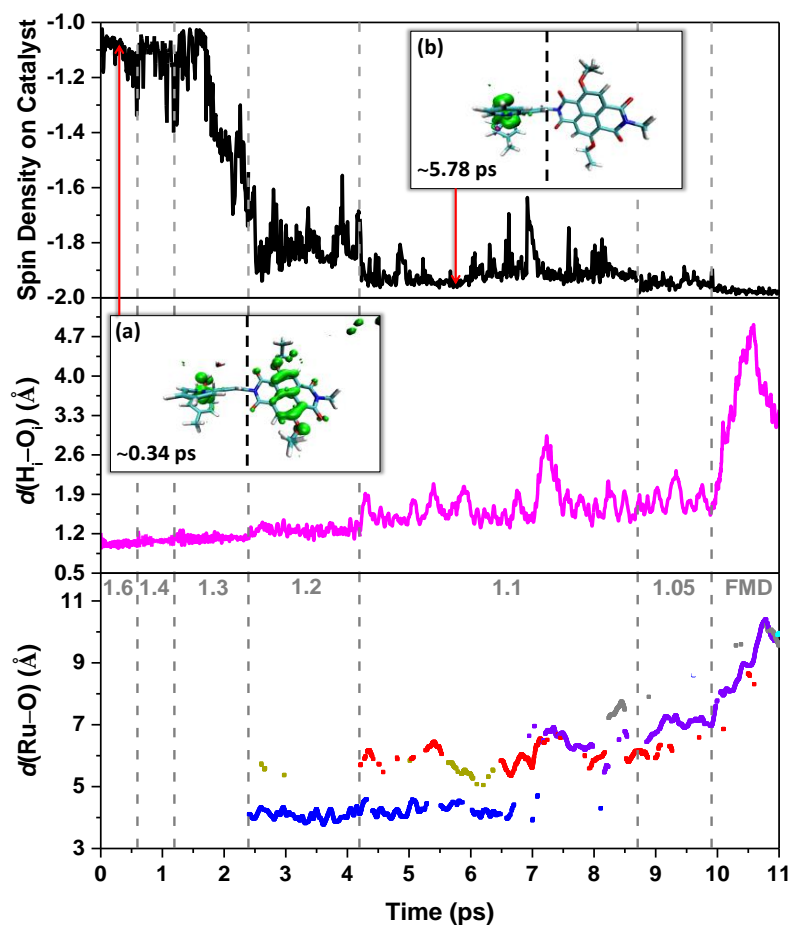


Figure 2.3. (top panel) The spin density integrated over the half of the simulation box including the catalyst (left-hand side of the dashed black line in the inset a and b) along the MD trajectories starting from the oxidized intermediate $^3([\text{Ru}^{\text{III}}\text{--OH}]^{2+}\text{--NDI}^+)$ (see route ① in Scheme 2.1). An integrated spin density value of -1 corresponds to one unpaired α electron. The starting configuration at $d(\text{H}_i\text{--O}_{ii}) = 1.6$ Å (see Scheme 2.2 for the atomic labels) has been extracted from a previous unconstrained simulation of the first catalytic intermediate. (middle panel) Time evolution of the geometrical parameter $d(\text{H}_i\text{--O}_i)$ (see Scheme 2.2) along the constrained and free MD (FMD) trajectory. (bottom panel) The distance between Ru and H_3O^+ , defined as an oxygen atom with 3 H within a radius of 1.2 Å, illustrating the proton diffusion during the MD simulations. The analysis of the trajectories shows that only one oxygen is in the H_3O^+ form at any time, and the excess proton associates primarily to four different oxygens (indicated with different colours: blue, gold, red and purple) during the simulation. The value of the constrained reaction coordinate $d(\text{H}_i\text{--O}_{ii})$ applied in the MD simulations is noted in grey. Inset (a) shows a snapshot from the beginning of the trajectory corresponding to a constraint value of 1.6 Å, where one unpaired α electron (green spin density isosurface) is localized on the catalyst and the other unpaired α electron on the NDI^+ ; Inset (b) shows a snapshot from the trajectory corresponding to a constraint value of 1.1 Å, where two unpaired α electrons are both localized on the catalyst.

of $d(\text{H}_i\text{--O}_{ii})$ and corresponding weakening of the $\text{H}_i\text{--O}_i$ bond (see Figure 2.3, top and middle). When $d(\text{H}_i\text{--O}_{ii}) = 1.2$ Å the H_i proton is shared between the

hydroxide and the attacking water molecule with an average $d(\text{H}_i\text{--O}_i)$ of ~ 1.2 Å, leading to the formation of the first H_3O^+ (see Figure 2.3, bottom). Further shortening of $d(\text{H}_i\text{--O}_{ii})$ to 1.1 Å induces full transfer of an electron from the catalyst to the oxidized NDI^{+} dye. This results in filling the hole on the NDI^{+} as shown in Figure 2.3, inset b, where no spin density is localized on the NDI. During the same constrained MD at 1.1 Å we observe that the $\text{H}_i\text{--O}_i$ bond is totally broken and the generated proton diffuses from O_{ii} of the attacking water molecule to neighboring water molecules (see Figure 2.3, bottom). At the end of the constrained MD simulation, the Ru catalyst has two unpaired α electrons as expected on the basis of previous calculations indicating that the $[\text{Ru}^{\text{IV}}=\text{O}]^{2+}$ intermediate has a triplet ground-state ($S = 1$).³⁹ The obtained product $^3([\text{Ru}^{\text{IV}}=\text{O}]^{2+}\text{--NDI})$ is verified to be stable at room temperature during the free MD simulation (FMD in Figure 2.3) as no proton or electron recombination is observed and the released proton diffuses through the solvent. The proton diffusion process in liquid water can be described by the Grotthuss mechanism involving covalent bond breaking and formation within the hydrogen-bonding network.^{82–89}

The free energy profile along the reaction coordinate $d(\text{H}_i\text{--O}_{ii})$ is estimated by numerical integration of the mean forces extracted from the constrained dynamics,^{56, 81} and is reported in Figure 2.4 (bottom). The mean force values corresponding to the applied constraints are presented in Figure 2.4 (top) together with the 100-point Akima spline interpolation utilized for the integration. In Figures A2.3 and A2.4, we show that the running average of the Lagrangian multiplier reaches a stable value even within a relatively short MD timescale of ~ 0.5 ps. The second catalytic step shows an activation energy barrier $\Delta G^* \approx 2.3$ kcal mol^{−1} (~ 0.10 eV) slightly higher than in the first catalytic step (see Table 2.1). Noticeably, a much larger driving force $\Delta G^\circ \approx -10.7$ kcal mol^{−1} (~ 0.46 eV) is found for this step compared to the first, indicating an exothermic process after the photooxidation and a quite stable product intermediate $^3([\text{Ru}^{\text{IV}}=\text{O}]^{2+}\text{--NDI})$ in the $S = 1$ state. The Ru– O_i bond is shortened from an average length of 1.93 Å to 1.76 Å through this reaction, extracted from the unconstrained MD simulation before and after the second catalytic step, which contributes to the stabilization of the obtained intermediate. These findings demonstrate that the second catalytic water oxidation step in route ① is thermodynamically

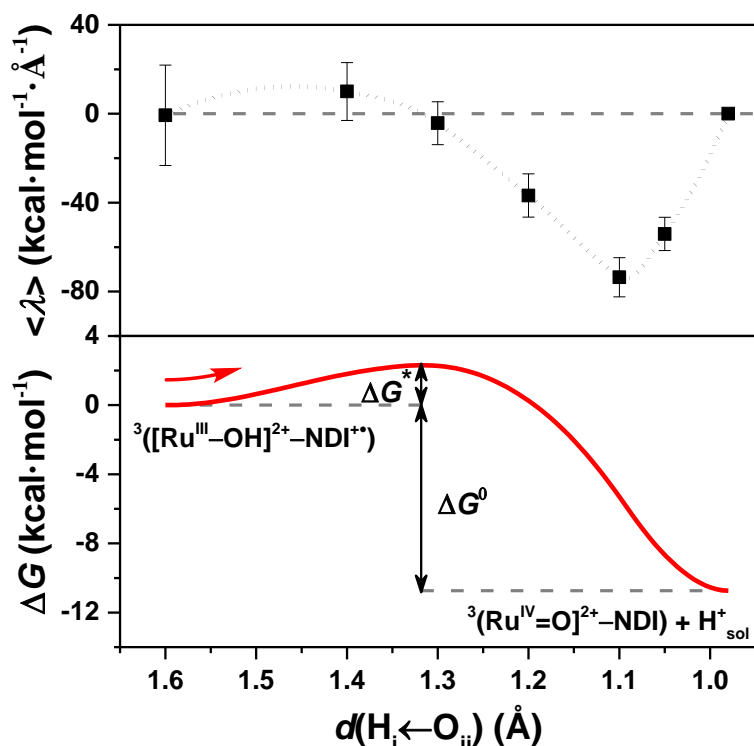


Figure 2.4. (top panel) The constraint mean force represented by the Lagrangian multiplier $\langle \lambda \rangle$ (black squares) computed for each constrained MD simulation as a function of the reaction coordinate $d(\text{H}_i \leftarrow \text{O}_{ii})$ along route ① for the triplet spin state. The mean force at the equilibrium distance $d(\text{H}_i - \text{O}_{ii}) = 0.98 \text{ \AA}$ evaluated in the FMD has been set to 0. The 100-point Akima spline interpolation (dotted line) is used to interpolate the mean forces including also the zero point at equilibrium. The error bars indicate the standard deviations. (bottom panel) Free energy profile along the reaction coordinate $d(\text{H}_i \leftarrow \text{O}_{ii})$ computed from thermodynamic integration of the interpolated time-averaged mean forces. The initial and final intermediates are also indicated.

favorable upon photooxidation of the dye and can indeed proceed at a high rate at room temperature given the low activation energy, similar to the first catalytic step (see Table 2.1).

The opposite spin orientation on NDI has been also investigated and the results are reported in Figures A2.5 – A2.7 and Table A2.3. The initial free MD equilibration for the oxidized intermediate $^1([\text{Ru}^{\text{III}}-\text{OH}]^{2+}-\text{NDI}^{+\bullet})$, in the $S = 0$ state, clearly shows the antiparallel spins (see inset b in Figure A2.7). Considering the relatively higher activation energy barrier and smaller driving force along route ② compared to that of route ① (see Table 2.1 and Figure A2.5), route ② is thermodynamically less favourable. Moreover, the product intermediate $^3([\text{Ru}^{\text{IV}}=\text{O}]^{2+}-\text{NDI})$ is found to be more stable than $^1([\text{Ru}^{\text{IV}}=\text{O}]^{2+}-\text{NDI})$ (see Figure A2.6 and Table A2.3), confirming that route ① is most likely for this catalytic step.

2.3.2 Third Catalytic Water Oxidation Step: O–O Bond Formation

The third catalytic step involves the O–O bond formation and is commonly found to be the most thermodynamically demanding process in catalytic water oxidation (see also Table A2.1 and Figure A2.1).^{34, 39, 90} To check whether the selected NDI dye is able to drive the third catalytic water oxidation step, AIMD simulations are performed for the oxidized complex $[\text{Ru}^{\text{IV}}=\text{O}]^{2+}\text{-NDI}^{+\bullet}$ in explicit water solvent.

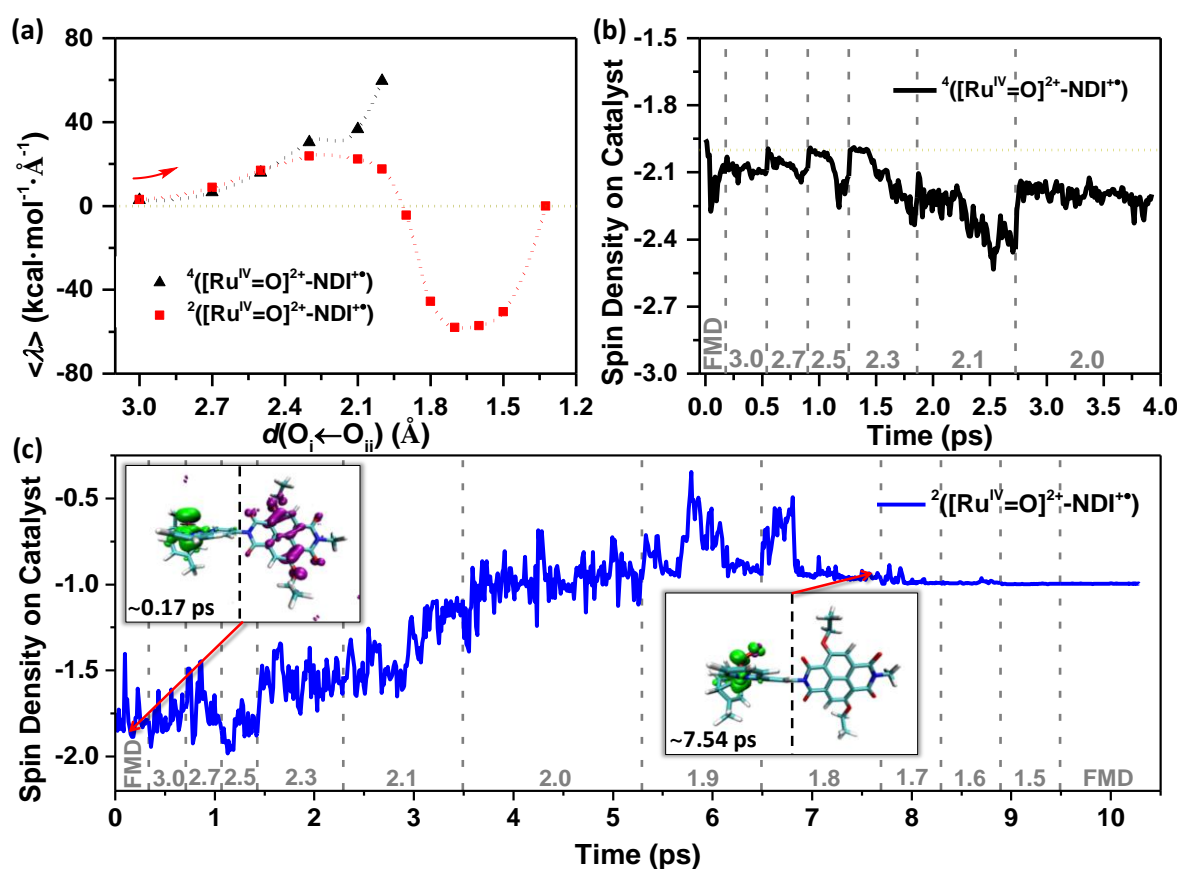
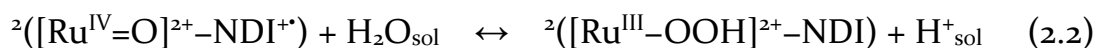


Figure 2.5. (a) Average constraint force represented by the Lagrangian multiplier $\langle \lambda \rangle$ computed for each constrained MD simulation with quartet multiplicity (black triangles) and doublet multiplicity (red squares) as a function of the reaction coordinate $d(\text{O}_i \leftarrow \text{O}_{ii})$. The Akima spline (100 points) is used to interpolate the mean forces (dotted lines). The point at $d(\text{O}_i \leftarrow \text{O}_{ii}) = 1.32 \text{ \AA}$ corresponds to the equilibrium product state and thus its $\langle \lambda \rangle$ is assumed to be zero. The spin density integrated over the half of the simulation box that includes the catalyst along the constrained and free MD trajectories is shown in (b) for the quartet and in (c) for the doublet state. In the panels (b) and (c) the value of the constrained reaction coordinate $d(\text{O}_i \leftarrow \text{O}_{ii})$ in the MD simulations is also indicated in grey. Inset (left) shows a snapshot from the FMD trajectory, where two unpaired α electrons (green spin density isosurface) are localized on the catalyst and one unpaired β electron (purple spin density isosurface) on the oxidized $\text{NDI}^{+\bullet}$; Inset (right) shows a snapshot from the final part of the trajectory corresponding to a constraint value of 1.8 \AA , where only one unpaired α electron is left on the catalyst.

In the $[\text{Ru}^{\text{IV}}=\text{O}]^{2+}-\text{NDI}^{+\bullet}$ intermediate there are two unpaired electrons localized on the catalyst and one unpaired electron on the oxidized dye. Two specific initial spin states are therefore investigated (see route ① in Scheme 2.1 and Table 2.1):

- (I) $^4([\text{Ru}^{\text{IV}}=\text{O}]^{2+}-\text{NDI}^{+\bullet})$ ($S = 3/2$): two unpaired α electrons (\uparrow) localized on the catalyst and one unpaired α electron localized on the oxidized $\text{NDI}^{+\bullet}$ dye;
- (II) $^2([\text{Ru}^{\text{IV}}=\text{O}]^{2+}-\text{NDI}^{+\bullet})$ ($S = 1/2$): two unpaired α electrons localized on the catalyst and one unpaired β electron (with opposite spin \downarrow) localized on the oxidized $\text{NDI}^{+\bullet}$ dye.

We perform constrained MD simulations for both spin states. The results show that the calculated time-averaged constraint force $\langle \lambda \rangle$ obtained in the quartet multiplicity case (I) increases systematically (see black triangles in Figure 2.5a) and no electron transfer from the catalyst to the oxidized $\text{NDI}^{+\bullet}$ occurs (see Figure 2.5b) when shortening the constraint distance $d(\text{O}_i \leftarrow \text{O}_{\text{ii}})$ (see Scheme 2.2b). This implies that the O–O bond formation is thermodynamically unfavorable for this spin alignment. Instead, the doublet state (II) facilitates the formation of this bond in the third catalytic step (see eq. 2.2, where $\text{H}_2\text{O}_{\text{sol}}$ represents the solvated attacking water molecule), demonstrating again the significant role of spin alignment in the investigated supramolecular complex.^{91–93} In the following we then focus only on the $S = 1/2$ spin state for the third redox couple.



The spin density for the reactant (doublet) in route ① (see eq. 2.2) shows as expected two unpaired electrons localized on the catalyst and one unpaired electron localized on the oxidized $\text{NDI}^{+\bullet}$ with antiparallel spin. (see Figure 2.5c, inset (left)).

According to the results of our AIMD simulations, the third catalytic water oxidation step can be described by three features: (1) attacking water rearrangement to reach a favorable orientation with respect to the oxygen ligand; (2) electron transfer from the WOC to the photoinduced hole on the oxidized $\text{NDI}^{+\bullet}$; (3) proton transfer and diffusion into the solvent bulk.

2.3.2.1 Attacking Water Rearrangement and Electron Transfer

After equilibration of the system during the free MD simulation, one water molecule in the vicinity of the $^3([Ru^{IV}=O]^{2+})$ group is selected as the attacking water molecule during the constrained MD trajectories (see Figure 2.6a). A few representative configurations with constrained $d(O_i \leftarrow O_{ii})$ values ranging from 3.0 to 2.1 Å are shown in Figure 2.6(b–f).

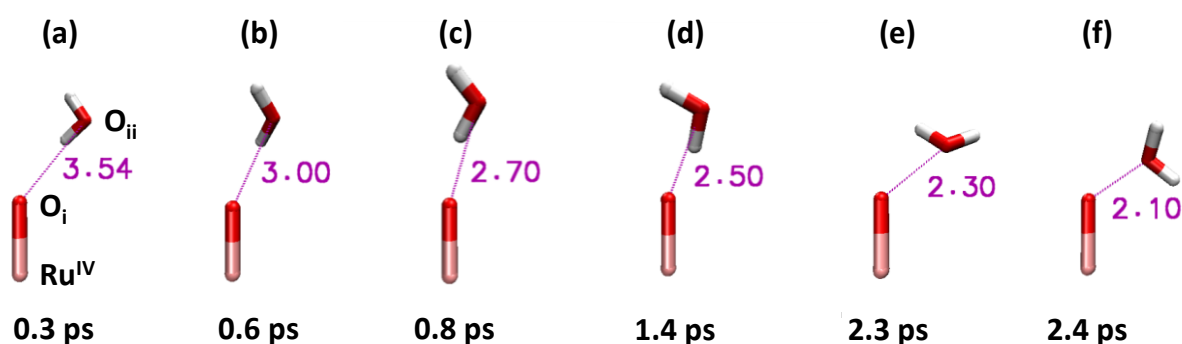


Figure 2.6. (a) Configuration of the attacking water molecule during the FMD at room temperature. (b) – (f) Snapshots from the constrained MD trajectories at different $d(O_i \leftarrow O_{ii})$ (in purple) with spin multiplicity $2S+1 = 2$. Only the attacking water molecule, the ruthenium metal center and the oxygen coordinating to it are shown explicitly. The orientation rearrangement of the attacking water molecule during this process is clearly visible.

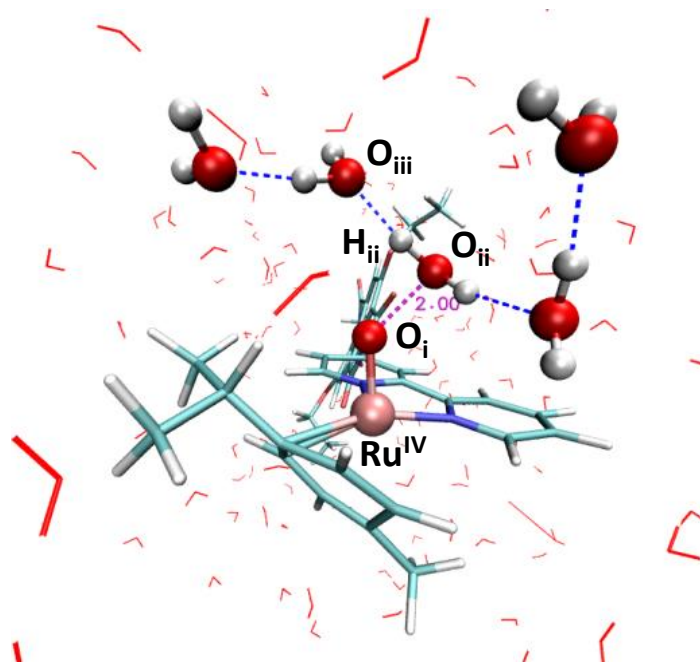


Figure 2.7. The attacking water molecule and the neighboring water molecules along the hydrogen-bonding network (dashed blue lines) at the beginning of the constrained simulation with $d(O_i \leftarrow O_{ii}) = 2.0$ Å.

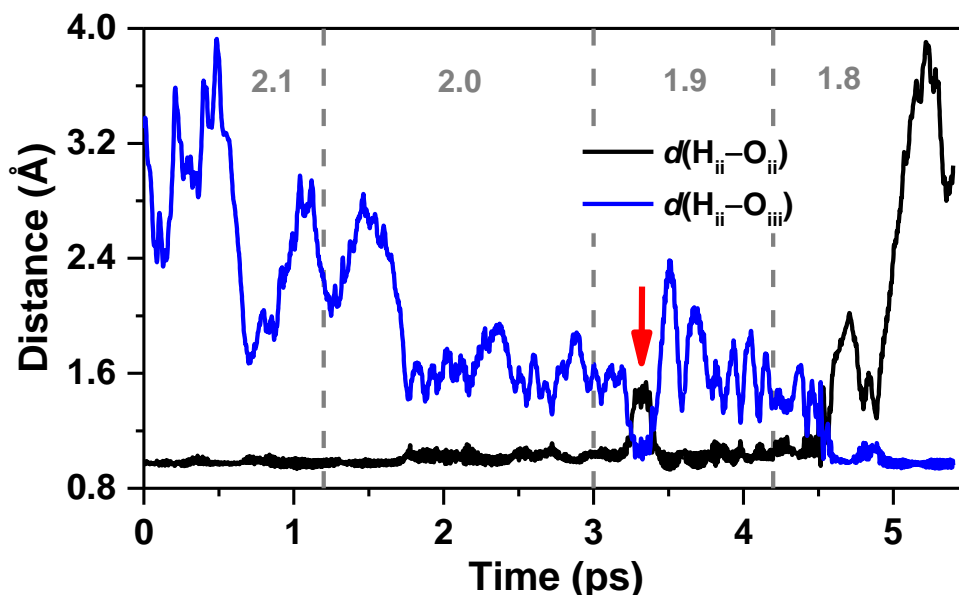


Figure 2.8. Time evolution of the geometrical parameter $d(\text{H}_{\text{ii}}-\text{O}_{\text{ii}})$ (black line) and $d(\text{H}_{\text{ii}}-\text{O}_{\text{iii}})$ (blue line) along the constrained MD simulations (route ①). See Figure 2.7 for the atomic labels. The value of the constrained reaction coordinate $d(\text{O}_{\text{i}}\leftarrow\text{O}_{\text{ii}})$ in the MD simulations is noted in grey. The red vertical arrow indicates a first proton transfer attempt during the constrained 1.9 Å simulation followed by fast back reaction.

The attacking water molecule has initially one hydrogen atom pointing to the oxygen ligand (O_{i}) of the $^3[\text{Ru}^{\text{IV}}=\text{O}]^{2+}$ center ($2.5 \text{ Å} < d(\text{O}_{\text{i}}\leftarrow\text{O}_{\text{ii}}) < 3.0 \text{ Å}$). When the constrained $d(\text{O}_{\text{i}}\leftarrow\text{O}_{\text{ii}})$ is shortened to 2.3 Å, the attacking water molecule starts to rotate and reaches a state with its oxygen atom (O_{ii}) now pointing towards the oxygen ligand (O_{i}), preparing for the O–O bond formation. Moreover, the attacking water molecule forms strong hydrogen bonds with neighboring water molecules at the beginning of the 2.0 Å simulation (see Figure 2.7). This hydrogen bonding network not only stabilizes the configuration of the attacking water molecule but also predisposes the system for the subsequent proton diffusion process.

The integrated spin density localized on the catalyst along the constrained MD trajectories is reported in Figure 2.5c to clarify the electron dynamics during this catalytic step. During the initial water attack stage ($2.5 \text{ Å} < d(\text{O}_{\text{i}}\leftarrow\text{O}_{\text{ii}}) < 3.0 \text{ Å}$), the spin density localized on the catalyst fluctuates around an average value of ~ -1.8 , corresponding to the expected triplet state of this catalyst intermediate, while one unpaired electron with antiparallel spin is localized on the oxidized NDI $^{+\bullet}$ (see Figure 2.5c, inset (left)). The shortening of $d(\text{O}_{\text{i}}\leftarrow\text{O}_{\text{ii}})$ from 2.5 Å to 2.0 Å induces the electron transfer from the catalyst to the oxidized NDI $^{+\bullet}$ dye, which

is facilitated by the rearrangement of the attacking water. The spin density localized on the catalyst during the constrained 2.0 Å simulation fluctuates around an average of -1 , indicating the accomplishment of the electron transfer and the filling of the photoinduced hole on the NDI⁺ dye. No proton transfer occurs during the constrained 2.0 Å dynamics, even though the electron transfer has already taken place. The H_{ii}–O_{ii} bond (see Scheme 2.2b) is however slightly weakened with a maximum distance ~ 1.1 Å (see Figure 2.8). When we further shorten the constrained $d(\text{O}_i \leftarrow \text{O}_{ii})$ from 1.9 to 1.5 Å, the proton transfer takes place (see next section) and the spin density on the catalyst reaches a stable value of -1 , indicating only one unpaired electron finally left on the catalyst (see Figure 2.5c, inset (right)) and no back reaction occurs even when the constraint is released (FMD).

2.3.2.2 Proton Diffusion

The time evolution of the $d(\text{H}_{ii} - \text{O}_{ii})$ and $d(\text{H}_{ii} - \text{O}_{iii})$ (see Figure 2.9b, top) shows that the H_{ii} proton does several attempts between 6.7 ps and 6.9 ps before eventually jumping from oxygen O_{ii} to O_{iii}. Almost simultaneously to the H_{ii} proton transfer from O_{ii} to O_{iii}, the H_{iii} proton makes a first spontaneous jump from oxygen O_{iii} to O_{iv}, as the acceptance of the H_{ii} proton by the oxygen O_{iii} weakens the H_{iii}–O_{iii} bond (see Figure 2.9b, middle, ~ 6.85 ps). The H_{iii} proton appears to be shared by the oxygen O_{iii} and O_{iv}, until it is fully transferred to O_{iv} (see Figure 2.9b, middle, ~ 7.2 ps). Soon after, the H_{iv} proton is successfully transferred from O_{iv} to O_v (see Figure 2.9b, bottom, ~ 7.4 ps). These results provide strong evidence that the nature of this proton diffusion process is well described by the Grotthuss mechanism.^{82–85} The excess proton diffuses further into the solvent bulk during the following constrained MD simulations with fixed $d(\text{O}_i \leftarrow \text{O}_{ii})$ from 1.7 to 1.5 Å. More importantly, no backward proton transfer is observed even after removing the constraint at the end of 1.5 Å simulation, showing the stability of the newly formed hydroperoxo intermediate $^2([\text{Ru}^{\text{III}} - \text{OOH}]^{2+} - \text{NDI})$ in the $S = 1/2$ state. For the FMD trajectory the $d(\text{O}_i - \text{O}_{ii})$ fluctuates around its average of 1.32 Å, indicating the formation of a strong O–O bond after the proton diffusion process. For comparison, the O–O bond length in molecular hydrogen peroxide is 1.47 Å.⁵⁶ The relatively short O–O bond can be further ascribed to the weakened O_{ii}–H_{ii} bond (see Figure 2.9a), which will be discussed in detail in the next section.

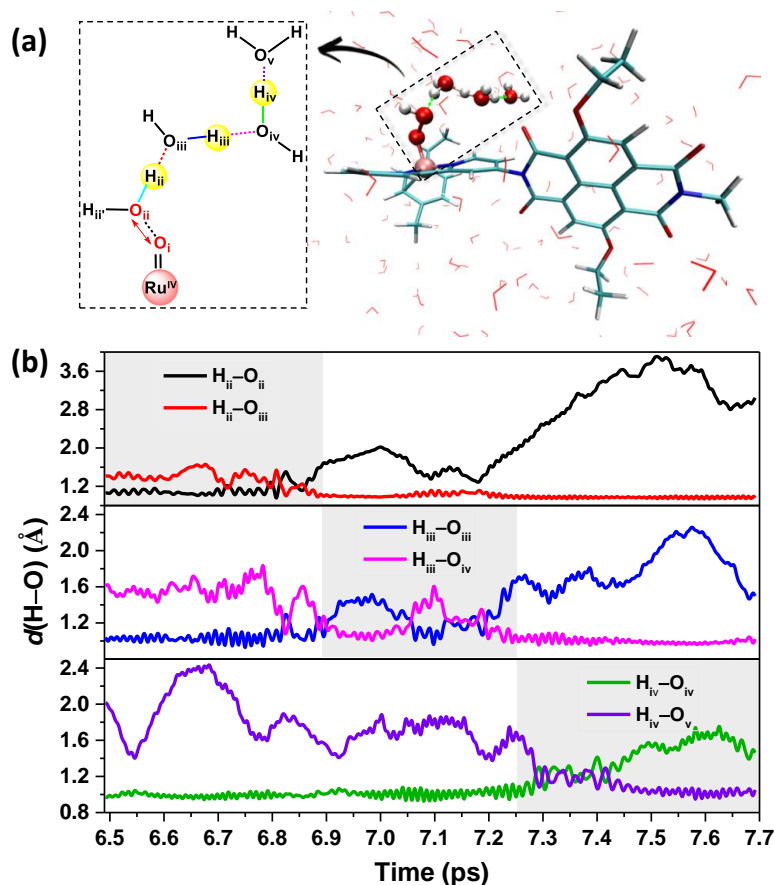


Figure 2.9. (a) Water molecules involved in the proton diffusion path from oxygen O_{ii} into the solvent bulk. (b) Time evolution of the $d(H-O)$ distances contributing to the proton diffusion along the constrained MD trajectory corresponding to the constraint value $d(O_i \leftarrow O_{ii}) = 1.8$ Å. The time range is consistent with Figure 2.5c.

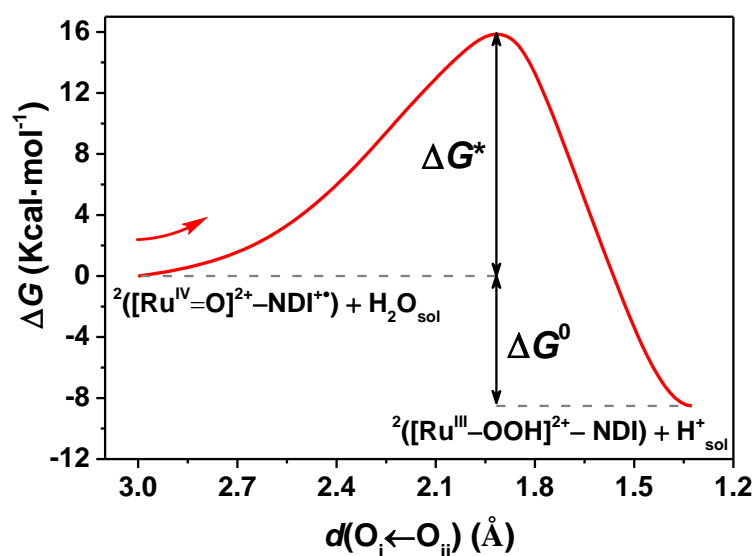


Figure 2.10. Free energy profile along the reaction coordinate $d(O_i \leftarrow O_{ii})$ computed by thermodynamic integration. All the constrained MD simulations are performed with doublet multiplicity, corresponding to having two unpaired α electrons on the Ru-based catalyst and one β electron on the oxidized NDI^{+*} . The initial and final intermediates are also indicated.

The time-averaged mean forces associated with the applied constraint are collected in Figure 2.5a (red squares), leading to the free energy profile shown in Figure 2.10 by thermodynamic integration. Well in line with the O–O bond formation representing the rate-limiting step, it presents a considerably higher activation energy barrier $\Delta G^* \approx 15.9 \text{ kcal mol}^{-1}$ ($\sim 0.69 \text{ eV}$) compared to the previous two catalytic steps (see Table 2.1). This step is indeed normally considered as the thermodynamic bottleneck of the water splitting process in mononuclear WOC.²¹ In addition to the involvement of the O–O bond formation, such a high reaction barrier can be partly attributed to the low-energy starting point, since the second intermediate $^3([\text{Ru}^{\text{IV}}=\text{O}]^{2+}\text{–NDI})$ is quite stable in the water solvent.³⁹ However, also this catalytic step leading to the intermediate $^2([\text{Ru}^{\text{III}}\text{–OOH}]^{2+}\text{–NDI})$ is found to be exothermic after photooxidation with a predicted driving force $\Delta G^0 \approx -8.5 \text{ kcal mol}^{-1}$ ($\sim 0.37 \text{ eV}$) (Figure 2.10). In spite of the considerably high activation energy barrier, the oxidized NDI⁺ dye is still capable of driving the formation of the O–O bond, provided that antiparallel spin alignment is achieved. According to transition state theory^{94–97}, the reaction rate k is determined by the activation free energy barrier ΔG^* according to

$$k = \frac{k_{\text{B}}T}{h} \cdot e^{-\frac{\Delta G^*}{RT}}. \quad (2.3)$$

The calculated rates of the first three catalytic steps along route ① (as well as route ②, for comparison) are listed in Table 2.1. The first two catalytic steps are very fast with a rate of $k = \sim 3.6 \times 10^{11} \text{ s}^{-1}$ and $k = \sim 1.3 \times 10^{11} \text{ s}^{-1}$ respectively, while the third step is around ten orders of magnitude slower. Although the third step involving the O–O bond formation with a rate of $k = \sim 15.7 \text{ s}^{-1}$ is unquestionably the rate-limiting step, the specific WOC coupled to the NDI dye shows a competitive rate compared to some characteristic Ru-based mononuclear WOCs.²¹ Due to the slow rate of this step, electron recombination from the semiconductor to the NDI might compete with the electron transfer from the WOC to the dye, therefore reducing the efficiency of the whole process.^{98–99}

Additionally, the third step along route ② (see Scheme 2.1) has been also investigated and the results are reported in Figure 2.11. The computed free energy profile shows that this route is thermodynamically viable, leading to the same product intermediate $^2([\text{Ru}^{\text{III}}\text{–OOH}]^{2+}\text{–NDI})$ in the $S = 1/2$ state as for route ①

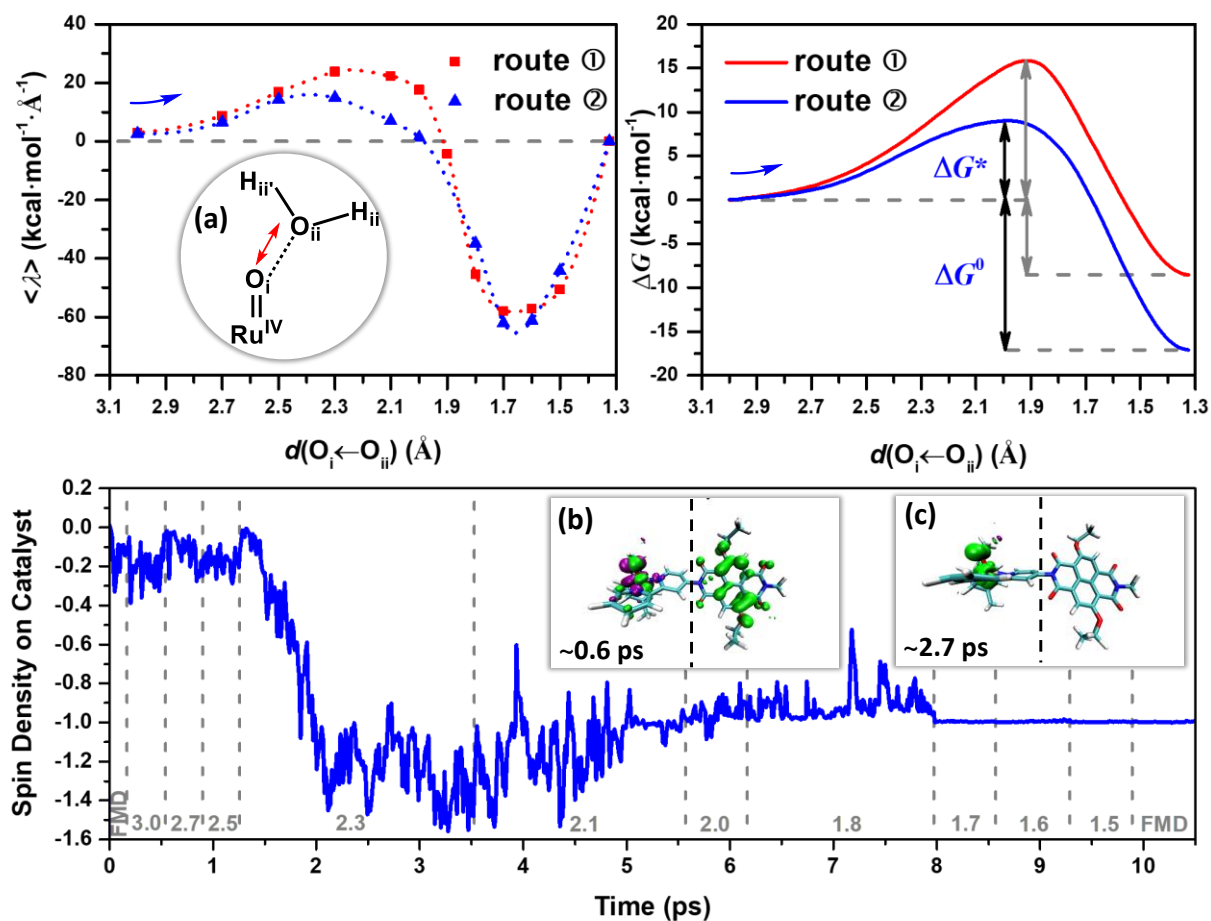


Figure 2.11. (top-left panel) Average constraint force represented by the Lagrangian multiplier $\langle \lambda \rangle$ computed for each constrained MD simulation of route ② (blue triangles) and ① (red squares, for comparison) as a function of the reaction coordinate $d(\text{O}_i \leftarrow \text{O}_{ii})$. The Akima spline (100 points) is used to interpolate the mean forces. The point at $d(\text{O}_i - \text{O}_{ii}) = 1.32$ \AA corresponds to the equilibrium product state and thus its $\langle \lambda \rangle$ is assumed to be zero. (top-right panel) Free energy profile along the reaction coordinate $d(\text{O}_i \leftarrow \text{O}_{ii})$ of route ② computed from thermodynamic integration, compared to the results for route ①. (bottom panel) The spin density integrated over the half of the simulation box that includes the catalyst along the constrained and FMD trajectory of route ②. The value of the constrained reaction coordinate $d(\text{O}_i \leftarrow \text{O}_{ii})$ in the MD simulations is noted in grey. Inset (a) shows the schematic structure of the first water molecule along the hydrogen-bonding network coordinated to the oxygen ligand. The red double-sided arrow indicates the reaction coordinate considered for $[\text{Ru}^{\text{IV}}=\text{O}]^{2+} \cdots (\text{H}_2\text{O})$ during the constrained MD simulations. Inset (b) and (c) show snapshots from the constrained MD trajectory, in which the spin density isosurface of α and β electrons in green and purple respectively. The labels refer to the time at which the snapshot has been taken along the collected trajectory.

(see Scheme 2.1 and Figure A2.8). However, the starting intermediate $^1([\text{Ru}^{\text{IV}}=\text{O}]^{2+} - \text{NDI})$ before photooxidation turned out to be much higher in energy than $^3([\text{Ru}^{\text{IV}}=\text{O}]^{2+} - \text{NDI})$ (see Figure A2.6, Tables A2.3 and A2.4).

2.3.3 Fourth Catalytic Water Oxidation Step

In this section we show that the NDI dye is definitely able to drive the subsequent fourth catalytic step. This is already evident by analyzing the free MD equilibration run carried out for 0.36 ps at the end of the third catalytic step, after having removed the excess proton from the simulation box. This MD trajectory shows that the $H_{ii'}$ proton of the hydroperoxo ligand is very weakly bound and essentially shared with the oxygen $O_{iii'}$ of an hydrogen-bonded water (see Scheme 2.2c), which is reflected in the temporary formation of the first H_3O^+ at the very beginning of the FMD simulation (see Figure 2.12, middle). In Figure 2.12 (top) the integrated spin density localized on the catalyst is also reported. Before photooxidation (dashed line in Figure 2.12) a value of -1 is found consistent with the doublet state of the catalyst. Thereafter, the oxidized intermediate $^3([Ru^{III}-OOH]^{2+}-NDI^{+*})$ is formed by removing an electron from the simulation box. A sharp increase of the spin density localized on the catalyst is then observed after photooxidation, indicating an almost instantaneous electron transfer process from the catalyst to the oxidized NDI^{+*} dye and the generation of a second unpaired electron leading to a triplet state on the catalyst. In Figure 2.12 we show how the spin density rapidly moves from the oxidized NDI^{+*} dye to the Ru-based catalyst along the trajectory. At the same time, the $H_{ii'}$ proton is rapidly released by the O_{ii} atom and transferred to the neighboring water molecules (Figure 2.12, middle). This very fast PCET process (only ~ 50 fs after photooxidation of the NDI dye) leads to the final catalytic intermediate $^3([Ru^{II}-OO]^{2+}-NDI)$ (see eq. 2.4). This free AIMD simulation demonstrates that the fourth PCET catalytic water oxidation step occurs without any significant activation energy barrier. Similar electron and nuclear dynamics are observed along route ② for this catalytic step, which ends up with a less stable intermediate $^1([Ru^{II}-OO]^{2+}-NDI)$ (see more details in Figures A2.9 and A2.10, Tables A2.4 and A2.5). This is consistent with the O_2 ligand being more stable in the $S = 1$ state.



After the proton transfer the distance between O_i and O_{ii} atoms shortens to an average value of ~ 1.24 Å (black line in Figure 2.12, bottom), confirming the formation of the $O=O$ bond (for comparison, the $O=O$ bond length in molecular O_2 is 1.21 Å). The final spin density mainly localizes on the two oxygen atoms (O_i

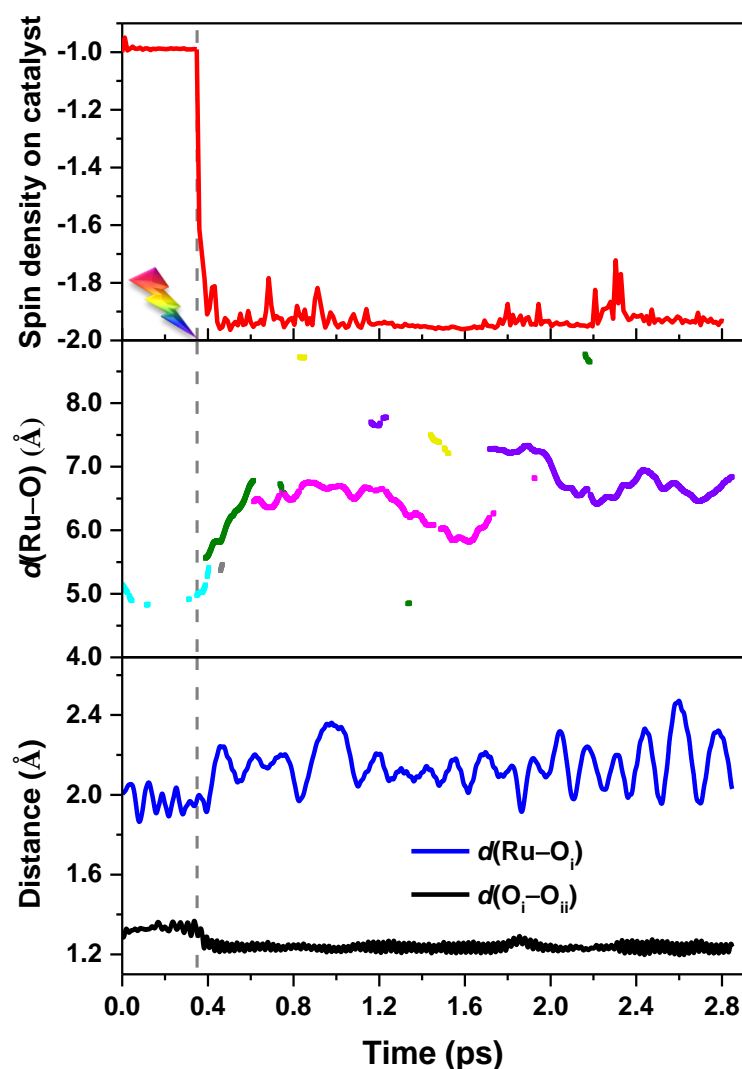


Figure 2.12. (top panel) The spin density integrated over the half of the simulation box including the catalyst before and after the photoinduced electron injection, which is mimicked by removing one electron from the system at 0.36 ps to generate an oxidized $^3([\text{Ru}^{\text{III}}-\text{OOH}]^{2+}-\text{NDI}^{+})$ (indicated by the grey dotted line). (middle panel) The distance between Ru and H_3O^+ measured for the free MD simulations. According to the simulations, the proton primarily bonds to four oxygens (cyan, dark green, magenta and purple). (bottom panel) Time evolution of the geometrical parameter $d(\text{Ru}-\text{O}_i)$ (blue line) and $d(\text{O}_i-\text{O}_{ii})$ (black line) along the free MD trajectory (see labelling in Scheme 2.2c).

and O_{ii}), providing strong evidence for the generation of the triplet molecular O_2 product (see Figure 2.13). As a result, the $\text{Ru}-\text{O}_i$ bond is considerably weakened (blue line in Figure 2.12, bottom), which indicates that the generated molecular O_2 can be easily exchanged with a water molecule in solution and thus regenerating the initial WOC state.

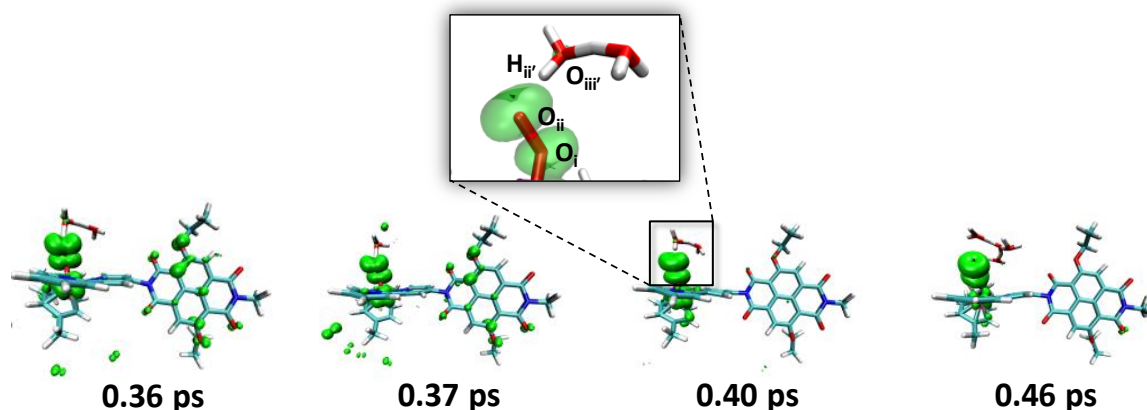


Figure 2.13. Spin density localization at different snapshots along the free MD trajectory for the final step in the catalytic cycle (see **Figure 2.12**). The hole (spin density) localized on the NDI immediately after photooxidation (0.36 ps) is very quickly filled by the electron from the catalyst within approximately 50 fs. In the snapshot taken at 0.4 ps the proton has been already transferred to the solvent water molecules nearby, temporarily forming a $(\text{O}_2\text{H}_5)^+$ complex (see enlarged inset above). The spin density at the end of the process is mostly localized on the O_2 ligand and shows the characteristic shape expected for the oxygen molecule (see also enlargement in the inset). A small amount of spin density can be seen localized on a few water molecules due to transient solvent polarization effects.

By analyzing the nuclear trajectory during the electron transfer process, we can observe a clear change in the dihedral angle ($\angle\text{C}_1\text{--}\text{N}_1\text{--}\text{C}_2\text{--}\text{C}_3$, see Scheme 2.1) around the C–N bond connecting the NDI and the Ru catalyst from an average value of $\sim 60^\circ$ to $90 - 100^\circ$. In Figure A2.11 the evolution of this angle together with the spin density evolution is reported, suggesting a correlation between this torsional motion and the electron dynamics. Coherence in the electron and nuclear motion has been suggested to play a role in electron transfer processes both in natural and artificial systems.^{54, 100} It might be interesting to further analyze the coupling between electronic and nuclear motion with quantum-classical simulations.

2.4. Conclusions

The whole photocatalytic water splitting cycle performed by the WOC–dye supramolecular complex $[\text{Ru}^{\text{II}}(\text{H}_2\text{O})]^{2+}$ –NDI dissolved in water has been systematically explored by means of DFT-based AIMD simulations at room temperature. The coupled electron and proton dynamics together with the solvent rearrangement are followed during the cycle, elucidating the catalytic mechanism of the four consecutive water oxidation steps.

The first three catalytic water oxidation steps are all exothermic with negative driving force ΔG° after photooxidation of the NDI dye. The electron transfer from the catalyst to the oxidized dye always precedes the proton diffusion into the solvent bulk. The first and the second PCET catalytic steps present a similar small activation free energy barrier of the order of a few $k_B T$ at room temperature. The second PCET step has a larger driving force compared to the first, suggesting a much more stable product intermediate $^3([Ru^{IV}=O]^{2+}-NDI)$. The third PCET catalytic step involving the O–O bond formation with a second attacking water has a considerably higher activation energy barrier. This is the rate-limiting step where recombination processes from the semiconductor into the oxidized dye might indeed reduce the quantum efficiency of the whole process. One possible strategy to mitigate this issue is to add a molecular rectifier bridge between the dye and the semiconductor surface.⁵⁴ It is found that the antiparallel spin alignment of unpaired electrons on the WOC and dye is essential for the occurrence of the O–O bond formation. The rearrangement of solvent water molecules and formation of a hydrogen-bonding network during the MD simulations further facilitate the subsequent proton diffusion process. Interestingly, the fourth PCET step occurs immediately after the photooxidation of the NDI dye without any energy barrier, leading to the final intermediate with the O₂ ligand. All these results demonstrate that the selected NDI dye is a promising dye sensitizer to integrate in a DS-PEC device: it is able to perform fast electron injection into TiO₂ upon visible light absorption, and in its oxidized form can drive the whole photocatalytic water splitting cycle when properly coupled to the Ru-based catalyst. Considering that the NDI is capable of extracting electrons from the catalyst over the whole cycle, PCET conversion mediated by quantum overlap and vibrationally assisted is a mechanism that may be difficult to suppress, which works to the advantage of smooth catalysis.¹⁰¹⁻¹⁰²

Further progress aimed at lowering the activation energy barrier of the third PCET catalytic step can be achieved by introducing extra proton acceptors¹⁰³⁻¹⁰⁸ near the active site, and/or by assembling the catalyst near an IEM¹⁰⁹⁻¹¹³ between the anode and cathode chambers, which would create a favorable environment to facilitate the proton release and transport through the membrane.

2.5 References

- [1] Dresselhaus, M. S.; Thomas, I. L. *Nature* **2001**, *414*, 332–337.
- [2] Chynoweth, D. P.; Owens, J. M.; Legrand, R. *Renewable Energy* **2001**, *22*, 1–8.
- [3] Lewis, N. S. *Science* **2007**, *315*, 798–801.
- [4] Nocera, D. G. *Acc. Chem. Res.* **2012**, *45*, 767–776.
- [5] Gust, D.; Moore, T. A.; Moore, A. L. *Acc. Chem. Res.* **2009**, *42*, 1890–1898.
- [6] Zaharieva, I.; Wichmann, J. M.; Dau, H. *J. Biol. Chem.* **2011**, *286*, 18222–18228.
- [7] Tachibana, Y.; Vayssieres, L.; Durrant, J. R. *Nat. Photonics* **2012**, *6*, 511–518.
- [8] Dau, H.; Zaharieva, I.; Haumann, M. *Curr. Opin. Chem. Biol.* **2012**, *16*, 3–10.
- [9] Jafari, T.; Moharrer, E.; Amin, A.; Miao, R.; Song, W.; Suib, S. *Molecules* **2016**, *21*, 900.
- [10] Kim, W.; Edri, E.; Frei, H. *Acc. Chem. Res.* **2016**, *49*, 1634–1645.
- [11] Xiang, C.; Weber, A. Z.; Ardo, S.; Berger, A.; Chen, Y.; Coridan, R.; Fountaine, K. T.; Haussener, S.; Hu, S.; Liu, R.; et al. *Angew. Chem., Int. Ed.* **2016**, *55*, 12974–12988.
- [12] Turan, B.; Becker, J.-P.; Urbain, F.; Finger, F.; Rau, U.; Haas, S. *Nat. Commun.* **2016**, *7*, 12681.
- [13] Grätzel, M. *Nature* **2001**, *414*, 338–344.
- [14] Liu, C.; Colón, B. C.; Ziesack, M.; Silver, P. A.; Nocera, D. G. *Science* **2016**, *352*, 1210–1213.
- [15] Haas, T.; Krause, R.; Weber, R.; Demler, M.; Schmid, G. *Nat. Catal.* **2018**, *1*, 32–39.
- [16] Inoue, H.; Shimada, T.; Kou, Y.; Nabetani, Y.; Masui, D.; Takagi, S.; Tachibana, H. *ChemSusChem* **2011**, *4*, 173–179.
- [17] Yu, Z.; Li, F.; Sun, L. *Energy Environ. Sci.* **2015**, *8*, 760–775.
- [18] Peerakiathajohn, P.; Yun, J.-H.; Wang, S.; Wang, L. *J. Photonics Energy* **2016**, *7*, 012006.
- [19] Ding, X.; Gao, Y.; Ye, L.; Zhang, L.; Sun, L. *ChemSusChem* **2015**, *8*, 3992–3995.
- [20] Moniz, S. J. A.; Shevlin, S. A.; Martin, D. J.; Guo, Z.-X.; Tang, J. *Energy Environ. Sci.* **2015**, *8*, 731–759.
- [21] Hetterscheid, D. G. H.; Reek, J. N. H. *Angew. Chem., Int. Ed.* **2012**, *51*, 9740–9747.
- [22] Concepcion, J. J.; Jurss, J. W.; Brennaman, M. K.; Hoertz, P. G.; Patrocinio, A. O. T.; Murakami Iha, N. Y.; Templeton, J. L.; Meyer, T. J. *Acc. Chem. Res.* **2009**, *42*, 1954–1965.
- [23] Duan, L.; Xu, Y.; Gorlov, M.; Tong, L.; Andersson, S.; Sun, L. *Chem. - Eur. J.* **2010**, *16*, 4659–4668.
- [24] Prévot, M. S.; Sivula, K. *J. Phys. Chem. C* **2013**, *117*, 17879–17893.
- [25] Swierk, J. R.; Mallouk, T. E. *Chem. Soc. Rev.* **2013**, *42*, 2357–2387.
- [26] Luo, J.; Im, J.-H.; Mayer, M. T.; Schreier, M.; Nazeeruddin, M. K.; Park, N.-G.; Tilley, S. D.; Fan, H. J.; Grätzel, M. *Science* **2014**, *345*, 1593–1596.
- [27] Liu, J.; Liu, Y.; Liu, N.; Han, Y.; Zhang, X.; Huang, H.; Lifshitz, Y.; Lee, S.-T.; Zhong, J.; Kang, Z. *Science* **2015**, *347*, 970–974.
- [28] Swierk, J. R.; Méndez-Hernández, D. D.; McCool, N. S.; Liddell, P.; Terazono, Y.; Pahk, I.; Tomlin, J. J.; Oster, N. V.; Moore, T. A.; Moore, A. L.; et al. *Proc. Natl. Acad. Sci. U. S. A.* **2015**, *112*, 1681–1686.
- [29] Verlage, E.; Hu, S.; Liu, R.; Jones, R. J. R.; Sun, K.; Xiang, C.; Lewis, N. S.; Atwater, H. A. *Energy Environ. Sci.* **2015**, *8*, 3166–3172.
- [30] de Respinis, M.; Joya, K. S.; De Groot, H. J. M.; D'Souza, F.; Smith, W. A.; van de Krol, R.; Dam, B. *J. Phys. Chem. C* **2015**, *119*, 7275–7281.
- [31] Ding, X.; Zhang, L.; Wang, Y.; Liu, A.; Gao, Y. *Coord. Chem. Rev.* **2018**, *357*, 130–143.
- [32] Brennaman, M. K.; Dillon, R. J.; Alibabaei, L.; Gish, M. K.; Dares, C. J.; Ashford, D. L.; House, R. L.; Meyer, G. J.; Papanikolas, J. M.; Meyer, T. J. *J. Am. Chem. Soc.* **2016**, *138*, 13085–13102.
- [33] Dau, H.; Limberg, C.; Reier, T.; Risch, M.; Roggan, S.; Strasser, P. *ChemCatChem* **2010**, *2*, 724–761.
- [34] Hughes, T. F.; Friesner, R. A. *J. Phys. Chem. B* **2011**, *115*, 9280–9289.

- [35] Akimov, A. V.; Neukirch, A. J.; Prezhdov, O. V. *Chem. Rev.* **2013**, *113*, 4496-4565.
- [36] McCool, N. S.; Swierk, J. R.; Nemes, C. T.; Saunders, T. P.; Schmuttenmaer, C. A.; Mallouk, T. E. *ACS Appl. Mater. Interfaces* **2016**, *8*, 16727-16735.
- [37] Concepcion, J. J.; Tsai, M.-K.; Muckerman, J. T.; Meyer, T. J. *J. Am. Chem. Soc.* **2010**, *132*, 1545-1557.
- [38] Pastore, M. *Computation* **2017**, *5*, 5.
- [39] de Ruiter, J. M.; Purchase, R. L.; Monti, A.; van der Ham, C. J. M.; Gullo, M. P.; Joya, K. S.; D'Angelantonio, M.; Barbieri, A.; Hetterscheid, D. G. H.; de Groot, H. J. M.; et al. *ACS Catal.* **2016**, *6*, 7340-7349.
- [40] Monti, A.; de Ruiter, J. M.; de Groot, H. J. M.; Buda, F. *J. Phys. Chem. C* **2016**, *120*, 23074-23082.
- [41] Meyer, T. J.; Huynh, M. H. V.; Thorp, H. H. *Angew. Chem., Int. Ed.* **2007**, *46*, 5284-5304.
- [42] Hammes-Schiffer, S. *Energy Environ. Sci.* **2012**, *5*, 7696-7703.
- [43] Hammes-Schiffer, S. *J. Am. Chem. Soc.* **2015**, *137*, 8860-8871.
- [44] Huynh, M. H. V.; Meyer, T. J. *Chem. Rev.* **2007**, *107*, 5004-5064.
- [45] Kishore, R. S. K.; Kel, O.; Banerji, N.; Emery, D.; Bollot, G.; Mareda, J.; Gomez-Casado, A.; Jonkheijm, P.; Huskens, J.; Maroni, P.; et al. *J. Am. Chem. Soc.* **2009**, *131*, 11106-11116.
- [46] Sakai, N.; Mareda, J.; Vauthey, E.; Matile, S. *Chem. Commun.* **2010**, *46*, 4225-4237.
- [47] Diac, A.; Matache, M.; Grosu, I.; Hädade, N. D. *Adv. Synth. Catal.* **2018**, *360*, 817-845.
- [48] Earmme, T.; Hwang, Y.-J.; Murari, N. M.; Subramaniyan, S.; Jenekhe, S. A. *J. Am. Chem. Soc.* **2013**, *135*, 14960-14963.
- [49] Choi, J.; Kim, K.-H.; Yu, H.; Lee, C.; Kang, H.; Song, I.; Kim, Y.; Oh, J. H.; Kim, B. J. *Chem. Mater.* **2015**, *27*, 5230-5237.
- [50] Kim, T.; Kim, J.-H.; Kang, T. E.; Lee, C.; Kang, H.; Shin, M.; Wang, C.; Ma, B.; Jeong, U.; Kim, T.-S.; et al. *Nat. Commun.* **2015**, *6*, 8547.
- [51] Ambrosio, F.; Martsinovich, N.; Troisi, A. *J. Phys. Chem. Lett.* **2012**, *3*, 1531-1535.
- [52] Zhang, L.; Cole, J. M. *ACS Appl. Mater. Interfaces* **2015**, *7*, 3427-3455.
- [53] Materna, K. L.; Crabtree, R. H.; Brudvig, G. W. *Chem. Soc. Rev.* **2017**, *46*, 6099-6110.
- [54] Monti, A.; Negre, C. F. A.; Batista, V. S.; Rego, L. G. C.; de Groot, H. J. M.; Buda, F. *J. Phys. Chem. Lett.* **2015**, *6*, 2393-2398.
- [55] Monti, A.; de Groot, H. J. M.; Buda, F. *J. Phys. Chem. C* **2014**, *118*, 15600-15609.
- [56] Bernasconi, L.; Kazaryan, A.; Belanzoni, P.; Baerends, E. J. *ACS Catal.* **2017**, *7*, 4018-4025.
- [57] Swart, M.; Ehlers, A. W.; Lammertsma, K. *Mol. Phys.* **2004**, *102*, 2467-2474.
- [58] Carvalho, A. T. P.; Swart, M. *J. Chem. Inf. Model* **2014**, *54*, 613-620.
- [59] Groenhof, A. R.; Ehlers, A. W.; Lammertsma, K. *J. Am. Chem. Soc.* **2007**, *129*, 6204-6209.
- [60] Conradie, J.; Ghosh, A. *J. Chem. Theory Comput.* **2007**, *3*, 689-702.
- [61] Vallés-Pardo, J. L.; Guijt, M. C.; Iannuzzi, M.; Joya, K. S.; de Groot, H. J. M.; Buda, F. *ChemPhysChem* **2012**, *13*, 140-146.
- [62] Liao, M.-S.; Watts, J. D.; Huang, M.-J. *J. Phys. Chem. A* **2007**, *111*, 5927-5935.
- [63] Güell, M.; Luis, J. M.; Siegbahn, P. E. M.; Solà, M. *J. Biol. Inorg. Chem.* **2009**, *14*, 273-285.
- [64] Klamt, A. *J. Phys. Chem.* **1995**, *99*, 2224-2235.
- [65] Klamt, A.; Jonas, V. *J. Chem. Phys.* **1996**, *105*, 9972-9981.
- [66] Te Velde, G.; Bickelhaupt, F. M.; Baerends, E. J.; Fonseca Guerra, C.; van Gisbergen, S. J. A.; Snijders, J. G.; Ziegler, T. *J. Comput. Chem.* **2001**, *22*, 931-967.
- [67] ADF2017, SCM, Theoretical Chemistry, Vrije Universiteit, Amsterdam, The Netherlands, <http://www.scm.com>.
- [68] Ma, C.; Piccinin, S.; Fabris, S. *ACS Catal.* **2012**, *2*, 1500-1506.
- [69] CPMD, <http://www.cpmc.org>, Copyright IBM Corp., 1990-2019, Copyright MPI für Festkörperforschung Stuttgart, 1997-2001.
- [70] Accelrys Software Inc., *Discovery Studio Modeling Environment*, Accelrys Software Inc., San Diego, **2012**.

- [71] Brooks, B. R.; Bruccoleri, R. E.; Olafson, B. D.; States, D. J.; Swaminathan, S.; Karplus, M. *J. Comput. Chem.* **1983**, *4*, 187-217.
- [72] Hartwigsen, C.; Goedecker, S.; Hutter, J. *Phys. Rev. B* **1998**, *58*, 3641-3662.
- [73] Lin, I. C.; Coutinho-Neto, M. D.; Felsenheimer, C.; von Lilienfeld, O. A.; Tavernelli, I.; Rothlisberger, U. *Phys. Rev. B* **2007**, *75*, 205131.
- [74] Humphrey, W.; Dalke, A.; Schulten, K. VMD: visual molecular dynamics. *J. Mol. Graphics* **1996**, *14*, 33-38.
- [75] VMD - Visual Molecular Dynamics, Theoretical Chemistry and Computational Biophysics Group, University Of Illinois, Urbana, U.S.A, **2016**.
- [76] Ciccotti, G.; Ferrario M. *Mol. Simul.* **2004**, *30*, 787-793.
- [77] Ensing, B.; Meijer, E. J.; Blöchl, P. E.; Baerends, E. J. *J. Phys. Chem. A* **2001**, *105*, 3300-3310.
- [78] Costanzo, F.; Della Valle, R. G. *J. Phys. Chem. B* **2008**, *112*, 12783-12789.
- [79] Otter, W. K. d.; Briels, W. J. *J. Chem. Phys.* **1998**, *109*, 4139-4146.
- [80] Sprik, M.; Ciccotti, G. *J. Chem. Phys.* **1998**, *109*, 7737-7744.
- [81] Bernasconi, L.; Baerends, E. J.; Sprik, M. *J. Phys. Chem. B* **2006**, *110*, 11444-11453.
- [82] de Grotthuss, C. J. T. *Biochim. Biophys. Acta, Bioenerg.* **2006**, *1757*, 871-875.
- [83] Agmon, N. *Chem. Phys. Lett.* **1995**, *244*, 456-462.
- [84] Cukierman, S. Et tu, *Biochim. Biophys. Acta, Bioenerg.* **2006**, *1757*, 876-885.
- [85] Markovitch, O.; Chen, H.; Izvekov, S.; Paesani, F.; Voth, G. A.; Agmon, N. *J. Phys. Chem. B* **2008**, *112*, 9456-9466.
- [86] Hassanali, A.; Giberti, F.; Cuny, J.; Kühne, T. D.; Parrinello, M. *Proc. Natl. Acad. Sci.* **2013**, *110*, 13723-13728.
- [87] Marx, D.; Chandra, A.; Tuckerman, M. E. *Chem. Rev.* **2010**, *110*, 2174-2216.
- [88] Codorniu-Hernández, E.; Kusalik, P. G. *Proc. Natl. Acad. Sci.* **2013**, *110*, 13697-13698.
- [89] Liang, R.; Li, H.; Swanson, J. M. J.; Voth, G. A. *Proc. Natl. Acad. Sci.* **2014**, *111*, 9396-9401.
- [90] Yang, X.; Hall, M. B. *J. Am. Chem. Soc.* **2010**, *132*, 120-130.
- [91] Lundberg, M.; Siegbahn, P. E. M. *Chem. Phys. Lett.* **2005**, *401*, 347-351.
- [92] Siegbahn, P. E. M. *Chem. - Eur. J.* **2006**, *12*, 9217-9227.
- [93] Guo, Y.; Li, H.; He, L.-L.; Zhao, D.-X.; Gong, L.-D.; Yang, Z.-Z. *Phys. Chem. Chem. Phys.* **2017**, *19*, 13909-13923.
- [94] Eyring, H. *J. Chem. Phys.* **1935**, *3*, 107-115.
- [95] Laidler, K. J.; King, M. C. *J. Phys. Chem.* **1983**, *87*, 2657-2664.
- [96] Pollak, E.; Talkner, P. *Chaos* **2005**, *15*, 026116.
- [97] Solis, B. H.; Hammes-Schiffer, S. *Inorg. Chem.* **2014**, *53*, 6427-6443.
- [98] Gish, M. K.; Lapidés, A. M.; Brennaman, M. K.; Templeton, J. L.; Meyer, T. J.; Papanikolas, J. M. *J. Phys. Chem. Lett.* **2016**, *7*, 5297-5301.
- [99] Chou, H.-H.; Yang, C.-H.; Lin, J. T. s.; Hsu, C.-P. *J. Phys. Chem. C* **2017**, *121*, 983-992.
- [100] Scholes, G. D. *J. Phys. Chem. Lett.* **2018**, *9*, 1568-1572.
- [101] Bruno, W. J.; Bialek, W., *Biophys. J.* **1992**, *63*, 689-699.
- [102] Moser, C. C.; Keske, J. M.; Warncke, K.; Farid, R. S.; Dutton, P. L., *Nature* **1992**, *355*, 796-802.
- [103] Chen, Z.; Concepcion, J. J.; Hu, X.; Yang, W.; Hoertz, P. G.; Meyer, T. J. *Proc. Natl. Acad. Sci.* **2010**, *107*, 7225-7229.
- [104] Hammes-Schiffer, S. *Acc. Chem. Res.* **2009**, *42*, 1881-1889.
- [105] Shaffer, D. W.; Xie, Y.; Concepcion, J. J. *Chem. Soc. Rev.* **2017**, *46*, 6170-6193.
- [106] Shaffer, D. W.; Xie, Y.; Szalda, D. J.; Concepcion, J. J. *J. Am. Chem. Soc.* **2017**, *139*, 15347-15355.
- [107] Meyer, T. J.; Sheridan, M. V.; Sherman, B. D. *Chem. Soc. Rev.* **2017**, *46*, 6148-6169.
- [108] Coggins, M. K.; Zhang, M. T.; Chen, Z.; Song, N.; Meyer, T. J. *Angew. Chem., Int. Ed.* **2014**, *53*, 12226-12230.

- [109] Varcoe, J. R.; Atanassov, P.; Dekel, D. R.; Herring, A. M.; Hickner, M. A.; Kohl, P. A.; Kucernak, A. R.; Mustain, W. E.; Nijmeijer, K.; Scott, K.; et al. *Energy Environ. Sci.* **2014**, 7, 3135-3191.
- [110] Ran, J.; Wu, L.; He, Y.; Yang, Z.; Wang, Y.; Jiang, C.; Ge, L.; Bakangura, E.; Xu, T. *J. Membr. Sci.* **2017**, 522, 267-291.
- [111] Gu, S.; Gong, K.; Yan, E. Z.; Yan, Y. *Energy Environ. Sci.* **2014**, 7, 2986-2998.
- [112] He, G.; Li, Z.; Zhao, J.; Wang, S.; Wu, H.; Guiver, M. D.; Jiang, Z. *Adv. Mater.* **2015**, 27, 5280-5295.
- [113] Hammarström, L. *Acc. Chem. Res.* **2015**, 48, 840-850.

A. Appendix

2.A.1. Calculated and Experimentally Measured Free Energy Change for each Catalytic Step along the Proposed Catalytic Mechanism

Table A2.1. Calculated ΔG_{calc} for each catalytic step along the proposed catalytic mechanism computed with the ADF program¹⁻² at the OPBE/TZP level, in comparison to the experimentally measured ΔG_{exp} for $[\text{Ru}^{\text{II}}-\text{OH}_2]^{2+}$ water oxidation catalyst (WOC) adjusted to pH 0 according to the Nernst Equation (adapted from Ref. 44 in the main text).

Step	Intermediates		ΔG_{calc} (eV)	ΔG_{exp} (eV)
1 st	$[\text{Ru}^{\text{II}}-\text{OH}_2]^{2+} \rightarrow [\text{Ru}^{\text{III}}-\text{OH}]^{2+}$	(I ₁ → I ₂)	0.87	0.67
2 nd	$[\text{Ru}^{\text{III}}-\text{OH}]^{2+} \rightarrow [\text{Ru}^{\text{IV}}=\text{O}]^{2+}$	(I ₂ → I ₃)	1.38	1.27
3 rd	$[\text{Ru}^{\text{IV}}=\text{O}]^{2+} \rightarrow [\text{Ru}^{\text{III}}-\text{OOH}]^{2+}$	(I ₃ → I ₄)	2.19	1.83
4 th	$[\text{Ru}^{\text{III}}-\text{OOH}]^{2+} \rightarrow [\text{Ru}^{\text{II}}-\text{OO}]^{2+}$	(I ₄ → I ₀)	0.73	
	$[\text{Ru}^{\text{II}}-\text{OO}]^{2+} \rightarrow [\text{Ru}^{\text{II}}-\text{OH}_2]^{2+}$	(I ₀ → I ₁)	-0.15	
	$2\text{H}_2\text{O} \rightarrow 2\text{H}_2 + \text{O}_2$		5.02	4.92

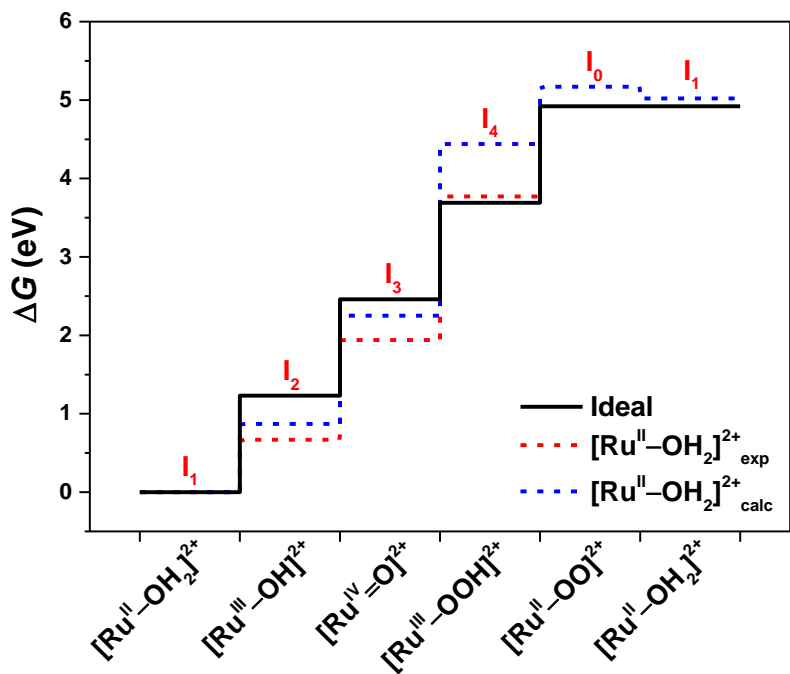


Figure A2.1. Free energy difference ΔG between intermediates along the catalytic pathway of the $[\text{Ru}^{\text{II}}-\text{OH}_2]^{2+}$ catalyst. DFT results (dashed blue line) are compared with the values extracted from electrochemical data (dashed red line). We also show for comparison the optimal catalyst case (black line) corresponding to a change in free energy of 1.23 eV for all four steps (adapted from Ref. 44 in the main text).

2.A.2. Frontier Molecular Orbital Energy Levels of four Intermediates along the Catalytic Pathway of the $[\text{Ru}^{\text{II}}\text{-OH}_2]^{2+}$ Catalyst

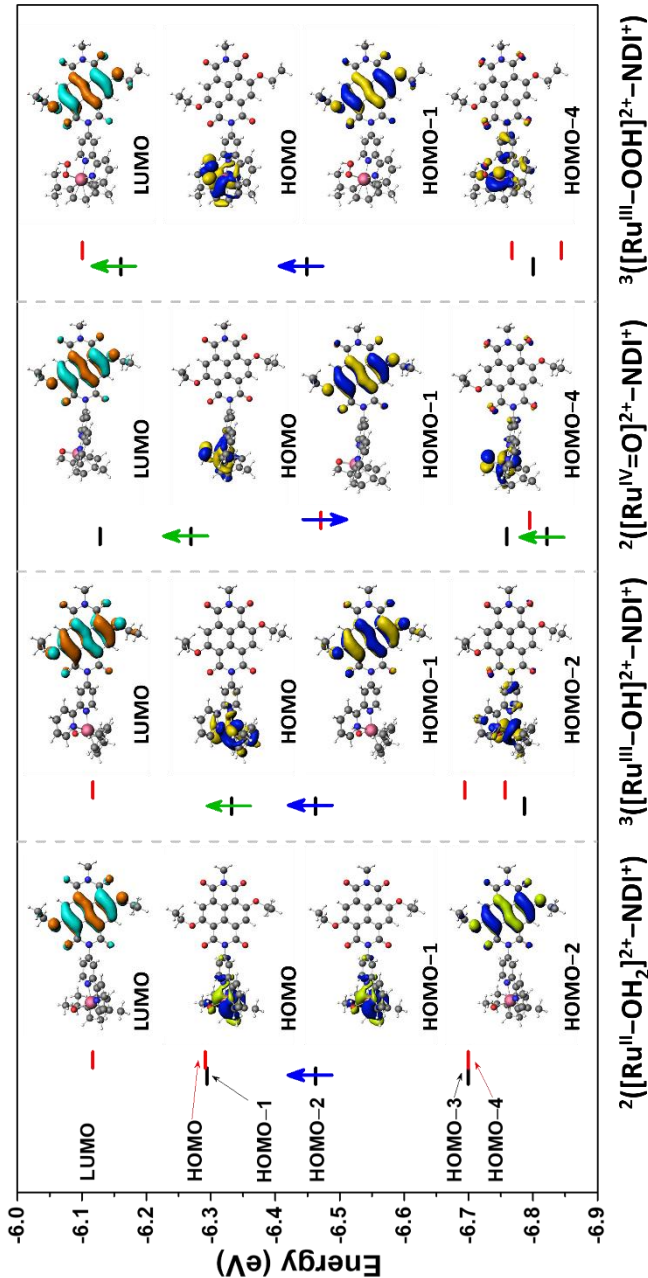


Figure A2.2. Selected frontier molecular orbitals of involved intermediates after photooxidation of NDI during the four consecutive catalytic steps in route ① computed with the ADF program using the OPBE functional and the TZP basis set. The continuum solvation model COSMO³⁻⁴ is used to describe the water environment. The left (black) and right (red) columns refer to as the α orbitals and β orbitals, respectively. Only the unpaired electrons are indicated by vertical arrows explicitly (green for unpaired electron localized on the catalyst and blue for unpaired electron on the oxidized NDI^{+*}). See Table A2.2 for the molecular energy levels.

For all these intermediates, the partially occupied molecular orbital localized on the NDI is always lower in energy than the HOMO of the supramolecular complex, which is localized on the ruthenium catalyst. This result suggests that for all the oxidized intermediates there is a driving force for electron transfer from the ruthenium catalyst to the NDI dye in continuum solvation model. The AIMD simulations presented in this work show that this is also the case in explicit solvent.

Table A2.2. Selected frontier molecular orbital energy levels and energy difference ΔE_{SOMO} (in eV) between SOMO WOC (HOMO WOC for $^2([\text{Ru}^{\text{II}}\text{-OH}_2]^{2+}\text{-NDI}^{+})$) and SOMO dye of four intermediates along the catalytic pathway of the $[\text{Ru}^{\text{II}}\text{-OH}_2]^{2+}$ catalyst following route (1) in Scheme 2.1 computed with the ADF program using the OPBE (and PBE for comparison) functional and the TZP basis set. The continuum solvation model COSMO is used to describe the water environment. Only the unpaired electrons are indicated by vertical arrows explicitly (green for unpaired electron localized on the catalyst and blue for unpaired electron on the oxidized NDI $^{+}$).

Intermediate	$^2([\text{Ru}^{\text{II}}\text{-OH}_2]^{2+}\text{-NDI}^{+})$		$^3([\text{Ru}^{\text{III}}\text{-OH}]^{2+}\text{-NDI}^{+})$		$^2([\text{Ru}^{\text{IV}}\text{=O}]^{2+}\text{-NDI}^{+})$		$^3([\text{Ru}^{\text{III}}\text{-OOH}]^{2+}\text{-NDI}^{+})$	
	\uparrow		\uparrow	\uparrow	\uparrow	\uparrow	\uparrow	\uparrow
OPBE								
Energy levels	Orbital	Energy	Orbital	Energy	Orbital	Energy	Orbital	Energy
LUMO	β	-6.1172	β	-6.1144	α	-6.1226	β	-6.1008
HOMO	β	-6.2913	α (SOMO WOC)	-6.3430	α (SOMO WOC)	-6.2750	α (SOMO WOC)	-6.1607
HOMO-1	α	-6.2940	α (SOMO dye)	-6.4600	β (SOMO dye)	-6.4682	α (SOMO dye)	-6.4491
HOMO-2	α (SOMO dye)	-6.4628	β	-6.6804	α	-6.7321	β	-6.7675
HOMO-3	β	-6.6995	β	-6.7566	β	-6.7648	α	-6.8002
HOMO-4	α	-6.6995	α	-6.7920	α	-6.8274	β	-6.8437
ΔE_{SOMO}		0.1714		0.1170		0.1932		0.2884
PBE								
Energy levels	Orbital	Energy	Orbital	Energy	Orbital	Energy	Orbital	Energy
LUMO	β	-6.1172	β	-6.1226	α	-6.1281	β	-6.1281
HOMO	β	-6.2723	α (SOMO WOC)	-6.3512	α (SOMO WOC)	-6.2641	α (SOMO WOC)	-6.1852
HOMO-1	α	-6.2723	α (SOMO dye)	-6.4355	β (SOMO dye)	-6.4383	α (SOMO dye)	-6.4410
HOMO-2	α (SOMO dye)	-6.4301	β	-6.6886	α	-6.7213	β	-6.7321
HOMO-3	β	-6.5716	β	-6.7349	α	-6.7430	α	-6.7539
HOMO-4	α	-6.5743	α	-6.7566	β	-6.7458	β	-6.8954
ΔE_{SOMO}		0.1578		0.0844		0.1742		0.2558

2.A.3. The Constraint Force and Running Average of the Constraint Force as a Function of Time

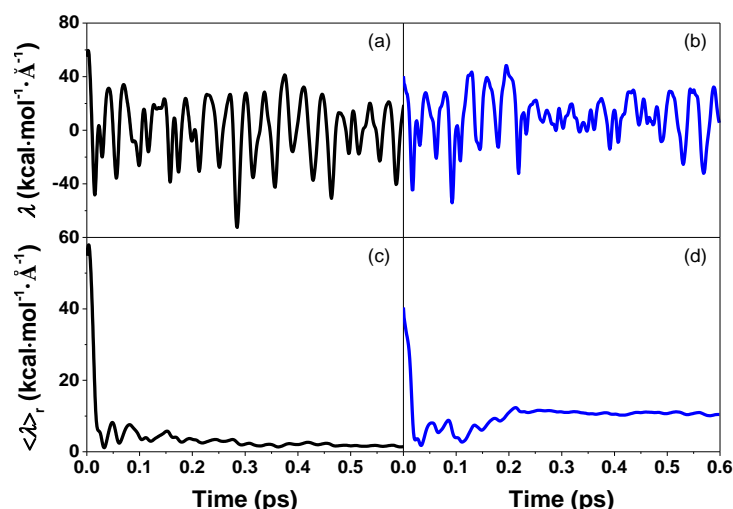


Figure A2.3. The constraint force (λ , in $\text{kcal mol}^{-1} \text{\AA}^{-1}$) and running average of the constraint force ($\langle \lambda \rangle_r$, in $\text{kcal mol}^{-1} \text{\AA}^{-1}$) as a function of time for two different distance constraints $d(\text{H}_i \leftarrow \text{O}_{ii}) = 1.6 \text{ \AA}$ (a, c) and $d(\text{H}_i \leftarrow \text{O}_{ii}) = 1.4 \text{ \AA}$ (b, d), respectively. The running average reaches a stable value even within this relatively short MD timescale of $\sim 0.5 \text{ ps}$.

2.A.4. Standard Deviation of Free Energy Profiles along the Reaction Coordinate $d(\text{H}_i \leftarrow \text{O}_{ii})$

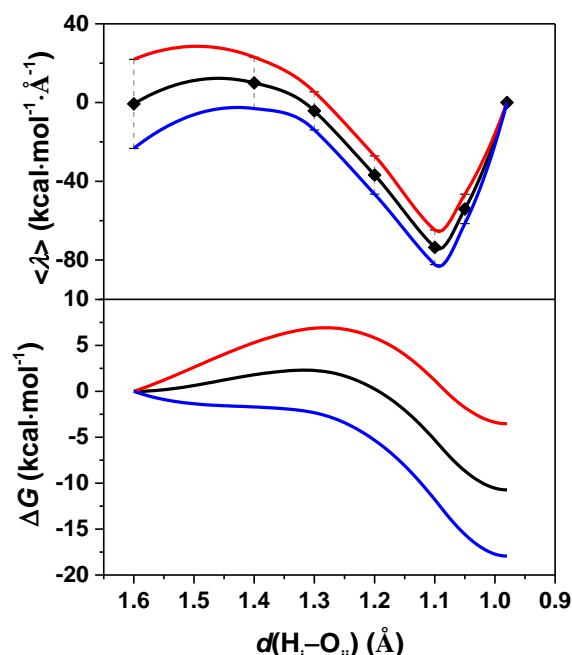


Figure A2.4. (top panel) Maximum (red) and minimum (blue) interpolations of the Lagrangian multiplier $\langle \lambda \rangle$ reproduced from Figure 2.4. The error bars indicate the standard deviations. (bottom panel) Free energy profiles along the reaction coordinate $d(\text{H}_i \leftarrow \text{O}_{ii})$ computed from thermodynamic integration of the interpolated time-averaged mean forces.

2.A.5. The Results with Antiparallel Spin Alignment on NDI along the MD Trajectories of second Catalytic Step in Route ②

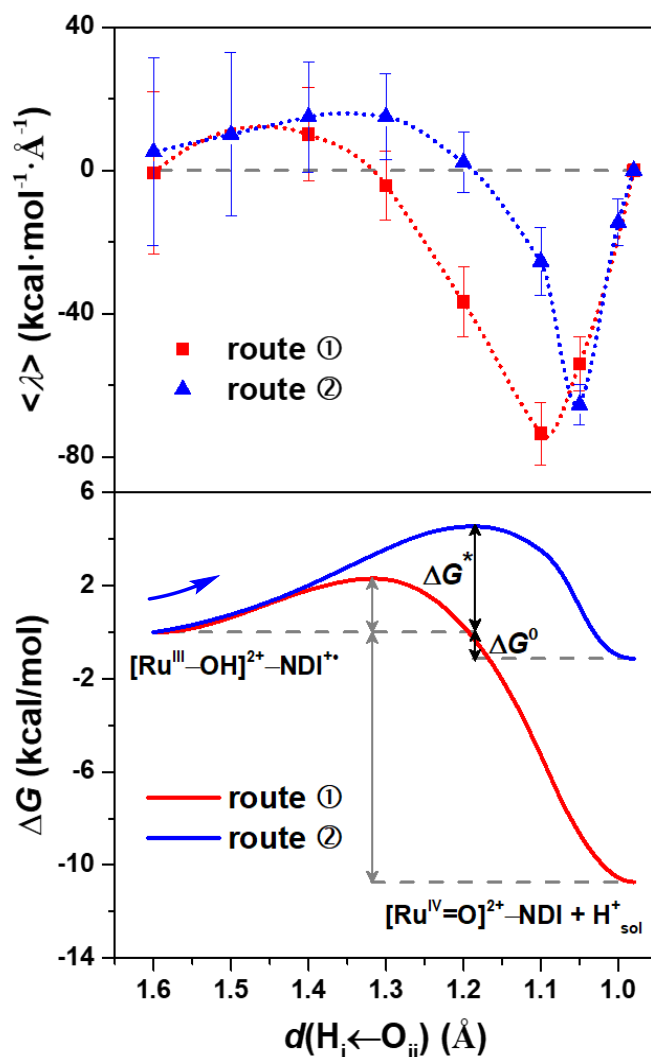


Figure A2.5. (top panel) The constraint mean force represented by the Lagrangian multiplier $\langle \lambda \rangle$ computed for each constrained MD simulation as a function of the reaction coordinate $d(H_i \leftarrow O_{ii})$ along route ② (blue triangles) and ① (red squares), for comparison. The mean force at the equilibrium distance $d(H_i \leftarrow O_{ii}) = 0.98$ Å evaluated in the free MD has been set to 0. The 100-point Akima spline interpolation (dotted lines) is used to interpolate the mean forces including also the zero point at equilibrium. (bottom panel) Free energy profile along the reaction coordinate $d(H_i \leftarrow O_{ii})$ of route ② (blue line) and ① (red line) computed from thermodynamic integration of the interpolated time-averaged mean forces. The initial and final intermediates are also indicated.

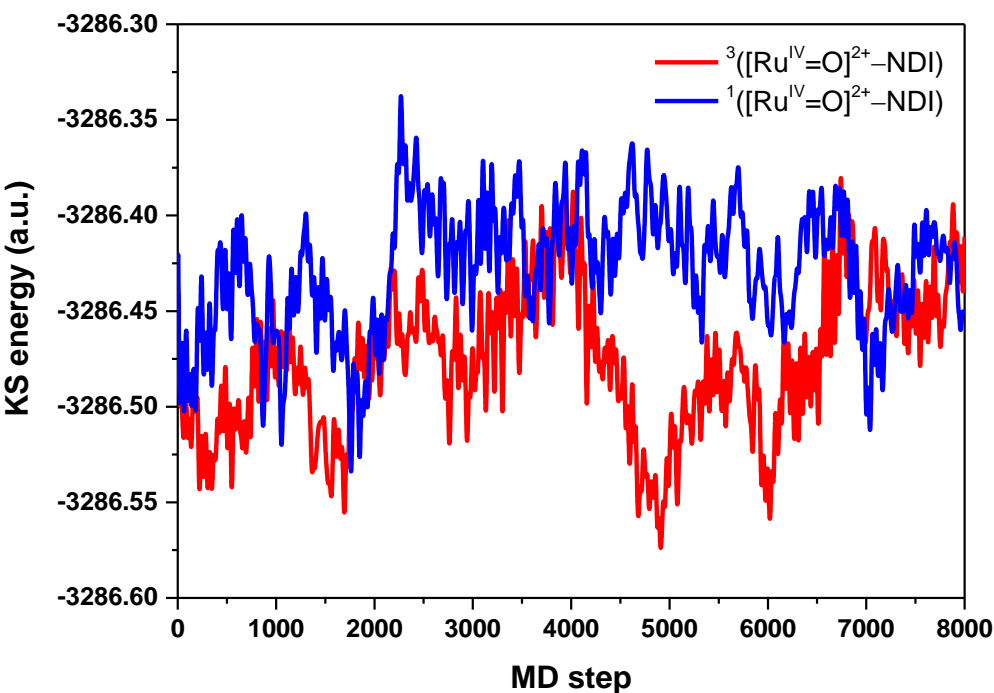


Figure A2.6. Time evolution of the KS energy of the product intermediates $^3([\text{Ru}^{\text{IV}}=\text{O}]^{2+}\text{-NDI})$ (red line) and $^1([\text{Ru}^{\text{IV}}=\text{O}]^{2+}\text{-NDI})$ (blue line) along the FMD trajectories after the second catalytic step. Although large energy fluctuations are observed during the MD simulations, the product intermediate $^3([\text{Ru}^{\text{IV}}=\text{O}]^{2+}\text{-NDI})$ is on average lower in energy than $^1([\text{Ru}^{\text{IV}}=\text{O}]^{2+}\text{-NDI})$ (see Table A2.3).

Table A2.3. Time-averaged KS energy of the product intermediates $^3([\text{Ru}^{\text{IV}}=\text{O}]^{2+}\text{-NDI})$ and $^1([\text{Ru}^{\text{IV}}=\text{O}]^{2+}\text{-NDI})$ and the energy difference (ΔE_{int}) between them along the free MD trajectories (see Figure A2.6).

$2S+1$	$[\text{Ru}^{\text{IV}}=\text{O}]^{2+}\text{-NDI}$		KS energy (eV)	ΔE_{int} (eV)
3	\uparrow	\uparrow	-89429.615	1.313
1	\uparrow	\downarrow	-89428.302	

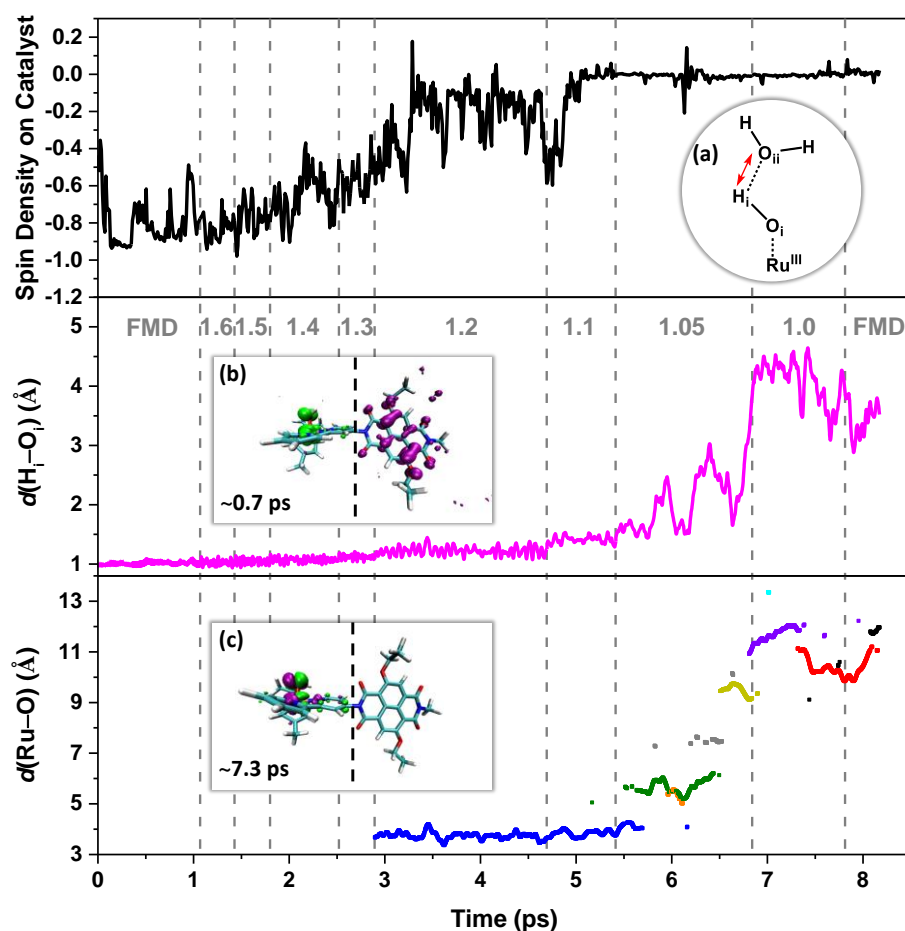


Figure A2.7. (top panel) The spin density integrated over the half of the simulation box including the catalyst (left-hand side of the dashed black line in the inset **b** and **c**) along the MD trajectories starting from the oxidized intermediate $^1([\text{Ru}^{\text{III}}-\text{OH}]^{2+}-\text{NDI}^+)$ (see route ② in Scheme 1). An integrated spin density value of -1 corresponds to one unpaired α electron. The starting configuration at $d(\text{H}_i-\text{O}_{\text{ii}}) = 1.6 \text{ \AA}$ has been extracted from a previous unconstrained simulation of the first catalytic intermediate for $\sim 1 \text{ ps}$ (with an average $d(\text{H}_i-\text{O}_{\text{ii}}) \approx 1.7 \text{ \AA}$). (middle panel) Time evolution of the geometrical parameter $d(\text{H}_i-\text{O}_i)$ along the constrained and FMD trajectory. (bottom panel) The distance between Ru and H_3O^+ , defined as an oxygen atom with 3 H within a radius of 1.2 \AA , as measured for a sequence of MD simulations. According to the simulations, only one oxygen is in the H_3O^+ form at any time, and although the proton associates with a number of different oxygens (indicated with different colours) during the simulation, it is primarily bonded to four oxygens (blue, gold, red and purple). The value of the constrained reaction coordinate $d(\text{H}_i-\text{O}_{\text{ii}})$ applied in the MD simulations is noted in grey. Inset (a) shows the schematic structure of the first few water molecules along the hydrogen-bonding network coordinated to the hydroxide ligand. The red double-sided arrow indicates the reaction coordinate considered for oxidized intermediate $^1([\text{Ru}^{\text{III}}-\text{OH}]^{2+}-\text{NDI}^+)$ during the constrained MD simulations. Inset (b) and (c) show snapshots from the FMD and constrained MD trajectories, in which the spin density isosurface of α and β electrons in green and purple respectively. The labels refer to the time at which the snapshot has been taken along the collected trajectory.

2.A.6. Computed Total Bonding Energy for each Reactant/Product with Different Spin Alignments for all Catalytic Intermediates

Table A2.4. Total bonding energy E_{tot} (in kcal mol⁻¹) computed for each catalytic intermediate at the DFT level. Computational details are described in section 2.1 of chapter 2. The spin alignment of the unpaired electron on the Ru-based catalyst and NDI (\uparrow for α electron and \downarrow for β electron) and the spin multiplicity of the system ($2S+1$) are also shown. ΔE_{int} (in kcal mol⁻¹) is the computed energy difference between different spin alignments and is calculated with respect to the lowest energy spin state for each catalytic step.

Step		Intermediate	$2S+1$	E_{tot}	ΔE_{int}
1 st	Reactant	[Ru ^{II} -OH ₂] ²⁺ -NDI ⁺ \uparrow	2	-13408.4	
	Product	[Ru ^{III} -OH] ²⁺ -NDI \uparrow	2	-13424.2	
2 nd	Reactant	[Ru ^{III} -OH] ²⁺ -NDI ⁺ \uparrow \downarrow [Ru ^{III} -OH] ²⁺ -NDI ⁺ \uparrow \uparrow	1 3	-13292.1 -13292.0	0 0.1
	Product	[Ru ^{IV} =O] ²⁺ -NDI \uparrow \downarrow [Ru ^{IV} =O] ²⁺ -NDI \uparrow \uparrow	1 3	-13298.1 -13305.6	7.5 0
	Reactant	[Ru ^{IV} =O] ²⁺ -NDI ⁺ \uparrow \uparrow \downarrow [Ru ^{IV} =O] ²⁺ -NDI ⁺ \uparrow \downarrow \uparrow	2 2	-13173.6 -13167.6	0 6.0
	Product	[Ru ^{III} -OOH] ²⁺ -NDI \uparrow	2	-13532.4	
4 th	Reactant	[Ru ^{III} -OOH] ²⁺ -NDI ⁺ \uparrow \downarrow [Ru ^{III} -OOH] ²⁺ -NDI ⁺ \uparrow \uparrow	1 3	-13400.9 -13400.3	0 0.6
	Product	[Ru ^{II} -OO] ²⁺ -NDI \uparrow \downarrow [Ru ^{II} -OO] ²⁺ -NDI \uparrow \uparrow	1 3	-13421.4 -13430.8	9.4 0

2.A.7. Combination of Free Energy Profiles along the Reaction Coordinate of Route ① and ②

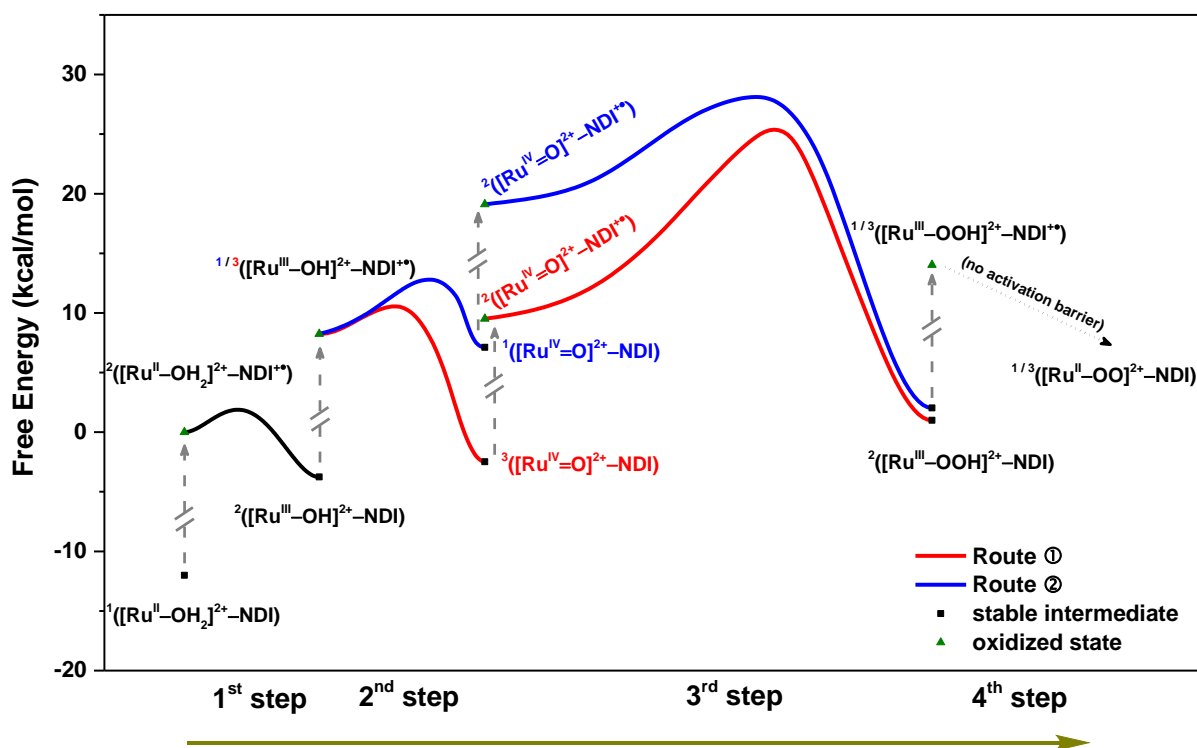


Figure A2.8. Combination of free energy profiles computed from thermodynamic integration for all steps in the catalytic cycle. For the first step (black line) only one spin state is possible. For the second and third step two different spin alignments are considered: route ① (red line) and route ② (blue line). The 4th step (black dotted arrow) is found to proceed spontaneously at room temperature for both parallel ($S = 1$) and antiparallel ($S = 0$) spin alignments, which implies no significant activation barrier. The black squares indicate the stable intermediates, while the green triangles correspond to the supramolecular complex after photooxidation of the NDI dye, leading to NDI^{**} . The dashed grey break arrow (not in scale) indicates the change in energy due to the photoinduced electron transfer from the NDI to the semiconductor. For the second and fourth step the two possible spin alignments after photooxidation are found to be essentially degenerate (see Table A2.4). The product $^2[\text{Ru}^{\text{III}}-\text{OOH}]^{2+}-\text{NDI}$ at the end of the third step can be only in the $S = 1/2$ state. The small free energy difference found between the two routes is due to statistical/numerical errors in the thermodynamic integration procedure.

2.A.8. The Results with Antiparallel Spin Alignment on NDI along the MD Trajectories of the fourth Catalytic Step in Route (2)

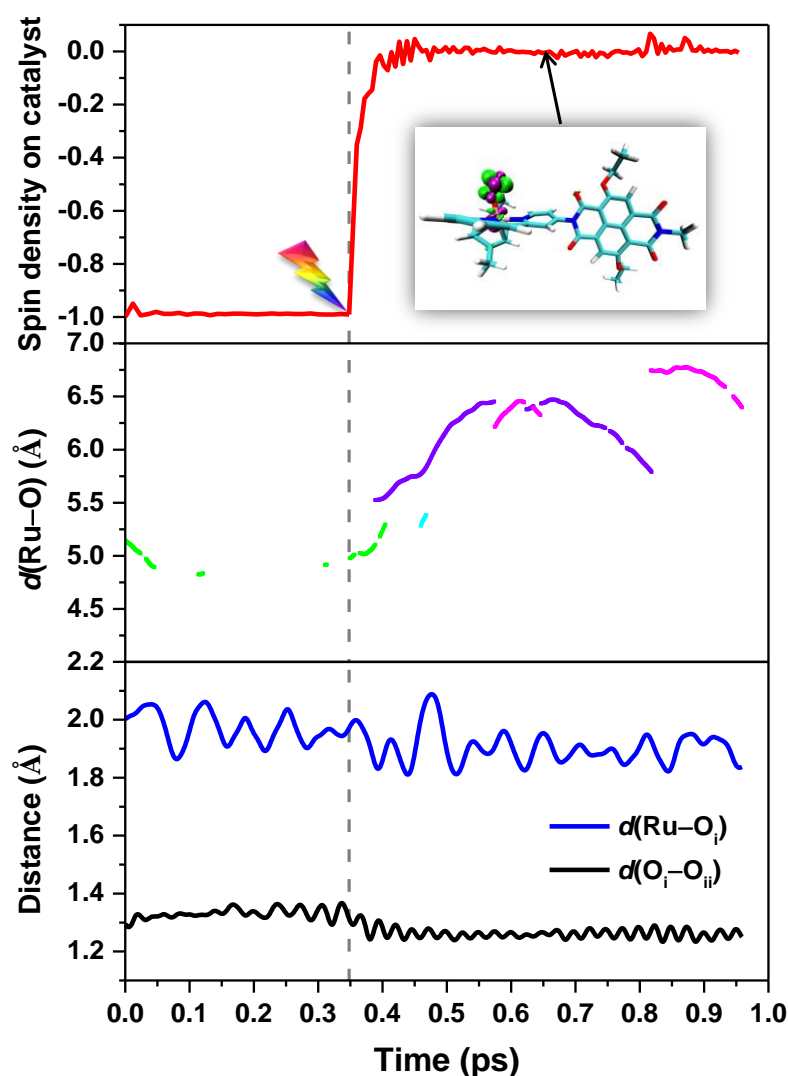


Figure A2.9. (top) The spin density integrated over the half of the simulation box including the catalyst before and after the photoinduced electron injection, which is mimicked by removing one electron from the system at 0.36 ps (indicated by the grey dotted line) to generate an oxidized $^1[\text{Ru}^{\text{III}}-\text{OOH}]^{2+}-\text{NDI}^{+*}$ in the $S = 0$ state (see Scheme 2.1). The inset shows the spin density isosurface computed at a snapshot taken at ~ 0.66 ps, clearly indicating that one unpaired α electron (green spin density isosurface) and one unpaired β electron (purple spin density isosurface) are localized on the catalyst. (middle) The distance between Ru and H_3O^+ measured for the FMD simulations. According to the simulations, the proton primarily bonds to three oxygens (green, purple and magenta). (bottom) Time evolution of the geometrical parameter $d(\text{Ru}-\text{O}_i)$ (blue line) and $d(\text{O}_i-\text{O}_{ii})$ (black line) along the FMD trajectory (see labeling in Scheme 2.2c).

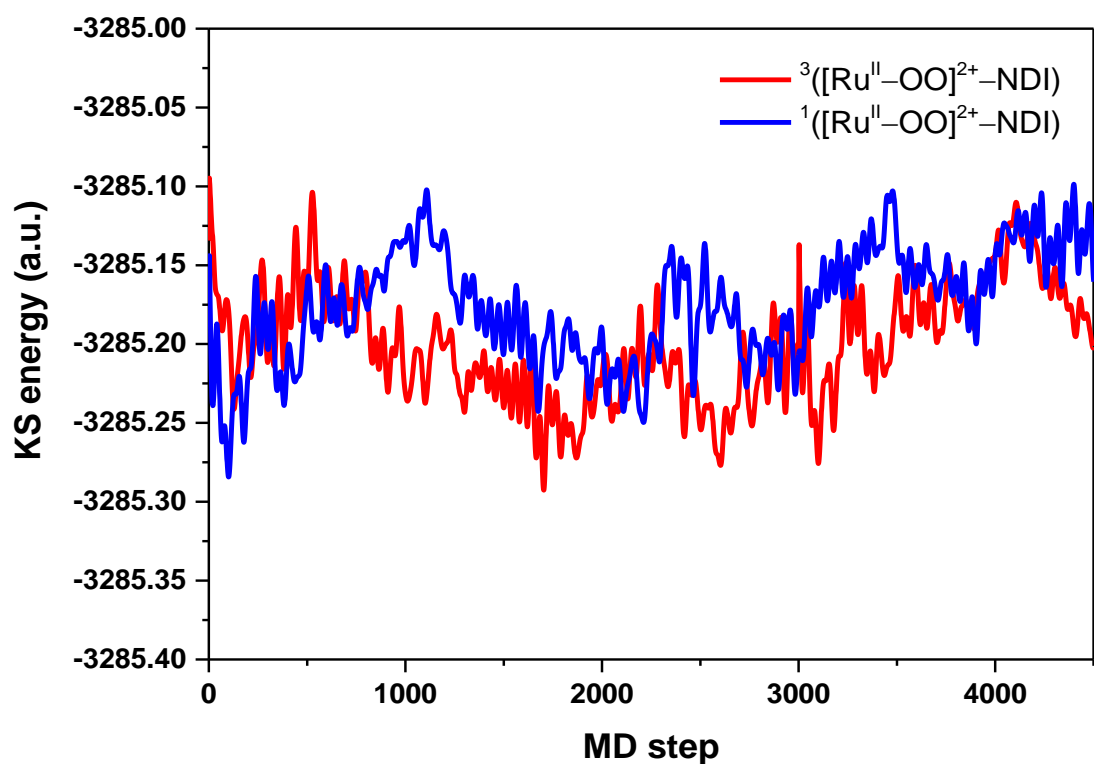


Figure A2.10. Time evolution of the KS energy of the product intermediates $^3([Ru^{II}-OO]^{2+}-NDI)$ (red line) and $^1([Ru^{II}-OO]^{2+}-NDI)$ (blue line) along the FMD trajectories after the fourth catalytic step. Although large fluctuations are observed during the MD simulations, the intermediate $^3([Ru^{II}-OO]^{2+}-NDI)$ indicates a relatively more stable product much lower in energy most of the time compared to the $^1([Ru^{II}-OO]^{2+}-NDI)$.

Table A2.5. Time-averaged KS energy of the product intermediates $^3([Ru^{II}-OO]^{2+}-NDI)$ and $^1([Ru^{II}-OO]^{2+}-NDI)$ and the energy difference between them (ΔE_{int}) along the FMD trajectories after the fourth catalytic step. The triplet state is on average almost 1 eV lower in energy than the singlet state.

$2S+1$	$[Ru^{II}-OO]^{2+}-NDI$	KS energy (eV)	ΔE_{int} (eV)
3	$\uparrow \uparrow$	-89395.046	0.962
1	$\uparrow \downarrow$	-89394.084	

2.A.9. Spin Density Integrated on the Catalyst and Time Evolution of the Dihedral Angle $\angle C_1-N_1-C_2-C_3$ along the MD Trajectories of each Catalytic Step in Route (1)

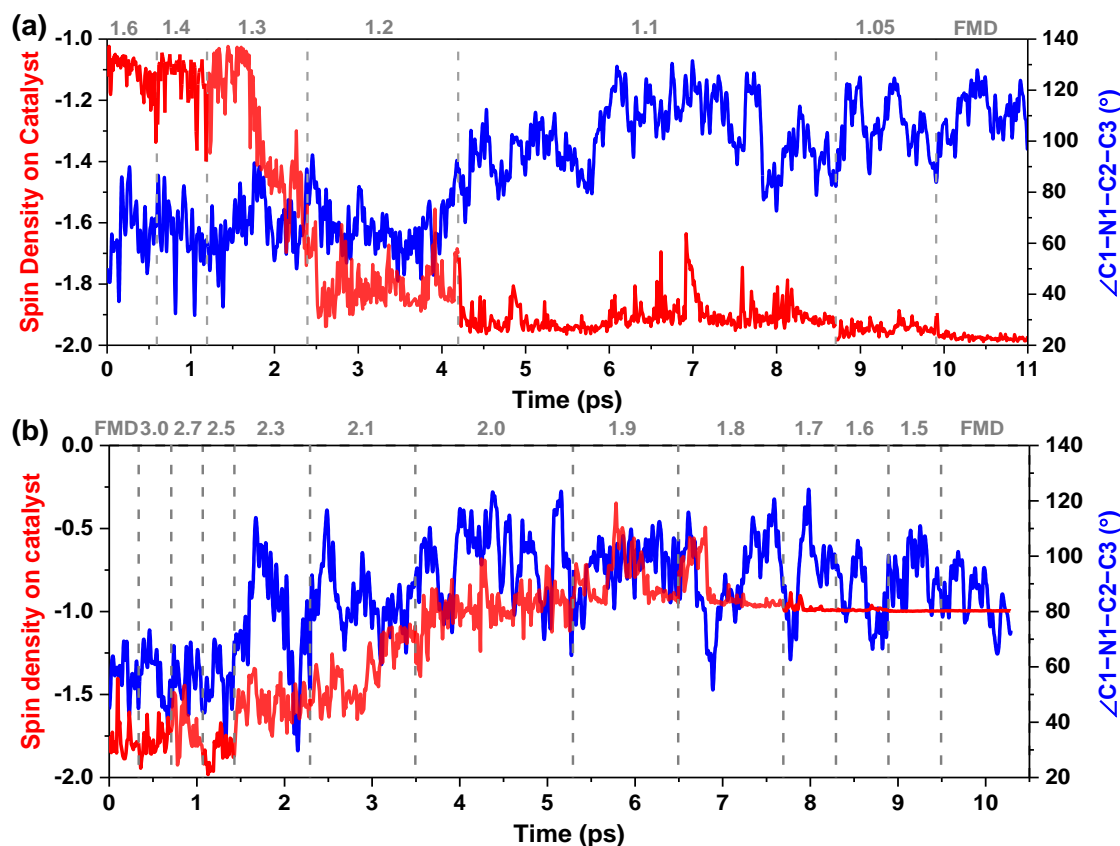


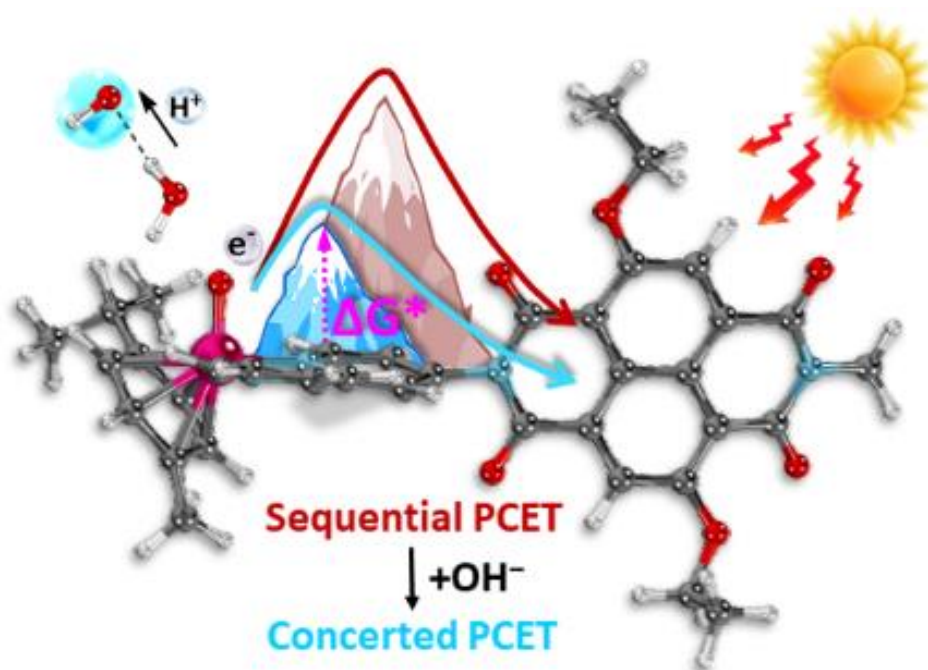
Figure A2.11. The spin density integrated over the half of the simulation box including the catalyst (red line) and time evolution of the geometrical parameter dihedral angle $\angle C_1-N_1-C_2-C_3$ (blue line) along the MD trajectories of (a) the second and (b) the third catalytic step (see labelling in Scheme 2.1), respectively. An integrated spin density value of -1 corresponds to one unpaired α electron. The value of the constrained reaction coordinate applied in the MD simulations for the second (a) and third (b) steps is noted in grey.

2.A.10. References

- [1] Te Velde, G.; Bickelhaupt, F. M.; Baerends, E. J.; Fonseca Guerra, C.; van Gisbergen, S. J. A.; Snijders, J. G.; Ziegler, T. *J. Comput. Chem.* **2001**, *22*, 931-967.
- [2] ADF2017, SCM, Theoretical Chemistry, Vrije Universiteit, Amsterdam, The Netherlands, <http://www.scm.com>.
- [3] Klamt, A. *J. Phys. Chem.* **1995**, *99*, 2224-2235.
- [4] Klamt, A.; Jonas, V. *J. Chem. Phys.* **1996**, *105*, 9972-9981.

CHAPTER 3

A Proton Acceptor near the Active Site Lowers Dramatically the O–O Bond Formation Energy Barrier



This chapter is based on:

Shao Yang, Huub J.M. de Groot, and Francesco Buda, *The Journal of Physical Chemistry Letters*, **2019**, 10, 7690-7697, DOI: 10.1021/acs.jpclett.9b02914.

3

Chapter

3

Abstract

The O–O bond formation process via water nucleophilic attack represents a thermodynamic and kinetic bottleneck in photocatalytic water oxidation because of the considerably high activation free energy barrier. It is of fundamental significance and challenging to find strategies to facilitate this reaction. The microscopic details of the photocatalytic water oxidation step involving the O–O bond formation in a catalyst–dye supramolecular complex are here elucidated by AIMD simulations in the presence of an extra proton acceptor. Introducing a proton acceptor group (OH^-) in the hydration shell near the catalytic active site accelerates the rate-limiting O–O bond formation by inducing a cooperative event proceeding via a concerted PCET mechanism and thus significantly lowering the activation free energy barrier. The in-depth insight provides a strategy for facilitating the photocatalytic water oxidation and for improving the efficiency of DS-PECs.

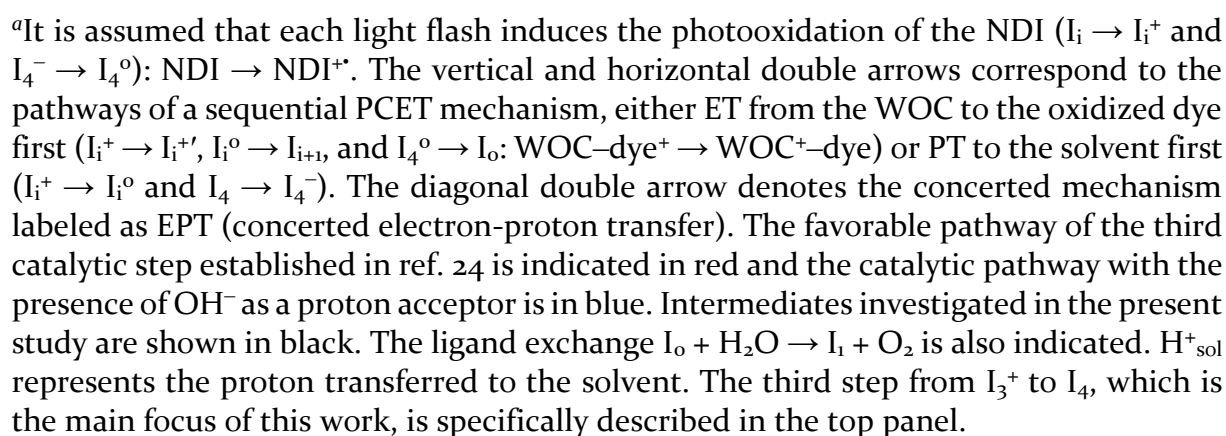
3.1. Introduction

Direct conversion of solar energy into storable fuels, as a credible alternative to fossil fuels, has long been considered as an attractive approach to meet long-term sustainable energy needs.^{1–3} DS-PECs for solar-driven water splitting provide an opportunity to develop artificial photosynthetic devices by integrating visible light-absorbing sensitizers with WOCs or HECs on metal-oxide electrodes.^{4–8} In DS-PECs, water is oxidized to oxygens and protons by photogenerated holes at the (photo-)anode whereas protons/CO₂ are reduced by photoinduced electrons at the (photo-)cathode to produce energy-rich H₂ or CO₂-derived fuels. The process is thermodynamically driven by the photooxidation of sensitizers which should be coupled with WOCs/HECs and anchored to a metal-oxide semiconductor surface.^{9–13}

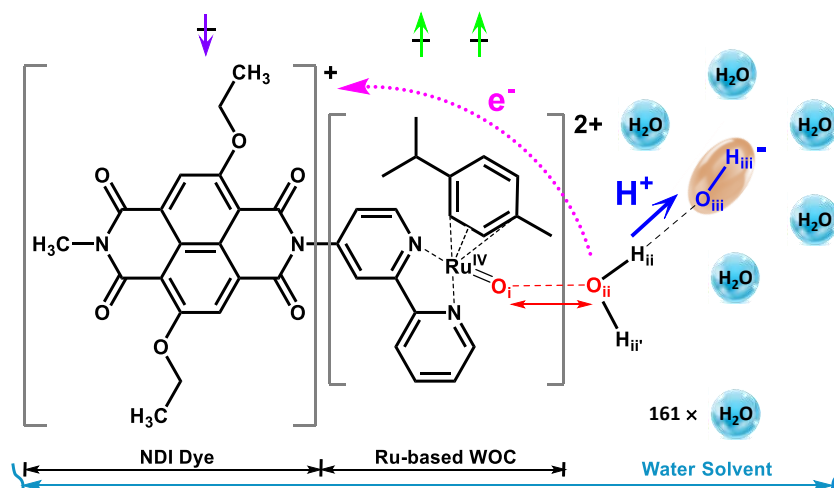
Although increasing effort has been devoted to developing efficient dye-sensitized photoanodes, the photocatalytic four-photon water oxidation half-reaction is still among the most crucial challenges throughout the entire process impeding the large-scale implementation of DS-PEC devices today.^{9–10} Among the four PCET^{14–15} steps involved in catalytic water oxidation, the O–O bond formation process represents a thermodynamic and kinetic bottleneck because of the considerably high activation free energy barrier, which is especially found when using mono-metallic catalysts that proceed via a water-nucleophilic attack mechanism.^{16–19} Therefore, better understanding of the mechanism of O–O bond formation is currently a key issue that has attracted enormous interest in the past decades.^{20–22} We recently explored *in silico* the whole photocatalytic water splitting cycle driven by a WOC–dye supramolecular complex [(cy)Ru^{II}bpy(H₂O)]²⁺–NDI ([Ru^{II}–OH₂]²⁺–NDI for short) solvated in explicit water by using AIMD simulations, which is indeed DFT-MD.^{23–24}

Specifically, the third catalytic water oxidation step involving the O–O bond formation proceeded more likely via a sequential PCET mechanism (see red arrows in Scheme 3.1)²⁵ and exhibited an activation free energy barrier ΔG^* as high as 15.9 kcal mol^{–1} (~0.69 eV). Using transition state theory, this energy barrier translates into a reaction rate $k = 15.7 \text{ s}^{-1}$.²⁴ On this time scale charge recombination from the semiconductor surface to the photooxidized dye becomes very likely, thus reducing the quantum efficiency of the process. It is

Scheme 3.1. The four PCET steps between the catalytic intermediates (I_i) from I_1 to I_0 for water oxidation.^a



Scheme 3.2. Schematic structure of the $^2[(\text{cy})\text{Ru}^{\text{IV}}\text{bpy}(\text{O})]^{2+}\text{--NDI}^{+*}$ complex ($^2([\text{Ru}^{\text{IV}}=\text{O}]^{2+}\text{--NDI}^{+*})$ for short) investigated in this work together with the attacking water molecule and the OH^- in the vicinity of the Ru center.^a



^aThe spin multiplicity value of $2S+1 = 2$ (total spin $S = 1/2$) in this case corresponds to two unpaired α electrons (\uparrow) localized on the catalyst and one unpaired β electron (\downarrow) on the oxidized NDI^{+*} . The red double-sided arrow indicates the reaction coordinate for the constrained MD simulations.

Although rate enhancement has been experimentally observed in catalytic water oxidation via ligand modification of WOCs^{29–34} as well as solvent environmental tuning^{35–40}, the intrinsic mechanism at the molecular level is hidden behind the ensemble measurements. Computational studies play an important role in exploring the catalytic reaction mechanism and predicting the free energy change between reactant and product.^{41–44} In particular, the catalytic water oxidation step involving the O–O bond formation process by single-site Ru metal complexes has been found to be 3 – 5 orders of magnitude faster with the addition of buffer bases owing to their involvement in either concerted atom-proton transfer (APT) or concerted electron-proton transfer (EPT) pathways.^{35, 41–42} However, the thermodynamic and kinetic details of the mechanisms to accelerate the O–O bond formation are still unaccounted for, especially when considering a visible-light sensitizer coupled to the WOC and a more explicit description of solvent effects.

Here we report how the introduction of an extra OH^- group as proton acceptor in the hydration shell near the catalytic active site facilitates the O–O bond formation process driven by the photooxidized dye in the $S = 1/2$ supramolecular complex $^2([\text{Ru}^{\text{IV}}=\text{O}]^{2+}\text{--NDI}^{+*})$ (see Scheme 3.2).

3.2 Computational Details

To obtain a quantitative description of the O–O bond formation process, we perform DFT-MD simulations using an orthorhombic box of dimensions $25.1 \times 17.7 \times 14.4 \text{ \AA}^3$ with periodic boundary conditions containing the $[\text{WOC}]^{2+}$ -dye solute, 161 water molecules, and one OH^- group. In plane wave based DFT-MD simulations with periodic boundary conditions, there is a spurious Coulomb interaction for charged systems introduced by the image charges. However, because of the large simulation box used and the screening from the explicit water molecules, the spurious effect of the periodic charges is estimated to be rather small (comparable to $k_{\text{B}}T$ at room temperature) and does not affect significantly the conclusions of our simulations (see also Appendix 3.A.1.5). DFT-MD is an ideal approach to accurately describe chemical reactions in explicit solvent.⁴⁵ The solvent description allows accurate predictions of the reaction mechanisms and activation free energy barriers, since the solvent directly participates in the reaction, as already emphasized in similar studies.⁴⁶⁻⁴⁹ All the simulations are performed at 300 K with the CPMD program⁵⁰, using GTH pseudopotentials for the transition metal⁵¹ ruthenium and DCACP pseudopotentials for the remaining atoms⁵², together with a plane wave cutoff of 70 Ry and the OPBE exchange-correlation functional⁵³ (see Appendix for more computational details). Considering the restrictions in the time scale of DFT-MD simulations, a constrained MD approach combined with thermodynamic integration was employed to compute the free energy profile along the O–O bond formation process.⁵⁴⁻⁵⁶ The constrained reaction coordinate is the distance between the oxygen atoms O_i and O_{ii} indicated by the red double arrow in Scheme 3.2.

3.3 Results and Discussion

3.3.1 Inclusion and Equilibration of an OH^- Ion in the Simulation Box.

One water in the second solvation shell of the ruthenium center was deprotonated to create a hydroxide ion ($\text{O}_{iii}\text{H}_{iii}^-$) in the system at the very beginning of the simulation (see Scheme 3.2). If the OH^- ion is within $\sim 8 \text{ \AA}$ of the Ru center, connected through a hydrogen bonded chain of water molecules,

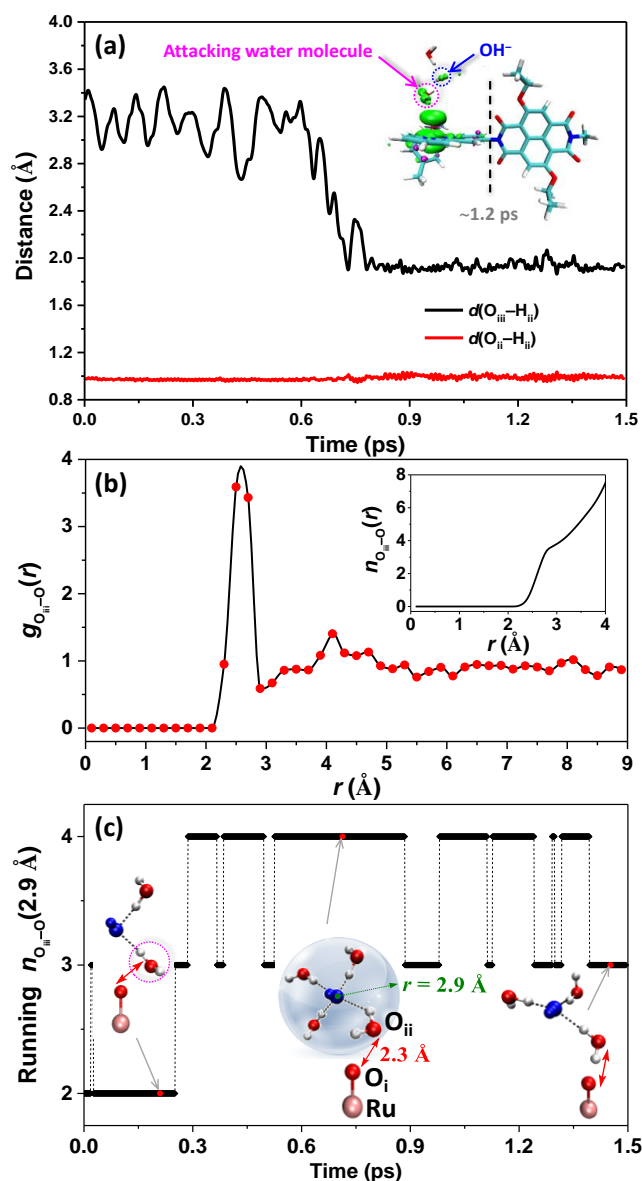


Figure 3.1. (a) Time evolution of the geometrical parameters $d(\text{O}_{\text{iii}}-\text{H}_{\text{ii}})$ (red line) and $d(\text{O}_{\text{iii}}\cdots\text{H}_{\text{ii}})$ (black line) along the initial equilibration MD trajectory corresponding to the constraint value $d(\text{O}_{\text{i}}-\text{O}_{\text{ii}}) = 2.3 \text{ \AA}$ (see Scheme 3.2 for the atomic labeling). The inset shows the spin density isosurface (green) computed at a snapshot taken at $\sim 1.2 \text{ ps}$, in the triplet state with two unpaired α electrons localized on the catalyst and no unpaired electron on the NDI dye. Only the $^3([\text{Ru}^{\text{IV}}=\text{O}]^{2+}-\text{NDI})$ complex, attacking water molecule (magenta dashed circle) and OH^- group (blue dashed circle) are shown explicitly. (b) Time-averaged $\text{O}_{\text{iii}}-\text{O}$ radial distribution function and the corresponding integrated coordination number (inset in panel a) calculated for the O_{iii} of the OH^- group in the equilibration simulation, in which the O labels the water atoms as opposite to the hydroxyl one. (c) Running coordination number of OH^- along the equilibration MD trajectory. The insets in panel c show representative instantaneous snapshots for configurations with different coordination number, in which the OH^- group is indicated in blue. Only the involved water molecules including the attacking water molecule (magenta dashed ellipse) hydrogen-bonded to the OH^- group, the ruthenium metal center and the oxo ligand coordinating to it are shown explicitly. The red double sided arrow indicates the constrained distance $d(\text{O}_{\text{i}}-\text{O}_{\text{ii}}) = 2.3 \text{ \AA}$.

the OH^- will move closer to the active site without any considerable energetic barrier by the Grotthuss mechanism.⁵⁷ Therefore the exact initial position of the OH^- is not so crucial and the mechanism will not change by placing the OH^- in the second hydration shell of the attacking water molecule. The reaction coordinate $d(\text{O}_i \leftarrow \text{O}_{ii})$ is initially fixed at 2.3 Å near the transition state according to the recently estimated reaction mechanism of O–O bond formation in a solvated system.²⁴ An initial DFT-MD simulation of about 1.5 ps is performed to equilibrate the local hydration environment around the OH^- group (see Appendix 3.A.1.4 for more computational details). During this equilibration run, a strong hydrogen bond between the OH^- group and the attacking water molecule is formed after about 0.8 ps with an average length $d(\text{O}_{iii} \cdots \text{H}_{ii}) \approx 1.9$ Å (see Figure 3.1a, black line). By tracking the spin density, two unpaired α electrons are observed to localize on the catalyst and no unpaired electron on the NDI dye (see Figure 3.1a, inset), which is consistent with the ground state of the $^3([\text{Ru}^{\text{IV}}=\text{O}]^{2+} - \text{NDI})$ intermediate known from previous investigations on this Ru-based catalyst.²⁴

The time-averaged $\text{O}_{iii}-\text{O}$ radial distribution function $g_{\text{O}_{iii}-\text{O}}(r)$ and the corresponding coordination number calculated in the equilibration simulation are presented in Figure 3.1b. The $g_{\text{O}_{iii}-\text{O}}(r)$ function shows a deep minimum at the $\text{O}_{iii}-\text{O}$ distance $r = \sim 2.9$ Å, clearly revealing the existence of a first hydration shell of OH^- .⁵⁸ Accordingly, the running coordination number ($n_{\text{O}_{iii}-\text{O}}(2.9 \text{ Å})$) of the OH^- group, defined as the number of water molecules with their oxygen atom within a radius of 2.9 Å around the oxygen atom (O_{iii}) of the OH^- group, is shown in Figure 3.1c. The $\text{OH}^-(\text{H}_2\text{O})_4$ complex is observed to be the dominant solvation structure for OH^- during this simulation, with four water molecules primarily coordinated to the OH^- via hydrogen bonds (see Figure 3.1c, inset). This result is consistent with the coordination number obtained by integrating the first peak of the $g_{\text{O}_{iii}-\text{O}}(r)$ function (see Figure 3.1b, inset) and in agreement with the characteristic microscopic solvation structure of the OH^- group in aqueous solution observed in previous simulations.^{58–64} All these evidences suggest a well-equilibrated solvation environment for the OH^- that represents a good starting point for the subsequent reaction mechanism investigation.

3.3.2 Photooxidation of the NDI and O–O Bond Formation

After this equilibration simulation, the photoinduced electron injection from the NDI to a TiO_2 semiconductor surface, *i.e.*, the photooxidation of the NDI dye, is mimicked by removing one electron from the simulation box. In previous work, we have demonstrated that the photoinduced electron injection is achieved on a time scale of ~ 1 ps.²³ To obtain a quantitative description of electron and proton dynamics, the variation of the total spin density localized on the NDI dye, and the time evolution of the distance between Ru and OH group (an O atom with only one H within a radius of 1.2 \AA) along the constrained/free DFT-MD trajectory after photooxidation of NDI are collected in Figure 3.2. Initially, the photo-induced hole is localized on the oxidized NDI^{+} (see Figure 3.2a and 3.2c), but it is quickly filled by an electron transferred from the attacking water molecule within 0.5 ps, leading to a minimum value around 0.1 of the spin density localized on NDI (see Figure 3.2a and 3.2e). Notice that during this ET the total spin $S = 1/2$ is assumed to be conserved. At the same time, the attacking water molecule transfers a proton (H_{ii} in Scheme 3.2) to the OH^- ion, which becomes a water molecule and no back reaction occurs (see Figure 3.2d and 3.2b blue line). This result indicates a cooperative event proceeding via a concerted PCET mechanism (see EPT in Scheme 3.1) that is completed within ~ 0.5 ps after the photooxidation of the NDI (see Figure 3.2a–3.2e).

In Figure 3.2e it is also apparent that the attacking water molecule has become an OH group carrying some spin density that indicates a strong radical character. One can indeed conclude that the hydroxide is first transferred close to the Ru(IV)=O , it acquires a radical character and thus generates a favorable condition for the O–O bond formation. The configuration shown in Figure 3.2e would be observed if the OH^- is placed initially as the direct attacking group next to the Ru(IV)=O . However, it is more appropriate to assume that the OH^- group will approach the active site in its more stable solvated complex as described in Figure 3.1. After short-term fluctuations, the spin density localized on the NDI stabilizes to an average value around 0.1 in the second half of the constrained MD simulation, indicating almost complete ET from the attacking water molecule to the oxidized NDI^{+} (see Figure 3.2a).

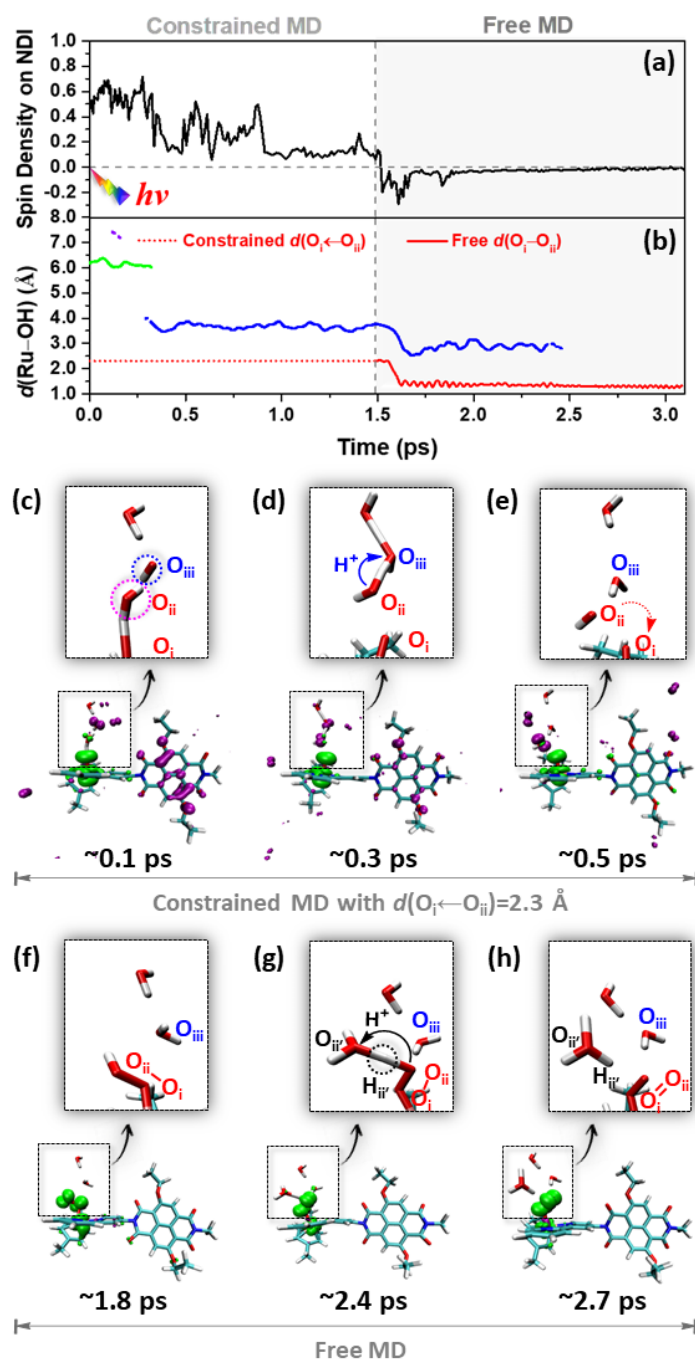


Figure 3.2 (a) The spin density integrated over the half of the simulation box that includes the NDI dye (right-hand side of the dashed black line in the inset of Figure 3.1a) along the constrained and free DFT-MD trajectories with the presence of OH⁻ group. An integrated spin density value of 1 corresponds to one unpaired β electron (\downarrow). (b) $d(\text{O}_i\text{--O}_{ii})$ distance during the constrained (red dotted line) and free (red solid line) MD trajectories. The green, purple, and blue lines show the instantaneous distance between the Ru and the OH group defined as an O atom with only one H atom within a radius of 1.2 Å. Different colors are used to underline when the OH is transferred from one hydration shell to another. The OH is initially in the second hydration shell at about 6 Å from the Ru (green line). The purple dots in the upper left corner indicate transient events in which a proton is accepted by a water molecule in the third hydration shell. Thus, the OH⁻ moves temporarily further away from the Ru complex and quickly jumps

back in the second hydration shell. After about 0.3 ps the proton is accepted from the attacking water and thus the OH moves closer to the Ru (blue line). (c)–(h) Spin density localization at different snapshots together with PT of third catalytic step (c→d→e), O–O bond formation process (e→f), and prior PT of fourth catalytic step (g→h) along the constrained/free MD trajectory shown in panels a and b. The labels refer to the time at which the snapshot has been taken. The snapshot taken at ~0.1 ps clearly indicates two unpaired α electrons (green spin density isosurface) localized on the catalyst and one unpaired β electron (purple spin density isosurface) on the oxidized NDI⁺ dye. Only the WOC–dye complex, attacking water molecule (magenta dashed circle), OH[−] group (blue dashed circle) and one nearby water molecule are shown explicitly (see enlargement in the insets). A small amount of spin density can be seen localized on a few water molecules due to transient solvent polarization effects.

This concerted PCET process occurs at the constrained reaction coordinate $d(\text{O}_i\leftarrow\text{O}_{ii}) = 2.3 \text{ \AA}$ in the presence of the OH[−] in the solvent. In contrast, without an additional proton acceptor the PCET occurs in a sequential (first ET, then PT, see red arrows in Scheme 3.1) mechanism and is completed only at $d(\text{O}_i\leftarrow\text{O}_{ii}) = 1.8 \text{ \AA}$.²⁴

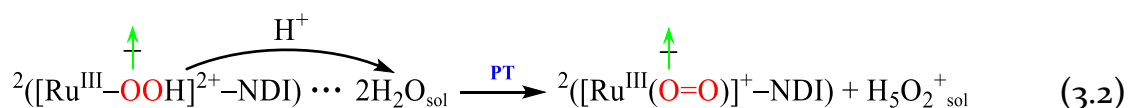
The release of the constraint between oxygens O_i and O_{ii} at ~1.5 ps enables the O–O bond formation, which proceeds in a very short time (within 0.2 ps) as the bond distance equilibrates at an average value $d(\text{O}_i\text{--O}_{ii})$ of ~1.36 Å (see red line in Figure 3.2b and 3.2f) (for comparison, the O–O bond length in molecular hydrogen peroxide is 1.47 Å), confirming the accomplishment of the rate-limiting catalytic step (see eq. 3.1). In eq. 3.1, H₂O_{sol} and OH[−]_{sol} represent the attacking water molecule and hydroxide ion in the solvent, respectively.

3.3.3 Spontaneous Proton Transfer Following OOH Ligand Formation

After the formation of the ²([Ru^{III}–OOH]²⁺–NDI) intermediate, the free DFT-MD simulation shows that the H_{ii'} of the hydroperoxyl ligand (see labeling in Scheme 3.2 and black dashed circle in Figure 3.2g) is strongly hydrogen-bonded to a neighboring water molecule. This hydrogen bond weakens the O_{ii}–H_{ii'} bond and facilitates the proton (H_{ii'}) release from the Ru^{III}–OOH center.



This proton is further transferred into the water bulk through a specific hydrogen-bonding network and finally forms a H₅O₂⁺ complex in the solvent after



~2.5 ps during this simulation (see Figure 3.2h and Figure A3.1 in Appendix). The last part of the FMD trajectory confirms the early formation of an O=O bond with an average $d(\text{O}_i-\text{O}_{ii})$ of ~1.29 Å (red line in Figure 3.2b, the O=O bond length in molecular O₂ is 1.21 Å for comparison) and a weakened Ru–O_i bond (see Figure A3.1a in Appendix). One triplet molecular O₂ can be produced and easily exchanged with a surrounding water molecule to generate the initial WOC state once the extra electron is transferred away from the Ru complex (see Scheme 3.1, I₄[−]→I₄^o→I_o). These findings provide convincing evidence for a quite active intermediate with a hydroperoxyl ligand after the O–O bond formation process as well as a considerably thermodynamically facile fourth water oxidation step (see eq. 3.2, where H₅O₂⁺_{sol} represents the hydrated excess proton complex). Interestingly, the barrier-less PT, usually considered as thermodynamically favorable after ET,⁶⁵ proceeds spontaneously with no need for prior ET, emphasizing the possibility of rate enhancement in water oxidation catalysis by tuning solvent environment to allow prior or facilitated PT in the system. It is noticeable the analogy in the sequence of reaction steps predicted by the simulation after the photooxidation of the NDI (*i.e.*, PCET followed by PT) and those observed in the oxygen evolving complex of PSII after the third light flash leading to O₂ evolution.²

3.3.4 Activation Free Energy Barrier and Reaction Rate Evaluation

Additional exploration with a constrained reaction coordinate $d(\text{O}_i\leftarrow\text{O}_{ii}) = 2.5$ Å after the initial equilibration simulation discussed above is also carried out and reported for completeness in Appendix 3.A.3. It is found that the PCET step could still take place when elongating the reaction coordinate $d(\text{O}_i\leftarrow\text{O}_{ii})$ to 2.5 Å with the presence of OH[−] as a proton acceptor in the solvent, although at a lower rate compared to the simulation with $d(\text{O}_i\leftarrow\text{O}_{ii}) = 2.3$ Å (within 1.2 ps after the photooxidation of NDI). However, rapid electron recombination is observed after the release of constraint, which induces the migration of the attacking water molecule away from the Ru^{IV}=O_i center and the subsequent back reaction of transferred proton to reproduce the original attacking water molecule (see Figure A3.2).

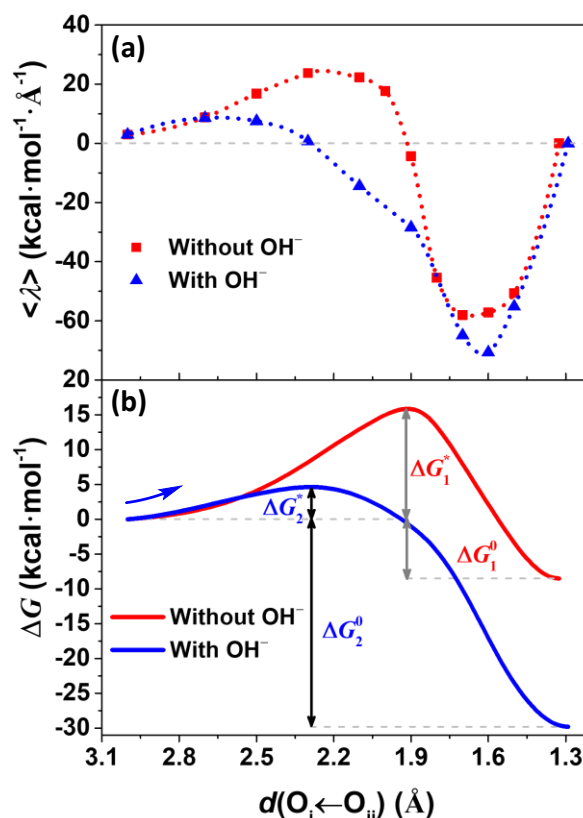


Figure 3.3. (a) Time-averaged constraint force represented by the Lagrangian multiplier $\langle \lambda \rangle$ computed for each constrained MD simulation as a function of the reaction coordinate $d(\text{O}_i \leftarrow \text{O}_{ii})$ with (blue triangles) and without (red squares) the OH^- , respectively. The Akima splines (100 points) is used to interpolate the mean forces. The mean force at the equilibrium distance $d(\text{O}_i - \text{O}_{ii}) = 1.29 \text{ \AA}$ evaluated in the free MD has been set to 0. (b) Free energy profile along the reaction coordinate $d(\text{O}_i \leftarrow \text{O}_{ii})$ computed by thermodynamic integration with (blue line) and without (red line) the OH^- , respectively. The results obtained without the presence of OH^- in the solvent are from Ref. 24.

In order to quantify the significant role of OH^- as a proton acceptor in the solvent in facilitating the rate-limiting water oxidation step involving the O–O bond formation process, the reaction coordinate $d(\text{O}_i \leftarrow \text{O}_{ii})$ is constrained to a series of fixed values to estimate the free energy profile along this reaction pathway (see Appendix 3.A.1.3 for more details). Figures 3.3a (blue triangles) and 3.3b (blue line) present the time-averaged mean forces corresponding to the applied constraint and associated free energy profile estimated by thermodynamic integration, respectively. The value of $\langle \lambda \rangle_{2.3 \text{ \AA}} \approx 0$ observed in Figure 3.3a indicates a transition state of this reaction with a $\text{O} \cdots \text{O}$ distance close to 2.3 \AA , which well explains why the O–O bond formation cannot occur at $d(\text{O}_i \leftarrow \text{O}_{ii}) = 2.5 \text{ \AA}$. In Table 3.1, we summarize the thermodynamic parameters for this PCET step involving the O–O bond formation with and without OH^- .

Noticeably, the calculated activation free energy barrier ΔG^* of this O–O bond formation process is dramatically lowered to ~ 4.3 kcal mol⁻¹ (~ 0.19 eV) compared to the case without the presence of OH⁻ in the solvent ($\Delta G^* \approx 15.9$ kcal mol⁻¹ (~ 0.69 eV)).²⁴

Table 3.1. The calculated activation free energy barrier ΔG^* (in kcal mol⁻¹) and reaction driving force ΔG^0 (in kcal mol⁻¹) with and without OH⁻ group as a proton acceptor. The last column shows the rate ratio (k_2/k_1) between the cases with (k_2 in s⁻¹) and without (k_1 in s⁻¹) the OH⁻ group.

Water Solvent	ΔG^*	ΔG^0	k_2/k_1
Without OH ⁻²⁴	15.9	-8.5	$\sim 2.83 \times 10^8$
With OH ⁻	4.3	-30.1	

This reaction step turns out to be significantly facilitated by introducing OH⁻ as proton acceptor near the active site to induce a concerted PCET mechanism. Moreover, the considerably larger driving force $\Delta G^0 \approx -30.1$ kcal mol⁻¹ (~ 1.31 eV) found with the OH⁻ can be partly attributed to the accomplishment of the spontaneous PT process after the formation of the hydroperoxyl ligand, which leads to a relatively stable intermediate ²([Ru^{III}(O=O)]⁺–NDI) compared to ²([Ru^{III}–OOH]²⁺–NDI).

The computed activation free energy barrier can be used to evaluate to what extent the introduction of OH⁻ group as a proton acceptor near the active site accelerates the rate of the O–O bond formation. According to standard transition state theory⁶⁶⁻⁶⁸, the reaction rate k can be expressed as

$$k = A \cdot e^{-\frac{\Delta G^*}{RT}}$$

(3.3)

One should keep in mind that in the DFT-MD simulations protons are treated classically and thus proton tunneling effects are neglected. In the current estimate, only the activation free energy barrier is considered as a main factor governing the reaction rate and the pre-exponential factor is regarded as constant. The calculated ratio of reactions rate ($k_2/k_1 \approx \sim 2.83 \times 10^8$) indicates an increase of over eight orders of magnitude for the O–O bond formation process in the presence of a OH⁻ as a proton acceptor near the active site (see Table 3.1), which is comparable with the experimental rate accelerations achieved by adding proton acceptor bases in the solution.^{35, 42}

3.4. Conclusions

In conclusion, the explicit solvent and dynamic description obtained with the adiabatic DFT-MD modelling approach reveals that the photooxidation of the NDI dye covalently bound to a highly active mononuclear Ru-based WOC provides a sufficient driving force for the ET from the attacking water molecule to the oxidized NDI⁺ dye and thus drives this photocatalytic water oxidation step. Introducing one OH[−] group as a proton acceptor near the active site induces a cooperative event proceeding via a concerted PCET mechanism, dramatically lowers the activation free energy barrier and thus significantly accelerates the O–O bond formation.

The mechanistic insight into facilitated O–O bond formation process provides a strategy for the improvement of the performance of DS-PEC devices by straightforward tuning of the solvent environment rather than developing novel catalysts for efficient water catalysis via tedious and costly synthesis technology. In this work we specifically use the OH[−] group as a conceptual example, but this can be easily replaced by other proton acceptors that would be less detrimental to the WOC stability. Based on these results, we propose a design strategy for a DS-PEC architecture in which the catalyst layer is located in the proximity of an ion-exchange membrane. In particular one could use assembly strategies similar to solid-state water electrolysis cell with alkaline membranes in which the OH[−] ions are transported to the catalyst layer through the anion exchange membrane and act as proton-withdrawing groups.⁶⁹

Moreover, the decoupling of tuning of the proton chemical potential from tuning the electron chemical potential would be essential to the design of future optimal DS-PEC devices. This will facilitate the photocatalytic water oxidation and simultaneously the proton diffusion through the membrane for the purpose of efficient hydrogen production.⁷⁰

3.5 References

- [1] Lewis, N. S. *Science* **2007**, *315*, 798-801.
- [2] Dau, H.; Zaharieva, I. *Acc. Chem. Res.* **2009**, *42*, 1861-1870.
- [3] Nocera, D. G. *Acc. Chem. Res.* **2012**, *45*, 767-776.
- [4] Li, L.; Duan, L.; Wen, F.; Li, C.; Wang, M.; Hagfeldt, A.; Sun, L. *Chem. Commun.* **2012**, *48*, 988-990.
- [5] Grätzel, M. *Nature* **2001**, *414*, 338-344.
- [6] Kohl, S. W.; Weiner, L.; Schwartsburd, L.; Konstantinovski, L.; Shimon, L. J. W.; Ben-David, Y.; Iron, M. A.; Milstein, D. *Science* **2009**, *324*, 74-77.
- [7] Xu, P.; Huang, T.; Huang, J.; Yan, Y.; Mallouk, T. E. *Proc. Natl. Acad. Sci. U.S.A.* **2018**, *115*, 6946-6951.
- [8] Yu, Z.; Li, F.; Sun, L. *Energy Environ. Sci.* **2015**, *8*, 760-775.
- [9] Swierk, J. R.; Mallouk, T. E. *Chem. Soc. Rev.* **2013**, *42*, 2357-2387.
- [10] Ding, X.; Zhang, L.; Wang, Y.; Liu, A.; Gao, Y. *Coord. Chem. Rev.* **2018**, *357*, 130-143.
- [11] Gibson, E. A. *Chem. Soc. Rev.* **2017**, *46*, 6194-6209.
- [12] Xu, P.; McCool, N. S.; Mallouk, T. E. *Nano Today* **2017**, *14*, 42-58.
- [13] Wang, D.; Eberhart, M. S.; Sheridan, M. V.; Hu, K.; Sherman, B. D.; Nayak, A.; Wang, Y.; Marquard, S. L.; Dares, C. J.; Meyer, T. J. *Proc. Natl. Acad. Sci. U.S.A.* **2018**, *115*, 8523-8528.
- [14] Gagliardi, C. J.; Vannucci, A. K.; Concepcion, J. J.; Chen, Z.; Meyer, T. J. *Energy Environ. Sci.* **2012**, *5*, 7704-7717.
- [15] Hammes-Schiffer, S. *Chem. Rev.* **2010**, *110*, 6937-6938.
- [16] Yang, X.; Hall, M. B. *J. Am. Chem. Soc.* **2010**, *132*, 120-130.
- [17] Concepcion, J. J.; Tsai, M.-K.; Muckerman, J. T.; Meyer, T. J. *J. Am. Chem. Soc.* **2010**, *132*, 1545-1557.
- [18] Privalov, T.; Sun, L.; Åkerman, B.; Liu, J.; Gao, Y.; Wang, M. *Inorg. Chem.* **2007**, *46*, 7075-7086.
- [19] Lin, X.; Hu, X.; Concepcion, J. J.; Chen, Z.; Liu, S.; Meyer, T. J.; Yang, W. *Proc. Natl. Acad. Sci. U.S.A.* **2012**, *109*, 15669-15672.
- [20] Cao, R.; Lai, W.; Du, P. *Energy Environ. Sci.* **2012**, *5*, 8134-8157.
- [21] Shaffer, D. W.; Xie, Y.; Szalda, D. J.; Concepcion, J. J. *J. Am. Chem. Soc.* **2017**, *139*, 15347-15355.
- [22] Meyer, T. J.; Sheridan, M. V.; Sherman, B. D. *Chem. Soc. Rev.* **2017**, *46*, 6148-6169.
- [23] Monti, A.; de Ruiter, J. M.; de Groot, H. J. M.; Buda, F. *J. Phys. Chem. C* **2016**, *120*, 23074-23082.
- [24] Shao, Y.; de Ruiter, J. M.; de Groot, H. J. M.; Buda, F. *J. Phys. Chem. C* **2019**, *123*, 21403-21414.
- [25] Hammes-Schiffer, S. *J. Am. Chem. Soc.* **2015**, *137*, 8860-8871.
- [26] Iordanova, N.; Hammes-Schiffer, S. *J. Am. Chem. Soc.* **2002**, *124*, 4848-4856.
- [27] Hatcher, E.; Soudackov, A. V.; Hammes-Schiffer, S. *J. Am. Chem. Soc.* **2004**, *126*, 5763-5775.
- [28] Horvath, S.; Fernandez, L. E.; Soudackov, A. V.; Hammes-Schiffer, S. *Proc. Natl. Acad. Sci. U.S.A.* **2012**, *109*, 15663-15668.
- [29] Maji, S.; Vigara, L.; Cottone, F.; Bozoglian, F.; Benet-Buchholz, J.; Llobet, A. *Angew. Chem., Int. Ed.* **2012**, *51*, 5967-5970.
- [30] Garrido-Barros, P.; Funes-Ardoiz, I.; Drouet, S.; Benet-Buchholz, J.; Maseras, F.; Llobet, A. *J. Am. Chem. Soc.* **2015**, *137*, 6758-6761.
- [31] Wilson, A. D.; Newell, R. H.; McNevin, M. J.; Muckerman, J. T.; Rakowski DuBois, M.; DuBois, D. L. *J. Am. Chem. Soc.* **2006**, *128*, 358-366.
- [32] Helm, M. L.; Stewart, M. P.; Bullock, R. M.; DuBois, M. R.; DuBois, D. L. *Science* **2011**, *333*, 863-866.

- [33] Bediako, D. K.; Solis, B. H.; Dogutan, D. K.; Roubelakis, M. M.; Maher, A. G.; Lee, C. H.; Chambers, M. B.; Hammes-Schiffer, S.; Nocera, D. G. *Proc. Natl. Acad. Sci. U.S.A.* **2014**, *111*, 15001-15006.
- [34] Solis, B. H.; Maher, A. G.; Honda, T.; Powers, D. C.; Nocera, D. G.; Hammes-Schiffer, S. *ACS Catal.* **2014**, *4*, 4516-4526.
- [35] Song, N.; Concepcion, J. J.; Binstead, R. A.; Rudd, J. A.; Vannucci, A. K.; Dares, C. J.; Coggins, M. K.; Meyer, T. J. *Proc. Natl. Acad. Sci. U.S.A.* **2015**, *112*, 4935-4940.
- [36] Norris, M. R.; Concepcion, J. J.; Fang, Z.; Templeton, J. L.; Meyer, T. J. *Angew. Chem., Int. Ed.* **2013**, *52*, 13580-13583.
- [37] Coggins, M. K.; Zhang, M.-T.; Chen, Z.; Song, N.; Meyer, T. J. *Angew. Chem., Int. Ed.* **2014**, *53*, 12226-12230.
- [38] Chen, Z.; Concepcion, J. J.; Song, N.; Meyer, T. J. *Chem. Commun.* **2014**, *50*, 8053-8056.
- [39] Stewart, D. J.; Concepcion, J. J.; Brennaman, M. K.; Binstead, R. A.; Meyer, T. J. *Proc. Natl. Acad. Sci. U.S.A.* **2013**, *110*, 876-880.
- [40] Vannucci, A. K.; Alibabaei, L.; Losego, M. D.; Concepcion, J. J.; Kalanyan, B.; Parsons, G. N.; Meyer, T. J. *Proc. Natl. Acad. Sci. U.S.A.* **2013**, *110*, 20918-20922.
- [41] Matheu, R.; Ertem, M. Z.; Benet-Buchholz, J.; Coronado, E.; Batista, V. S.; Sala, X.; Llobet, A. *J. Am. Chem. Soc.* **2015**, *137*, 10786-10795.
- [42] Chen, Z.; Concepcion, J. J.; Hu, X.; Yang, W.; Hoertz, P. G.; Meyer, T. J. *Proc. Natl. Acad. Sci. U.S.A.* **2010**, *107*, 7225-7229.
- [43] Xie, Y.; Shaffer, D. W.; Lewandowska-Andralojc, A.; Szalda, D. J.; Concepcion, J. J. *Angew. Chem., Int. Ed.* **2016**, *55*, 8067-8071.
- [44] Govindarajan, N.; Tiwari, A.; Ensing, B.; Meijer, E. J. *Inorg. Chem.* **2018**, *57*, 13063-13066.
- [45] Marx, D.; Hutter, J. *Ab initio molecular dynamics: basic theory and advanced methods*; Cambridge University Press: Cambridge, U.K., 2009.
- [46] Handgraaf, J.-W.; Meijer, E. J. *J. Am. Chem. Soc.* **2007**, *129*, 3099-3103.
- [47] Ma, C.; Piccinin, S.; Fabris, S. *ACS Catal.* **2012**, *2*, 1500-1506.
- [48] Pavlova, A.; Meijer, E. J. *ChemPhysChem* **2012**, *13*, 3492-3496.
- [49] Vallés-Pardo, J. L.; Guijt, M. C.; Iannuzzi, M.; Joya, K. S.; de Groot, H. J. M.; Buda, F. *ChemPhysChem* **2012**, *13*, 140-146.
- [50] CPMD, <http://www.cpmc.org>, Copyright IBM Corp., 1990-2019, Copyright MPI für Festkörperforschung Stuttgart, 1997-2001.
- [51] Hartwigsen, C.; Goedecker, S.; Hutter, J. *Phys. Rev. B* **1998**, *58*, 3641-3662.
- [52] Lin, I. C.; Coutinho-Neto, M. D.; Felsenheimer, C.; von Lilienfeld, O. A.; Tavernelli, I.; Rothlisberger, U. *Phys. Rev. B* **2007**, *75*, No. 205131.
- [53] Swart, M.; Ehlers, A. W.; Lammertsma, K. *Mol. Phys.* **2004**, *102*, 2467-2474.
- [54] Ciccotti, G.; Ferrario, M. *Mol. Simul.* **2004**, *30*, 787-793.
- [55] Ensing, B.; Meijer, E. J.; Blöchl, P. E.; Baerends, E. J. *J. Phys. Chem. A* **2001**, *105*, 3300-3310.
- [56] Costanzo, F.; Della Valle, R. G. *J. Phys. Chem. B* **2008**, *112*, 12783-12789.
- [57] de Ruiter, J. M. Explorations of water oxidation catalysis in explicit solvent. Ph.D. Thesis, Leiden University, October 2018.
- [58] Lee, S. H.; Rasaiah, J. C. *Mol. Simul.* **2010**, *36*, 69-73.
- [59] Crespo, Y.; Hassanali, A. *J. Phys. Chem. Lett.* **2015**, *6*, 272-278.
- [60] Tuckerman, M.; Laasonen, K.; Sprik, M.; Parrinello, M. *J. Chem. Phys.* **1995**, *103*, 150-161.
- [61] Tuckerman, M.; Laasonen, K.; Sprik, M.; Parrinello, M. *J. Phys. Chem.* **1995**, *99*, 5749-5752.
- [62] Chen, B.; Ivanov, I.; Park, J. M.; Parrinello, M.; Klein, M. L. *J. Phys. Chem. B* **2002**, *106*, 12006-12016.
- [63] Botti, A.; Bruni, F.; Imberti, S.; Ricci, M. A.; Soper, A. K. *J. Chem. Phys.* **2004**, *120*, 10154-10162.
- [64] Agmon, N.; Bakker, H. J.; Campen, R. K.; Henchman, R. H.; Pohl, P.; Roke, S.; Thämer, M.; Hassanali, A. *Chem. Rev.* **2016**, *116*, 7642-7672.

- [65] de Ruiter, J. M.; de Groot, H. J. M.; Buda, F. *ChemCatChem* **2018**, *10*, 4594-4601.
- [66] Eyring, H. *J. Chem. Phys.* **1935**, *3*, 107-115.
- [67] Laidler, K. J.; King, M. C. *J. Phys. Chem.* **1983**, *87*, 2657-2664.
- [68] Pollak, E.; Talkner, P. *Chaos* **2005**, *15*, No. 026116.
- [69] Leng, Y.; Chen, G.; Mendoza, A. J.; Tighe, T. B.; Hickner, M. A.; Wang, C.-Y. *J. Am. Chem. Soc.* **2012**, *134*, 9054-9057.
- [70] Achtyl, J. L.; Unocic, R. R.; Xu, L.; Cai, Y.; Raju, M.; Zhang, W.; Sacci, R. L.; Vlassiuk, I. V.; Fulvio, P. F.; Ganesh, P.; et al. *Nat. Commun.* **2015**, *6*, No. 6539.

3.A. Appendix

3.A.1. Computational Details

3.A.1.1 Geometry Optimization at DFT Level

The initial geometry of the WOC–dye complex was optimized at the DFT level employing the OPBE exchange–correlation functional¹ and the TZP basis set.² The OPBE functional has shown to be accurate in describing transition-metal complexes, including Ru-based WOCs.^{3–6} In the geometry optimization, the continuous solvation model COSMO^{7–8} for water was used. These calculations are performed with the ADF software package.^{9–10}

3.A.1.2 Simulation Box

To obtain a realistic description of the catalytic reaction steps, the solvent was explicitly introduced in the simulations. The solvent environment for the CPMD simulations was generated using Discovery Studio 2.5.¹¹ The solvent was equilibrated for 0.2 ns using the TIP3P model implemented in the CHARMM force field and CFF partial charge parameters at 300 K,¹² while the [WOC]²⁺–dye complex was kept fixed. The volume was then adjusted using constant pressure for 0.2 ns, after which the system was further allowed to evolve with constant volume for 2 ns. Periodic boundary conditions are applied with a time step of $\delta t = 5$ a.u. (1 a.u. = 0.0242 fs).

3.A.1.3 Free Energy Profile

To estimate the free energy profile of catalytic reaction steps that are unlikely to occur spontaneously during the typical AIMD simulation time scale, constrained MD and the so-called Blue Moon approach were employed as a rare event simulation technique.^{13–15} The reaction coordinate (in this case the distance between two oxygen atoms O_i and O_{ii} , $d(O_i \leftarrow O_{ii})$, as shown in Scheme 3.1) is constrained to a series of fixed values x in range of 3.0 – 1.5 Å after the initial equilibrium simulation and subsequent photooxidation of NDI along this facilitated reaction pathway. A time-averaged constraint force $\langle \lambda \rangle_x$ for each value of the reaction coordinate x is obtained, which should be equal to zero at an equilibrium or transition state. The free energy change for this promoted catalytic step is then established by interpolating the mean forces with a 100-point Akima splines function and integrating the signed forces $\langle \lambda \rangle_x$ along the reaction path.^{16–}

¹⁹ Trajectory analysis and visualization for the CPMD output were carried out using VMD program.²⁰⁻²¹

3.A.1.4 *Initial AIMD Equilibration Simulation*

An initial AIMD simulation of about 1.5 ps is performed to equilibrate the local hydration environment around the OH⁻ group. In particular, the coordination number of the oxygen atom (O_{iii}) belonging to the OH⁻ group was constrained to one within a radius of 1.2 Å during this simulation to maintain the geometry of the OH⁻ group and prevent its diffusion via the hydrogen-bonding network.²²

3.A.1.5 *Effect of Periodic Boundary Conditions*

In plane wave based DFT-MD simulations the periodic boundary conditions introduce a spurious Coulomb interaction for charged systems due to the image charges. In our work we compared the free energy profiles for two DFT-MD simulations with and without a OH⁻ ion. The total charge of the system is 2⁺ or 3⁺ in these two cases, respectively. The error introduced by the spurious Coulomb interaction can be estimated by considering the size of the MD box (25.1 × 17.7 × 14.4 Å³) and the fact that the MD simulation box contains 161 water molecules that will strongly screen the spurious Coulomb interaction. A rough estimate of the Coulomb potential generated by a positive charge that takes into account the length of the box and the relative permittivity of water gives a value of ~0.46 kcal mol⁻¹ for 2⁺ and ~0.69 kcal mol⁻¹ for 3⁺, respectively. These energies are quite small and comparable to the thermal energy $k_B T$ at room temperature (~0.59 kcal mol⁻¹). Moreover, these energies are at least one order of magnitude smaller than the computed free energy changes in the two systems considered (see Table 3.1 in chapter 3). We can therefore conclude that the error introduced by the periodic boundary conditions does not affect significantly the conclusions of our work.

3.A.2. Prior PT of the fourth Catalytic Water Oxidation Step

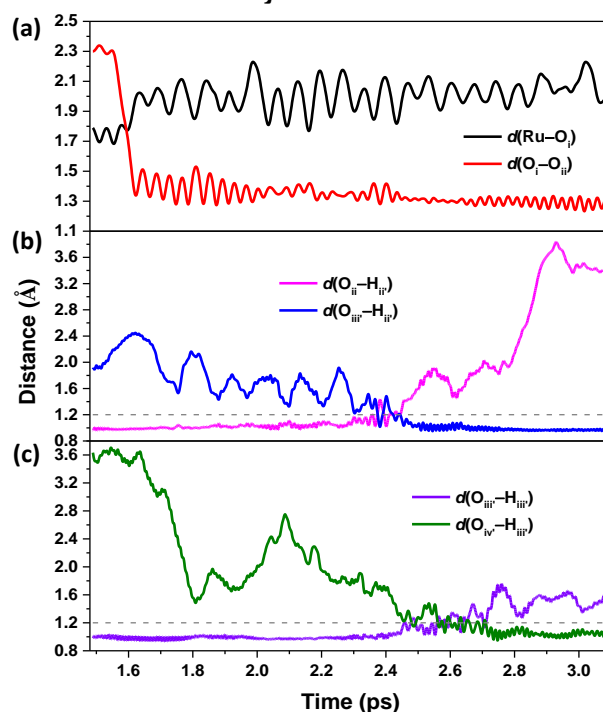


Figure A3.1. Time evolution of the geometrical parameters along the FMD trajectory after the third catalytic water oxidation step. The time range is consistent with Figure 3.2b

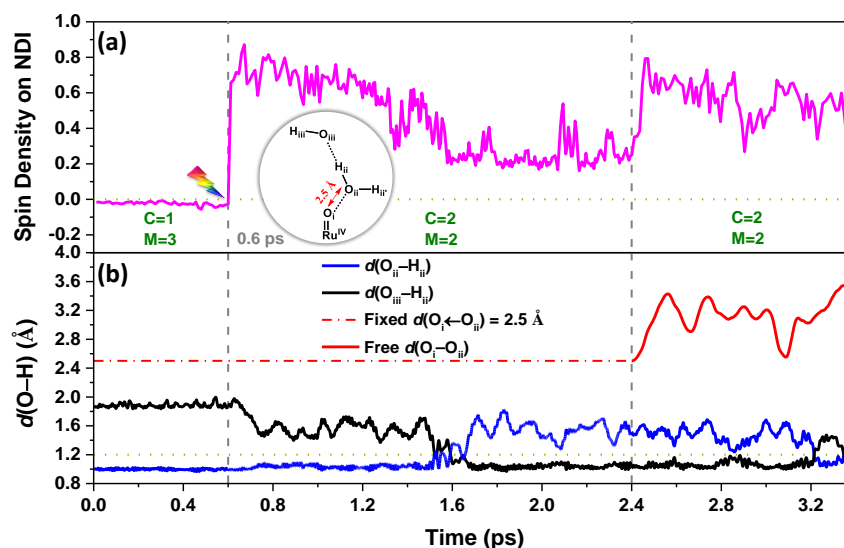
3.A.3. Exploration with Constrained Reaction Coordinate $d(\text{O}_i \leftarrow \text{O}_{ii}) = 2.5 \text{ \AA}$ 

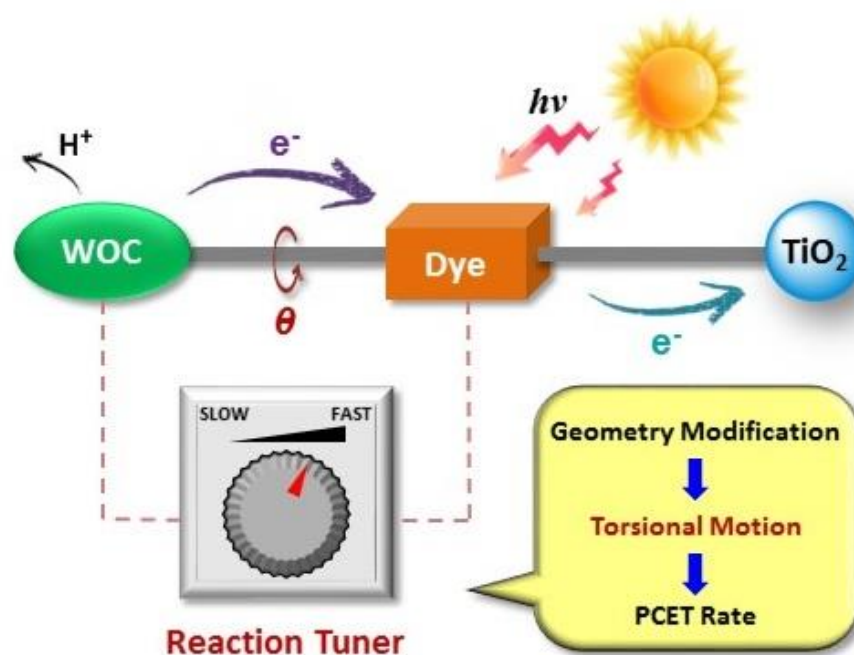
Figure A3.2. (a) The spin density integrated over the half of the simulation box including the NDI along the constrained and FMD trajectories. An integrated spin density value of 1 corresponds to one unpaired β electron. The red double sided arrow indicates the reaction coordinate $d(\text{O}_i \leftarrow \text{O}_{ii}) = 2.5 \text{ \AA}$. Grey dashed line at 0.6 ps: the photooxidation of NDI. Grey dashed line at 2.4 ps: remove constraint. (b) Time evolution of the geometrical parameters $d(\text{O}_i \leftarrow \text{O}_{ii})$, $d(\text{O}_{ii} \leftarrow \text{H}_{ir})$, and $d(\text{O}_{iii} \leftarrow \text{H}_{ir})$ along the constrained and free MD trajectories. Inset shows a the schematic structure of the attacking water molecule and the extra OH⁻.

3.A.4. References

- [1] Swart, M.; Ehlers, A. W.; Lammertsma, K. *Mol. Phys.* **2004**, *102*, 2467-2474.
- [2] Monti, A.; de Ruiter, J. M.; de Groot, H. J. M.; Buda, F. *J. Phys. Chem. C* **2016**, *120*, 23074-23082.
- [3] Carvalho, A. T. P.; Swart, M. *J. Chem. Inf. Model.* **2014**, *54*, 613-620.
- [4] Groenhof, A. R.; Ehlers, A. W.; Lammertsma, K. *J. Am. Chem. Soc.* **2007**, *129*, 6204-6209.
- [5] Conradie, J.; Ghosh, A. *J. Chem. Theory Comput.* **2007**, *3*, 689-702.
- [6] Vallés-Pardo, J. L.; Guijt, M. C.; Iannuzzi, M.; Joya, K. S.; de Groot, H. J. M.; Buda, F. *ChemPhysChem* **2012**, *13*, 140-146.
- [7] Klamt, A. *J. Phys. Chem.* **1995**, *99*, 2224-2235.
- [8] Klamt, A.; Jonas, V. *J. Chem. Phys.* **1996**, *105*, 9972-9981.
- [9] te Velde, G.; Bickelhaupt, F. M.; Baerends, E. J.; Fonseca Guerra, C.; van Gisbergen, S. J. A.; Snijders, J. G.; Ziegler, T. *J. Comput. Chem.* **2001**, *22*, 931-967.
- [10] ADF2017, SCM. Theoretical Chemistry, Vrije Universiteit, Amsterdam, The Netherlands, <http://www.scm.com>.
- [11] Accelrys Software Inc. *Discovery studio modeling environment*, Accelrys Software Inc.: San Diego, 2012.
- [12] Brooks, B. R.; Brucoleri, R. E.; Olafson, B. D.; States, D. J.; Swaminathan, S.; Karplus, M. *J. Comput. Chem.* **1983**, *4*, 187-217.
- [13] Ciccotti, G.; Ferrario, M. *Mol. Simul.* **2004**, *30*, 787-793.
- [14] Ensing, B.; Meijer, E. J.; Blöchl, P. E.; Baerends, E. J. *J. Phys. Chem. A* **2001**, *105*, 3300-3310.
- [15] Costanzo, F.; Della Valle, R. G. *J. Phys. Chem. B* **2008**, *112*, 12783-12789.
- [16] Otter, W. K. d.; Briels, W. J. *J. Chem. Phys.* **1998**, *109*, 4139-4146.
- [17] Sprik, M.; Ciccotti, G. *J. Chem. Phys.* **1998**, *109*, 7737-7744.
- [18] Bernasconi, L.; Baerends, E. J.; Sprik, M. *J. Phys. Chem. B* **2006**, *110*, 11444-11453.
- [19] Bernasconi, L.; Kazaryan, A.; Belanzoni, P.; Baerends, E. J. *ACS Catal.* **2017**, *7*, 4018-4025.
- [20] Humphrey, W.; Dalke, A.; Schulten, K. *J. Mol. Graphics* **1996**, *14*, 33-38.
- [21] VMD – Visual Molecular Dynamics. *Theoretical Chemistry and Computational Biophysics Group*, University of Illinois: Urbana, 2016.
- [22] Crespo, Y.; Hassanali, A. *J. Phys. Chem. Lett.* **2015**, *6*, 272-278.

CHAPTER 4

Tuning the Proton-Coupled Electron Transfer Rate by Ligand Modification in Catalyst-Dye Supramolecular Complexes



This chapter is based on:

Yang Shao, Huub J.M. de Groot, and Francesco Buda, *ChemSusChem*, **2021**, 14, 479-486, DOI: 10.1002/cssc.202001863.

4

Abstract

In view of the considerably high activation energy barrier of the O–O bond formation photocatalytic step in water oxidation, it is essential to understand if and how nonadiabatic factors can accelerate the PCET rate in this process to find rational design strategies facilitating this step. Here we perform constrained AIMD simulations to investigate this rate-limiting step in a series of catalyst–dye supramolecular complexes functionalized with different alkyl groups on the catalyst component. These structural modifications lead to tuneable thermodynamic driving forces, PCET rates, and vibronic coupling with specific resonant torsional modes. These results reveal that such resonant coupling between electronic and nuclear motions contributes to crossing catalytic barriers in PCET reactions by enabling semiclassical coherent conversion of a reactant into a product. Our results provide insight on how to engineer efficient catalyst–dye supramolecular complexes by functionalization with steric substituents for high-performance DS-PECs.

4.1. Introduction

Solar-driven water splitting via DS-PEC devices is an area of rapid technological growth, and is considered to be a promising scalable, affordable and sustainable technology for direct solar-to-fuel conversion to produce strategically valuable and storable hydrogen, or hydrocarbons from CO₂.¹⁻² Decentralized PEC offers intrinsic advantages since the integration of the PV and electrocatalytic steps in one device operating at low current density reduces overpotential and concentration losses compared to centralized electrolysis driven by PV.³ For one complete water splitting cycle in DS-PECs, four photons are absorbed at the photoanode, generating holes on the light-harvesting dye that should provide sufficient driving force for the four-proton/four-electron water oxidation half-reaction catalyzed by a WOC. The four photo-generated electrons migrate to the (photo)cathode to be consumed for the hydrogen production or for CO₂ reduction.⁴⁻⁵ Despite the effort in the development of novel DS-PECs, which have been improved either in the photoelectrodes⁶⁻⁷ or in the IEM⁸⁻¹⁰, the overall yield of the water oxidation half-reaction is limited. In particular the O–O bond formation step represents a thermodynamic and kinetic bottleneck for productive forward ET.¹¹ This leads to low yield, often less than 20%, due to charge recombination losses at the dye-electrode interface¹²

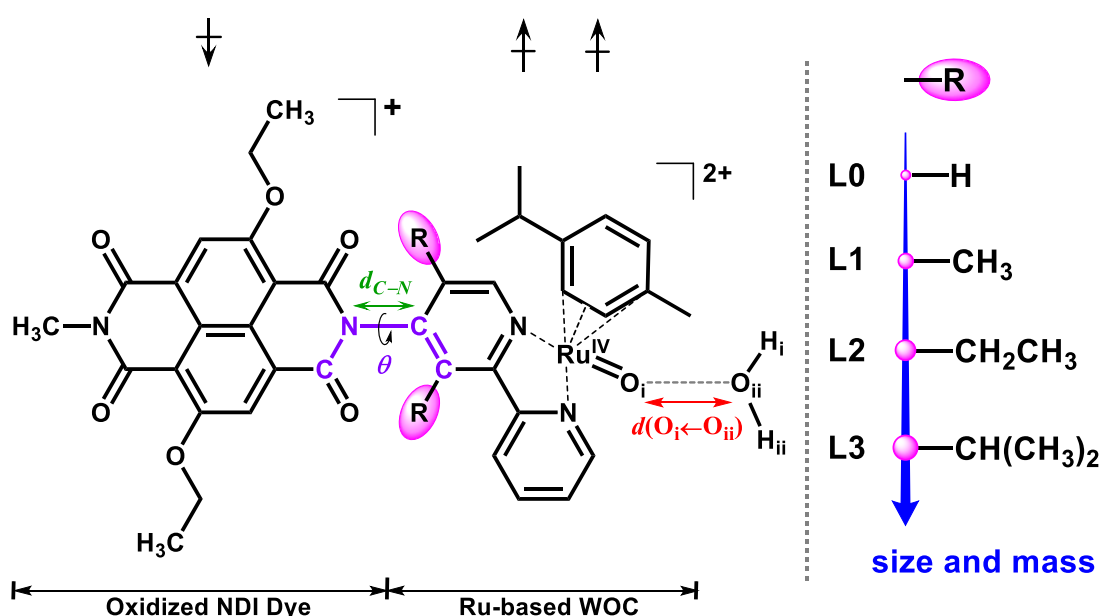
PCET¹³⁻¹⁷ plays an essential role in the photocatalytic four-proton/four-electron oxidation of water. Proper assembly of the components in the WOC–dye supramolecular complex provides channels for PCET steps in which the electron and proton are transferred in different directions and the dye is regenerated to its initial state.^{11, 18} The critical O–O bond formation process with mononuclear catalysts is found to be the most challenging and the rate-limiting step in catalytic water oxidation.¹⁹⁻²⁰ Significant rate enhancement has been achieved either by modifying the ligand of the WOC or by tuning the solvent environment, in which computational studies act as a powerful technique.²¹⁻²⁶

In catalysis, electrons are generally considered to be in equilibrium with their atomic surrounding, and reactions are thought to proceed adiabatically over catalytic barriers. While recent analysis of PCET reactions acknowledge the importance of nonadiabatic terms connecting electronic states, these are usually treated as probabilistic events for the conversion of reactants into products in the

context of nonadiabatic transition state theory.²⁷ However, when reactant and product levels cross due to molecular vibrations, resonant vibronic coupling can be established over an avoided crossing that provides a fast deterministic semiclassical coherent channel from the reactant to the product output, in particular for asymmetric systems that evolve along a torsional degree of freedom.¹¹ While we have found convincing evidence that resonant coupling is important for energy transfer and separation of charges^{28–30}, the purpose of this study is to investigate the possibility for resonant coupling at the crossing of the reactant and product states for the O–O bond formation in water oxidation, and if this offers an attractive chemical engineering principle to achieve near-unity yield in photochemical water oxidation.

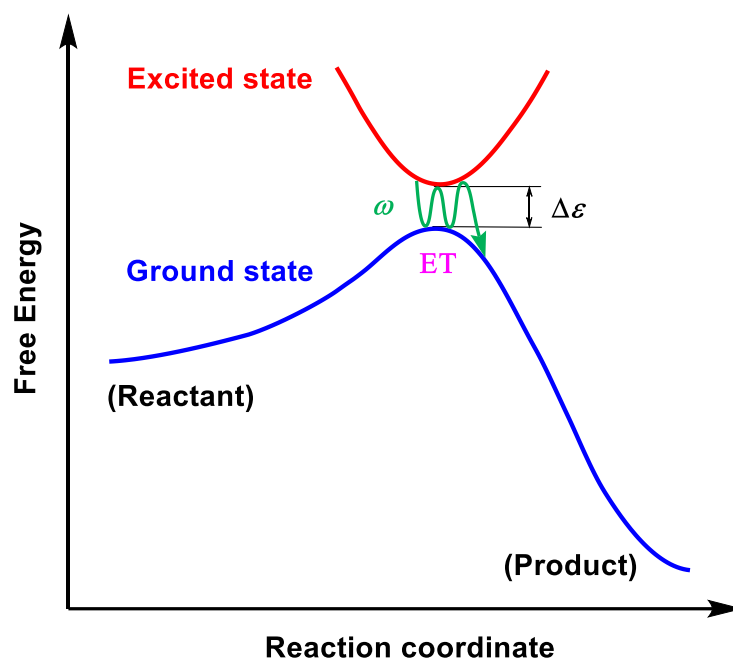
In the context of PCET reactions in artificial photosynthesis, the photocatalytic water splitting cycle in a WOC–dye supramolecular complex $[(\text{cy})\text{Ru}^{\text{II}}\text{bpy}(\text{H}_2\text{O})]^{2+}$ –NDI has recently been systematically investigated *in silico*, providing the driving

Scheme 4.1. Schematic structure of complexes **L0** – **L3** ($^2[(\text{Ru}^{\text{IV}}=\text{O})_i^{2+}\text{–NDI}^{+*}]$, $i = 0 - 3$) after the photooxidation of NDI dye together with the attacking water molecule in the vicinity of Ru center^a



^aThe dihedral angle θ and the C–N bond studied in this work are indicated in purple and green, respectively. The spin multiplicity $2S+1 = 2$ for a net spin $S = 1/2$ in this case corresponds to two unpaired α electrons (\uparrow) localized on the catalyst and one unpaired β electron (\downarrow) on the oxidized NDI⁺. The red double-sided arrow indicates the reaction coordinate $d(\text{O}_i \leftarrow \text{O}_{ii})$ considered in the constrained MD simulations.

Scheme 4.2. Schematic illustration of the resonant coupling between electronic and nuclear motions in the investigated system. $\Delta\varepsilon$ stands for the excitation energy around the transition state. ω represents the vibrational frequency of the torsional angle θ .



force and the energy barrier of each PCET step by DFT-MD simulations.^{11, 31} The computed energy barrier ($\Delta G^* = 15.9 \text{ kcal mol}^{-1}$) and corresponding reaction rate ($k = 15.7 \text{ s}^{-1}$) confirm that the third catalytic PCET step involving the O–O bond formation is indeed the kinetic bottleneck of the entire catalytic water oxidation half-reaction, which would increase the possibility of deleterious charge recombination and thus lower the quantum yield.^{11, 32}

In this work we explore the possibility of enhancing the rate of this critical PCET step in the WOC–dye complex $[(\text{cy})\text{Ru}^{\text{II}}\text{bpy}(\text{H}_2\text{O})]^{2+}$ –NDI by modifying the bipyridine ligand that is covalently bound to the NDI dye (see Scheme 4.1). Specifically, a series of alkyl groups varying in size and mass were introduced in the bpy residue near the C–N bond connecting the WOC and the NDI dye (**L0** – **L3** in Scheme 4.1). The rationale for this choice is to affect the torsional motion at the interface between the WOC and the dye in order to match the associated nuclear frequency (ω) to the resonance condition for the electron transfer process ($\omega \approx \Delta\varepsilon$, see Scheme 4.2).²⁹ This is inspired by the correlation between the torsional motion and the electron dynamics observed in our previous investigation of the catalytic cycle.¹¹

4.2. Results and Discussion

Understanding the impact of coherent coupling between electron and nuclear motions in catalytic reactions, such as the rate of this PCET reaction in the WOC–dye complex, is of particular interest and great significance.^{33–35} With this aim, we perform DFT-MD simulations following the Car-Parrinello approach to obtain accurate predictions of the activation energy barrier.³⁶ We show how the ET is coherently coupled to a specific torsional motion, and how the reaction rate of this catalytic PCET reaction in the WOC–dye complex ($^2\text{[Ru}^{\text{IV}}\text{=O}]^{2+}\text{–NDI}^+$), see Scheme 4.1) is affected by the ligand modifications.

4.2.1 Geometry Optimization of the WOC–Dye Complexes

The initial geometry of the photooxidized WOC–dye complexes **L0** – **L3** is optimized at the DFT level employing the OPBE exchange–correlation functional³⁷ and the TZP basis set in implicit solvation (COSMO) with the ADF software package^{38–39} (see Appendix 4.A.1 for more computational details).³¹ The increase in

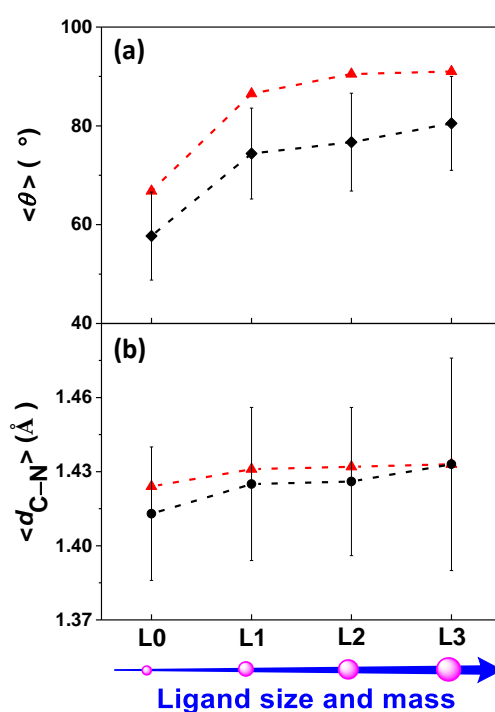


Figure 4.1. (a) Time-averaged dihedral angle ($\langle \theta \rangle$ in $^\circ$), (b) C–N bond length ($\langle d_{\text{C–N}} \rangle$ in \AA), and corresponding standard deviations of complexes **L0** – **L3** during the constrained MD simulations in explicit water solvation. For comparison, the dihedral angle θ (in $^\circ$) and C–N bond length $d_{\text{C–N}}$ (in \AA) of complexes **L0** – **L3** after geometry optimization with the ADF program using the OPBE functional, TZP basis set and implicit solvation (COSMO) are indicated in red triangles.

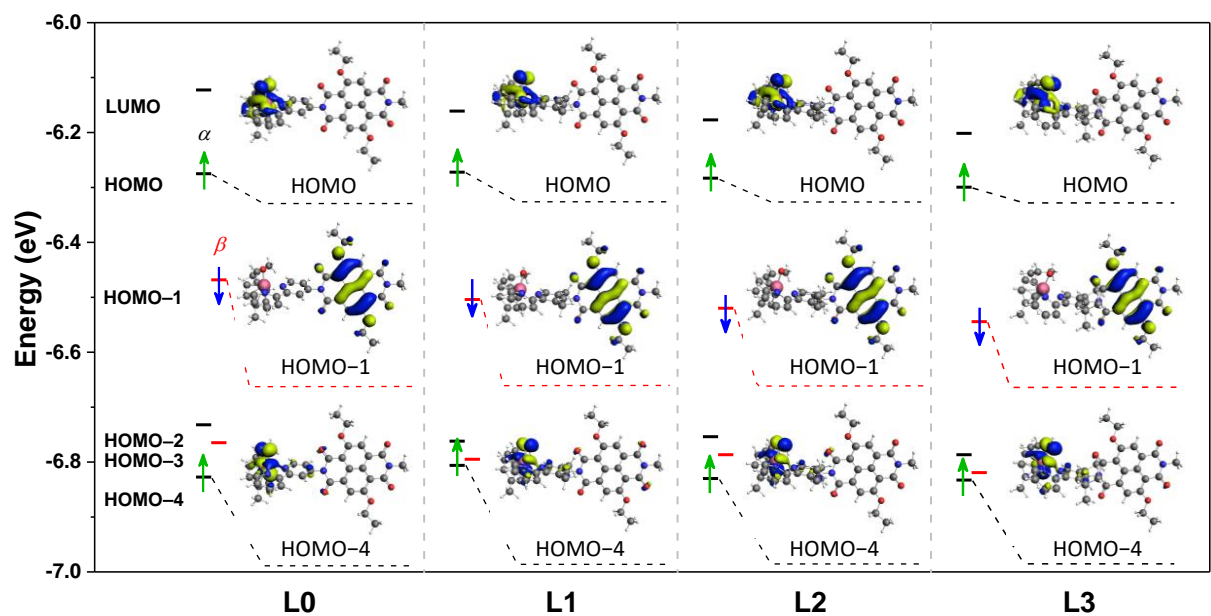


Figure 4.2. Selected frontier molecular orbitals of complexes **L0** – **L3** ($^2([\text{Ru}^{\text{IV}}=\text{O}]_i^{2+}-\text{NDI}^+)$, $i = 0 - 3$) after photooxidation of the NDI dye computed with the ADF program using the OPBE functional and the TZP basis set. The continuum solvation model COSMO is used to describe the water environment. Energy levels are indicated in black for spin α and in red for spin β orbitals, respectively. Only the unpaired electrons are explicitly indicated by vertical arrows (green for an unpaired electron localized on the catalyst and blue for an unpaired electron on the oxidized NDI^+) and the corresponding isosurface representation is shown in the inset. See Table 4.1 for the molecular energy levels.

Table 4.1. Selected frontier molecular orbital energy levels and energy difference ΔE_{SOMO} between SOMO dye and SOMO WOC of complexes **L0** – **L3** ($^2([\text{Ru}^{\text{IV}}=\text{O}]_i^{2+}-\text{NDI}^+)$, $i = 0 - 3$) after the photooxidation of NDI dye.^a

Intermediate		$^2([\text{Ru}^{\text{IV}}=\text{O}]_i^{2+}-\text{NDI}^+)$ ($i = 0 - 3$)			
		\uparrow	\uparrow	\downarrow	
Energy level	Orbital	L0	L1	L2	L3
LUMO	α	-6.123	-6.161	-6.177	-6.202
HOMO (SOMO WOC)	α	-6.275	-6.272	-6.283	-6.299
HOMO-1 (SOMO dye)	β	-6.468	-6.504	-6.520	-6.544
HOMO-2	α	-6.732	-6.762	-6.754	-6.787
HOMO-3	β	-6.765	-6.795	-6.787	-6.819
HOMO-4 (SOMO WOC)	α	-6.827	-6.806	-6.830	-6.833
ΔE_{SOMO}		-0.193	-0.231	-0.237	-0.245

^aThe initial geometry of all the complexes **L0** – **L3** are optimized with the ADF program using the OPBE functional and the TZP basis set. The continuum solvation model COSMO is used to describe the water environment. Only the unpaired electrons are indicated by vertical arrows explicitly (green for unpaired electrons localized on the catalyst and blue for unpaired electrons on the oxidized NDI^+). All energies are in eV.

size and mass of the ligand R leads to an elongation of the C–N bond ($d_{\text{C-N}}$) that links the WOC and dye components. In addition, the dihedral angle (θ) around the C–N bond increases going from **L0** to **L3**, due to the steric hindrance from bulky substituents (see Figure 4.1 and Table A4.1 in Appendix 4.A.2). The initial geometry will determine the sign of the dihedral angle as steric hindrance prevents the system to flip from a positive value of θ to an equivalent geometry with an opposite value, effectively breaking this symmetry.

Using the optimized geometry of the photooxidized WOC–dye complexes, we analyze the electronic structure and in particular the frontier molecular orbitals that play a crucial role in the PCET step and in regenerating the ground state of the dye. Figure 4.2 illustrates the frontier molecular orbital energy levels together with an isosurface corresponding to the SOMOs of complexes **L0** – **L3**. The corresponding energy levels are also listed in Table 4.1. For all these complexes, the SOMO localized on the oxidized NDI⁺ (SOMO dye) is always lower in energy than the HOMO of the supramolecular complex, which is localized on the ruthenium catalyst (SOMO WOC). The energy difference between the SOMO dye and the SOMO WOC (see ΔE_{SOMO} in Table 4.1) is found to systematically increase as the size and mass of the ligand R increases from complex **L0** ($\Delta E_{\text{SOMO}} = -0.193$ eV) to **L3** ($\Delta E_{\text{SOMO}} = -0.245$ eV). This result suggests an increasingly larger driving force for electron transfer from the ruthenium catalyst to the oxidized NDI dye due to the geometrical distortion induced by the steric hindrance from bulky substituents.

4.2.2 Equilibration of WOC–Dye Complexes in the Explicit Solvent Model

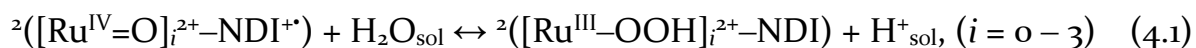
An accurate description of the PCET reaction and corresponding free energy profile requires an explicit inclusion of the water environment as it is crucially involved in the reaction process.^{11, 26, 32} Therefore, an orthorhombic box of dimensions $25.1 \times 17.7 \times 14.4 \text{ \AA}^3$ with periodic boundary conditions containing the WOC–dye solute **L0** – **L3** together with 162 explicit water molecules is used in the DFT-MD simulations performed with the CPMD program⁴⁰. The DFT electronic structure is determined by using the OPBE exchange-correlation functional³⁷, GTH pseudopotentials for the ruthenium transition metal⁴¹ and DCACP pseudopotentials for the remaining atoms⁴², together with a plane wave cutoff of 70 Ry (see Appendix 4.A.1). An initial free DFT-MD simulation of 0.6 ps at room temperature is performed for each $[\text{WOC}]^{2+}$ –dye solvated system to equilibrate the

solvation environment. Prior to this DFT-MD run, the systems have been already pre-equilibrated with a classical force field (see Appendix 4.A.1.2).

In a previous work³¹ we have demonstrated that upon photoexcitation the NDI is able to inject an electron at a dye-sensitized TiO₂ semiconductor surface on a time scale of ~1 ps. It is therefore reasonable to assume in the following analysis that the system is already in its oxidized form [WOC]²⁺–dye⁺ at the beginning of the simulation for this catalytic PCET step driven by the complexes **L0** – **L3**. The photooxidation of the NDI dye is mimicked by removing one electron from the simulation box after the initial equilibration simulation for each system considered. Subsequently, the oxidized state is further equilibrated for another 0.6 ps at room temperature. We show in Figure A4.1 (see Appendix 4.A.3) that the running average of the KS energy reaches a stable value even within this relatively short MD timescale of ~0.6 ps. Notice that during all the MD simulations after the photooxidation of the NDI, we only focus on the most favorable reaction route recently reported¹¹ with a total electron spin angular momentum $S = 1/2$. This is assumed to be conserved along the reaction coordinate since the O–O bond formation is thermodynamically unfavorable for the $S = 3/2$ case.¹¹ When the spin density is tracked along the equilibration MD simulation for the solvated [WOC]²⁺–dye⁺ systems, two unpaired α electrons (\uparrow) are observed to localize on the catalyst and one unpaired β electron (\downarrow) on the NDI dye in all the systems (see insets in Figure A4.2). Thermal fluctuations of the total spin density localized on the NDI dye, of the dihedral angle θ and C–N bond length d_{C-N} along this FMD trajectory are also collected in Figure A4.2 (see Appendix 4.A.3).

4.2.3 Constrained MD Simulations of the O–O Bond Formation Step

After this equilibration simulation, the constrained MD approach combined with thermodynamic integration is then employed to estimate the free energy profile of the third catalytic water oxidation step (see the redox couple in eq 4.1, where H₂O_{sol} and H⁺_{sol} represent the solvated attacking water molecule and proton respectively):



In eq. 4.1 the total spin multiplicity $2S+1 = 2$ is maintained over the WOC–dye system, with doubly charged WOC catalytic intermediates on both sides of the

redox couple. Hence one electronic spin quantum is internally transferred from the NDI to the WOC, while one unit of charge is released into the solvent environment in the form of a proton. The use of constrained MD is appropriate here since this reaction is a rare event on the typical DFT-MD simulation time scale.⁴³ The constrained reaction coordinate is the distance between the oxygen atoms O_i and O_{ii} indicated by the red double-sided arrow in Scheme 4.1 (see Appendix 4.A.1 for more computational details). In similar computational work on O–O bond formation, metadynamics simulations have been used as an alternative enhanced sampling method.^{44–47} In particular, in a very recent work in addition to the O–O distance, a second collective variable has been included to keep track of the proton transfer.⁴⁷ In our investigation, we didn't introduce additional constraints for the proton transfer to avoid a bias on the proton acceptor.

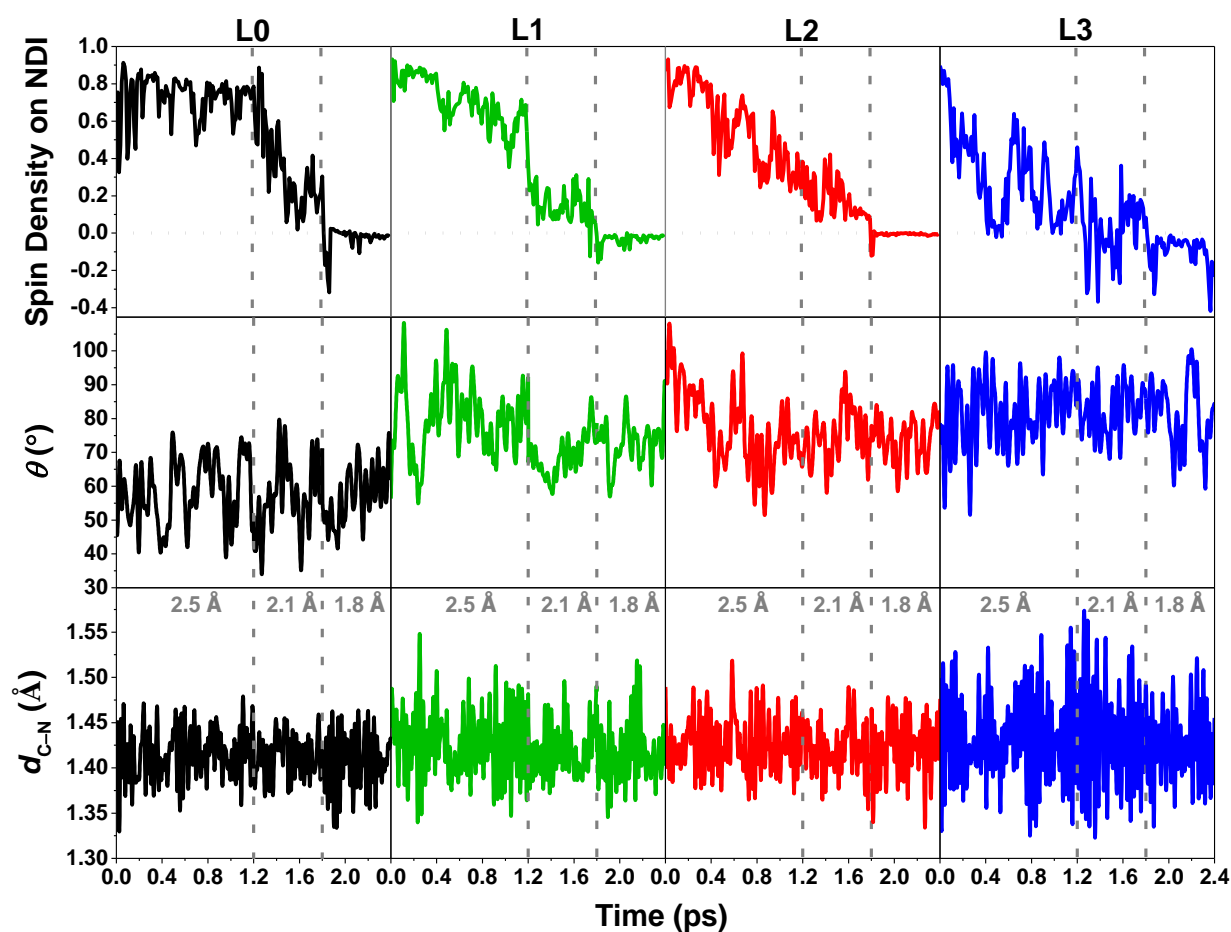


Figure 4.3. Spin density integrated over half of the simulation box including the NDI dye, time evolution of the θ and d_{C-N} of complexes **L0** – **L3** along the constrained MD trajectories. An integrated spin density value of 1 corresponds to one unpaired β electron (\uparrow). The value of the constrained reaction coordinate $d(O_i \leftarrow O_{ii})$ in the MD simulations is noted in grey.

In order to explore the correlation between the electronic and nuclear motions in these WOC–dye complexes, the variation of the spin density on the NDI dye together with the time evolution of the dihedral angle θ and C–N bond length $d_{\text{C-N}}$ for complexes **L0** – **L3** along the constrained MD trajectories are collected in Figure 4.3. The time-averaged dihedral angle $\langle\theta\rangle$, C–N bond length $\langle d_{\text{C-N}}\rangle$, and corresponding standard deviations for all complexes **L0** – **L3** during the constrained MD simulations are presented in Table A4.1 and Figure 4.1 for a quantitative comparison. According to the results of our DFT-MD simulations, the introduction of a ligand R larger in size and mass than hydrogen in complexes **L1** – **L3** gives rise to an increasing dihedral angle ($74.7 - 80.5^\circ$), and longer C–N bond ($1.426 - 1.433 \text{ \AA}$) as well as larger fluctuations during the dynamics compared to those of complex **L0** (57.7° , 1.413 \AA). The trend of the computed time average $\langle\theta\rangle$ and $\langle d_{\text{C-N}}\rangle$ when gradually enlarging the size and mass of ligand R from **L0** to **L3** is consistent with the static DFT results (see Table A4.1 and black scatters in Figure 4.1).

The ET is affected by the dynamic structure and starts already in the constrained MD with the reaction coordinate value $d(\text{O}_i \leftarrow \text{O}_{ii}) = 2.5 \text{ \AA}$ in **L1** – **L3**, while it occurs only after further shortening the reaction coordinate $d(\text{O}_i \leftarrow \text{O}_{ii})$ to 2.1 \AA in the case of **L0** (Figure 4.3, top panels). In particular for **L3** there is oscillatory behaviour. Initially the ET from the WOC to the photoinduced hole on the oxidized NDI occurs very rapidly already with $d(\text{O}_i \leftarrow \text{O}_{ii}) = 2.5 \text{ \AA}$, as it can be visualized by the spin density on the NDI going to zero in about 0.4 ps . This rapid event is then followed by a partial back transfer and pronounced fluctuations. The electron keeps transferring back and forth between the WOC and dye even when we further continue the constrained 2.5 \AA MD simulation for another $\sim 0.6 \text{ ps}$ (see Appendix 4.A.4). In Figure A4.4 in Appendix 4.A.5, we show that the running average of the constraint force reaches a stable value within the constrained 2.5 \AA MD timescale of $\sim 1.2 \text{ ps}$ for complexes **L0** – **L3** although large fluctuations on spin density could still be observed at the end of this simulation.

In all cases, the ET is completed at $d(\text{O}_i \leftarrow \text{O}_{ii}) = 1.8 \text{ \AA}$ with a stable integrated spin density value of 0 on the NDI (see also Appendix 4.A.6, where we show a longer constrained simulation with $d(\text{O}_i \leftarrow \text{O}_{ii}) = 1.8 \text{ \AA}$ for **L3**), corresponding to the final state with one unpaired α electron (\uparrow) localized on the catalyst and no unpaired electron on the NDI dye, which is regenerated to its initial ground state. The PT

from the attacking water molecule to the solvent only occurs during this constrained 1.8 Å simulation when the ET is completed. In particular, the proton H_i diffuses into the solvent bulk via a “chain” of hydrogen-bonded water molecules, which can be well described by the Grotthuss mechanism⁴⁸⁻⁴⁹ (see Appendix 4.A.7). This mechanism has been already observed in our previous works^{11, 32}. The reaction coordinate $d(O_i \leftarrow O_{ii})$ is then further shortened to 1.6 Å to better explore the complete free energy profile along this reaction pathway and no back reaction occurs (see Appendix 4.A.8). More importantly, no back-transfer of either an electron or a proton is observed even after the release of the constraint between O_i and O_{ii} at the end of the 1.6 Å simulation, confirming the stability of the final product (see eq. 4.1) after the O–O bond formation (see Appendix 4.A.9).

The facilitation of ET by ligand modification can be partially attributed to the larger driving force for bulkier substituents from **L0** to **L3** as discussed earlier in terms of molecular orbital energies (see Figure 4.2). However, another important factor could be a resonant coupling between electronic and nuclear motion that will be discussed further in a next section.

4.2.4 Free Energy Profile and Reaction Rate Estimation

Based on all the constrained DFT-MD simulations performed, the free energy profile along the reaction coordinate $d(O_i \leftarrow O_{ii})$ of **L0** – **L3** can be computed using the Blue Moon ensemble approach.^{43, 50-51} This will allow for a quantitative evaluation of the effect of the ligand modification on the rate enhancement for this catalytic water oxidation step. The time-averaged forces associated with the applied constraints, the interpolation of the time-averaged mean forces used for this analysis, and the corresponding free energy profile obtained via thermodynamic integration of **L0** – **L3** are presented in Figure 4.4 (see Appendix 4.A.1 for computational details and Appendix 4.A.10 for error bar of each time-averaged mean force).

It is apparent from Figure 4.4b that the obtained activation energy barrier for O–O bond formation decreases systematically as an effect of the increasing steric hindrance by substitution of ligand R in the sequence **L0** → **L1** → **L2** → **L3**. In addition, following the same sequence, the transition state occurs earlier, *i.e.*, at larger values of $d(O_i \leftarrow O_{ii})$ along the reaction coordinate. The key thermodynamic

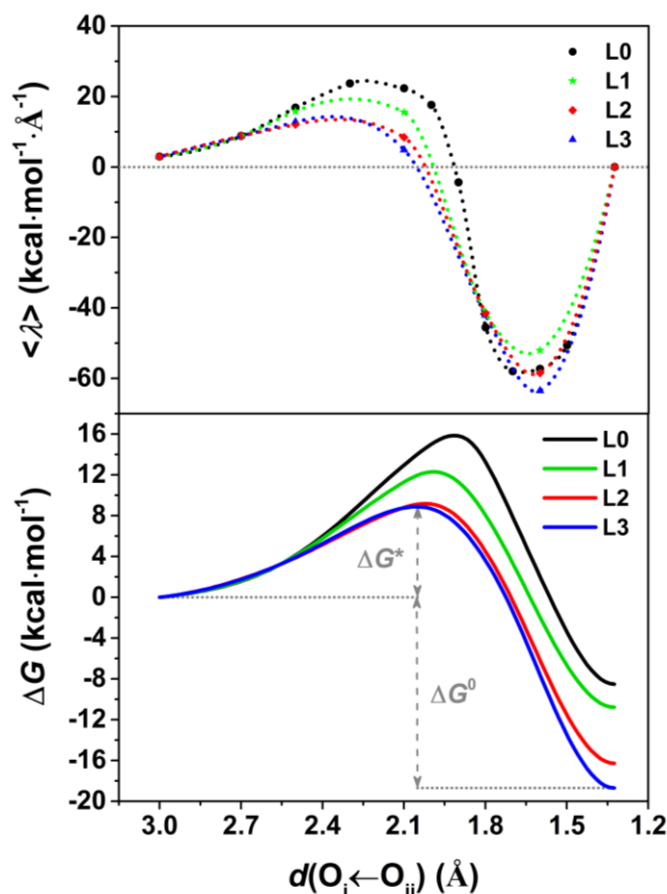


Figure 4.4. (a) Time-averaged constraint force represented by the Lagrangian multiplier $\langle \lambda \rangle$ computed for each constrained MD simulation as a function of the reaction coordinate $d(\text{O}_i \leftarrow \text{O}_{ii})$ for complexes **L0** – **L3**. The Akima splines (100 points) is used to interpolate the mean forces. (b) Free energy profile along the reaction coordinate $d(\text{O}_i \leftarrow \text{O}_{ii})$ computed from thermodynamic integration for complexes **L0** – **L3**. The time-averaged constraint forces and associated free energy profile for **L0** are taken from ref. 11 for comparison.

parameters extracted from the free energy profile of **L0** – **L3** for this water oxidation step are summarized in Table 4.2. The energy difference ΔE_{SOMO} between the SOMO dye and the SOMO WOC of complexes **L0** – **L3** after the photooxidation of the NDI dye is also included in Table 4.2 for comparison. In particular the calculated activation free energy barriers ΔG^* , 9.2 kcal mol⁻¹ (~0.40 eV) and 8.9 kcal mol⁻¹ (~0.39 eV) for **L2** and **L3** respectively, are dramatically lowered almost by half in comparison with that of **L0** (15.9 kcal mol⁻¹ (~0.69 eV)), indicating that this catalytic process is significantly facilitated by the changes in electronic and structural dynamics resulting from the ligand modification. It should be emphasized that the photooxidation of the NDI dye makes this reaction exothermic in all considered cases. However, following the order **L0** → **L1** → **L2** →

L3 the driving force becomes stronger, since ΔG^0 increases systematically from -8.5 to -18.7 kcal mol⁻¹. Table 4.2 shows a clear inverse correlation between the driving force and the activation free energy, which is consistent with Hammond’s postulate.⁵² Interestingly, the variation in ΔG^0 is much larger than the increase in the static molecular orbital energy difference ΔE_{SOMO} (see Table 4.2), pointing to the importance of dynamical (entropic) effects.

Table 4.2. Computed activation energy barrier ΔG^* (in kcal mol⁻¹), thermodynamic driving force ΔG^0 (in kcal mol⁻¹), and estimated reaction rate k (in s⁻¹) of the third PCET step involving the O–O bond formation for the complexes **L0** – **L3**, together with the energy difference (ΔE_{SOMO} in kcal mol⁻¹) between SOMO dye and SOMO WOC of complexes **L0** – **L3** obtained with static DFT calculations. The results for **L0** are taken from ref. 11.

WOC–dye complex	ΔG^*	ΔG^0	ΔE_{SOMO}	k
L0 ¹¹	15.9	−8.5	−4.5	15.7
L1	12.3	−10.8	−5.1	6.6×10 ³
L2	9.2	−16.3	−5.5	1.2×10 ⁶
L3	8.9	−18.7	−5.6	2.0×10 ⁶

The computed activation free energy barrier ΔG^* of **L0** – **L3** can be used to determine the reaction rate k according to transition state theory^{53–55}. The predicted reaction rate reported in Table 4.2 validates the Blue Moon constrained MD approach and shows an enhancement of up to 5 orders of magnitude from **L0** ($k = 15.7$ s⁻¹) to **L3** ($k = \sim 2.0 \times 10^6$ s⁻¹) as an effect of the ligand modification. To address now the crucial question about the origin of this very large effect on the activation energy barrier and hence the reaction rate, we look into the coupling between the electronic and the nuclear motion.

4.2.5 Coupling between Electronic and Nuclear Motions

To resolve possible resonant coupling between the electron transfer process and specific nuclear motions and how this affects the reaction rate of this catalytic water oxidation step, it is convenient to analyze the DFT-MD trajectories in the frequency domain.²⁸ Thus, the Fourier transform of the velocity autocorrelation function is calculated for the time evolution of the spin density and for the thermal fluctuations of θ and $d_{\text{C-N}}$ along the constrained MD trajectories corresponding to Figure 4.3, in which the ET takes place. The Fourier transform of the electron-

transfer time evolution as well as the VDOS of θ and $d_{\text{C-N}}$ are presented in Figure 4.5. We focus on the range of 0 – 1000 cm^{-1} since the overlap between nuclear and electronic spectra found at frequencies higher than 1000 cm^{-1} is negligible (see Appendix 4.A.11).

In Figure 4.5 (top panel), the starting complex **L0** shows for each spectrum one main peak, which is located at 566, 726, or 854 cm^{-1} for spin density (red), θ (blue), and $d_{\text{C-N}}$ (grey), respectively. The modification of ligand R in complex **L1** – **L3** induces the appearance of a second peak at lower frequencies in the spectrum of the ET and θ , while the spectrum of $d_{\text{C-N}}$ stays essentially unchanged. Noticeably,

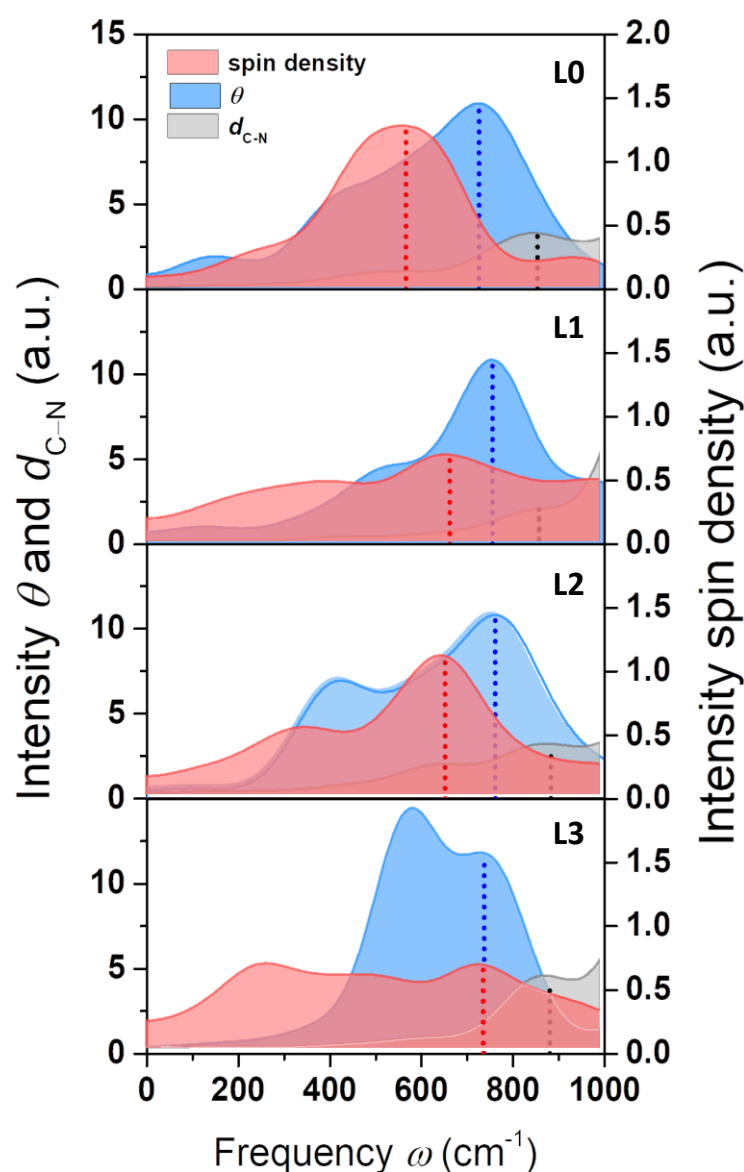


Figure 4.5. Frequency spectrum associated to the ET (red) and the VDOS of θ (blue) and $d_{\text{C-N}}$ (grey) for complexes **L0** – **L3** extracted from the constrained 2.5 Å and 2.1 Å MD trajectories corresponding to Figure 4.3.

the main peak of the ET spectrum (red dotted lines in Figure 4.5) is clearly shifted to higher frequency going from **L0** to **L1** – **L3**, leading to increasing overlap with the higher-frequency peak in the spectrum of θ (see blue dotted lines in Figure 4.5). In particular, these two peaks are both centered at around 735 cm^{-1} for the **L3** complex (see Figure 4.5). These results strongly suggest that the ligand modifications induce resonance due to converging timescales of the nuclear vibration of θ and the electronic motion of the charge transfer. The C–N stretching mode instead appears to have less overlap with the ET frequency spectrum. Considering the accelerated reaction rate obtained by modification of the ligand R (see Table 4.2), one is tempted to conclude that the resonance condition achieved between the ET frequencies and the VDOS of θ plays a dominant role in accelerating a catalytic reaction between different electronic states. In other words, the ligand modifications increase the nonadiabatic coupling between reactant and product states, which contributes to the acceleration of the reaction rate in a semiclassical, coherent conversion process that is deterministic instead of probabilistic.

Chapter

4

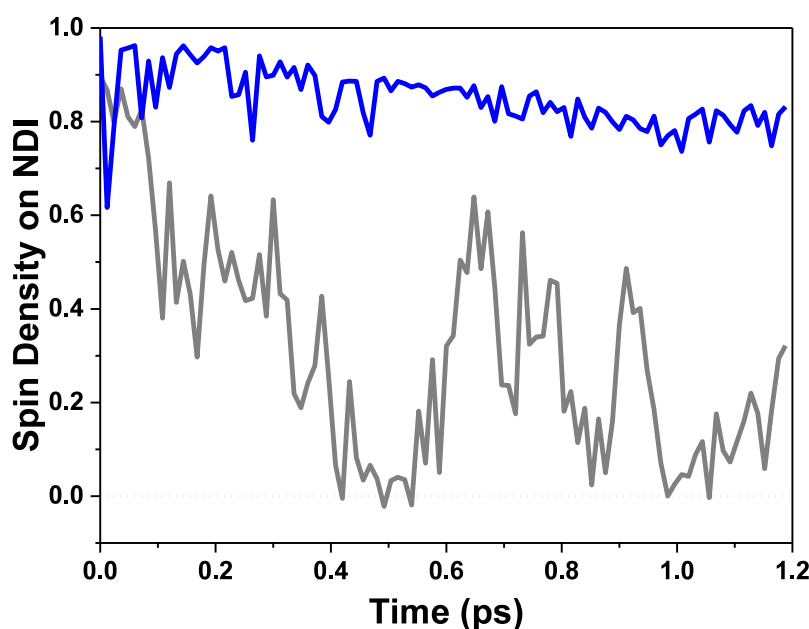


Figure 4.6. Spin density integrated over half of the simulation box including the NDI dye of complex **L3** along the constrained 2.5 \AA MD trajectory with fixed $\theta = 91^\circ$ after the photooxidation of NDI dye (blue line). Before this constrained MD simulation, a simulation of $\sim 0.36\text{ ps}$ with fixed $\theta = 91^\circ$ was performed to equilibrate the solvated system. The data without constraint on the θ of **L3** (grey line) is also presented for comparison, which is extracted from Figure 4.3.

In order to further validate the relevance of vibronic coupling in determining the reaction rate, an additional constrained DFT-MD simulation was carried out for **L3** after the photooxidation of NDI with $d(\text{O}_i\leftarrow\text{O}_{ii}) = 2.5 \text{ \AA}$ and with fixed $\theta = 91^\circ$, as this is the θ obtained from the DFT geometry optimization of **L3** (see Figure 4.1). The time evolution of the spin density localized on the NDI shows that the electron transfer from the WOC to the oxidized NDI dye is strongly inhibited when fixing θ (see Figure 4.6), which highlights the crucial role of this particular nuclear motion in facilitating the ET process. One can also notice that the value of θ extracted from the optimized geometries is about the same for the initial intermediate and for the final product after this catalytic step (see Appendix 4.A.12). Therefore, by fixing the value of θ we are not preventing a specific change in θ from the initial to the final value, but we are only removing the vibrational motion of θ , and thus the coupling with the electronic charge fluctuations.

One further argument supporting the idea of an increased nonadiabatic coupling driving catalysis going from **L0** to **L3** is based on the calculation of the excitation energies near the transition states $\Delta\epsilon$. The results from time-dependent density functional theory (TD-DFT) calculations (see Appendix 4.A.13) show that the energy difference between the ground state and the first excited state $\Delta\epsilon$, which corresponds to the charge transfer state, decreases from $\sim 1.8 \text{ kcal mol}^{-1}$ for **L0** to $\sim 1.3 \text{ kcal mol}^{-1}$ for **L3**. This energy difference is comparable to the energy of the characteristic torsional frequencies ($\omega = 735 \text{ cm}^{-1} = 2.1 \text{ kcal mol}^{-1}$) shown in Figure 4.5.

4.3. Conclusions

In conclusion, we have shown that by changing the mass and size of the ligand **R** at the interface between the WOC and the dye, one can accelerate the PCET reaction step associated to the O–O bond formation by several orders of magnitude. The structural modifications modulate the dihedral angle at the WOC–dye linkage, the electronic structure of the supramolecular complexes, the characteristic frequencies associated with the electron transfer dynamics, and the torsional motion around this link. A similar strategy has been very recently used by synthetically modifying an iron chromophore to interfere with specific atomic motions and resulting in a dramatically different charge transfer lifetime.⁵⁶ This frequency tuning leads to a resonance condition that increases the coupling

between electronic and nuclear motions and facilitates the ET step from the WOC to the oxidized dye in the region of the crossing of reactant and product states, in a process previously denoted NCAP.^{3, 29, 57-58} The computed free energy profiles for this PCET reaction show a considerable decrease in activation energy and increase in the driving force. We expect that the in-depth insight into the acceleration of this specific catalytic water oxidation step provides a general and rational engineering approach for the improvement of the performance of DS-PEC devices from a structural design perspective, which can also be achieved by modifying other ligands around the connecting region or replacing the linker between WOC and dye.

4.4 References

- [1] Grätzel, M., *Nature* **2001**, *414*, 338-344.
- [2] Ardo, S.; Fernandez Rivas, D.; Modestino, M. A.; Schulze Greiving, V.; Abdi, F. F.; Alarcon Llado, E.; Artero, V.; Ayers, K.; Battaglia, C.; Becker, J.-P.; Bederak, D.; Berger, A.; Buda, F.; Chinello, E.; Dam, B.; Di Palma, V.; Edvinsson, T.; Fujii, K.; Gardeniers, H.; Geerlings, H.; Hashemi, S. M.; Haussener, S.; Houle, F.; Huskens, J.; James, B. D.; Konrad, K.; Kudo, A.; Kunturu, P. P.; Lohse, D.; Mei, B.; Miller, E. L.; Moore, G. F.; Muller, J.; Orchard, K. L.; Rosser, T. E.; Saadi, F. H.; Schüttauf, J.-W.; Seger, B.; Sheehan, S. W.; Smith, W. A.; Spurgeon, J.; Tang, M. H.; van de Krol, R.; Vesborg, P. C. K.; Westerik, P., *Energy Environ. Sci.* **2018**, *11*, 2768-2783.
- [3] Purchase, R.; Cogdell, R.; Breitling, F.; Stadler, V.; Hulst, N. v.; Kramer, G.-J.; Ramirez, A.; Zwiijnenberg, R.; Kallergi, A.; Baan, J. B. d.; Rudra, I.; de Groot, H. J. M. *Semi-Synthetic Responsive Matrices for Artificial Photosynthesis, In Series on Chemistry, Energy and the Environment*, (Eds.: K. M., Kadish, R. Gullard), World Scientific, **2019**; pp. 47-69.
- [4] Swierk, J. R.; Mallouk, T. E., *Chem. Soc. Rev.* **2013**, *42*, 2357-2387.
- [5] Gibson, E. A., *Chem. Soc. Rev.* **2017**, *46*, 6194-6209.
- [6] Xu, P.; McCool, N. S.; Mallouk, T. E., *Nano Today* **2017**, *14*, 42-58.
- [7] Wang, D.; Eberhart, M. S.; Sheridan, M. V.; Hu, K.; Sherman, B. D.; Nayak, A.; Wang, Y.; Marquard, S. L.; Dares, C. J.; Meyer, T. J., *Proc. Natl. Acad. Sci.* **2018**, *115*, 8523-8528.
- [8] Varcoe, J. R.; Atanassov, P.; Dekel, D. R.; Herring, A. M.; Hickner, M. A.; Kohl, P. A.; Kucernak, A. R.; Mustain, W. E.; Nijmeijer, K.; Scott, K.; Xu, T.; Zhuang, L., *Energy Environ. Sci.* **2014**, *7*, 3135-3191.
- [9] Chabi, S.; Papadantonakis, K. M.; Lewis, N. S.; Freund, M. S., *Energy Environ. Sci.* **2017**, *10*, 1320-1338.
- [10] Ran, J.; Wu, L.; He, Y.; Yang, Z.; Wang, Y.; Jiang, C.; Ge, L.; Bakangura, E.; Xu, T., *J. Membr. Sci.* **2017**, *522*, 267-291.
- [11] Shao, Y.; de Ruiter, J. M.; de Groot, H. J. M.; Buda, F., *J. Phys. Chem. C* **2019**, *123*, 21403-21414.
- [12] Janna Olmos, J. D.; Becquet, P.; Gront, D.; Sar, J.; Dąbrowski, A.; Gawlik, G.; Teodorczyk, M.; Pawlak, D.; Kargul, J., *RSC Adv.* **2017**, *7*, 47854-47866.
- [13] Hammes-Schiffer, S., *Chem. Rev.* **2010**, *110*, 6937-6938.
- [14] Gagliardi, C. J.; Vannucci, A. K.; Concepcion, J. J.; Chen, Z.; Meyer, T. J., *Energy Environ. Sci.* **2012**, *5*, 7704-7717.
- [15] Hammes-Schiffer, S., *J. Am. Chem. Soc.* **2015**, *137*, 8860-8871.
- [16] Horvath, S.; Fernandez, L. E.; Soudackov, A. V.; Hammes-Schiffer, S., *Proc. Natl. Acad. Sci.* **2012**, *109*, 15663-15668.
- [17] Solis, B. H.; Hammes-Schiffer, S., *Inorg. Chem.* **2014**, *53*, 6427-6443.
- [18] Ding, X.; Zhang, L.; Wang, Y.; Liu, A.; Gao, Y., *Coord. Chem. Rev.* **2018**, *357*, 130-143.
- [19] Yang, X.; Hall, M. B., *J. Am. Chem. Soc.* **2010**, *132*, 120-130.
- [20] Concepcion, J. J.; Tsai, M.-K.; Muckerman, J. T.; Meyer, T. J., *J. Am. Chem. Soc.* **2010**, *132*, 1545-1557.
- [21] Chen, Z.; Concepcion, J. J.; Hu, X.; Yang, W.; Hoertz, P. G.; Meyer, T. J., *Proc. Natl. Acad. Sci.* **2010**, *107*, 7225-7229.
- [22] Maji, S.; Vigara, L.; Cottone, F.; Bozoglian, F.; Benet-Buchholz, J.; Llobet, A., *Angew. Chem. Int. Ed.* **2012**, *51*, 5967-5970.
- [23] Garrido-Barros, P.; Funes-Ardoiz, I.; Drouet, S.; Benet-Buchholz, J.; Maseras, F.; Llobet, A., *J. Am. Chem. Soc.* **2015**, *137*, 6758-6761.
- [24] Song, N.; Concepcion, J. J.; Binstead, R. A.; Rudd, J. A.; Vannucci, A. K.; Dares, C. J.; Coggins, M. K.; Meyer, T. J., *Proc. Natl. Acad. Sci.* **2015**, *112*, 4935-4940.

- [25] Matheu, R.; Ertem, M. Z.; Benet-Buchholz, J.; Coronado, E.; Batista, V. S.; Sala, X.; Llobet, A., *J. Am. Chem. Soc.* **2015**, *137*, 10786-10795.
- [26] Govindarajan, N.; Tiwari, A.; Ensing, B.; Meijer, E. J., *Inorg. Chem.* **2018**, *57*, 13063-13066.
- [27] Hammes-Schiffer, S.; Tully, J. C., *J. Chem. Phys.* **1995**, *103*, 8528-8537.
- [28] Monti, A.; Negre, C. F. A.; Batista, V. S.; Rego, L. G. C.; de Groot, H. J. M.; Buda, F., *J. Phys. Chem. Lett.* **2015**, *6*, 2393-2398.
- [29] Menzel, J. P.; de Groot, H. J. M.; Buda, F., *J. Phys. Chem. Lett.* **2019**, *10*, 6504-6511.
- [30] Li, X.; Buda, F.; de Groot, H. J. M.; Sevink, G. J. A., *J. Phys. Chem. B* **2020**, *124*, 4026-4035.
- [31] Monti, A.; de Ruiter, J. M.; de Groot, H. J. M.; Buda, F., *J. Phys. Chem. C* **2016**, *120*, 23074-23082.
- [32] Shao, Y.; de Groot, H. J. M.; Buda, F., *J. Phys. Chem. Lett.* **2019**, *10*, 7690-7697.
- [33] Kazuo, T.; Yasuki, A.; Takehiro, Y.; Kota, H., *Chemical Theory Beyond the Born-Oppenheimer Paradigm: Nonadiabatic Electronic and Nuclear Dynamics in Chemical Reactions*. World Scientific, **2014**.
- [34] Yamamoto, K.; Takatsuka, K., *ChemPhysChem* **2015**, *16*, 2534-2537.
- [35] Yamamoto, K.; Takatsuka, K., *Phys. Chem. Chem. Phys.* **2018**, *20*, 12229-12240.
- [36] Marx, D.; Hutter, J., *Ab initio molecular dynamics: basic theory and advanced methods*. Cambridge University Press, **2009**.
- [37] Swart, M.; Ehlers, A. W.; Lammertsma, K., *Mol. Phys.* **2004**, *102*, 2467-2474.
- [38] te Velde, G.; Bickelhaupt, F. M.; Baerends, E. J.; Fonseca Guerra, C.; van Gisbergen, S. J. A.; Snijders, J. G.; Ziegler, T., *J. Comput. Chem.* **2001**, *22*, 931-967.
- [39] ADF2017, SCM, Theoretical Chemistry, Vrije Universiteit, Amsterdam, The Netherlands, <http://www.scm.com>.
- [40] CPMD, <http://www.cpmd.org>, Copyright IBM Corp., 1990-2019; Copyright MPI für Festkörperforschung Stuttgart, 1997-2001.
- [41] Hartwigsen, C.; Goedecker, S.; Hutter, J., *Phys. Rev. B* **1998**, *58*, 3641-3662.
- [42] Lin, I. C.; Coutinho-Neto, M. D.; Felsenheimer, C.; von Lilienfeld, O. A.; Tavernelli, I.; Rothlisberger, U., *Phys. Rev. B* **2007**, *75*, 205131.
- [43] Ciccotti, G.; Ferrario, M., *Mol. Simul.* **2004**, *30*, 787-793.
- [44] Vallés-Pardo, J. L.; Guijt, M. C.; Iannuzzi, M.; Joya, K. S.; de Groot, H. J. M.; Buda, F., *ChemPhysChem* **2012**, *13*, 140-146.
- [45] Piccinin, S.; Sartorel, A.; Aquilanti, G.; Goldoni, A.; Bonchio, M.; Fabris, S., *Proc. Natl. Acad. Sci.* **2013**, *110*, 4917-4922.
- [46] Schilling, M.; Cunha, R. A.; Lubner, S., *J. Chem. Theory Comput.* **2020**, *16*, 2436-2449.
- [47] Schilling, M.; Cunha, R. A.; Lubner, S., *ACS Catal.* **2020**, *10*, 7657-7667.
- [48] Agmon, N., *Chem. Phys. Lett.* **1995**, *244*, 456-462.
- [49] de Grotthuss, C. J. T., *Biochim. Biophys. Acta, Bioenerg.* **2006**, *1757*, 871-875.
- [50] Ensing, B.; Meijer, E. J.; Blöchl, P. E.; Baerends, E. J., *J. Phys. Chem. A* **2001**, *105*, 3300-3310.
- [51] Costanzo, F.; Della Valle, R. G., *J. Phys. Chem. B* **2008**, *112*, 12783-12789.
- [52] Hammond, G. S., *J. Am. Chem. Soc.* **1955**, *77*, 334-338.
- [53] Eyring, H., *J. Chem. Phys.* **1935**, *3*, 107-115.
- [54] Laidler, K. J.; King, M. C., *J. Phys. Chem.* **1983**, *87*, 2657-2664.
- [55] Pollak, E.; Talkner, P., *Chaos* **2005**, *15*, 026116.
- [56] Paulus, B. C.; Adelman, S. L.; Jamula, L. L.; McCusker, J. K., *Nature* **2020**, *582*, 214-218.
- [57] Haken, H.; Reineker, P., *Z. Phys.* **1972**, *249*, 253.
- [58] Haken, H.; Strobl, G., *Z. Phys.* **1973**, *262*, 135.

4.A. Appendix

4.A.1. Computational Details

4.A.1.1 Geometry Optimization at DFT Level

The OPBE exchange-correlation functional¹ and the TZP basis set² were employed in the geometry optimization of the initial and final states of WOC–dye complexes **L0** – **L3**. The OPBE functional has shown to be accurate in describing transition-metal complexes, including Ru-based WOCs.^{3–6} In the geometry optimization, the continuous solvation model COSMO^{7–8} for water was used. These calculations are performed with the ADF software package.^{9–10}

4.A.1.2 Simulation Box

To obtain a realistic description of the catalytic reaction step, the solvent was explicitly introduced in the simulations. The solvent environment for the CPMD simulations was generated using Discovery Studio 2.5.¹¹ The solvent was equilibrated for 0.2 ns using the TIP3P model implemented in the CHARMM force field and CFF partial charge parameters at 300 K,¹² while the [WOC]²⁺–dye complex was kept fixed. The volume was then adjusted using constant pressure for 0.2 ns, after which the system was further allowed to evolve with constant volume for 2 ns. PBC are applied with a time step of $\delta t = 5$ a.u. (1 a.u. = 0.0242 fs).

4.A.1.3 Effect of Periodic Boundary Conditions

In plane wave based AIMD simulations the periodic boundary conditions introduce a spurious Coulomb interaction for charged systems due to the image charges. This effect can be important for charged systems when dealing with isolated molecules/clusters in the simulation box. However, because of the quite large simulation box ($25.1 \times 17.7 \times 14.4 \text{ \AA}^3$) used and the fact that the MD simulation box contains 162 water molecules that will strongly screen the spurious Coulomb interaction, the spurious effect of periodic charges is estimated to be rather small (~ 0.01 eV). We can therefore conclude that the error introduced by the periodic boundary conditions does not affect significantly the conclusions of our work.

4.A.1.4 Free Energy Profile

To estimate the activation free energy barrier of the catalytic reaction step involving the O–O bond formation that is unlikely to occur spontaneously during

the typical AIMD simulation time scale, constrained MD and the so-called Blue Moon approach were employed as a rare event simulation technique.¹³⁻¹⁵ The reaction coordinate (in this case the distance between two oxygen atoms O_i and O_{ii} , $d(O_i \leftarrow O_{ii})$, as shown in Scheme 4.1) is constrained to a series of fixed values in range of 2.5 – 1.6 Å after the initial equilibrium simulation and subsequent photooxidation of NDI along this reaction pathway. A time-averaged constraint force $\langle \lambda \rangle$ for each value of the reaction coordinate is obtained, which should be equal to zero at an equilibrium or for a transition state. In our previous work we learned that the $d(O_i \leftarrow O_{ii}) = 3.0$ Å and 1.325 Å on the reaction coordinates are quite close to the initial/final equilibrium state and far from the transition state. This leads us to conclude that the modification of ligand R has minor effect on the position close to the initial/final equilibrium state and that all the complexes **L0** – **L3** share the same value for the constraint forces at the reaction coordinate $d(O_i \leftarrow O_{ii}) = 3.0$ Å, 2.7 Å, and 1.325 Å.¹⁶ The activation free energy barrier for this catalytic step is then established by interpolating the mean forces with a 100-point Akima splines function and integrating the signed forces $\langle \lambda \rangle$ along the reaction path.¹⁷⁻²⁰ Trajectory analysis and visualization for the CPMD output were carried out using the VMD program.²¹⁻²²

4.A.1.5 Reaction Rate

The computed activation free energy barrier can be used to evaluate to what extent the geometry modification accelerates the rate of the third water oxidation step involving the O–O bond formation. According to transition state theory²³⁻²⁵, the reaction rate k determined by the activation energy barrier ΔG^* can be expressed as

$$k = \frac{k_B T}{h} \cdot e^{-\frac{\Delta G^*}{RT}}.$$

One should keep in mind that in DFT-MD simulations protons are treated classically and thus proton tunneling effects are neglected. In the current calculation, only the activation energy barrier is considered as a main factor governing the reaction rate.

4.A.2. Geometrical Parameters

Table A4.1. Calculated geometrical parameters for complexes **L0** – **L3**.

Complex	θ^a	$\langle\theta\rangle^b$	σ_1^b	$d_{\text{C-N}}^a$	$\langle d_{\text{C-N}}\rangle^b$	σ_2^b
L0	66.8	57.7	8.9	1.424	1.413	0.027
L1	86.5	74.4	9.2	1.431	1.425	0.031
L2	90.5	76.7	9.9	1.432	1.426	0.030
L3	91.0	80.5	9.5	1.433	1.433	0.043

^aDihedral angle θ (in $^\circ$) and C–N bond length $d_{\text{C-N}}$ (in Å) of complexes **L0** – **L3** extracted from the static DFT calculations. ^bTime-averaged dihedral angle $\langle\theta\rangle$ (in $^\circ$), C–N bond length $\langle d_{\text{C-N}}\rangle$ (in Å), and corresponding standard deviations of complexes **L0** – **L3** during the free and constrained MD simulations after the photooxidation of NDI dye. See Scheme 4.1 for the identification of the dihedral angle and the C–N bond.

4.A.3. FMD Equilibration Simulation after Photooxidation of **L0** – **L3**

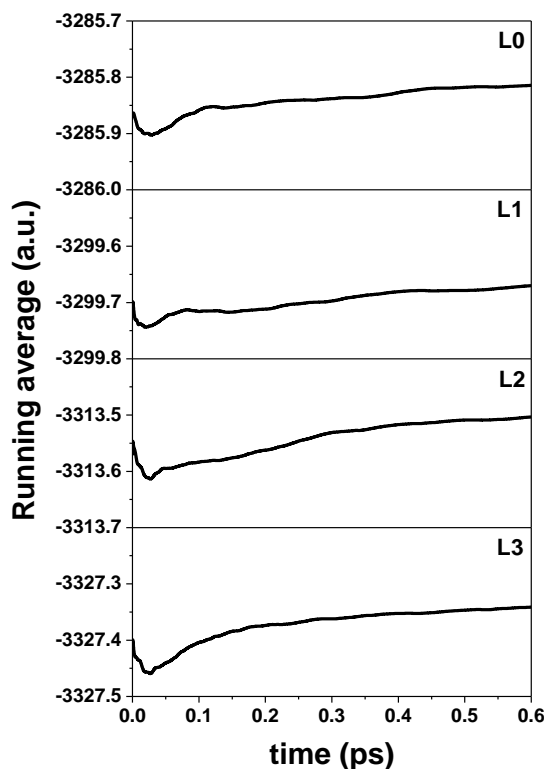


Figure A4.1. The running average of the Kohn-Sham (KS) energy (in a.u.) as a function of time for the equilibration simulation of the photooxidized complexes **L0** – **L3**, respectively. The running average reaches a stable value even within this relatively short MD timescale of ~0.6 ps.

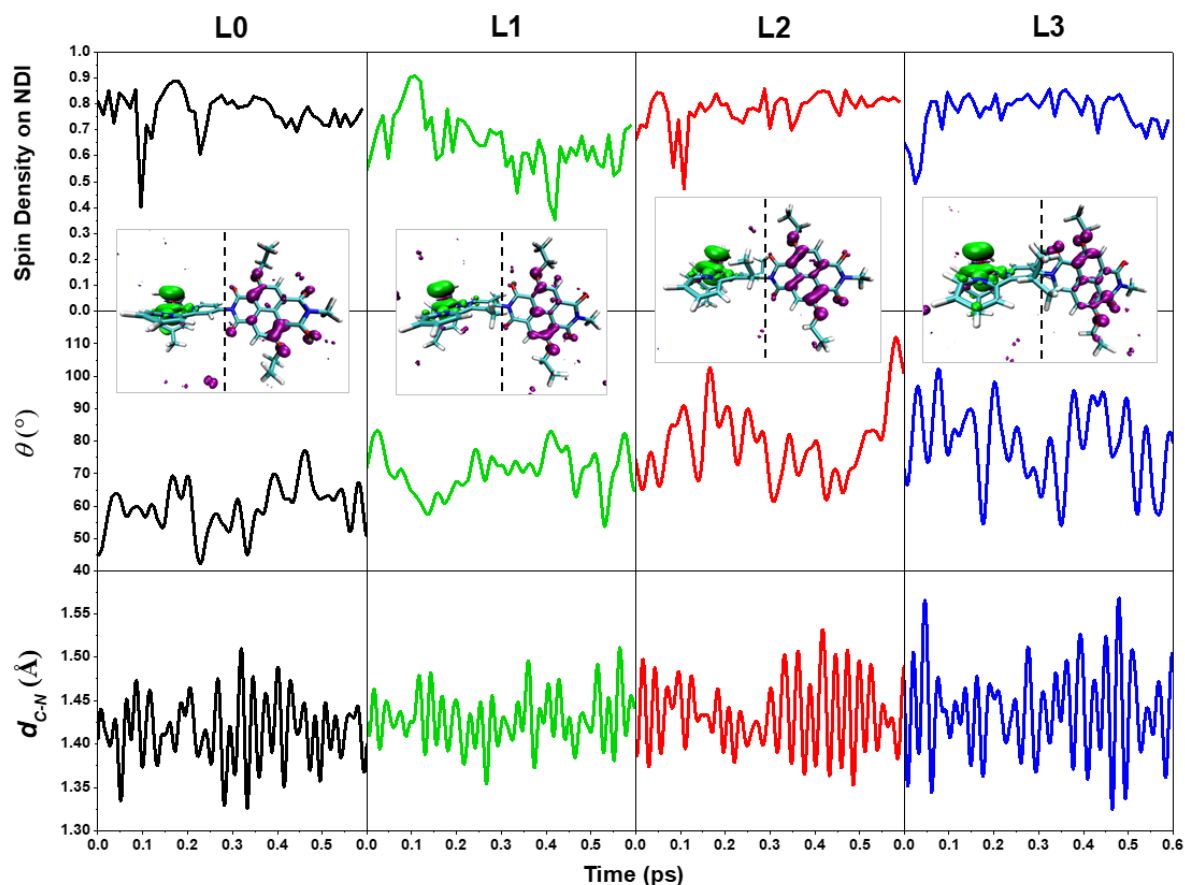


Figure A4.2. Spin density integrated over half of the simulation box including the NDI dye (right-hand side of the dashed black line in the insets), time evolution of θ and d_{C-N} of complexes **L0** – **L3** ($^2([Ru^{IV}=O]_i^{2+}-NDI^+)$, $i = 0 - 3$) along the FMD trajectories after the photooxidation of NDI dye. The insets show the spin density isosurface computed at a snapshot taken at the end of each FMD simulation of complexes **L0** – **L3**, respectively, in the doublet state with two unpaired α electrons localized on the catalyst (green spin density isosurface) and one unpaired β electron on the NDI dye (purple spin density isosurface). An integrated spin density value of 1 corresponds to one unpaired β electron (\uparrow).

4.A.4. Continued Constrained 2.5 Å MD Simulation for L1

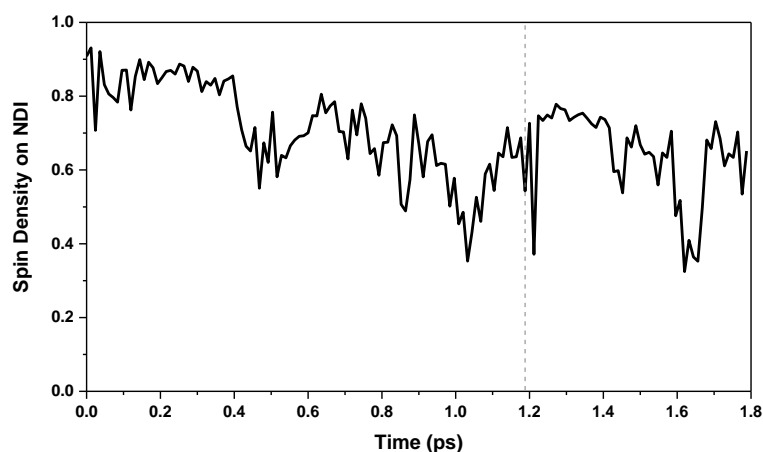


Figure A4.3. Spin density integrated over half of the simulation box including the NDI dye of complex **L1** along the longer constrained 2.5 Å MD trajectory. This figure clearly shows that the spin density fluctuates considerably during the overall constrained 2.5 Å MD simulation, indicating that the electron transfers back and forth between the WOC and dye. In other words, the ET is not completed in such a MD timescale at the current stage of the reaction coordinate $d(\text{O}_i \leftarrow \text{O}_{ii}) = 2.5 \text{ Å}$.

4.A.5. Running Average of the Constraint Force as a Function of Time

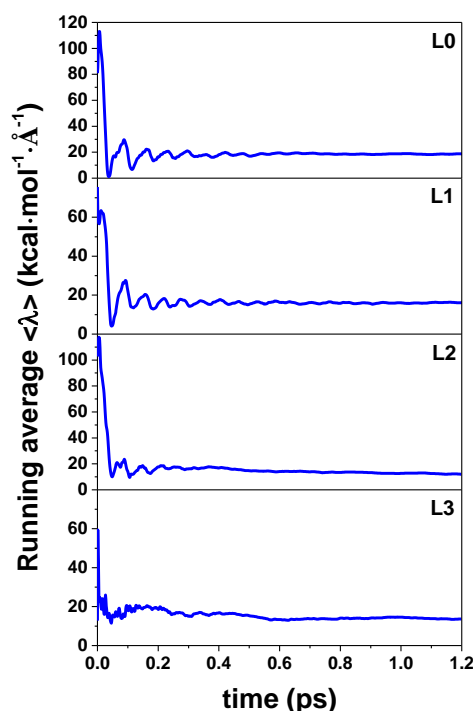


Figure A4.4. The running average of the constraint force $\langle \lambda \rangle$ (in kcal mol⁻¹ Å⁻¹) as a function of time for the distance constraint $d(\text{O}_i \leftarrow \text{O}_{ii}) = 2.5 \text{ Å}$ of complexes **L0** – **L3**, respectively. The running average reaches a stable value within this MD timescale of ~1.2 ps.

4.A.6. Continued Constrained 1.8 Å MD Simulation for L3

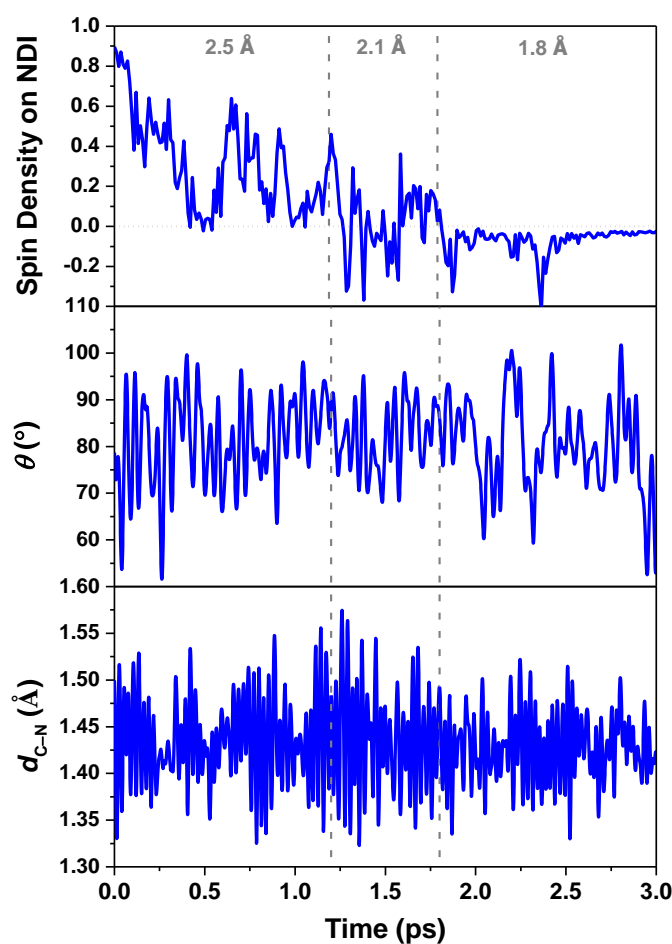


Figure A4.5. Spin density integrated over half of the simulation box including the NDI dye (top panel), time evolution of θ (middle panel) and d_{C-N} (bottom panel) of complex **L3** only along the constrained MD trajectories after the photooxidation of NDI dye. The value of the constrained reaction coordinate $d(O_i \leftarrow O_{ii})$ in the MD simulations is noted in grey.

4.A.7. Proton Transfer for L0 – L3 at $d(\text{O}_i \leftarrow \text{O}_{ii}) = 1.8 \text{ \AA}$

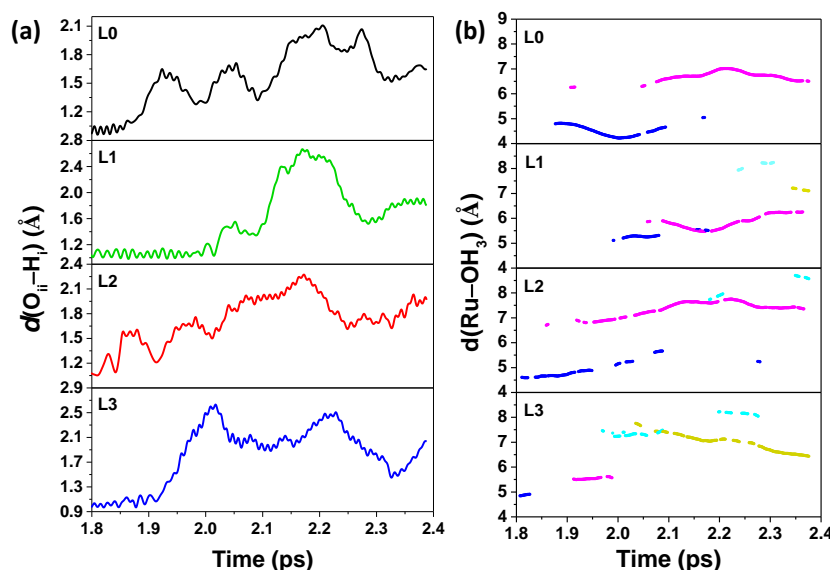


Figure A4.6. (a) Time evolution of the geometrical parameter $d(\text{O}_{ii}-\text{H}_i)$ along the constrained MD trajectory with $d(\text{O}_i \leftarrow \text{O}_{ii}) = 1.8 \text{ \AA}$ for complexes **L0** – **L3**. (b) The distance between Ru and H_3O^+ , defined as an oxygen atom with 3 H within a radius of 1.2 \AA , illustrating the proton diffusion during the constrained 1.8 \AA MD simulations for complexes **L0** – **L3**. The analysis of the trajectories shows that only one oxygen is in the H_3O^+ form at any time, and the excess proton associates primarily to 2 – 4 different oxygens (indicated with different colours) during the simulation. This figure clearly shows that the proton diffuses from the first solvation shell of the ruthenium center to the second or even third and fourth solvation shell rapidly within this relatively short MD timescale of $\sim 0.6 \text{ ps}$. The time range is consistent with that in **Figure 4.3**.

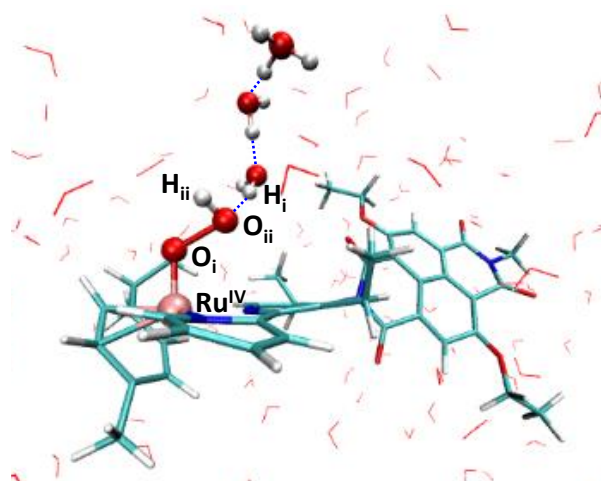


Figure A4.7. Snapshot taken at the end of the constrained 1.8 \AA simulation for complex **L2**. The attacking water molecule and the neighboring water molecules forming the hydrogen-bonded chain are represented with ball & stick. The dashed blue lines indicate the hydrogen bonds. This figure clearly shows that the proton H_i has been totally released by the attacking water molecule and diffuses rapidly into the solvent bulk via a “chain” of hydrogen-bonded water molecules even within the MD timescale of $\sim 0.6 \text{ ps}$.

4.A.8. Constrained 1.6 Å MD Simulation

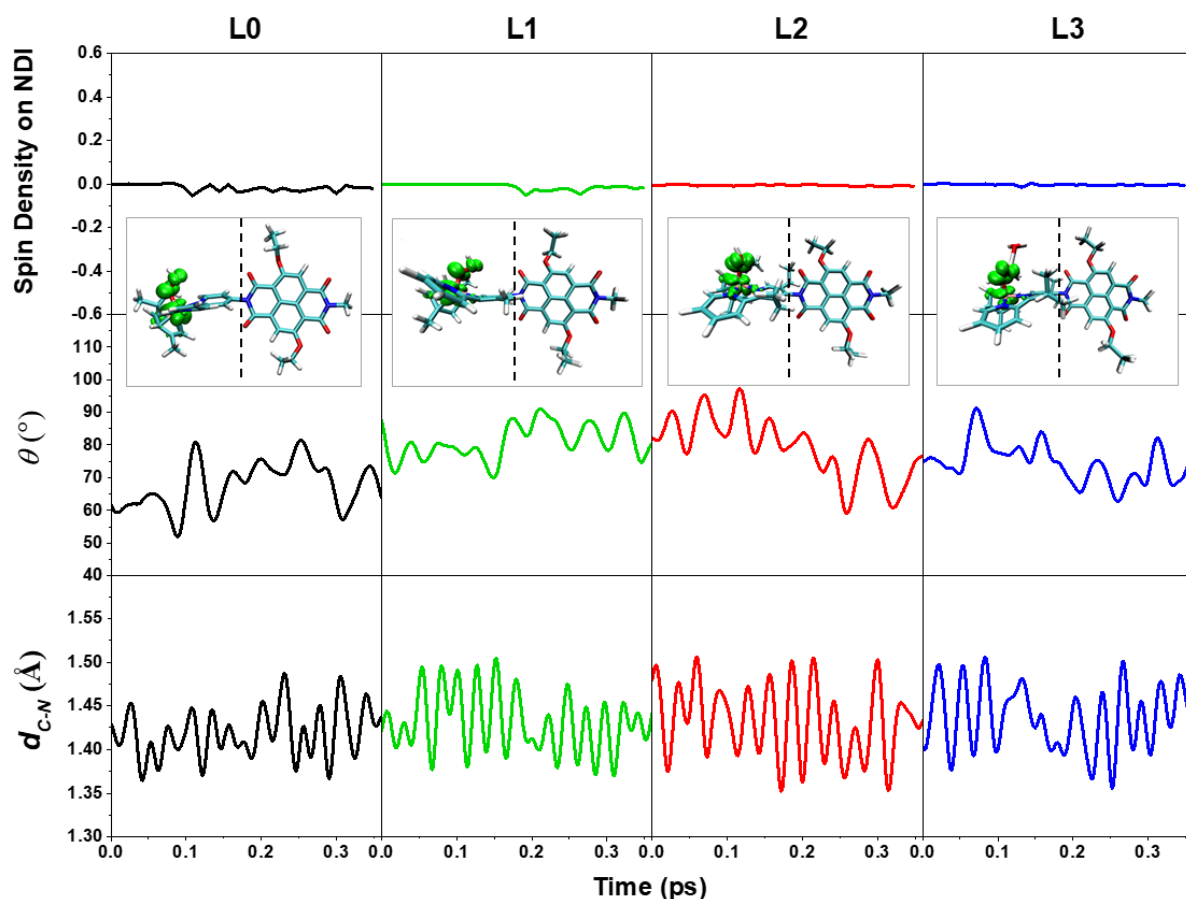


Figure A4.8. Spin density integrated over half of the simulation box including the NDI dye (right-hand side of the dashed black line in the insets), time evolution of θ and d_{C-N} of complexes **L0** – **L3** along the constrained 1.6 Å MD trajectories after the PCET process. The insets show the spin density isosurface computed at a snapshot taken at the end of each MD simulation of complexes **L0** – **L3**, respectively, in the doublet state with one unpaired α electron localized on the catalyst (green spin density isosurface) and no unpaired β electron on the NDI dye. An integrated spin density value of -1 corresponds to one unpaired α electron (\uparrow).

4.A.9. O–O Bond Formation during the FMD Simulation

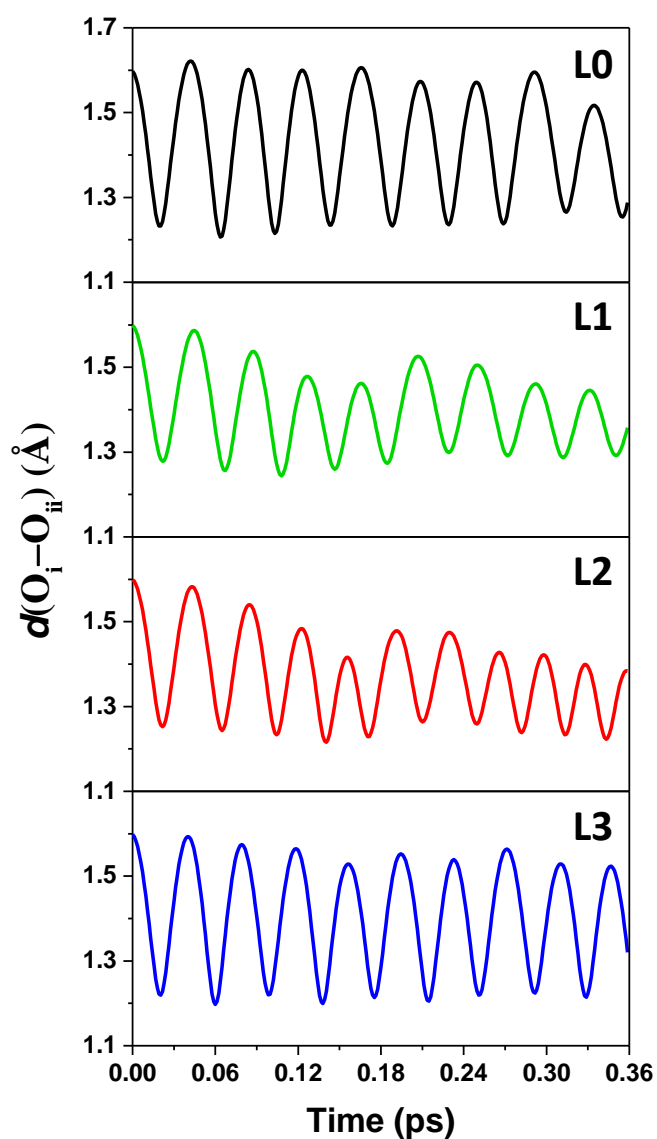


Figure A4.9. Time evolution of the distance between two oxygen atoms O_i and O_{ii} ($d(O_i-O_{ii})$) along the FMD trajectory after the release of constraint at the end of the constrained 1.6 Å MD simulation of complexes **L0** – **L3**.

4.A.10. Time-averaged Constraint Force and Standard Deviation

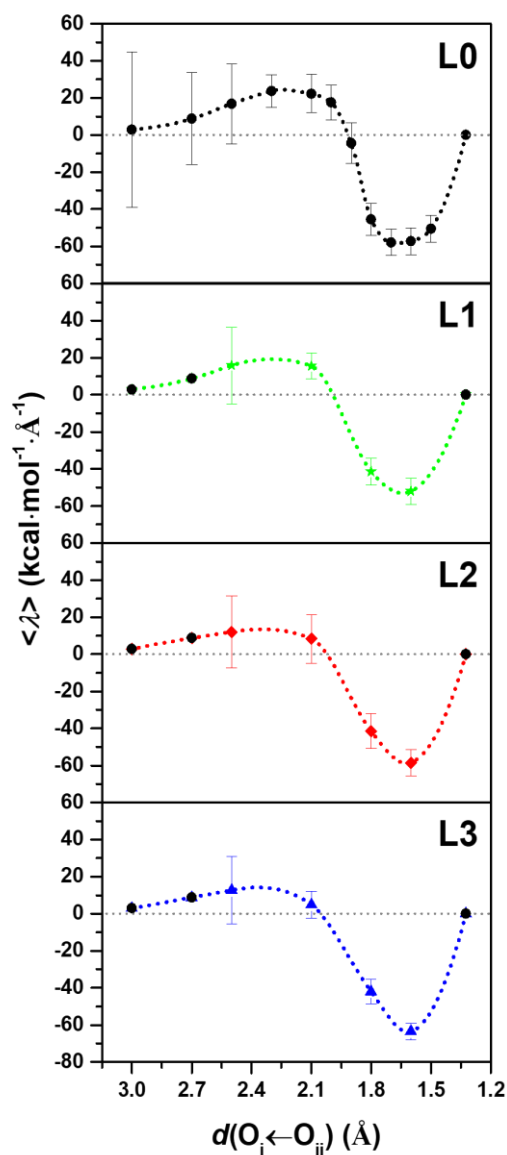


Figure A4.10. Time-averaged constraint force represented by the Lagrangian multiplier $\langle \lambda \rangle$ computed for each constrained MD simulation as a function of the reaction coordinate $d(O_i \leftarrow O_{ii})$ for complexes **L0** – **L3**. The Akima splines (100 points) is used to interpolate the mean forces. The error bars indicate the standard deviations.

4.A.11. Fourier Transform and VDOS

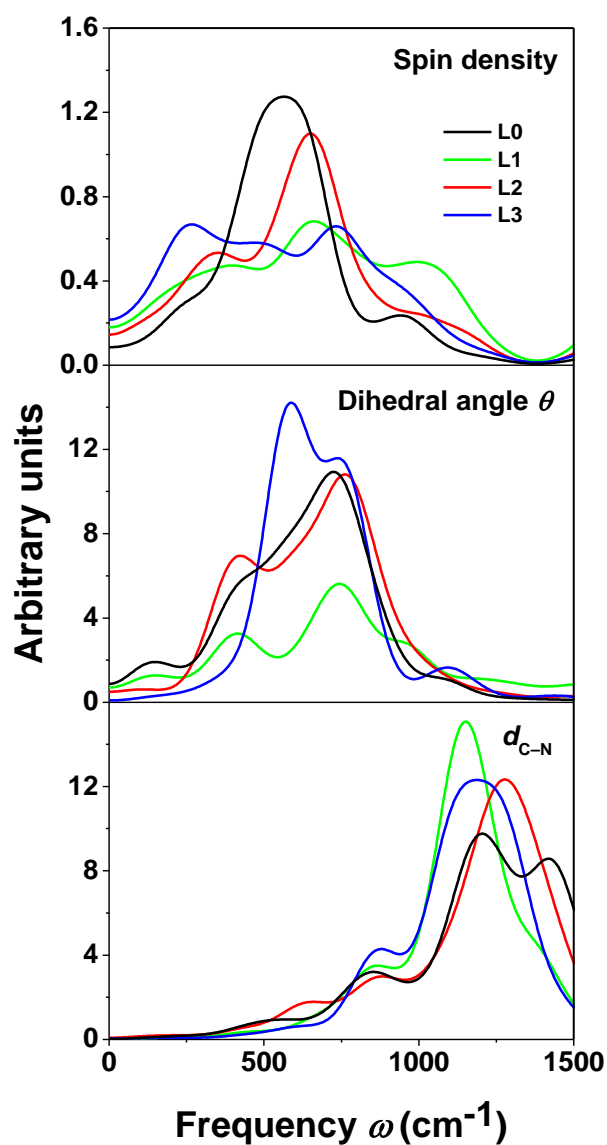


Figure A4.11. Frequency spectrum associated to the ET (top) and the VDOS of the θ (middle) and the $d_{\text{C-N}}$ (bottom) for complexes **L0** – **L3** extracted from the constrained 2.5 Å and 2.1 Å MD trajectories corresponding to **Figure 4.3**.

4.A.12. Geometry Optimization after PCET

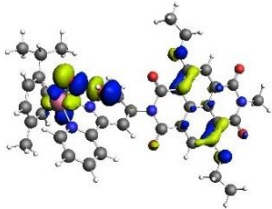
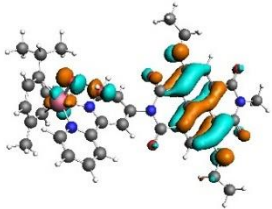
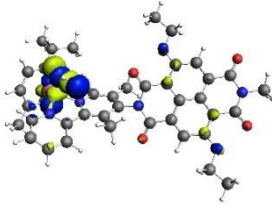
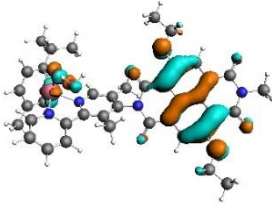
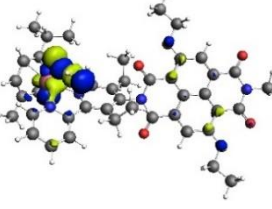
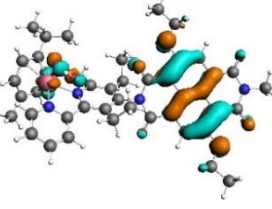
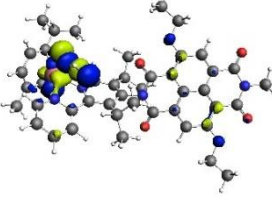
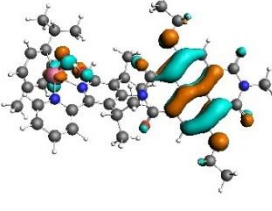
Table A4.2. Calculated geometrical parameters of the initial and final intermediates after geometry optimization for complexes **L0** – **L3**.

Complex	Intermediate			
	Ru=O ^a		Ru-OOH ^b	
	θ_{ini}	$d_{\text{C-N}_{\text{ini}}}$	θ_{fin}	$d_{\text{C-N}_{\text{fin}}}$
L0	66.8	1.424	66.5	1.422
L1	86.5	1.431	86.7	1.428
L2	90.5	1.432	90.3	1.428
L3	91.0	1.433	90.3	1.428

^a θ_{ini} (in °) and $d_{\text{C-N}_{\text{ini}}}$ (in Å) of the initial intermediate (Ru=O) after geometry optimization for complexes **L0** – **L3** extracted from the static DFT calculations. ^b θ_{fin} (in °) and $d_{\text{C-N}_{\text{fin}}}$ (in Å) of the final intermediate (Ru-OOH) after the third PCET step for complexes **L0** – **L3** extracted from the static DFT calculations. See **Scheme 4.1** for the atomic labeling.

4.A.13. TD-DFT Calculation of the Excitation Energies near Transition State

Table A4.3. Excitation energy $\Delta\epsilon$ (in kcal mol⁻¹), oscillator strengths f , and related molecular orbitals for the first excitation of **L0** – **L3** together with the attacking water molecule.^a

Complex	$d(\text{O}_i\text{--O}_{ii})$	$\Delta\epsilon$	f	HOMO	LUMO
L0	1.9	1.788	0.011		
L1	2.0	1.646	0.009		
L2	2.0	1.307	0.006		
L3	2.0	1.291	0.005		

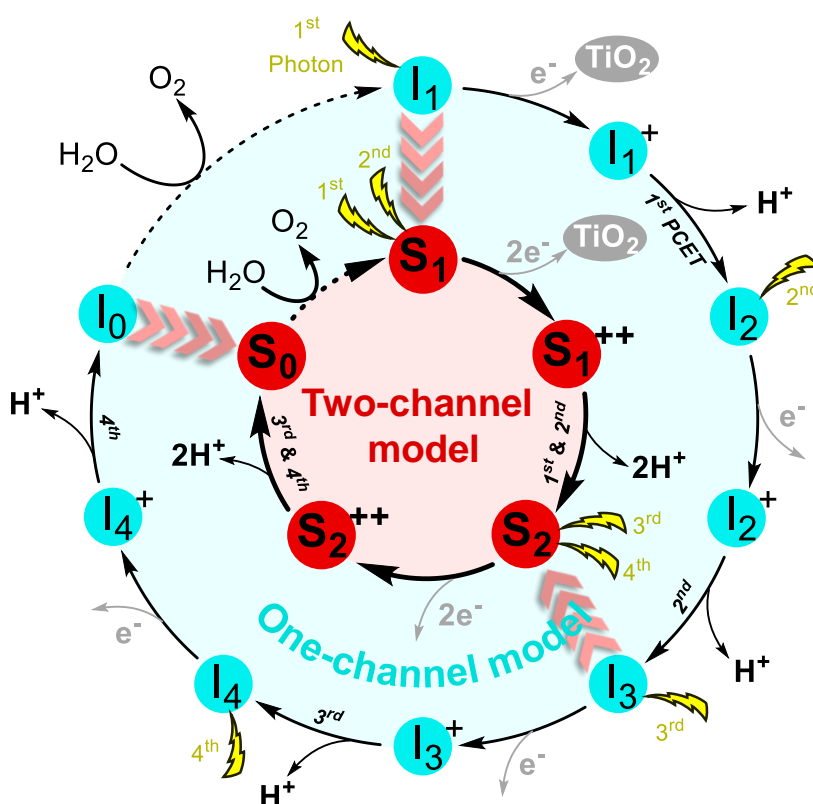
^aThe geometry of all the complexes **L0** – **L3** together with the attacking water molecule are first optimized with the ADF program using OPBE functional and the TZP basis set. The TD-DFT calculations are then performed at the same level. The continuum solvation model COSMO is used to describe the water environment. The distance between the two oxygen atoms O_i and O_{ii} ($d(\text{O}_i\text{--O}_{ii})$, Å) is fixed to certain values which is taken around the transition state according to **Figure 4.4**. The first excitation is mainly related to the transition from HOMO (SOMO WOC) to LUMO (SOMO dye).

4.A.14. References

- [1] Swart, M.; Ehlers, A. W.; Lammertsma, K. *Mol. Phys.* **2004**, *102*, 2467-2474.
- [2] Monti, A.; de Ruiter, J. M.; de Groot, H. J. M.; Buda, F. *J. Phys. Chem. C* **2016**, *120*, 23074-23082.
- [3] Carvalho, A. T. P.; Swart, M. *J. Chem. Inf. Model.* **2014**, *54*, 613-620.
- [4] Groenhof, A. R.; Ehlers, A. W.; Lammertsma, K. *J. Am. Chem. Soc.* **2007**, *129*, 6204-6209.
- [5] Conradie, J.; Ghosh, A. *J. Chem. Theory and Comput.* **2007**, *3*, 689-702.
- [6] Vallés-Pardo, J. L.; Guijt, M. C.; Iannuzzi, M.; Joya, K. S.; de Groot, H. J. M.; Buda, F. *ChemPhysChem* **2012**, *13*, 140-146.
- [7] Klamt, A. *J. Phys. Chem.* **1995**, *99*, 2224-2235.
- [8] Klamt, A.; Jonas, V. *J. Chem. Phys.* **1996**, *105*, 9972-9981.
- [9] te Velde, G.; Bickelhaupt, F. M.; Baerends, E. J.; Fonseca Guerra, C.; van Gisbergen, S. J. A.; Snijders, J. G.; Ziegler, T. *J. Comput. Chem.* **2001**, *22*, 931-967.
- [10] ADF2017, SCM, Theoretical Chemistry, Vrije Universiteit, Amsterdam, The Netherlands, <http://www.scm.com>.
- [11] Accelrys Software Inc. Discovery Studio Modeling Environment, Accelrys Software Inc.: San Diego, 2012.
- [12] Brooks, B. R.; Bruccoleri, R. E.; Olafson, B. D.; States, D. J.; Swaminathan, S.; Karplus, M. *J. Comput. Chem.* **1983**, *4*, 187-217.
- [13] Ciccotti, G.; Ferrario, M. *Mol. Simul.* **2004**, *30*, 787-793.
- [14] Ensing, B.; Meijer, E. J.; Blöchl, P. E.; Baerends, E. J. *J. Phys. Chem. A* **2001**, *105*, 3300-3310.
- [15] Costanzo, F.; Della Valle, R. G. *J. Phys. Chem. B* **2008**, *112*, 12783-12789.
- [16] Shao, Y.; de Ruiter, J. M.; de Groot, H. J. M.; Buda, F. *J. Phys. Chem. C* **2019**, *123*, 21403-21414.
- [17] Otter, W. K. d.; Briels, W. J. *J. Chem. Phys.* **1998**, *109*, 4139-4146.
- [18] Sprik, M.; Ciccotti, G. *J. Chem. Phys.* **1998**, *109*, 7737-7744.
- [19] Bernasconi, L.; Baerends, E. J.; Sprik, M. *J. Phys. Chem. B* **2006**, *110*, 11444-11453.
- [20] Bernasconi, L.; Kazaryan, A.; Belanzoni, P.; Baerends, E. J. *ACS Catal.* **2017**, *7*, 4018-4025.
- [21] Humphrey, W.; Dalke, A.; Schulten, K. *J. Mol. Graphics* **1996**, *14*, 33-38.
- [22] VMD - Visual Molecular Dynamics. *Theoretical Chemistry and Computational Biophysics Group*, University Of Illinois: Urbana, 2016.
- [23] Eyring, H. *J. Chem. Phys.* **1935**, *3*, 107-115.
- [24] Laidler, K. J.; King, M. C. *J. Phys. Chem.* **1983**, *87*, 2657-2664.
- [25] Pollak, E.; Talkner, P. *Chaos* **2005**, *15*, 026116.

CHAPTER 5

Two-Channel Model for Electron Transfer in a Dye–Catalyst–Dye Supramolecular Complex



This chapter is to be submitted as:

Two-Channel model for Electron Transfer in a Dye–Catalyst–Dye Supramolecular Complex for Photocatalytic Water Splitting, 2021, to be submitted.

5

Abstract

To improve the performance of DS-PEC devices for splitting water, the tailoring of the photocatalytic four-photon water oxidation half-reaction represents a principle challenge of fundamental significance. Here we consider a Ru-based WOC covalently bound to two NDI dye functionalities providing comparable driving forces and channels for electron transfer. Constrained AIMD simulations are performed to investigate the photocatalytic cycle of this two-channel model for photocatalytic water splitting. The introduction of a second light-harvesting dye in the Ru-based dye–WOC–dye supramolecular complex enables two separate electron-transfer channels, leading to a five-step catalytic cycle with three intermediates and two doubly oxidized states. The total spin $S = 1$ is conserved during the catalytic process, and the system proceeds from the Ru=O intermediate to the final Ru–O₂ intermediate with a triplet molecular O₂ ligand that is eventually released into the environment. The in-depth insight into the proposed photocatalytic cycle of the two-channel model provides a strategy for the development of novel high-efficiency supramolecular complexes for DS-PEC devices with conservation of spin multiplicity along the reaction coordinate as a guiding principle.

5.1. Introduction

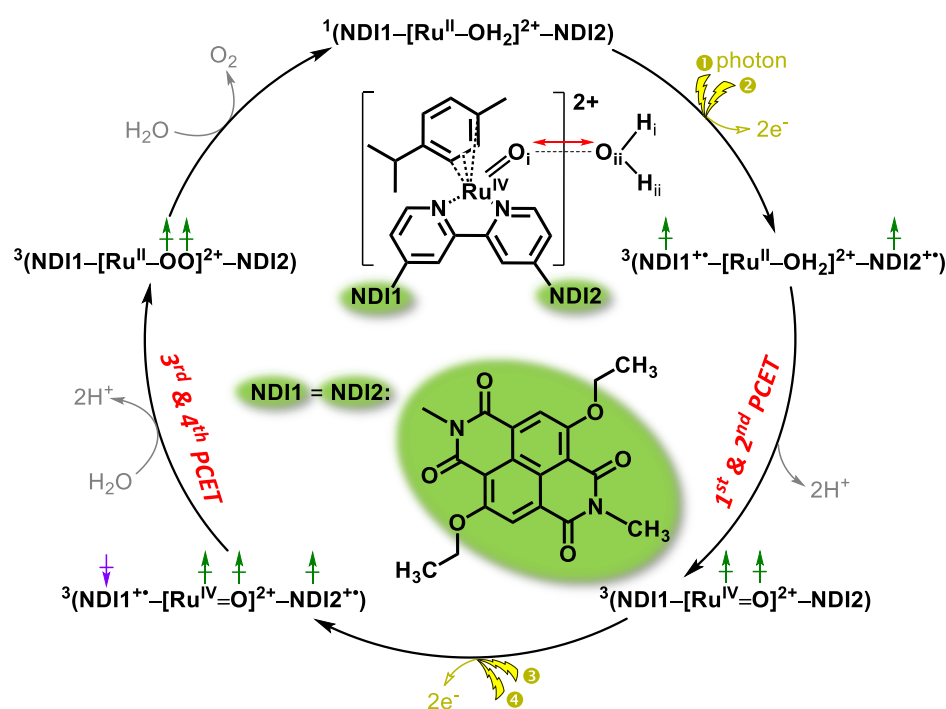
Artificial photosynthesis, inspired by nature, with the goal of conversion of solar energy into chemical energy, has attracted growing interest in the past decades.¹⁻
² In particular, DS-PECs that can drive water splitting through the absorption of sunlight, have the potential to produce clean and renewable chemical fuels, *e.g.* in the form of molecular energy-rich hydrogen, to meet the future global energy demand in an environmentally sustainable way.³⁻⁷ Two half reactions are involved when the water splitting process proceeds in two physically separated electrode compartments, the oxygen evolution reaction (OER) for water oxidation, and the hydrogen evolution reaction (HER) for proton reduction.⁸⁻⁹ For the catalytic water splitting in DS-PECs, the high activation free energy barrier for the O–O bond formation process represents a thermodynamic and kinetic bottleneck, and the OER half-reaction is considered the rate-determining step.¹⁰⁻¹¹

The solar-driven four-photon water oxidation half-reaction occurs at the photoanode, and is always initiated by light absorption at the molecular sensitizers and subsequent electron injection from the dye in the excited state into the electrode. Owing to a proper molecular assembly of the WOC and the dye components in a WOC–dye supramolecular complex, the photooxidation of the dye should be followed by a PCET¹²⁻¹⁶ process within the water oxidation catalytic cycle: The electron is used for the regeneration of the dye to its initial state, while the proton is being transferred to a different direction, into the environment.¹⁷ Computational studies serve as a powerful technique for guiding the development of efficient dye-sensitized photoanodes¹⁸⁻²³ by rate enhancement of photocatalytic water oxidation in DS-PEC devices and the modulation of the mechanism of operation by the solvent environment²⁴⁻²⁶. A great majority of the computational effort has been devoted to lowering the activation free energy barrier of the third catalytic water oxidation step involving the rate-limiting O–O bond formation process, in which a single channel for the ET from the WOC to the photooxidized dye was explored.²⁶

Since 1970, Kok's classical *S*-state cycle model of photosynthetic water oxidation involving five oxidation states ($S_0 \rightarrow 4$) has been the paradigm for the understanding of oxygen evolution.²⁷ By taking into account the role and sequence of deprotonation events as well, an extended *S*-state cycle has been

introduced by Dau *et al.*, in which eight successive steps starting from I_0 lead to I_8 and only then the O_2 is formed and released.²⁸ In other words, the I -cycle model involves not only four oxidizing equivalents but also four bases prior to the dioxygen formation. For sequential alternating proton and electron transfer¹⁷ or concerted PCET²⁶ according to the Kok or Dau cycle in natural or artificial oxygenic photosynthesis, every individual catalytic PCET step can only proceed after the accomplishment of the previous catalytic step.²⁹ We conjecture that the overall efficiency of oxygenic photosynthesis would be reasonably improved if catalytic steps could run from two excited dye motifs in parallel, and thereby combining two PCET steps without stable intermediates in between.

Scheme 5.1. Proposed photocatalytic cycle of the two-channel model for water splitting by a Ru-based dye–WOC–dye system^a



^aSchematic Structure of the third intermediate $^3(\text{NDI1}-[(\text{cy})\text{Ru}^{\text{IV}}(\text{O})\text{bpy}]^{2+}-\text{NDI2})$ complex (indicated as $^3(\text{NDI1}-[\text{Ru}^{\text{IV}}=\text{O}]^{2+}-\text{NDI2})$) together with the attacking water molecule, as explicitly shown in the inset. It is assumed that each light flash induces an electron injection (golden arrows) from the NDI1/NDI2 to the semiconductor electrode or to the next stage in a tandem cell, leading to the photooxidation of NDI1/NDI2: $\text{NDI1/NDI2} \rightarrow \text{NDI1}^+/\text{NDI2}^+$. Green (α electrons) and purple (β electrons) vertical arrows depict the spin of unpaired electrons located on the WOC and on the two NDI dyes. The red double-sided arrow indicates the reaction coordinate $d(\text{O}_i \leftarrow \text{O}_{ii})$ considered in the constrained MD simulations. The superscript on the left indicates the spin multiplicity $2S+1$ for each intermediate and oxidized state.

In this work an additional dye molecule is introduced in the catalyst–dye supramolecular complex $^1[(\text{cy})\text{Ru}^{\text{II}}\text{bpy}(\text{H}_2\text{O})]^{2+}\text{--NDI}$ (cy = *p*-cymene, bpy = 2,2'-bipyridine, NDI = 2,6-diethoxy-1,4,5,8-diimide-naphthalene) for photocatalytic water splitting, which has been systematically investigated *in silico* recently,^{17, 26, 30} leading to the dye–WOC–dye supramolecular complex $^1(\text{NDI1}\text{--}[(\text{cy})\text{Ru}^{\text{II}}\text{bpy}(\text{H}_2\text{O})]^{2+}\text{--NDI2})$ with the total spin $S = 0$ (indicated shortly as $^1(\text{NDI1}\text{--}[\text{Ru}^{\text{II}}\text{--H}_2\text{O}]^{2+}\text{--NDI2})$ in Scheme 5.1, where $\text{NDI1} = \text{NDI2} = \text{NDI}$). The goal of this modification is to rearrange the sequence of catalytic intermediates by having first the absorption of two photons, followed by the transfer of two electrons and two protons. The incorporation of two NDI dye functionalities covalently bound to the bipyridine ligand of the catalytic motif, provides two parallel channels for ET, enabling theoretically concurrent ET events from the WOC to the oxidized dyes NDI1^{+} and NDI2^{+} . Scheme 5.1 presents the proposed photocatalytic cycle of the two-channel model for water splitting by the Ru-based dye–WOC–dye system. An extended photocatalytic cycle considering all possible reaction pathways is reported in Scheme A5.1 for completeness (See Appendix 5.A.2). Given that the spin alignment of unpaired electrons on the WOC and dye has turned out to play a significant role in the PCET reactions in the one-channel model (see **Chapter 2** of this thesis), only the most favorable pathways with proper spin alignments are explored for the two-channel model (see Scheme 5.1). Specifically, the first half of the cycle for the two-channel model is initiated by the co-photooxidation of two NDI dyes, which leaves one α unpaired electron (\uparrow) on each NDI dye with the total spin $S = 1$. This choice is based on the previous finding for the one-channel model where the triplet spin configuration was found to be more favorable for the second PCET step. Instead, for the third step involving the O–O bond formation process in the one-channel model, it is found that the antiparallel spin alignment of the unpaired electrons on the WOC ($\uparrow\downarrow$) and dye (\downarrow) is essential for this reaction. Thus for the second half of the cycle, the antiparallel spin alignment of unpaired electrons on the two NDI dyes is considered: in this way the total spin $S = 1$ is preserved until the formation of the triplet oxygen, which eventually leaves the complex and brings the spin multiplicity back to the singlet state (see Scheme 5.1).¹⁷

Here, we report how the introduction of parallel channels for ET changes the number of involved intermediates and the sequence of reaction events along the

photocatalytic cycle in the dye–WOC–dye system by using AIMD simulations, which can provide accurate predictions of the reaction mechanism and activation energy barrier.³¹ Since the catalytic step involving the O–O bond formation has long been considered the rate-limiting step for the photocatalytic water oxidation half-reaction, we focus on the second half of the catalytic cycle starting from the second intermediate $^3(\text{NDI1} - [\text{Ru}^{\text{IV}}=\text{O}]^{2+} - \text{NDI2})$ (see bottom right in Scheme 5.1) to provide insight into the impact of the two electron-transfer channels on the reaction efficiency.

5.2. Results and Discussion

5.2.1 Geometry Optimization of the Dye–WOC–Dye Complex with DFT.

The initial geometry of the dye–WOC–dye complex $^3(\text{NDI1} - [\text{Ru}^{\text{IV}}=\text{O}]^{2+} - \text{NDI2})$ was optimized at the DFT level employing the OPBE exchange-correlation functional³² and the TZP (triple- ζ polarized) Slater-type basis set with the ADF software package^{33–34} (see Appendix 5.A.1 for more computational details).³⁰ To check if the photooxidized dyes coupled to the Ru-based WOC exert thermodynamic driving forces for the subsequent catalytic steps, the frontier molecular orbital energy levels together with the singly occupied molecular orbitals (SOMOs) of the doubly-oxidized complex $^3(\text{NDI1}^{+*} - [\text{Ru}^{\text{IV}}=\text{O}]^{2+} - \text{NDI2}^{+*})$ with total spin $S = 1$ (see Scheme 5.1) are shown in Figure A5.1 and the corresponding energy values are listed in Table A5.1 (see Appendix 5.A.3). A closed systems approach simulation³⁵ with $S = 1$ allows to have the same total spin for the initial ($^3[\text{Ru}^{\text{IV}}=\text{O}]^{2+}$) and for the final ($^3[\text{Ru}^{\text{II}}-\text{O}_2]^{2+}$) intermediates, thus avoiding the need for intersystem crossing during the reaction: The electronic state of the $^3[\text{Ru}^{\text{IV}}=\text{O}]^{2+}$ WOC is in a triplet configuration, while the two unpaired electrons on the photooxidized dyes are in an antiparallel arrangement. It is found that both the alignment of the energy levels and the spin alignment are favorable for the subsequent ET steps involving the O–O bond formation since the SOMOs localized on the NDI dyes (SOMO dye1 and SOMO dye2) with antiparallel spins are lower in energy than the HOMO of the dye–WOC–dye complex localized on the WOC (SOMO WOC) (see Figure A5.1). The orbital energy difference between the SOMO WOC and the SOMO dyes is $\Delta E_{\text{SOMO-1}} = \sim 0.18$ and $\Delta E_{\text{SOMO-2}} = \sim 0.21$ eV, respectively (see Table A5.1).

5.2.2 Equilibration of the System and Photooxidation of two NDI Dyes.

An orthorhombic box of dimensions $25.5 \times 22.4 \times 15.4 \text{ \AA}^3$ with periodic boundary conditions containing the dye–WOC–dye solute $^3(\text{NDI1}-[\text{Ru}^{\text{IV}}=\text{O}]^{2+}-\text{NDI2})$ ($S = 1$) together with 212 explicit water molecules was used in the AIMD simulations to get accurate predictions of the catalytic reaction and free energy profile. AIMD simulations were carried out with the CPMD program.³⁶ The electronic structure was determined using GTH pseudopotentials for the ruthenium transition metal³⁷ and dispersion-corrected pseudopotentials (DCACP) for the remaining atoms³⁸, together with a plane wave cutoff of 70 Ry and the OPBE exchange–correlation functional³² (see Appendix 5.A.1 for more computational details). An initial free AIMD simulation of 0.6 ps at room temperature (300 K) was performed for the solvated system to further equilibrate the solvation environment (see section 5.A.1.2).

The system is assumed to be already in its doubly-oxidized form of dye⁺–[WOC]²⁺–dye⁺ at the beginning of the constrained AIMD simulation for the second half of the cycle, since the photoinduced electron injection from the selected NDI to a TiO₂ semiconductor surface can be achieved on a time scale of ~1 ps, as has been demonstrated in previous work.³⁰ The photooxidation is mimicked by removing two electrons from the simulation box after the initial equilibration simulation of the dye–WOC–dye system leading to a total charge of 4+. A free AIMD simulation for another 0.6 ps at room temperature is performed to further equilibrate the fully oxidized system with the total spin $S = 1$ corresponding to antiparallel spins on the two NDI dyes. This antiparallel spin alignment refers to the most favorable reaction pathway for the one-channel model reported in our recent work, where the total spin angular momentum $S = 1$ was assumed to be conserved in the AIMD simulation studies, since the O–O bond formation was thermodynamically unfavorable for the parallel spin alignment on WOC and dye with $S = 2$.¹⁷ When tracking the spin density along the free AIMD simulation, it is found that two unpaired α electrons (\uparrow) localize on the WOC at the Ru^{IV}=O group, one unpaired β electron (\downarrow) on NDI1, and one unpaired α electron (\uparrow) on NDI2 in the system after the photooxidation of the two NDI dyes (see the inset in Figure A5.2). No ET occurs at this stage, which is an indication of the stability of the initial state of the oxidized complex $^3(\text{NDI1}^{+}-[\text{Ru}^{\text{IV}}=\text{O}]^{2+}-\text{NDI2}^{+})$ ($S = 1$).

5.2.3 Constrained AIMD Simulations and Catalytic Water Oxidation Steps.

To explore the catalytic water oxidation steps involving bond-forming and bond-breaking processes, which are normally considered as rare events on the characteristic AIMD simulation time scale, the constrained MD approach was employed in the simulations to control the reaction coordinate after the re-equilibration of the photooxidized system.³⁹ The constrained reaction coordinate in this case is the distance between the oxygen atom O_i on the Ru complex and the O_{ii} oxygen of the attacking water indicated by the red double-sided arrow in

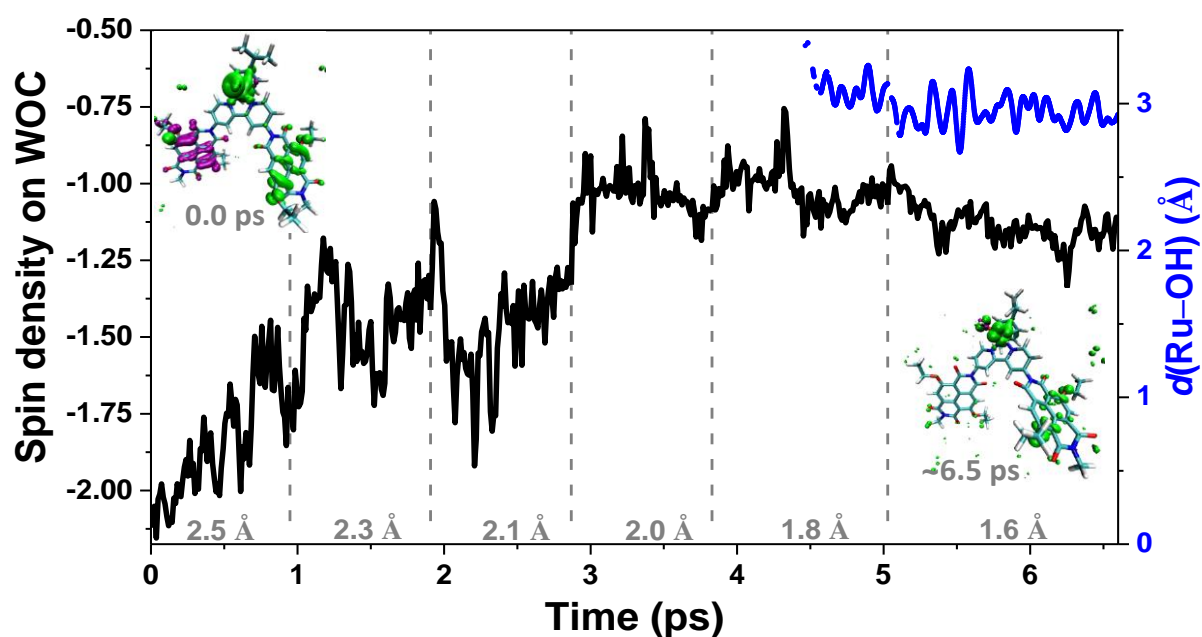


Figure 5.1. Spin density integrated over the upper half of the simulation box including the WOC (black line) and time evolution of the distance between Ru and the OH $d(\text{Ru}-\text{OH})$ (blue line) along the constrained MD trajectories. The OH is defined as an O atom with only one H within a radius of 1.2 Å, illustrating the PT during the MD simulations. Inset left shows the spin density isosurface computed at a snapshot taken at the beginning of the constrained 2.5 Å MD simulation (0.0 ps), clearly indicating two unpaired α electrons (\uparrow in green) localized on the catalyst, one unpaired β electron on NDI1 (\downarrow in purple), and one unpaired α electron on NDI2 (\uparrow in green). Inset right shows the spin density isosurface computed at the end of the constrained 1.6 Å simulation (~6.5 ps). According to the simulations, one proton of the attacking water is totally released during the constrained 1.6 Å simulation and only oxygen O_{ii} is in the OH form at any time. An integrated spin density value of -2 corresponds to two unpaired α electron (\uparrow). The value of the constrained reaction coordinate $d(O_i \leftarrow O_{ii})$ in the MD simulations is noted in grey. The water molecules are omitted for clarity in both cases and only the initial intermediate $^3(\text{NDI1}^{+*}-[\text{Ru}^{\text{IV}}=\text{O}]^{2+}-\text{NDI2}^{+*})$ ($S = 1$) and the transient final intermediate $^3(\text{NDI1}-[\text{Ru}^{\text{III}}-\text{OOH}]^{2+}-\text{NDI2}^{+*})$ ($S = 1$) are shown explicitly. See Scheme 5.1 for the atomic labelling.

Scheme 5.1 (see Appendix 5.A.1 for more computational details). In order to visualize when and how the electron transfers from the WOC to the oxidized NDI dyes (see NDI1 and NDI2 in Scheme 5.1), the spin density was tracked during the AIMD simulations. The variation of the spin density localized on the WOC (black line) together with the time evolution of the distance between Ru and the OH $d(\text{Ru}-\text{OH})$ (blue line) along the constrained MD trajectories are collected in Figure 5.1. The initial value of -2 for the spin density corresponds to the triplet state with two unpaired electrons on the WOC.

For the two-channel model starting with the oxidized $^3(\text{NDI1}^+ - [\text{Ru}^{\text{IV}}=\text{O}]^{2+} - \text{NDI2}^+)$ ($S = 1$) complex (see Figure 5.1, inset (left)), the ET starts at the reaction coordinate $d(\text{O}_i \leftarrow \text{O}_{ii}) = 2.5 \text{ \AA}$ (see Figure 5.1, black line), while in the one-channel model it was actually observed at the reaction coordinate $d(\text{O}_i \leftarrow \text{O}_{ii}) = 2.1 \text{ \AA}$.¹⁷ The shortening of $d(\text{O}_i \leftarrow \text{O}_{ii})$ from 2.5 \AA to 2.0 \AA induces the complete ET from the WOC to the oxidized NDI1 with spin density localized on the WOC fluctuating around an average value of -1 . After short-term fluctuations of spin density localized on the WOC, the dye system that is initially in the $\text{dye}^+ - [\text{WOC}]^{2+} - \text{dye}^+$ state ends up with one unpaired α electron (\uparrow) localized on the WOC and one unpaired α electron (\uparrow) on the NDI2 at the end of the constrained 1.8 \AA MD simulation. Moreover, the PT from the attacking water molecule to the solvent is first observed during the constrained 1.8 \AA MD simulation when tracking the distance between Ru and the OH $d(\text{Ru}-\text{OH})$ along the constrained MD trajectories (see Figure 5.1, blue line): here the OH is defined as an O atom with only one H within a radius of 1.2 \AA . Subsequently, the released proton H_i diffuses into the solvent bulk via a “chain” of hydrogen-bonded water molecules following a Grotthuss-type mechanism^{17, 23, 30, 40-41} and no back reaction occurs after $\sim 5.2 \text{ ps}$ along the constrained 1.6 \AA MD trajectory (see Appendix 5.A.5). It is also noticeable that during the constrained 1.6 \AA MD simulation, the integrated spin density gets an average value smaller than -1 , which can be attributed to the initial attempts of the fourth ET process from the WOC to the oxidized NDI2 (see Figure 5.1, inset (right)).

At the end of the constrained 1.6 \AA MD simulation, the constraint on the reaction coordinate was released and the system is allowed to evolve freely. The time evolution of the distance between the oxygen atoms O_i and O_{ii} $d(\text{O}_i - \text{O}_{ii})$, the variation of the total spin density localized on the WOC, and the distance

between Ru and H_3O^+ (defined as an O atom with three H within a radius of 1.2 Å) along the free MD trajectory after releasing the constraint are collected in Figure 5.2 for quantitative descriptions of electron and proton dynamics.

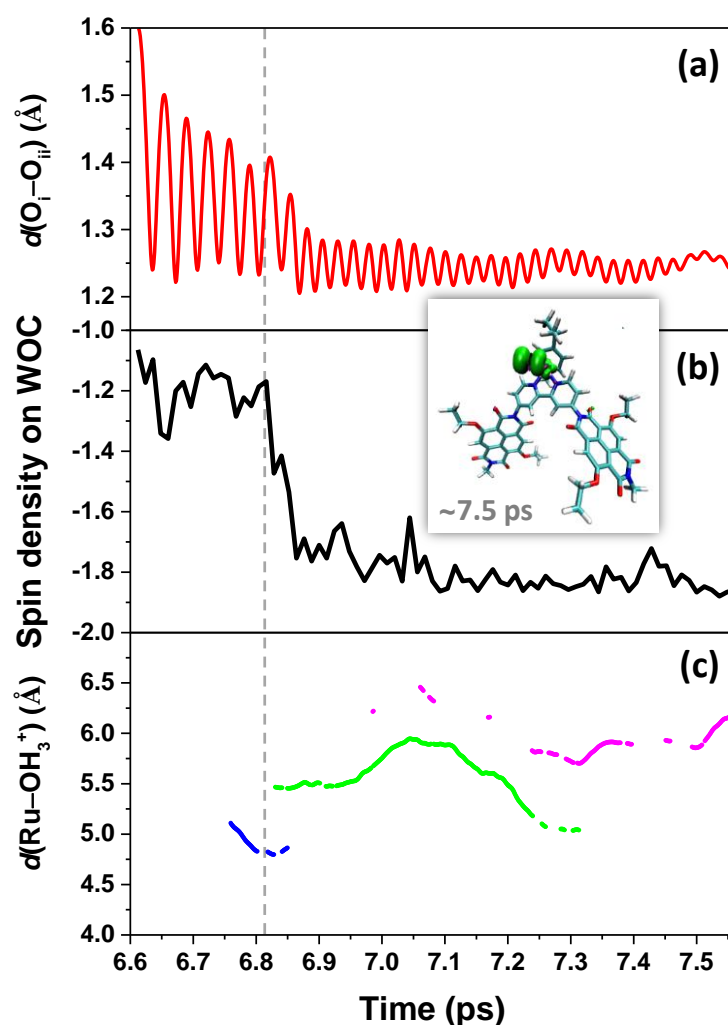
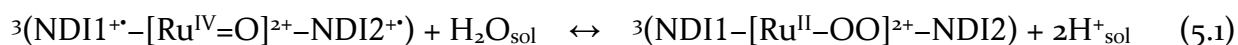


Figure 5.2. (a) Time evolution of the geometrical parameter $d(\text{O}_i-\text{O}_{ii})$, (b) spin density integrated over upper half of the simulation box including the WOC, and (c) distance between Ru and the H_3O^+ $d(\text{Ru}-\text{OH}_3^+)$ along the free MD trajectory after releasing the constraint at the end of the constrained 1.6 Å MD simulation. The H_3O^+ is defined as an O atom with 3 H within a radius of 1.2 Å, illustrating the second PT during the MD simulation. According to the simulations, only one oxygen is in the H_3O^+ form at any time, and the second excess proton associates primarily to three different oxygens (indicated with different colors: blue, green, and magenta) during the simulation. An integrated spin density value of -2 corresponds to two unpaired α electrons (\uparrow). The inset shows the spin density isosurface computed for a snapshot taken at the end of the free MD simulation, which indicates clearly that the spin density is mostly localized on the O_2 ligand and shows the characteristic shape expected for the oxygen molecule. The water molecules are omitted for clarity and only the final intermediate $\text{NDI1}-[\text{Ru}^{\text{II}}-\text{OO}]^{2+}-\text{NDI2}$ ($S = 1$) is shown explicitly. The time range is consistent with Figure 5.1. See Scheme 5.1 for the atomic labelling.

consistent with the formation of a transient Ru–OOH state in the third catalytic water oxidation step (for comparison, the O–O bond length in molecular hydrogen peroxide is 1.47 Å). After 0.2 ps (at ~6.8 ps in Figure 5.2, dashed vertical line) a fast ET process from the WOC to the oxidized NDI2 takes place (see Figure 5.2b). This ET process is strongly coupled to the fourth PT from the hydroperoxo ligand to the solvent bulk (see Figure 5.2c). Notice that two protons (H_i and H_{ii}) diffuse independently from each other into the solvent at this stage and we only focus on the second released proton H_{ii} in Figure 5.2c. The distance between the oxygen atoms O_i and O_{ii} equilibrates quickly to an average value $d(\text{O}_i\text{--O}_{ii})$ of ~1.25 Å. Although we have a higher proton density compared to the one-channel model, we observe that the fourth PCET catalytic water oxidation step proceeds spontaneously following the formation of the O–O bond. Subsequently the system reaches the final intermediate $^3(\text{NDI1}^+[\text{Ru}^{\text{II}}\text{--OO}]^{2+}\text{--NDI2})$ ($S = 1$) (see Scheme 5.1 and eq. 5.1, where H₂O_{sol} and H⁺_{sol} represent the solvated attacking water molecule and solvated proton respectively).



In this final complex with an average value of $d(\text{O}_i\text{--O}_{ii}) = \sim 1.25$ Å two unpaired α electrons (\uparrow) are localized on the dioxygen ligand (see Figure 5.2, inset), indicating the formation of the O=O double bond in the triplet state as in molecular oxygen (the O=O bond length in molecular O₂ in the triplet state is 1.21 Å for comparison). The O₂ ligand can then be exchanged by a water molecule and the complex is ready for the next catalytic cycle. All these results indicate that the third and fourth catalytic steps proceed in a concerted way with no stable intermediate between these two steps. This result is at variance with the case of the one-channel model since the complex with a hydroperoxo ligand is a stable intermediate in the one-channel model, while it is here only a transient Ru–OOH state developing into the final intermediate (see Scheme 5.2).¹⁷

5.2.4 Free Energy Profile and Reaction Rate Evaluation.

Having established that the second half of the catalytic water oxidation cycle starting from the doubly photooxidized supramolecular complex $^3(\text{NDI1}^+[\text{Ru}^{\text{IV}}=\text{O}]^{2+}\text{--NDI2}^{*})$ ($S = 1$) proceeds combining two sequential steps without stable intermediates in between, it is relevant to evaluate how difficult it

is to activate these reactions in such a two-channel model. The reaction coordinate $d(\text{O}_i \leftarrow \text{O}_{ii})$ is constrained to a series of fixed values to estimate the free energy profile along this reaction pathway using the Blue Moon ensemble approach and thermodynamic integration (see Appendix 5.A.1.3 for more details).^{39, 42-43} The time-averaged mean forces associated with the applied constraints, the interpolation of the time-averaged mean forces used for this analysis, and the corresponding free energy profile of the two-channel model as a function of the reaction coordinate $d(\text{O}_i \leftarrow \text{O}_{ii})$ are reported in Figure 5.3 (see Appendix 5.A.1.3 for computational details). Table 5.1 summarizes the thermodynamics parameters for the O–O bond formation process extracted from these results.

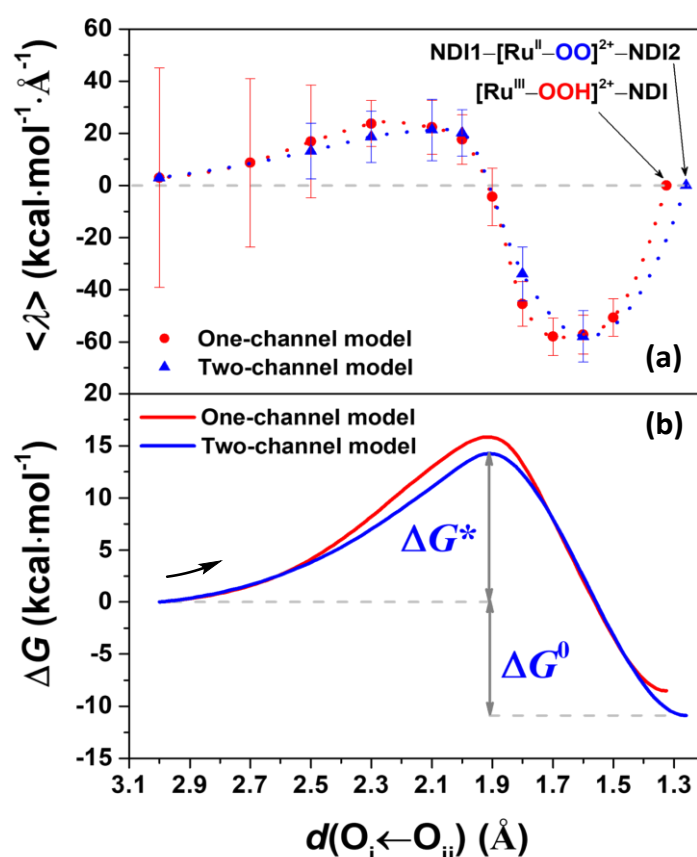


Figure 5.3. (a) Time-averaged constraint force represented by the Lagrangian multiplier $\langle \lambda \rangle$ computed for each constrained MD simulation as a function of the reaction coordinate $d(\text{O}_i \leftarrow \text{O}_{ii})$ in the two-channel model. The Akima splines (100 points) is used to interpolate the mean forces. The final intermediates corresponding to the MD simulations for the one-channel and two-channel models are both indicated. (b) Free energy profile along the reaction coordinate $d(\text{O}_i \leftarrow \text{O}_{ii})$ computed by thermodynamic integration. The time-averaged constraint forces and associated free energy profile obtained in the one-channel model from a previous study is also presented for comparison (see Ref. 17). The error bars indicate the standard deviations.

Table 5.1. The calculated activation energy barrier (ΔG^* in kcal mol⁻¹), reaction driving force (ΔG^o in kcal mol⁻¹), and the reaction rate (k in s⁻¹) corresponding to the one-/two-channel models. The results for the one-channel model are taken from ref. 17.

Model	ΔG^*	ΔG^o	k
One-channel ¹⁷	15.9	-8.5	15.7
Two-channel	14.3	-10.9	230.4

The calculated activation free energy barrier (ΔG^*) for the two-channel model is 14.3 kcal mol⁻¹ (~ 0.62 eV), which is slightly lower than the 15.9 kcal mol⁻¹ (~ 0.69 eV) computed with the same approach for the one-channel model¹⁷ (see Table 5.1). However, this conclusion might be affected by the statistical error in the time-averaged mean forces. If we use this barrier for the estimation of the reaction rate according to transition state theory⁴⁴⁻⁴⁶ (see Appendix 5.A.1.4 for computational details), the predicted reaction rate of the two-channel model is $k = 230.4$ s⁻¹, which is faster than that obtained for the one-channel model ($k = 15.7$ s⁻¹). One should keep in mind that the two-channel model ends up with the final intermediate ³(NDI1-[Ru^{II}-OO]²⁺-NDI2) ($S = 1$) (see Scheme 5.1 and Figure 5.3) rather than an intermediate with a hydroperoxo ligand as in the one-channel model (²([Ru^{III}-OOH]²⁺-NDI) ($S = 1/2$))¹⁷ as a result of the introduction of the second electron-transfer channel. Furthermore, the larger thermodynamic driving force $\Delta G^o = -10.9$ kcal mol⁻¹ (~ 0.47 eV) obtained in the two-channel model can be reasonably attributed to the accomplishment of the barrier-less fourth catalytic water splitting PCET step under the condition that the second dye NDI2 is photooxidized. This result suggests a relatively more stable final intermediate ³(NDI1-[Ru^{II}-OO]²⁺-NDI2) ($S = 1$) (see Scheme 5.1) lower in energy than an alternative in-between intermediate ³(NDI1-[Ru^{III}-OOH]²⁺-NDI2⁺) ($S = 1$) (see Scheme A5.1).

In order to verify the feasibility of the entire proposed photocatalytic cycle for the two-channel model, the first half of the photocatalytic cycle was also investigated by using the same computational approach (see Appendix 5.A.6 for details). According to the results of our simulations, the first and second catalytic steps, starting from the initial intermediate ¹(NDI1-[Ru^{II}-OH₂]²⁺-NDI2) ($S = 0$) and ending with the intermediate ³(NDI1-[Ru^{IV}=O]²⁺-NDI2) ($S = 1$) (see 1st & 2nd

PCET in Scheme 5.1), can proceed with a low activation free energy barrier of ~ 4 kcal mol⁻¹ after the photooxidation of the two NDI dyes (see Figure A5.5). In this case we assume that one attacking water molecule is approaching H_{iii} while at the same time another attacking water molecule approaches H_{iv} (see Figure A5.4). The ¹(NDI1–[Ru^{II}–OH₂]²⁺–NDI2) is in the S = 0 state due to the triplet molecular oxygen dissociating from the complex, leaving the singlet behind. The spins are parallel on the NDI in this first part (see Figure A5.4). and the spin is built up in steps. Apparently the Ru selects the appropriate spin from the NDI to build up its high spin magnetic ion state. Hence, the metal ion operates as a spin shuttle during catalysis. In the first part it selects the matching spin from the NDI to build up spin multiplicity, and in the second part it preserves the spin multiplicity and passes on a triplet to the oxygen.

5.3. Conclusions

In conclusion, the introduction of the second NDI dye in the dye–WOC–dye complex for photocatalytic water splitting provides an extra channel for ET, which enables the concurrent event of ET from the WOC to the two separate NDI dyes. The dynamical description of the proposed photocatalytic cycle of the two-channel model obtained with adiabatic AIMD simulations and explicit solvation demonstrates that the third and fourth catalytic steps can proceed one after the other without stable intermediates in between. Although the estimated activation free energy barrier of the combined third and fourth catalytic steps for the two-channel model is similar to that of the one-channel model, the introduction of the second ET channel removes one intermediate in the cycle: the system can now proceed without changing the total spin of the supramolecular complex, from the Ru=O intermediate to the final intermediate with a triplet molecular O₂ product. Overall, this study suggests that having the WOC coordinated to more than one dye at the photoanode of a DS-PEC device can have beneficial effects in the rate and efficiency of the photocatalytic cycle: this is achieved by having the co-photooxidation of the two dyes and an antiparallel spin alignment of the unpaired electrons on the dyes.

5.4. References

- [1] Grätzel, M. *Nature* **2001**, *414*, 338-344.
- [2] Berardi, S.; Drouet, S.; Francas, L.; Gimbert-Surinach, C.; Guttentag, M.; Richmond, C.; Stoll, T.; Llobet, A. *Chem. Soc. Rev.* **2014**, *43*, 7501-7519.
- [3] Zhang, S.; Ye, H.; Hua, J.; Tian, H. *EnergyChem* **2019**, *1*, 100015.
- [4] Yun, S.; Vlachopoulos, N.; Qurashi, A.; Ahmad, S.; Hagfeldt, A. *Chem. Soc. Rev.* **2019**, *48*, 3705-3722.
- [5] Zahran, Z. N.; Tsubonouchi, Y.; Mohamed, E. A.; Yagi, M. *ChemSusChem* **2019**, *12*, 1775-1793.
- [6] Xu, P.; McCool, N. S.; Mallouk, T. E. *Nano Today* **2017**, *14*, 42-58.
- [7] Brennaman, M. K.; Dillon, R. J.; Alibabaei, L.; Gish, M. K.; Dares, C. J.; Ashford, D. L.; House, R. L.; Meyer, G. J.; Papanikolas, J. M.; Meyer, T. J. *J. Am. Chem. Soc.* **2016**, *138*, 13085-13102.
- [8] Yu, Z.; Li, F.; Sun, L. *Energy Environ. Sci.* **2015**, *8*, 760-775.
- [9] Ding, X.; Zhang, L.; Wang, Y.; Liu, A.; Gao, Y. *Coord. Chem. Rev.* **2018**, *357*, 130-143.
- [10] Lyons, M. E. G.; Doyle, R. L.; Browne, M. P.; Godwin, I. J.; Rovetta, A. A. S. *Curr. Opin. Electrochem.* **2017**, *1*, 40-45.
- [11] Xu, P.; Huang, T.; Huang, J.; Yan, Y.; Mallouk, T. E. *Proc. Natl. Acad. Sci.* **2018**, *115*, 6946-6951.
- [12] Hammes-Schiffer, S. *Chem. Rev.* **2010**, *110*, 6937-6938.
- [13] Gagliardi, C. J.; Vannucci, A. K.; Concepcion, J. J.; Chen, Z.; Meyer, T. J. *Energy Environ. Sci.* **2012**, *5*, 7704-7717.
- [14] Hammes-Schiffer, S. *J. Am. Chem. Soc.* **2015**, *137*, 8860-8871.
- [15] Horvath, S.; Fernandez, L. E.; Soudackov, A. V.; Hammes-Schiffer, S. *Proc. Natl. Acad. Sci.* **2012**, *109*, 15663-15668.
- [16] Solis, B. H.; Hammes-Schiffer, S. *Inorg. Chem.* **2014**, *53*, 6427-6443.
- [17] Shao, Y.; de Ruiter, J. M.; de Groot, H. J. M.; Buda, F. *J. Phys. Chem. C* **2019**, *123*, 21403-21414.
- [18] Swierk, J. R.; Mallouk, T. E. *Chem. Soc. Rev.* **2013**, *42*, 2357-2387.
- [19] Wang, D.; Eberhart, M. S.; Sheridan, M. V.; Hu, K.; Sherman, B. D.; Nayak, A.; Wang, Y.; Marquard, S. L.; Dares, C. J.; Meyer, T. J. *Proc. Natl. Acad. Sci.* **2018**, *115*, 8523-8528.
- [20] Maji, S.; Vigara, L.; Cottone, F.; Bozoglian, F.; Benet-Buchholz, J.; Llobet, A. *Angew. Chem. Int. Ed.* **2012**, *51*, 5967-5970.
- [21] Garrido-Barros, P.; Funes-Ardoiz, I.; Drouet, S.; Benet-Buchholz, J.; Maseras, F.; Llobet, A. *J. Am. Chem. Soc.* **2015**, *137*, 6758-6761.
- [22] Matheu, R.; Ertem, M. Z.; Benet-Buchholz, J.; Coronado, E.; Batista, V. S.; Sala, X.; Llobet, A. *J. Am. Chem. Soc.* **2015**, *137*, 10786-10795.
- [23] Shao, Y.; de Groot, H. J. M.; Buda, F. *ChemSusChem* **2020**, *13*.
- [24] Song, N.; Concepcion, J. J.; Binstead, R. A.; Rudd, J. A.; Vannucci, A. K.; Dares, C. J.; Coggins, M. K.; Meyer, T. J. *Proc. Natl. Acad. Sci.* **2015**, *112*, 4935-4940.
- [25] Chen, Z.; Concepcion, J. J.; Hu, X.; Yang, W.; Hoertz, P. G.; Meyer, T. J. *Proc. Natl. Acad. Sci.* **2010**, *107*, 7225-7229.
- [26] Shao, Y.; de Groot, H. J. M.; Buda, F. *J. Phys. Chem. Lett.* **2019**, *10*, 7690-7697.
- [27] Kok, B.; Forbush, B.; McGloin, M. *Photochem. Photobiol.* **1970**, *11*, 457-475.
- [28] Dau, H.; Haumann, M. *Biochim. Biophys. Acta, Bioenerg.* **2007**, *1767*, 472-483.
- [29] Haumann, M.; Liebisch, P.; Müller, C.; Barra, M.; Grabolle, M.; Dau, H. *Science* **2005**, *310*, 1019-1021.
- [30] Monti, A.; de Ruiter, J. M.; de Groot, H. J. M.; Buda, F. *J. Phys. Chem. C* **2016**, *120*, 23074-23082.

- [31] Marx, D.; Hutter, J., *Ab initio molecular dynamics: basic theory and advanced methods*. Cambridge University Press, **2009**.
- [32] Swart, M.; Ehlers, A. W.; Lammertsma, K. *Mol. Phys.* **2004**, *102*, 2467-2474.
- [33] te Velde, G.; Bickelhaupt, F. M.; Baerends, E. J.; Fonseca Guerra, C.; van Gisbergen, S. J. A.; Snijders, J. G.; Ziegler, T., *J. Comput. Chem.* **2001**, *22*, 931-967.
- [34] ADF2017, SCM, Theoretical Chemistry, Vrije Universiteit, Amsterdam, The Netherlands, <http://www.scm.com>.
- [35] de Ruiter, J. M.; Buda, F. *Phys. Chem. Chem. Phys.* **2017**, *19*, 4208..
- [36] CPMD, <http://www.cpmd.org>, Copyright IBM Corp., 1990-2019; Copyright MPI für Festkörperforschung Stuttgart, 1997-2001.
- [37] Hartwigsen, C.; Goedecker, S.; Hutter, J., *Phys. Rev. B* **1998**, *58*, 3641-3662.
- [38] Lin, I. C.; Coutinho-Neto, M. D.; Felsenheimer, C.; von Lilienfeld, O. A.; Tavernelli, I.; Rothlisberger, U., *Phys. Rev. B* **2007**, *75*, 205131.
- [39] Ciccotti, G.; Ferrario, M., *Mol. Simul.* **2004**, *30*, 787-793.
- [40] Agmon, N., *Chem. Phys. Lett.* **1995**, *244*, 456-462.
- [41] de Grotthuss, C. J. T., *Biochim. Biophys. Acta, Bioenerg.* **2006**, *1757*, 871-875.
- [42] Ensing, B.; Meijer, E. J.; Blöchl, P. E.; Baerends, E. J., *J. Phys. Chem. A* **2001**, *105*, 3300-3310.
- [43] Costanzo, F.; Della Valle, R. G., *J. Phys. Chem. B* **2008**, *112*, 12783-12789.
- [44] Eyring, H., *J. Chem. Phys.* **1935**, *3*, 107-115.
- [45] Laidler, K. J.; King, M. C., *J. Phys. Chem.* **1983**, *87*, 2657-2664.
- [46] Pollak, E.; Talkner, P., *Chaos* **2005**, *15*, 026116.

5.A. Appendix

5.A.1. Computational Details

5.A.1.1 Geometry Optimization at DFT Level

The OPBE exchange-correlation functional¹ and the TZP (triple- ζ polarized) Slater-type basis set² were employed in the geometry optimization of the initial state of the dye–WOC–dye complex. The OPBE functional has shown to be accurate in describing transition-metal complexes, including Ru-based WOCs.^{3–6} In the geometry optimization, the continuous solvation model (COSMO^{7–8}) for water was used. These calculations are performed with the ADF software package.^{9–10}

5.A.1.2 Simulation Box

To obtain a realistic description of the catalytic reaction step, the solvent was explicitly introduced in the simulations. The solvent environment for the CPMD simulations was generated using Discovery Studio 2.5.¹¹ The solvent was equilibrated for 0.2 ns using the TIP3P model implemented in the CHARMM force field and CFF partial charge parameters at 300 K,¹² while the dye–[WOC]²⁺–dye complex was kept fixed. The volume was then adjusted using constant pressure for 0.2 ns, after which the system was further allowed to evolve with constant volume for 2 ns. Periodic boundary conditions are applied with a time step of $\delta t = 5$ a.u. (1 a.u. = 0.0242 fs).

5.A.1.3 Free Energy Profile

To estimate the activation free energy barrier of the catalytic reaction step involving the O–O bond formation that is unlikely to occur spontaneously during the typical AIMD simulation time scale, constrained MD and the so-called Blue Moon approach were employed as a rare event simulation technique.^{13–15} The reaction coordinate (in this case the distance between two oxygen atoms O_i and O_{ii} , $d(O_i \leftarrow O_{ii})$, as shown in Scheme 5.1) is constrained to a series of fixed values x in range of 2.5 – 1.6 Å after the initial equilibrium simulation and subsequent photooxidation of two NDI dyes along this reaction pathway. A time-averaged constraint force $\langle \lambda \rangle_x$ for each value of the reaction coordinate x is obtained, which should be equal to zero at an equilibrium or transition state. Based also on our previous work on a similar supramolecular complex, we can safely assume that

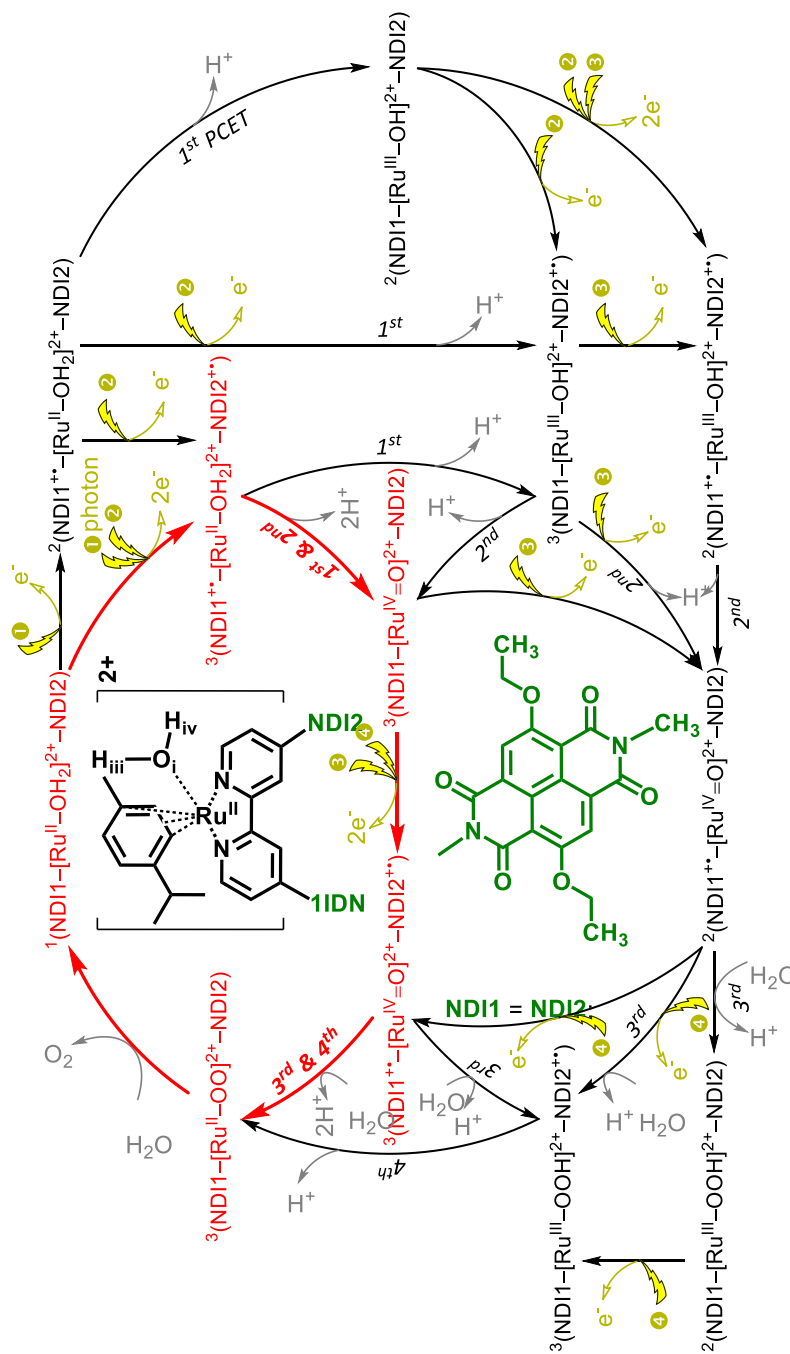
for a value of the reaction coordinate $d(\text{O}_i \leftarrow \text{O}_{ii}) = 3.0 \text{ \AA}$ the system is in an equilibrium state with $\langle \lambda \rangle_{3.0 \text{ \AA}}$ equals to zero.¹⁶ The activation free energy barrier for this catalytic step is then established by interpolating the mean forces with a 100-point Akima splines function and integrating the signed forces $\langle \lambda \rangle_x$ along the reaction path.¹⁷⁻²⁰ Trajectory analysis and visualization for the CPMD output were carried out using VMD.²¹⁻²²

5.A.1.4 Reaction Rate

The computed activation free energy barrier can be used to evaluate to what extent the geometry modification accelerates the rate of the third water oxidation step involving the O–O bond formation. According to transition state theory²³⁻²⁵, the reaction rate (k) determined by the activation energy barrier (ΔG^*) can be expressed as

$$k = \frac{k_B T}{h} \cdot e^{-\frac{\Delta G^*}{RT}},$$

Where ΔG^* represents the activation free energy barrier, k_B , h , R and T are the Boltzmann constant, the Planck constant, the universal gas constant and thermodynamic temperature, respectively. One should keep in mind that in the DFT-based MD simulations protons are treated classically and thus proton tunneling effects are neglected. In the current calculation, only the activation energy barrier is considered as a main factor governing the reaction rate.



^aSchematic Structure of the starting intermediate $^1[(\text{cy})\text{Ru}^{\text{II}}\text{bpy}(\text{H}_2\text{O})]^{2+}-(\text{NDI})_2$ complex (indicated shortly as $^1(\text{NDI})_2-[\text{Ru}^{\text{II}}-\text{OH}_2]^{2+}-\text{NDI}_2$) on the top of the scheme, as explicitly shown in the inset. It is assumed that each light flash induces an electron injection (golden arrows) from the $\text{NDI}_1/\text{NDI}_2$ to the semiconductor electrode or to the next stage in a tandem cell, leading to the photooxidation of $\text{NDI}_1/\text{NDI}_2$: $\text{NDI}_1/\text{NDI}_2 \rightarrow \text{NDI}_1^{+ \cdot}/\text{NDI}_2^{+ \cdot}$. All the possible pathways for the dye-WOC-dye complex after introducing an extra NDI dye are considered in this scheme. In the current work we only focus on the case involving the photooxidation of two NDI dyes and the stable intermediates involved as shown in Scheme 5.1 are indicated in red. The transient states indicated in black are not investigated in this work.

5.A.3. Molecular Orbital and Electronic Structure

Table A5.1. Selected frontier molecular orbital energy levels and energy difference between the highest SOMO WOC and SOMO dye1/dye2 ($\Delta E_{\text{SOMO-1}}/\Delta E_{\text{SOMO-2}}$, in eV) of intermediate $^3(\text{NDI1}^{+*}-[\text{Ru}^{\text{IV}}=\text{O}]^{2+}-\text{NDI2}^{+*})$ after the photooxidation of two NDI dyes.^a

Intermediate		$^3(\text{NDI1}^{+*}-[\text{Ru}^{\text{IV}}=\text{O}]^{2+}-\text{NDI2}^{+*})$			
		\downarrow	\uparrow	\uparrow	\uparrow
Energy level	Orbital	Energy			
HOMO (SOMO WOC)	α	-6.302			
HOMO-1 (SOMO dye1)	β	-6.482			
HOMO-2 (SOMO dye2)	α	-6.509			
HOMO-3	α	-6.773			
HOMO-4	β	-6.806			
HOMO-5 (SOMO WOC)	α	-6.838			
$\Delta E_{\text{SOMO-1}}$		0.180			
$\Delta E_{\text{SOMO-2}}$		0.207			

^aOnly the unpaired electrons are indicated by vertical arrows explicitly (green for unpaired electron localized on the catalyst and blue for unpaired electron on the oxidized NDI⁺). SOMO represents the singly occupied molecular orbital.

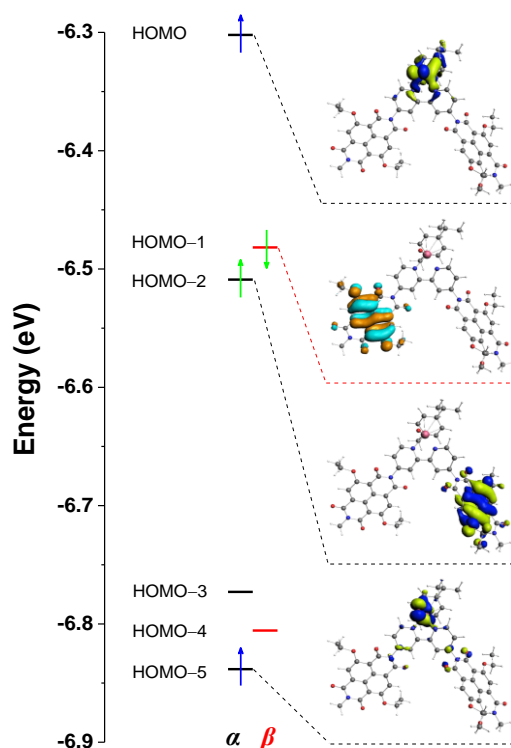


Figure A5.1. Selected frontier molecular orbitals of intermediate $^3(\text{NDI1}^{+*}-[\text{Ru}^{\text{IV}}=\text{O}]^{2+}-\text{NDI2}^{+*})$ after the photooxidation of two NDI dyes computed with the ADF program using the OPBE functional and the TZP basis set. The left (black) and right (red) orbital energy levels refer to the α orbitals and β orbitals, respectively. Only the unpaired electrons are indicated by vertical arrows explicitly (blue for unpaired electron localized on the catalyst and green for the unpaired electron on the oxidized NDI⁺). See **Table A5.1** for the molecular energy levels and the energy difference between SOMO WOC and SOMO dye.

5.A.4. Spin Density after Photooxidation of two NDI Dyes

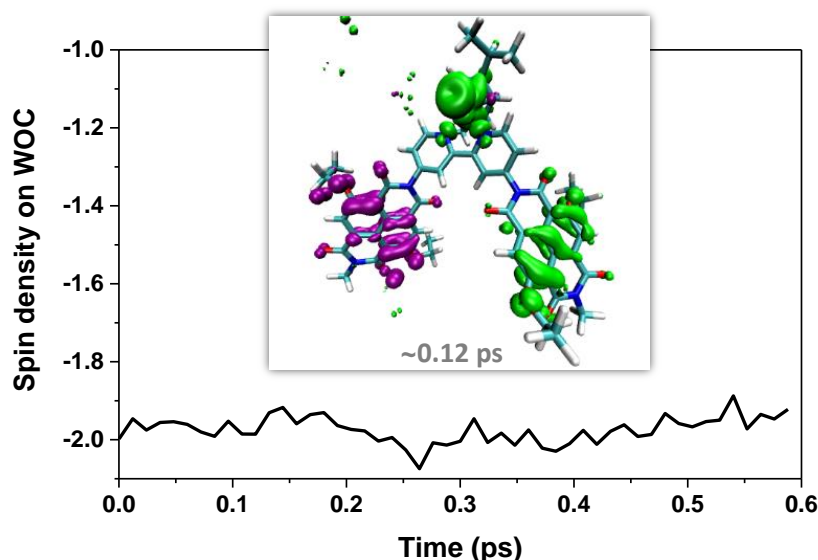


Figure A5.2. Spin density integrated over the part of the simulation box including the WOC along the free MD trajectory after the photooxidation of two NDI dyes. Inset shows the spin density isosurface computed at a snapshot taken at ~ 0.12 ps, clearly indicating two unpaired α electrons (\uparrow in green) localized on the catalyst, one unpaired β electron on NDI1 (\downarrow in purple), and one unpaired α electron on NDI2 (\uparrow in green). See Scheme 5.1 for the atomic labelling. The water molecules are omitted for clarity and only the intermediate $^3(\text{NDI1}^{+\bullet}-[\text{Ru}^{\text{IV}}=\text{O}]^{2+}-\text{NDI2}^{+\bullet})$ is shown explicitly.

5.A.5. PT step during the Constrained 1.8 Å Simulation

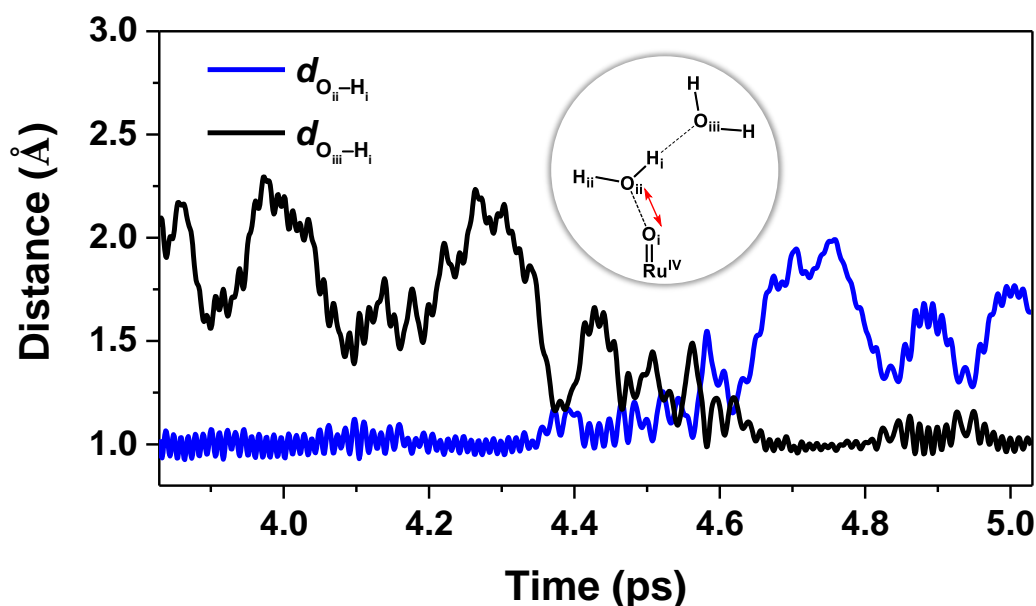


Figure A5.3. Time evolution of the geometrical parameters $d_{\text{O}_{\text{ii}}-\text{H}_{\text{i}}}$ (blue line) and $d_{\text{O}_{\text{iii}}-\text{H}_{\text{i}}}$ (black line) along the constrained MD trajectory with $d(\text{O}_{\text{i}}-\text{O}_{\text{ii}}) = 1.8$ Å. The inset shows the schematic structure of the first two water molecules along the hydrogen-bonding network coordinated to the oxygen ligand. The time range is consistent with that in Figure 5.1.

5.A.6. First Half of the Catalytic Cycle

The initial geometry of the dye–WOC–dye complex $^1(\text{NDI1} - [\text{Ru}^{\text{II}} - \text{OH}_2]^{2+} - \text{NDI2})$ ($S = 0$) was optimized at the DFT level employing the OPBE exchange-correlation functional¹ and the TZP (triple- ζ polarized) Slater-type basis set² with the ADF software package^{9–10}. In the geometry optimization, the continuous solvation model (COSMO^{7–8}) for water was used.

To obtain a realistic description of the catalytic reaction step, the solvent was explicitly introduced in the simulations. An orthorhombic box of dimensions $26.5 \times 20.1 \times 16.3 \text{ \AA}^3$ with periodic boundary conditions containing the dye–WOC–dye solute $^1(\text{NDI1} - [\text{Ru}^{\text{II}} - \text{OH}_2]^{2+} - \text{NDI2})$ ($S = 0$) together with 222 explicit water molecules was used in the AIMD simulations to get accurate predictions of the catalytic reaction, which was carried out with the CPMD program.²⁶

Two reaction coordinates were considered in our constrained MD simulations, corresponding to the distances between $\text{H}_{\text{iii}}/\text{H}_{\text{iv}}$ and the oxygen atom of its neighboring water molecule (see the atomic labeling in Scheme A5.1 and Figure A5.4). The reaction coordinates $d(\text{H}_{\text{iii}} \leftarrow \text{O})$ as well as $d(\text{H}_{\text{iv}} \leftarrow \text{O})$ are constrained to a series of fixed values x in range of $1.4 - 1.05 \text{ \AA}$ simultaneously after the initial equilibrium simulation and subsequent photooxidation of two NDI dyes. In this way, we assume that one attacking water molecule approaches to H_{iii} and another attacking water molecule to H_{iv} at the same time. The photooxidation of the NDI dyes (NDI1 and NDI2) was mimicked by removing two electrons from the simulation box after the initial equilibration simulation of the dye–WOC–dye system, after which a free MD (FMD) simulation of around 1.1 ps at room temperature was performed to equilibrate the oxidized state $^3(\text{NDI1}^{+*} - [\text{Ru}^{\text{II}} - \text{OH}_2]^{2+} - \text{NDI2}^{+*})$ with the total spin $S = 1$.

According to the results of our simulations, one unpaired α electron (\uparrow) is observed to localize on NDI1 and one unpaired α electron (\uparrow) on NDI2 in the system (see inset (i) in Figure A5.4) when tracking the spin density along the free MD simulation after the photooxidation of the NDI dyes, which is in good agreement with the ground state of the oxidized complex $^3(\text{NDI1}^{+*} - [\text{Ru}^{\text{II}} - \text{OH}_2]^{2+} - \text{NDI2}^{+*})$ ($S = 1$). The shortening of $d(\text{H}_{\text{iii}} \leftarrow \text{O})$ and $d(\text{H}_{\text{iv}} \leftarrow \text{O})$ from 1.4 \AA to 1.1 \AA induces the electron transfer from the WOC to the oxidized NDI dyes (see Figure A5.4a) The $\text{O}_i - \text{H}_{\text{iii}}$ and $\text{O}_i - \text{H}_{\text{iv}}$ bonds (see inset (iii) in Figure A5.4 for the atomic

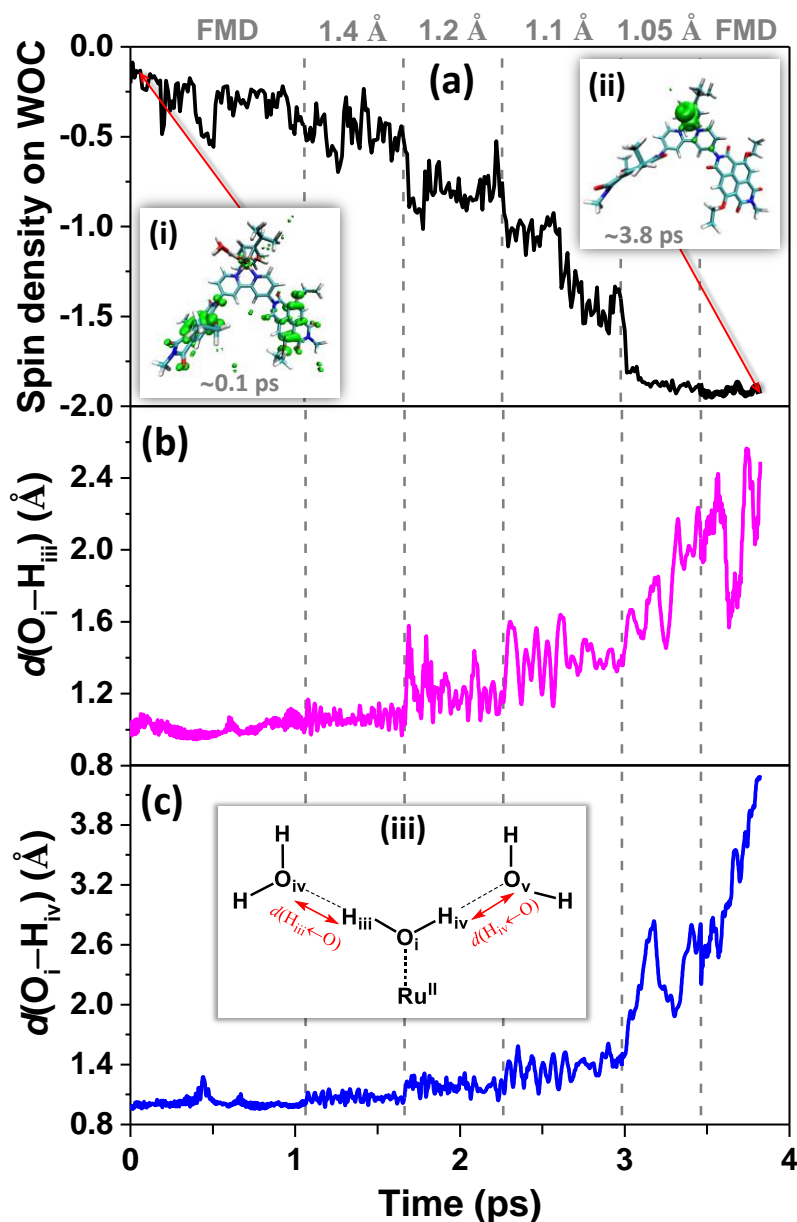


Figure A5.4. (a) Spin density integrated over the part of the simulation box including the WOC, time evolution of the geometrical parameters (b) $d(\text{O}_i\text{--H}_{\text{iii}})$ and (c) $d(\text{O}_i\text{--H}_{\text{iv}})$ along the free/constrained MD trajectories after the photooxidation of two NDI dyes. The inset (i) shows the spin density isosurface computed for a snapshot taken at ~0.1 ps, clearly indicating the intermediate $^3(\text{NDI1}^+[\text{Ru}^{\text{II}}\text{--OH}_2]^{2+}\text{--NDI2}^+)$ with one unpaired α electron (\uparrow in green) localized on each NDI dye. Inset (ii) shows the spin density isosurface computed for a snapshot taken at the end of the free MD (FMD) simulation, ~3.8 ps, clearly indicating the final intermediate $^3(\text{NDI1}[\text{Ru}^{\text{IV}}\text{=O}]^{2+}\text{--NDI2})$ with two unpaired α electrons (\uparrow in green) localized on the WOC. Inset (iii) shows the schematic structure of the first two water molecules along the hydrogen-bonding network coordinated to the ligand water molecule. For clarity, only the supramolecular complex and the attacking water molecules are shown explicitly. An integrated spin density value of -2 corresponds to two unpaired α electrons (\uparrow). The value of the constrained reaction coordinate $d(\text{H}_{\text{iii}}\text{--O})/d(\text{H}_{\text{iv}}\text{--O})$ in the MD simulations is noted in grey.

labeling) finally break when we further shorten the $H_{iii}\cdots O_{iv}$ and $H_{iv}\cdots O_v$ distances to 1.05 Å (see Figure A5.4b and A5.4c), which occurs almost at the same time as the accomplishment of the electron transfer (see Figure A5.4a). No back-transfer of either an electron or a proton is observed after the release of the constraints from the system following the constrained 1.05 Å simulation. This confirms the stability of the final product ${}^3(\text{NDI1} - [\text{Ru}^{\text{IV}}=\text{O}]^{2+} - \text{NDI2})$ ($S = 1$) with two unpaired α electrons localized on the WOC after the first and second catalytic PCET steps (see inset (ii) in Figure A5.4). All these results indicate that the first and second catalytic steps are able to proceed and complete at the same stage after the photooxidation of two NDI dyes.

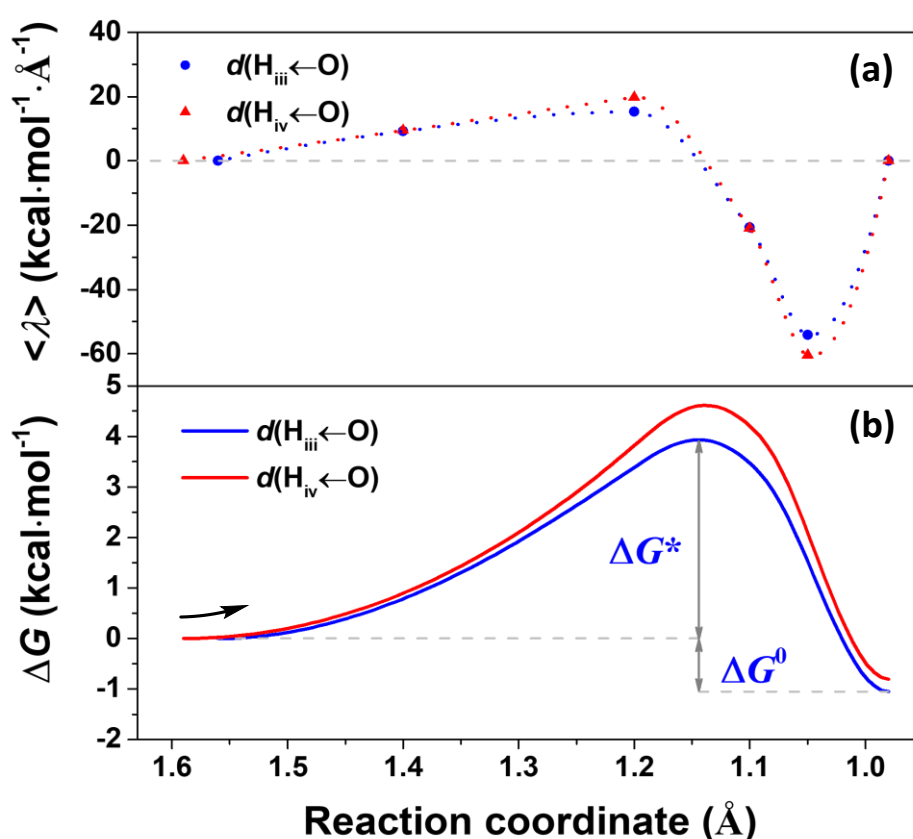


Figure A5.5. (a) Time-averaged constraint force represented by the Lagrangian multiplier $\langle \lambda \rangle$ computed for each constrained MD simulation as a function of the reaction coordinate $d(H_{iii} \leftarrow O)$ and $d(H_{iv} \leftarrow O)$ in the two-channel model. The mean force at the equilibrium distance $d(H_{iii} \leftarrow O) = 1.56$ Å/ $d(H_{iv} \leftarrow O) = 1.59$ Å and $d(H_{iii} \leftarrow O) = 0.98$ Å/ $d(H_{iv} \leftarrow O) = 0.98$ Å evaluated in the FMD simulations before and after the reaction, corresponding to the initial and final states along the reaction coordinates $d(H_{iii} \leftarrow O)$ and $d(H_{iv} \leftarrow O)$ respectively, have been assumed to be zero. The Akima splines (100 points) is used to interpolate the mean forces. (b) Free energy profile along the reaction coordinates $d(H_{iii} \leftarrow O)$ and $d(H_{iv} \leftarrow O)$ computed from thermodynamic integration.

Table A5.2. The calculated activation free energy barrier (ΔG^* in kcal mol⁻¹), reaction driving force (ΔG^o in kcal mol⁻¹), and the reaction rate (k in s⁻¹) corresponding to the reaction coordinates $d(\text{H}_{\text{iii}}\leftarrow\text{O})$ and $d(\text{H}_{\text{iv}}\leftarrow\text{O})$.

Reaction coordinate	ΔG^*	ΔG^o	k
$d(\text{H}_{\text{iii}}\leftarrow\text{O})$	3.9	-1.1	8.9×10^9
$d(\text{H}_{\text{iv}}\leftarrow\text{O})$	4.6	-0.8	2.8×10^9

Based on all the constrained MD simulations performed, the free energy profile along the reaction coordinates $d(\text{H}_{\text{iii}}\leftarrow\text{O})$ and $d(\text{H}_{\text{iv}}\leftarrow\text{O})$ of the oxidized complex $^3(\text{NDI1}^{+}\text{--}[\text{Ru}^{\text{II}}\text{--OH}_2]^{2+}\text{--NDI2}^{+})$ ($S = 1$) can be computed using the Bluemoon ensemble approach.¹³⁻¹⁵ The time-averaged forces associated with the applied constraints $d(\text{H}_{\text{iii}}\leftarrow\text{O})$ and $d(\text{H}_{\text{iv}}\leftarrow\text{O})$, the interpolation of the time-averaged mean forces used for this analysis, and the corresponding free energy profiles obtained via thermodynamic integration of the oxidized complex $^3(\text{NDI1}^{+}\text{--}[\text{Ru}^{\text{II}}\text{--OH}_2]^{2+}\text{--NDI2}^{+})$ ($S = 1$) are presented in Figure A5.5. Table A5.2 summarizes the key thermodynamic parameters extracted from the free energy profiles corresponding to the reaction coordinates $d(\text{H}_{\text{iii}}\leftarrow\text{O})$ and $d(\text{H}_{\text{iv}}\leftarrow\text{O})$ for the first half of the catalytic water oxidation cycle.

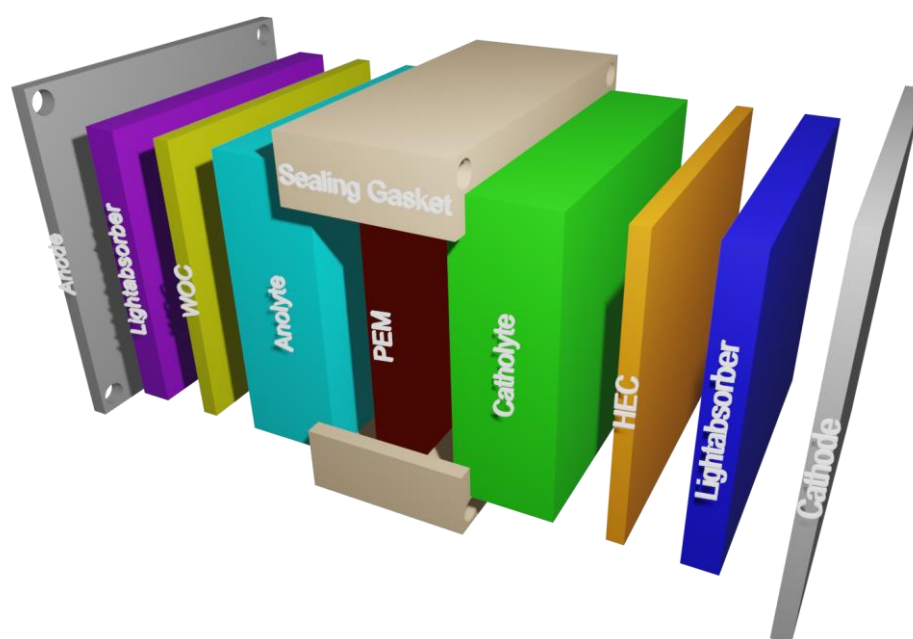
The obtained free energy profiles for these two PCET processes reported in Figure S5 show similar activation free energy barriers $\Delta G^* \approx 3.9$ kcal mol⁻¹ (0.17 eV) and $\Delta G^* \approx 4.6$ kcal mol⁻¹ (0.20 eV), corresponding to the reaction coordinates $d(\text{H}_{\text{iii}}\leftarrow\text{O})$ and $d(\text{H}_{\text{iv}}\leftarrow\text{O})$ respectively in the two-channel model (see Table A5.2). This is consistent with the comparable activation barriers of the first and second catalytic PCET steps in the one-channel model^{2, 16}. The maximum of the free energy profile corresponds to a reaction coordinate $d(\text{H}_{\text{iii}}\leftarrow\text{O})/d(\text{H}_{\text{iv}}\leftarrow\text{O})$ of 1.14/1.14 Å, suggesting an identified transition state with a smaller $\text{H}_{\text{iii}}\cdots\text{O}/\text{H}_{\text{iv}}\cdots\text{O}$ distance compared to that of the first/second catalytic PCET step in one-channel model. This concurrent event of the first two PCET processes is found to be fast and exothermic with the negative driving forces and high reaction rates $\Delta G^o \approx -1.1$ kcal mol⁻¹ (0.05 eV)/ $k \approx 8.9\times 10^9$ s⁻¹ and $\Delta G^o \approx -0.8$ kcal mol⁻¹ (0.03 eV)/ $k \approx 2.8\times 10^9$ s⁻¹ corresponding to the reaction coordinates $d(\text{H}_{\text{iii}}\leftarrow\text{O})$ and $d(\text{H}_{\text{iv}}\leftarrow\text{O})$, respectively, indicating that the selected NDI dyes are able to cooperatively drive this concurrent event in such a dye-WOC-dye system.

5.A.7. References

- [26] Swart, M.; Ehlers, A. W.; Lammertsma, K. *Mol. Phys.* **2004**, *102*, 2467-2474.
- [27] Monti, A.; de Ruiter, J. M.; de Groot, H. J. M.; Buda, F. *J. Phys. Chem. C* **2016**, *120*, 23074-23082.
- [28] Carvalho, A. T. P.; Swart, M. *J. Chem. Inf. Model.* **2014**, *54*, 613-620.
- [29] Groenhof, A. R.; Ehlers, A. W.; Lammertsma, K. *J. Am. Chem. Soc.* **2007**, *129*, 6204-6209.
- [30] Conradie, J.; Ghosh, A. *J. Chem. Theory and Comput.* **2007**, *3*, 689-702.
- [31] Vallés-Pardo, J. L.; Guijt, M. C.; Iannuzzi, M.; Joya, K. S.; de Groot, H. J. M.; Buda, F. *ChemPhysChem* **2012**, *13*, 140-146.
- [32] Klamt, A. *J. Phys. Chem.* **1995**, *99*, 2224-2235.
- [33] Klamt, A.; Jonas, V. *J. Chem. Phys.* **1996**, *105*, 9972-9981.
- [34] te Velde, G.; Bickelhaupt, F. M.; Baerends, E. J.; Fonseca Guerra, C.; van Gisbergen, S. J. A.; Snijders, J. G.; Ziegler, T. *J. Comput. Chem.* **2001**, *22*, 931-967.
- [35] ADF2017, SCM, Theoretical Chemistry, Vrije Universiteit, Amsterdam, The Netherlands, <http://www.scm.com>.
- [36] Accelrys Software Inc. Discovery Studio Modeling Environment, Accelrys Software Inc.: San Diego, 2012.
- [37] Brooks, B. R.; Brucoleri, R. E.; Olafson, B. D.; States, D. J.; Swaminathan, S.; Karplus, M. *J. Comput. Chem.* **1983**, *4*, 187-217.
- [38] Ciccotti, G.; Ferrario, M. *Mol. Simul.* **2004**, *30*, 787-793.
- [39] Ensing, B.; Meijer, E. J.; Blöchl, P. E.; Baerends, E. J. *J. Phys. Chem. A* **2001**, *105*, 3300-3310.
- [40] Costanzo, F.; Della Valle, R. G. *J. Phys. Chem. B* **2008**, *112*, 12783-12789.
- [41] Shao, Y.; de Ruiter, J. M.; de Groot, H. J. M.; Buda, F. *J. Phys. Chem. C* **2019**, *123*, 21403-21414.
- [42] Otter, W. K. d.; Briels, W. J. *J. Chem. Phys.* **1998**, *109*, 4139-4146.
- [43] Sprik, M.; Ciccotti, G. *J. Chem. Phys.* **1998**, *109*, 7737-7744.
- [44] Bernasconi, L.; Baerends, E. J.; Sprik, M. *J. Phys. Chem. B* **2006**, *110*, 11444-11453.
- [45] Bernasconi, L.; Kazaryan, A.; Belanzoni, P.; Baerends, E. J. *ACS Catal.* **2017**, *7*, 4018-4025.
- [46] Humphrey, W.; Dalke, A.; Schulten, K. *J. Mol. Graphics* **1996**, *14*, 33-38.
- [47] VMD - Visual Molecular Dynamics. *Theoretical Chemistry and Computational Biophysics Group*, University Of Illinois: Urbana, 2016.
- [48] Eyring, H. *J. Chem. Phys.* **1935**, *3*, 107-115.
- [49] Laidler, K. J.; King, M. C. *J. Phys. Chem.* **1983**, *87*, 2657-2664.
- [50] Pollak, E.; Talkner, P. *Chaos* **2005**, *15*, 026116.
- [51] CPMD, <http://www.cpmc.org>, Copyright IBM Corp., 1990-2019; Copyright MPI für Festkörperforschung Stuttgart, 1997-2001.

CHAPTER 6

Conclusions and Outlook



6

6.1. Conclusions

As a virtually inexhaustible source, solar energy plays a major role in future global energy scenarios. Solar-driven water splitting via DS-PEC devices is a scalable, affordable and sustainable technology of great potential for direct conversion of solar energy into storable chemical fuels to produce clean, cost-efficient and environmentally friendly H_2 or CO_2 -derived fuels and thus to contribute to the transformation of a sustainable society from the blueprint to reality. However, to improve the overall yield of the photocatalytic water splitting is a challenge. It is limited by the water oxidation half-reaction, which consists of four catalytic PCET steps. In particular the third PCET step involving the O–O bond formation is difficult, which impedes the development towards commercialization and large-scale terrestrial implementation of DS-PEC devices.

Although rate enhancement has been experimentally realized in catalytic water oxidation to a limited extent via the engineering of novel WOCs, as well as fine-tuning of the solvent environment, the intrinsic mechanisms at the molecular level along the reaction coordinate are obscured in ensemble measurements, in particular for systems driven by WOC–dye supramolecular complexes. To further facilitate the reaction, it is necessary to elucidate beforehand key factors determining the rate of predominant catalytic processes. Computational studies serve as a very useful tool complementary to experiment, play an important role in providing an accurate and detailed microscopic description of the nuclear and electronic dynamics for the catalytic processes along the reaction coordinate, can predict the free energy profile from reactant to product, and provide an in-depth understanding of the intrinsic catalytic mechanisms.

The explicit aim of this thesis is to provide an in-depth understanding of the catalytic mechanisms for the water oxidation half-reaction in WOC–dye supramolecular complexes and to find rational strategies to facilitate the involved catalytic reactions. The computational methods used to reach this goal are DFT calculations and DFT-based molecular dynamics (AIMD) simulations. This thesis is divided into three parts: (i) **Chapter 2** elucidates the catalytic mechanism along the whole photocatalytic water splitting cycle by a Ru-based WOC–dye supramolecular complex; (ii) **Chapters 3** and **4** provide flexible strategies for facilitating the photocatalytic water oxidation, specifically the rate-limiting third catalytic step involving the O–O bond formation; (iii) **Chapter 5** proposes a Ru-

based dye–WOC–dye supramolecular complex with two separate electron-transfer channels for the photoanode of DS-PEC devices and explores the proposed photocatalytic water splitting cycle. More specifically, the rate enhancement in **Chapter 3** is achieved by tuning the solvent environment, whereas in **Chapter 4** by ligand modification on the catalyst component.

An ideal dye should meet the stringent requirements of absorbing a significant fraction of the visible spectrum and having at the same time an appropriate redox potential to drive the whole catalytic water oxidation cycle when coupled with an efficient WOC. In **Chapter 2**, the whole visible light-driven photocatalytic water splitting cycle performed by the WOC–dye supramolecular complex $[\text{Ru}^{\text{II}}(\text{H}_2\text{O})]^{2+}$ –NDI in explicit water solvent is systematically explored by means of CPMD simulations at room temperature, in which we consider all possible spin alignments between unpaired electrons on the WOC and on the oxidized NDI^+ . It is demonstrated that the selected NDI dye is a promising dye sensitizer to integrate in a DS-PEC device since it is able to sufficiently drive the whole catalytic cycle after photooxidation when properly coupled to the Ru-based catalyst. The predicted activation free energy barriers indicate that the first three catalytic PCET steps are all exothermic and the fourth catalytic step is barrier-less after photooxidation of the NDI dye. The third catalytic step involving the O–O bond formation is confirmed to be the rate-limiting step because of its considerably high activation energy barrier. Furthermore, the coupled electron and proton dynamics together with the solvent rearrangement during the cycle are followed to elucidate the catalytic mechanism of the four consecutive catalytic PCET steps. This analysis provides strong evidence for the significant role of spin alignment and solvent rearrangement in facilitating the catalytic PCET processes. The importance of solvent environmental tuning in the acceleration of the third catalytic PCET process is investigated in detail in **Chapter 3**. The results presented in **Chapter 2** expand the current understanding of the photocatalytic water oxidation mechanism and provide guidelines for the optimization of high-performance DS-PEC devices.

Since the O–O bond formation process via water nucleophilic attack (WNA) has emerged in **Chapter 2**, in line with previous literature, as the thermodynamic and kinetic bottleneck in photocatalytic water oxidation, it is of fundamental significance and yet challenging to find strategies to facilitate this reaction.

Motivated by the crucial role of the solvent environment emphasized in **Chapter 2**, one additional charged OH^- group is introduced as a proton acceptor in the hydration shell near the catalytic active site to demonstrate the effect of varying charge and proton chemical potential in **Chapter 3**. In this way it is possible to resolve how and to what extent the O–O bond formation process is facilitated by tailoring the solvent environment. Since the same WOC–dye supramolecular complex considered in **Chapter 2** and **Chapter 3**, the results obtained are quantitatively comparable. The explicit solvent and dynamic description obtained with the adiabatic DFT-MD simulation approach reveals that the presence of a proton acceptor (OH^-) induces a cooperative event proceeding via a concerted PCET mechanism, dramatically lowers the activation free energy barrier, and thus significantly accelerates the O–O bond formation. The mechanistic insight into facilitated O–O bond formation process provides a strategy for the improvement of the performance of DS-PEC devices by straightforward tuning of the environment.

Since coherence in the electronic and nuclear motion has been suggested to play a role in electron transfer processes in both natural and artificial systems, which appears indistinctly in **Chapter 2** as well, it is essential to understand if and how resonant coupling can accelerate the rate-limiting O–O bond formation process in catalytic water oxidation. In **Chapter 4**, structural modifications in a series of WOC–dye supramolecular complexes functionalized with different alkyl groups on the catalyst component are found to modulate the value of the dihedral angle at the WOC–dye linkage. This affects the electronic structure of the supramolecular complexes, the characteristic frequencies associated with the electron transfer dynamics, and the torsional motion around this link. The frequency tuning leads to a resonance condition that increases the coupling between electronic and nuclear motions and facilitates the ET step from the WOC to the oxidized dye in the region of the crossing of reactant and product states. The computed free energy profiles for this PCET reaction show a considerable decrease in activation energy and increase in the driving force. We expect that the in-depth insight into the acceleration of this specific catalytic water oxidation step provides a general and rational engineering approach for the improvement of the performance of DS-PEC devices from a structural design perspective, which can also be achieved by modifying other ligands around the connecting region or

replacing the linker between WOC and dye.

To make the utmost of solar energy, a two-channel model for ET in a dye–WOC–dye supramolecular complex for photocatalytic water splitting is proposed in **Chapter 5**, in which a Ru-based water oxidation catalyst (WOC) is covalently bounded to two NDI dyes. Compared to the one-channel model described in **Chapter 2**, the introduction of the second light-harvesting dye in the dye–WOC–dye complex enables two parallel electron-transfer channels, which theoretically allows for concurrent ET events from the WOC to the two separate oxidized dyes. The realistic and dynamical description of the proposed photocatalytic cycle of the two-channel model obtained with constrained AIMD approach demonstrates that the third and fourth catalytic steps can proceed consecutively without stable intermediates in between, as well as the coupled first and second catalytic steps, leading to a five-step catalytic cycle with three intermediates and two doubly oxidized states, whereas the one-channel model presented in **Chapter 2** follows a nine-step cycle. Two intermediates of the WOC–dye complex in the one-channel model become transients in the two-channel model. In addition, intermediates, oxidized states, and transients for the combined first half and second half of the catalytic cycle are all exhibiting a spin multiplicity of 3, leading to triplet oxygen to be released without the need for *e.g.* intersystem crossing between configurations with different overall spin multiplicity. Thus, electronic spin appears a conserved quantity along the reaction coordinate of the water oxidation process. The in-depth insight into the proposed photocatalytic cycle of the investigated two-channel model provides a strategy for the improvement of the overall efficiency of DS-PEC devices from the perspective of reaction intermediate reassignment, sequence rearrangement and conservation of spin multiplicity.

6.2. Outlook

Thanks to the predictive power of CPMD simulations, the underlying reaction mechanisms of the photocatalytic water oxidation processes have been well elucidated in this thesis, especially for such a large system containing a WOC–dye supramolecular complex and explicit description of the water solvent. Although strategies for facilitating the O–O bond formation in catalytic water oxidation have been provided in **Chapters 3** and **4**, a considerable gap exists between theoretical/experimental proofs and large-scale implementation. Efforts in the development of novel DS-PEC devices will continue in the future with the main focus remaining on the understanding of factors limiting the overall efficiency of solar-to-fuel conversion and the search of rational strategies for accelerating the photocatalytic water oxidation. Luckily, computational techniques will act as a tempting, powerful but inexpensive tool on this long discovery journey from empirical to informed approaches.¹

To achieve the final goal of near-unity yield in photochemical water oxidation, considerable work needs to be done by forthcoming computational studies, part of which is likely to go in several potential directions of great interest and importance:

- I. Charge recombination from the semiconductor into the oxidized dye is a main factor limiting the quantum yield of the whole photocatalytic water splitting process,²⁻³ which is not covered in this thesis. It might be interesting to include the catalytic water oxidation process and at the same time the electron injection in one MD simulation to address the competition between the ET from the WOC to the oxidized dye and the charge recombination from the semiconductor to the oxidized dye, although it is challenging due to the different time scales of the processes occurring upon photoexcitation.⁴
- II. In **Chapter 3**, we specifically use the OH[−] group as a conceptual example, but this can be easily replaced by other proton acceptors with different proton charge ratio, such as OAc[−], HPO₄^{2−}, PO₄^{3−}.⁵⁻⁷ The ones that would be less detrimental to the WOC stability are more desirable. In addition, assembly strategies similar to a solid-state water electrolysis cell with alkaline membranes might be interesting to be employed as a design strategy for a DS-PEC architecture, in which the OH[−] ions are transported to the catalyst layer

through the anion exchange membrane and act as proton-withdrawing groups to facilitate the O–O bond formation.⁸

- III. Recently, we have found convincing evidence that Nonadiabatic Conversion by Adiabatic Passage involving resonant coupling of reactant and product states is important for energy transfer and separation of charges,^{9–11} which is also corroborated by the results presented in **Chapter 4**. To further unveil the nonadiabatic effects that can accelerate the PCET process in WOC–dye supramolecular complexes in a more direct way, it might be interesting to calculate the nonadiabatic coupling between reactant and product electronic states with existing approaches¹² or methods to be developed to enable quantitative evaluation.
- IV. For an integrated solar-driven DS-PEC device, the overall solar-to-fuel conversion efficiency depends not only on the material properties of all the individual components but also on the device design. Multiphysics simulation software can represent a powerful tool for the prediction of device efficiencies, the operating conditions, and the evaluation of novel device architectures and concepts.^{13–14} A combination of microscopic and macroscopic modelling and simulation might be interesting for the design and improvement of DS-PEC devices, in which DFT and AIMD calculations provide estimates of crucial parameters to be used as input in macroscopic modeling. In these operating conditions one could understand how properties at the molecular level can determine the overall performance of integrated systems at the device level.

6.3. References

- [1] Schilling, M.; Cunha, R. A.; Luber, S. *ACS Catal.* **2020**, *10*, 7657-7667.
- [2] Gish, M. K.; Lapides, A. M.; Brennaman, M. K.; Templeton, J. L.; Meyer, T. J.; Papanikolas, J. M. *J. Phys. Chem. Lett.* **2016**, *7*, 5297-5301.
- [3] Chou, H.-H.; Yang, C.-H.; Lin, J. T. s.; Hsu, C.-P. *J. Phys. Chem. C* **2017**, *121*, 983-992.
- [4] Monti, A.; de Ruiter, J. M.; de Groot, H. J. M.; Buda, F. *J. Phys. Chem. C* **2016**, *120*, 23074-23082.
- [5] Stewart, D. J.; Concepcion, J. J.; Brennaman, M. K.; Binstead, R. A.; Meyer, T. J. *Proc. Natl. Acad. Sci.* **2013**, *110*, 876-880.
- [6] Coggins, M. K.; Zhang, M.-T.; Chen, Z.; Song, N.; Meyer, T. J. *Angew. Chem. Int. Ed.* **2014**, *53*, 12226-12230.
- [7] Song, N.; Concepcion, J. J.; Binstead, R. A.; Rudd, J. A.; Vannucci, A. K.; Dares, C. J.; Coggins, M. K.; Meyer, T. J. *Proc. Natl. Acad. Sci.* **2015**, *112*, 4935-4940.
- [8] Leng, Y.; Chen, G.; Mendoza, A. J.; Tighe, T. B.; Hickner, M. A.; Wang, C.-Y. *J. Am. Chem. Soc.* **2012**, *134*, 9054-9057.
- [9] Monti, A.; Negre, C. F. A.; Batista, V. S.; Rego, L. G. C.; de Groot, H. J. M.; Buda, F. *J. Phys. Chem. Lett.* **2015**, *6*, 2393-2398.
- [10] Menzel, J. P.; de Groot, H. J. M.; Buda, F. *J. Phys. Chem. Lett.* **2019**, *10*, 6504-6511.
- [11] Li, X.; Buda, F.; de Groot, H. J. M.; Sevink, G. J. A. *J. Phys. Chem. B* **2020**, *124*, 4026-4035.
- [12] Faraji, S.; Matsika, S.; Krylov, A. I. *J. Chem. Phys.* **2018**, *148*, 044103.
- [13] Haussener, S.; Xiang, C.; Spurgeon, J. M.; Ardo, S.; Lewis, N. S.; Weber, A. Z. *Energy Environ. Sci.* **2012**, *5*, 9922-9935.
- [14] Xiang, C.; Weber, A. Z.; Ardo, S.; Berger, A.; Chen, Y.; Coridan, R.; Fountaine, K. T.; Haussener, S.; Hu, S.; Liu, R.; Lewis, N. S.; Modestino, M. A.; Shaner, M. M.; Singh, M. R.; Stevens, J. C.; Sun, K.; Walczak, K. *Angew. Chem. Int. Ed.* **2016**, *55*, 12974-12988.

Summary

By utilizing freely available sunlight, DS-PEC devices split water into molecular oxygen, protons and electrons via four consecutive PCET steps at the photoanode, which combines sensitizers for visible light absorption and efficient WOCs for catalytic water splitting. The photocatalytic four-photon water oxidation half-reaction is a chemical challenge and often limit over the entire water splitting cycle. Better understanding of the catalytic mechanisms at the molecular level and in-depth exploration of the factors affecting the PCET processes are urgently needed at present in the field of artificial photosynthesis and will provide guidelines for engineering and optimization of high-performance DS-PEC devices for solar-driven water splitting. Computational simulations provide a powerful technique for the collection of convincing microscopic chemical engineering paradigms ahead of their experimental realization.

The whole photocatalytic water splitting cycle performed by a WOC–dye supramolecular complex in explicit water solvent is systematically explored in **Chapter 2**. The results indicate that the selected NDI dye is able to drive the whole catalytic cycle after photooxidation when properly coupled to the Ru-based catalyst. The first three catalytic PCET steps are all exothermic and the fourth catalytic step is barrier-less. The third catalytic step involving the O–O bond formation is confirmed to be the rate-limiting step because of the high activation energy barrier. For this step antiparallel spin alignment of unpaired electrons on the WOC and dye appears essential for the reaction to proceed well. The microscopic details provide strong evidence for the significant role of the rearrangement of solvent water molecules in facilitating the catalytic PCET processes. The in-depth insight in the photocatalytic water oxidation mechanism provides guidelines for the design and optimization of efficient photoanodes for DS-PEC devices.

Considering that the O–O bond formation process represents a thermodynamic and kinetic bottleneck in photocatalytic water oxidation, it is essential to find

strategies to lower the activation free energy barrier of the third catalytic step. **Chapter 3** elucidates how and to what extent the O–O bond formation process can be facilitated by tuning the solvent environment. The introduction of an additional OH[−] group as a proton acceptor in the hydration shell near the active site induces a cooperative event proceeding via a concerted PCET mechanism, which dramatically lowers the activation free energy barrier, and thus significantly accelerates the O–O bond formation. The mechanistic insight provides a flexible and simple strategy for facilitating the photocatalytic water oxidation and for improving the efficiency of DS-PEC devices.

To understand if and how nonadiabatic factors accelerate the PCET rate of the O–O bond formation, a series of WOC–dye supramolecular complexes functionalized with different alkyl groups on the catalyst component are investigated in **Chapter 4**. The structural modifications modulate not only the value of the dihedral angle at the WOC–dye linkage, but also the electronic structure of the supramolecular complexes and the characteristic frequencies associated with the electron transfer dynamics and the torsional motion around this link. These structural modifications then lead to tunable thermodynamic driving forces, PCET rates, and vibronic coupling with specific resonant torsional modes. Such resonant coupling between electronic and nuclear motions turns out to facilitate the crossing of catalytic barriers in PCET reactions by enabling semiclassical coherent conversion of a reactant into a product. These results provide a general and rational approach on how to engineer efficient WOC–dye supramolecular complexes for high-performance DS-PEC devices from a structural design perspective.

In **Chapter 5**, the photocatalytic water oxidation process driven by a dye–WOC–dye supramolecular complex in explicit water solvent is investigated. The introduction of the second NDI dye provides an extra electron-transfer channel, *i.e.* a two-channel model for ET, allowing for the concurrent transfer of two electrons in different directions from the WOC to the two oxidized dyes separately. The third and fourth catalytic steps are observed to proceed consecutively without stable intermediates in between, leading to a five-step catalytic cycle. The total spin $S = 1$ is conserved during the catalytic process, and the system proceeds from the Ru=O intermediate to the final Ru–O₂ intermediate with a triplet molecular O₂ ligand that is eventually released into the environment.

Samenvatting

Door gebruik te maken van het beschikbare zonlicht is een DS-PEC apparaat in staat om water te splitsen in moleculaire zuurstof, protonen en elektronen via vier opeenvolgende PCET stappen. Dit gebeurt aan de fotoanode, die een sensibilisator bevat voor de absorptie van zichtbaar licht, gekoppeld aan een efficiënte WOC voor katalytische splitsing van water. De ontwikkeling van de fotokatalytische water oxidatie half-reactie met vier fotonen is een chemische uitdaging en is in het algemeen het meest lastige deel van de water splitsing cyclus. Een beter begrip van de katalytische mechanismen op het moleculaire niveau, een diepgaande verkenning van de factoren die de PCET processen beïnvloeden, en het identificeren van richtlijnen voor het ontwerpen en optimaliseren van hoog-functionerende DS-PEC apparaten voor zonlicht-gedreven water splitsing met hoge chemische opbrengst zijn dringend gewenst voor de ontwikkeling van de artificiële fotosynthese. Computer simulaties bieden een krachtige techniek voor het identificeren van nieuwe, overtuigende paradigma's voor ontwerp op microscopisch chemisch niveau en lopen daarbij ver voor op wat experimenteel gerealiseerd kan worden.

In **hoofdstuk 2** wordt de volledige fotokatalytische watersplitsing cyclus systematisch onderzocht, door een supramoleculair WOC-kleurstof complex expliciet in water te modelleren. Het resultaat geeft aan dat als de geselecteerde NDI op de juiste manier covalent aan de Ruthenium katalysator gebonden is, deze in staat is om de volledige katalytische cyclus stapsgewijs voort te drijven met foto-oxidatie. De simulaties bevestigen dat de derde katalytische stap, waarbij de O-O band gevormd wordt, de kinetisch limiterende stap is als gevolg van de hoge activatie energie. Voor deze stap lijkt anti-parallelle oriëntatie van de spins van de ongepaarde elektronen op de WOC en de kleurstof essentieel te zijn voor de goede voortgang van de reactie. De microscopische simulaties leveren een sterk bewijs voor de belangrijke rol die de herschikking van watermoleculen, die deel van het oplosmiddel uitmaken, speelt in het faciliteren van de katalytische PCET

processen. Het diepgaande inzicht in het fotokatalytische water oxidatie mechanisme geeft richtlijnen voor het ontwerp en de optimalisatie van efficiënte foto-anodes voor DS-PEC apparaten.

Omdat de vorming van de O–O band de belangrijkste thermodynamische en kinetische bottleneck is in fotokatalytische water oxidatie, is het essentieel om nieuwe strategieën te vinden om de activatie energy barrière van de derde katalytische stap omlaag te brengen. **Hoofdstuk 3** verheldert hoe en in hoeverre de vorming van de O–O band gefaciliteerd kan worden door de oplosmiddel omgeving aan te passen. De introductie van een extra OH[−] groep als proton-acceptor nabij de actieve kern induceert een coöperatief proces via een gecoördineerd PCET mechanisme, waarbij de energie barrière sterk verlaagd wordt, wat tot een versnelde O–O band formatie leidt. Het mechanistische inzicht geeft een eenvoudige en flexibele strategie voor het faciliteren van fotokatalytische water oxidatie en voor het verhogen van de efficiency van DS-PEC apparaten.

Om te begrijpen of en hoe niet-adiabatische factoren de PCET vorming van de O–O binding kunnen versnellen, wordt in **hoofdstuk 4** een serie van WOC–kleurstof supramoleculaire complexen gefunctionaliseerd met verschillende alkylgroepen op de katalysator componenten. De structurele aanpassingen moduleren niet alleen de waarde van de tweevlakshoek bij de link van het WOC–kleurstof complex, maar hebben ook een significante invloed op de elektronische structuur van de supramoleculaire complexen en op de karakteristieke frequenties geassocieerd met de elektronische overgangsdynamica en de torsie bewegingen rond deze link. De structurele aanpassingen leiden vervolgens tot verstelbare thermodynamische drijvingskrachten, PCET snelheden, en vibronische koppeling met specifieke resonantie torsie modes. Een dergelijke resonante koppeling tussen elektronische en nucleaire bewegingen blijkt het kruisen van energetische barrières in de PCET reactie te faciliteren door semiklassieke coherente conversie van een reactant in een product mogelijk te maken. Deze resultaten geven een algemene en rationele benadering voor het ontwerpen van een efficiënt WOC–kleurstof supramoleculair complex voor hoog-rendement DS-PEC systemen vanuit het perspectief van het ontwerpen van chemische structuren.

In **hoofdstuk 5** wordt het fotokatalytische water oxidatie proces gedreven door een kleurstof–WOC–kleurstof supramoleculair complex in een expliciet waterig milieu onderzocht. De introductie van een tweede NDI kleurstof molecuul biedt een extra elektron-overdrachtskanaal, oftewel een twee-kanaal model voor ET, waarbij de gelijktijdige overdracht van twee elektronen in twee verschillende richtingen van de WOC naar de twee geoxideerde kleurstoffen individueel mag plaatsvinden. De derde en vierde katalytische stappen vinden hier gelijktijdig plaats zonder stabiele tussenvormen, wat leidt tot een vijf stappen katalytische cyclus met drie intermediären en twee overgangstoestanden. De totale spin wordt opgebouwd naar $S = 1$, gedurende de eerste fase en wordt geconserveerd gedurende de tweede fase van het katalytische proces, waarbij het systeem overgaat van een Ru=O intermediair naar een uiteindelijke Ru–O₂ intermediair met een triplet moleculair zuurstof ligand dat tenslotte in de omgeving vrij kan komen.

List of Publications

Main Publications:

- **Yang Shao**, Jessica M. de Ruiter, Huub J.M. de Groot, and Francesco Buda, Photocatalytic Water Splitting Cycle in a Dye–Catalyst Supramolecular Complex: *Ab Initio* Molecular Dynamics Simulations, *J. Phys. Chem. C*, **2019**, 123, 21403–21414. DOI: 10.1021/acs.jpcc.9b06401 (**Chapter 2**)
- **Yang Shao**, Huub J.M. de Groot, and Francesco Buda, Proton Acceptor near the Active Site Lowers Dramatically the O–O Bond Formation Energy Barrier in Photocatalytic Water Splitting, *J. Phys. Chem. Lett.*, **2019**, 10, 7690–7697. DOI: 10.1021/acs.jpclett.9b02914 (**Chapter 3**)
- **Yang Shao**, Huub J.M. de Groot, and Francesco Buda, Tuning the Proton-Coupled Electron-Transfer Rate by Ligand Modification in Catalyst–Dye Supramolecular Complexes for Photocatalytic Water Splitting, *ChemSusChem*, **2021**, 14, 479–486. (Featured as VIP paper)
DOI: 10.1002/cssc.202001863 (**Chapter 4**)
- **Yang Shao**, Huub J.M. de Groot, and Francesco Buda, Two-Channel Model for Electron Transfer in a Dye–Catalyst–Dye Supramolecular Complex, **2021**, manuscript to be submitted. (**Chapter 5**)

Other publications not included in this thesis:

- Xuequan Zhou, Maria Mytiliniou, Jonathan Hilgendorf, Ye Zeng, Panagiota Papadopoulou, **Yang Shao**, Erik Bos, Maxime A. Siegler, Francesco Buda, Alexander Kros, Roman I. Koning, Doris Heinrich, and Sylvestre Bonnet, Intracellular dynamic assembly of deep-red-emitting supramolecular nanostructures based on Pt...Pt metallophilic interaction, **2021**, submitted.
- Xuequan Zhou, Wen Sun, Peiyuan Wang, Vadde Ramu, Suhua Jiang, Selda Abyar, Panagiota Papadopoulou, **Yang Shao**, Maxime A Siegler, Francesco Buda, Alexander Kros, Sylvestre Bonnet, Self-assembling Cyclopalladated Photosensitizers for Photodynamic Therapy: Tumor Accumulation and Anti-tumor Activity in a Skin Melanoma Xenograft, **2021**, manuscript in preparation.
- Xiaoqing Lu,[†] **Yang Shao**,[†] Ke Li, Zigang Zhao, Shuxian Wei, and Wenyue Guo, Role of Functionalized Acceptors in Heteroleptic Bipyridyl Cu(I) Complexes for Dye-Sensitized Solar Cells, *Electron. Mater. Lett.*, **2016**, 12, 589–595. DOI: 10.1007/s13391-016-6035-z. ([†]Both authors contributed equally.)

- Shuxian Wei, **Yang Shao**, Xiaofan Shi, Xiaoqing Lu, Ke Li, Zigang Zhao, Chen Guo, Houyu Zhu, and Wenyue Guo, Heteroleptic Cu (I) Complexes Integrating Functionalized Chromophores for Dye-Sensitized Solar Cells: An In-depth Analysis of Electronic Structure, Spectrum, Excitation, and Intramolecular Electron Transfer. *Org. Electron.*, **2016**, 29, 142-150. DOI: 10.1016/j.orgel.2015.12.004.
- Shuxian Wei, Ke Li, Xiaoqing Lu, Zigang Zhao, **Yang Shao**, Yong Dang, Shaoren Li, and Wenyue Guo, Theoretical Insight into Electronic Structure and Optoelectronic Properties of Heteroleptic Cu(I)-based Complexes for Dye-Sensitized Solar Cells. *Mater. Chem. Phys.*, **2016**, 173, 139-145. DOI: 10.1016/j.matchemphys.2016.01.049.
- **Yang Shao**, Xiaoqing Lu, Ke Li, Zigang Zhao, Xiaofan Shi, Dongliang Jin, Houyu Zhu, Guangwu Yang, and Wenyue Guo, Theoretical Insight into Photo-induced Intramolecular Electron Transfer in Heterodinuclear Ru(II)-Co(III) complexes, *Mater. Chem. Phys.*, **2015**, 162, 6-10. DOI: 10.1016/j.matchemphys.2015.05.041.
- Xiaoqing Lu,[†] **Yang Shao**,[†] Shuxian Wei, Zigang Zhao, Ke Li, Chen Guo, Weili Wang, Mingmin Zhang, and Wenyue Guo, Effect of the Functionalized π -bridge on Porphyrin Sensitizers for Dye-Sensitized Solar Cells: an In-depth Analysis of Electronic structure, Spectrum, Excitation, and Intramolecular Electron Transfer. *J. Mater. Chem. C*, **2015**, 3, 10129-10139. DOI: 10.1039/C5TC02286J. ([†]Both authors contributed equally.)
- Kunpeng Guo, Zhixiang Gao, Jun Cheng, **Yang Shao**, Xiaoqing Lu, and Hua Wang, Linear Thiophene-containing π -conjugated Aldehydes with Aggregation-induced Emission for Building Solid Red Luminophors. *Dyes Pigm.*, **2015**, 115, 166-171. DOI: 10.1016/j.dyepig.2014.12.017.
- Shuxian Wei, Xiaofan Shi, Xiaoqing Lu, **Yang Shao**, Dongliang Jin, Zhigang Deng, Zigang Zhao, Ke Li, and Wenyue Guo, Cu(I)-Based Sensitizers Featuring 6,6'-Dimethyl-4,4'-Dicarboxylate-2,2'-Bipyridine with Functionalized 2,9-Dimethyl-1,10-Phenanthroline Ligands: A Structural, Electronic and Spectral Investigation. *Sci. Adv. Mater.*, **2015**, 7, 1361-1367. DOI: 10.1166/sam.2015.2052.
- Xiaoqing Lu, Weili Wang, Shuxian Wei, Chen Guo, **Yang Shao**, Mingmin Zhang, Zhigang Deng, Houyu Zhu, and Wenyue Guo, Initial Reduction of CO₂ on Perfect and O-defective CeO₂(111) Surfaces: Towards CO or COOH? *RSC adv.*, **2015**, 5, 97528-97535. DOI: 10.1039/C5RA17825H.
- Xiaofan Shi, Xiaoqing Lu, **Yang Shao**, Shuxian Wei, Qing Zhu, Dongliang Jin, Zhigang Deng, and Wenyue Guo, Theoretical Investigation on Novel Porphyrin Dyes with Functionalized Bridge and Donor Groups for Dye-Sensitized Solar Cells. *Sci. Adv. Mater.*, **2014**, 6, 2595-2602. DOI: 10.1166/sam.2014.2007.
- Shuxian Wei, Xiaoqing Lu, Xiaofan Shi, Zhigang Deng, **Yang Shao**, Lianming Zhao, Wenyue Guo, and Chi-Man Lawrence Wu, Theoretical Insight into Organic Dyes Incorporating Triphenylamine-Based Donors and Binary-Conjugated Bridges for Dye-Sensitized Solar Cells. *Int. J. Photoenergy*, **2014**, 2014, 280196. DOI: 10.1155/2014/280196.
- Dongliang Jin, Xiaoqing Lu, Mingmin Zhang, Shuxian Wei, Qing Zhu, Xiaofan Shi, **Yang Shao**, Weili Wang, and Wenyue Guo, The Adsorption Behaviour of CH₄ on Microporous Carbons: Effects of Surface Heterogeneity. *Phys. Chem. Chem. Phys.*, **2014**, 16, 11037-11046. DOI: 10.1039/C3CP55107E.

Curriculum Vitae

Yang Shao was born on March 10th, 1990 in the north-central part of Shandong province, China. He grew up in a county-level city – Shouguang, the “home of vegetables” in China, located on an alluvial plain drained by the Mihe River that flows down from Qingzhou city. It stretches to the Bohai Sea, where you can conquer a mountain in one step, since Jing Mountain is the only mountain in Shouguang and at the same time the smallest mountain in China. It measures at just 60 cm high and 70 cm wide, and yet is not classified as a rock.

In 2009, he went to Dongying city, which is in the same Shandong province, and enrolled as a bachelor student at China University of Petroleum to study materials physics. In 2011, he moved to the new university campus in Qingdao, where he developed an interest in solar cells and obtained his bachelor degree in 2013. Successively, he joined the New Energy Materials Group as a recommended candidate to perform computational research under the supervision of Prof. dr. Wen Yue Guo and Prof. dr. Xiaoqing Lu (currently the leader of New Energy and Environmental Science Group), where he started his master research on dye-sensitized solar cells by means of DFT calculations. In 2016, he obtained his master degree in Materials Engineering and was rated as “Outstanding Graduate Student of Shandong Province”.

In September 2016, thanks to the funding from Chinese Scholarship Council (CSC), he moved to Leiden, the Netherlands, and started his PhD project under the supervision of Dr. Francesco Buda and Prof. dr. Huub de Groot at Leiden Institute of Chemistry, Leiden University. During his PhD research in the field of artificial photosynthetic water splitting, he extended his research skills to DFT-based *ab initio* molecular and finite element simulations. He also wrote codes with Python to assist in data analysis. In the time of his PhD he gave poster presentations at the Holland Research School of Molecular Chemistry (HRSMC) Annual Symposium (UvA, 2017), Reedijk Symposium (LU, 2018), Royal Dutch Chemical Association (KNCV) Division Computational & Theoretical Chemistry (VU, 2019). In addition, part of his work has been selected to be orally presented at the International Union of Pure and Applied Chemistry (IUPAC) (Paris, 2019) and Chemistry as Innovating Science (CHAINS) (Eindhoven, 2019).

Acknowledgments

It has been a hard time for everyone since the breakout of Coronavirus worldwide, almost one year now, which makes everything difficult and complicated. Luckily, at the end of 2020, I am reaching the destination of my PhD journey. Here, I would like to express my sincere gratitude to everyone who has helped and supported me in the past four years.

First and foremost, I would like to thank my promotor Prof. dr. Huub de Groot and my supervisor Dr. Francesco Buda. Franco, I will always be grateful to you for having been an incredible supervisor and mentor. Thank you for always being there with your kindness and thoughtfulness and for supporting and guiding me with your expertise, wisdom, and patience. I will never forget the pictures of us discussing or working late together in the evening and even at night. Huub, thank you for giving me the opportunity to pursue my PhD at Leiden University and for always giving key insightful comments and suggestions, which makes my publications and thesis better ones. I will definitely answer ‘Yes!’ the next time you ask me ‘Are you happy?’ since I’m glad that you like the outcomes of my research.

My gratitude to the BPOC/SSNMR members. Zhongwu and Xinmeng, I really enjoy the period we work in the same office. Thank you for always treating me like a little brother, especially in the early days of my arrival in the Netherlands. Rubin, thank you for all the scientific and non-scientific conversations we have during the coffee breaks and our walk around Leiden and even in Belgium. We had great times trying cuisines from different countries together. Jan Paul, you have made the best beer I’ve ever drunk. Thank you for always giving valuable supports and suggestions for my research. Dario, thank you for encouraging me every day while I was writing my thesis, and “everything would be great”. Laura, thank you for your kind help with the Dutch translation of my thesis. Jessica, thank you for helping me to start my research at the very beginning of my PhD.

Tirong and Lolita, thank you for helping me to turn on my PC every week during the lockdowns due to COVID-19. Liesbeth, as the heart of our group and always with a smile on your face, a lot of thanks to you for taking care of everything and for always being kind, friendly, and helpful. Agur, Alia, Anjali, Brijith, Chuang, Dieuwertje, Emanuela, Emiel, Faezeh, Fatemeh, Fons, Karthick, Kiran, Lijin, Maithili, Remco, Rianne, Rico, Suzanne, Titus, Vidya, Yuliya, as well as other people I met in the university, thank you all for making my PhD journey colorful and memorable.

I would also like to thank all my Chinese friends in Leiden. Especially, Mengjie, Xuequan, Xiaoting, and Shengxiang, I'm so lucky to have you as my heart-to-heart friends in a foreign country. Thank you for your company and support in the past four years. We tried a lot of things for the first time together that we had never done before, and maybe for the last time. I will never forget the relaxing, exciting, and wonderful time we had at the weekend dinners and during our trips around Europe. I wish you lots of opportunities and an infinitely bright future.

Special gratitude to China Scholarship Council (CSC) and Leiden University for funding and supporting my PhD study in all forms.

Last but not least, my heartfelt gratitude goes to my big family. Thanks to my parents, parents-in-law, my wife, and siblings for their strong support, love, understanding, and encouragement all the time and for taking care of my dear son who came into our life at the beginning of my 4th year of my PhD and is definitely the best “publication” in my academic career. No words can express my gratitude for all you have done for me. My highest gratitude and appreciation is deserved to my beloved wife. Thank you for giving me the opportunity of being a happy and joyful father and for taking care of our parents and everything well in my absence. You have more energy than you can imagine. Now it's time for me to bear the burden of life and take care of you all.